

**SPECTROSCOPIC STUDY OF METAL–RARE GAS  
COMPLEXES AND THE VIBRATIONAL DYNAMICS  
OF *para*-FLUOROTOLUENE**

**CAROLYN DAWN WITHERS**

**Thesis submitted to the University of Nottingham for  
the degree of Doctor of Philosophy**

**DECEMBER 2011**

## Abstract

This work contains two main areas of research within the field of bonding and spectroscopy. The first is the interactions of metals and metal ions with rare gas atoms; the second concerns vibrational dynamics in *para*-fluorotoluene (*p*FT). The research has been carried out as part of a collaboration between the SOCAR and Reid groups at the University of Nottingham and also involved external research teams.

The work combines the results from experiments employing several different spectroscopic techniques with theoretical calculations, which support the experimental data, assist in their interpretation and provide new information.

Resonance enhanced multiphoton ionisation spectroscopy is employed to investigate the Au–Xe and Au–Ne neutral complexes in the region of the  $6^2P_J \leftarrow 6^2S_{1/2}$  Au atomic transition. High-level *ab initio* calculations provide further insight, which is necessary to explain the unusual spectra obtained. A theoretical study of complexes containing Group 2 metal cations and rare gases also reveals some unexpected trends that are related to some of the effects seen in the Au–RG series.

A combination of nanosecond zero electron kinetic energy spectroscopy and time-resolved picosecond photoelectron spectroscopy is employed to investigate the vibrational dynamics of *p*FT. Excitation *via* several different vibrational states allows the study of a Fermi resonance, statistical intramolecular vibrational energy redistribution and an intermediate case that shows evidence of so-called “doorway states”.

***This thesis is dedicated to Mum and Dad.  
Thank you for all your love and support.***

**xxx**

## **Acknowledgements**

Firstly I would like to thank my supervisor, Tim Wright, for his excellent teaching, guidance and encouragement.

It has been a pleasure to work with the friendly people in the SOCAR group. I worked most closely with Richard Plowright and Adrian Gardner, who I would particularly like to thank for working insane hours to acquire very pretty spectra and explaining lots of things that wouldn't have made sense otherwise.

Other members of the SOCAR Group, past and present, who have contributed to the collection and processing of data and theoretical calculations include Mark Watkins, Victor Tamé-Reyes and summer and project students Kayla Gutsmedl, Jaiya Bhandari and Jack Graneek.

Thanks to Katharine Reid and the members of her group who collaborated with us on the *para*-fluorotoluene work: Julia Davies, who recorded the VMI-PES data and spent many patient hours explaining the finer points of IVR to me and Alistair Green, who taught me how to analyse the data.

I would also like to thank our external collaborators, Ed Lee, Michael Morse, Larry Viehland and Bill Breckenridge.

Thanks to the University of Nottingham and the EPSRC for funding.

I am very grateful to my family and friends for their love and encouragement and for believing in me. Worthy of particular mention are my beloved siblings, Paula, Nicky and Keith, my best friend Willow, Andy, Helen and the rest of my small group from Trent Vineyard.

Most importantly of all, I give thanks to Jesus Christ, without whom I can do nothing.

# Contents

<b>1.</b>	<b>Introduction</b>	<b>1</b>
	1.1. Interactions between Metals and Rare Gases	1
	1.2. Vibrational Dynamics in <i>para</i> -Fluorotoluene	2
	<b>References</b>	<b>3</b>
<b>2.</b>	<b>Background and Methods Employed in the Study of Metal-Rare Gas Complexes</b>	<b>5</b>
	2.1 Introduction	5
	2.2 Vibrational Levels and the Morse Potential	6
	2.3 Rotational Energy Levels	8
	2.4 Franck-Condon Factors	9
	2.5 Experimental Methods	11
	2.5.1 REMPI Technique	11
	2.5.2 Equipment Employed in REMPI Experiments	11
	2.6 Analysing REMPI Data	15
	2.6.1 Birge-Sponer Analysis	15
	2.6.2 LeRoy-Bernstein Analysis	15
	2.6.3 Isotopic Analysis	17
	2.7 Theoretical Methods	18
	2.8 Analysing Theoretical Results	19
	<b>References</b>	<b>20</b>
<b>3.</b>	<b>Electronic Spectroscopy of Au-RG Complexes (RG=Ne, Xe)</b>	<b>22</b>
	3.1 Introduction	22
	3.1.1 Au-Xe	22
	3.1.2 Au-Ne	24
	3.2 Experimental Methods	25
	3.3 Au-Xe Results	26
	3.3.1 Theoretical Results	26
	3.3.2 Experimental Results	27
	3.3.3 Franck-Condon Simulation	30
	3.3.4 Discussion	31

3.4 Au–Ne Results	39
3.4.1 Theoretical Results	39
3.4.2 Experimental Results	41
3.4.3 Franck-Condon Simulations	44
3.4.4 Discussion	48
3.5 Trends in the Au–RG series	49
3.6 Conclusions	51
<b>References</b>	<b>53</b>
<b>4. Theoretical Study of M<sup>+</sup>–RG and M<sup>2+</sup>–RG Complexes (M=Ca–Ra; RG=He–Rn)</b>	<b>56</b>
4.1 Introduction	56
4.2 Computational Details	58
4.3 Results	61
4.4 Trends	70
4.5 Discussion	72
4.6 Conclusions	84
<b>References</b>	<b>85</b>
<b>5. Theoretical Study of M<sup>+</sup>–RG and M<sup>2+</sup>–RG Complexes (M=Be, Mg; RG=He–Rn)</b>	<b>89</b>
5.1 Introduction	89
5.2 Computational Details	89
5.3 Results	91
5.4 Trends	98
5.5 Discussion	102
5.6 Conclusions	111
<b>References</b>	<b>113</b>
<b>6. Study of the Vibrational Dynamics of <i>para</i>-Fluorotoluene</b>	<b>117</b>
6.1 Introduction	117
6.2 Assignment of Vibrational Modes and Eigenstates	120
6.3 IVR Lifetimes	123

6.4 Nanosecond Zero Electron Kinetic Energy Spectroscopy	125
6.4.1 ZEKE Technique	125
6.4.2 Equipment Employed in ZEKE Experiments	126
6.5 Picosecond Photoelectron Spectroscopy	127
6.5.1 Photoelectron Spectroscopy Technique	127
6.5.2 Analysing VMI-PES Data	128
6.6 Introduction to Current Study	132
6.7 REMPI	132
6.8 $S_1$ $1^1$ Fermi Resonance	133
6.8.1 Results	133
6.8.2 Discussion	137
6.9 $S_1$ $18a^1$	140
6.9.1 Results	140
6.9.2 Discussion	144
6.10 $S_1$ $13^1$	145
6.10.1 Results	145
6.10.2 Discussion	149
6.11 $S_1$ $7a^1$	149
6.11.1 Results	149
6.11.2 Discussion	153
6.12 Conclusions	154
<b>References</b>	<b>155</b>
<b>7. Theoretical Study of <math>Cl^-</math>-RG Complexes (RG=He-Rn)</b>	<b>157</b>
7.1 Introduction	157
7.2 Computational Details	158
7.3 Results	159
7.4 Trends	162
7.5 Discussion	165
7.6 Conclusions	167
<b>References</b>	<b>168</b>
<b>Appendix A: Glossary of Acronyms/Abbreviations</b>	<b>171</b>

## Figures

### Chapter 2

2.1	General form of a diatomic potential energy curve.	7
2.2	Schematic diagram showing some allowed transitions to a higher excited electronic state.	10
2.3	Overview of REMPI apparatus.	12
2.4	Side view of vacuum chamber.	13
2.5	Opposite side view of vacuum chamber.	14
2.6	Rear view of vacuum chamber.	14
2.7	An example of a Birge-Sponer plot from theoretical data.	16

### Chapter 3

3.1	Schematic diagram showing the relationship between the atomic state combinations and the complex electronic states.	23
3.2	REMPI spectrum obtained from the $D^2\Pi_{1/2} \leftarrow X^2\Sigma_{1/2}^+$ transition in Au-Xe/Franck-Condon simulation.	28
3.3	Two-colour REMPI spectrum of Au-Xe in the region of the Au ( $6^2P_{3/2}$ ) energy.	29
3.4	Franck-Condon simulation of REMPI spectrum in Figure 3.3.	31
3.5	Schematic energy level diagram showing the energy region close to the Au $6^2P_j$ levels.	32
3.6	CASSCF + MRCI + Q + SO calculations on the excited states of Au-Xe.	35
3.7	CASSCF+MRCI+Q/aVQZ calculations for the $D^2\Pi_{1/2, 3/2}$ and $E^2\Sigma_{1/2}^+$ states of Au-Ne.	41
3.8	Single-colour REMPI of the $D^2\Pi_{1/2} \leftarrow X^2\Sigma_{1/2}^+$ transition for $^{197}\text{Au}-^{20}\text{Ne}$ .	42
3.9	Low energy region of the $D^2\Pi_{1/2} \leftarrow X^2\Sigma_{1/2}^+$ transition for $^{197}\text{Au}-^{20}\text{Ne}$ and $^{197}\text{Au}-^{22}\text{Ne}$ .	42
3.10	LeRoy-Bernstein and Birge-Sponer plots for the observed $^{197}\text{Au}-^{20}\text{Ne}$ spectrum.	43
3.11	Franck-Condon simulation of the observed $^{197}\text{Au}-^{20}\text{Ne}$ spectrum.	45
3.12	Simulated rotational profiles for the vibrational features in the experimental Au-Ne spectrum	46

3.13	Franck-Condon simulation of the $D^2\Pi_{3/2} \leftarrow X^2\Sigma_{1/2}^+$ transition for Au-Ar.	47
<b>Chapter 4</b>		
4.1	Variation in $R_e$ for $M^{n+}$ -RG (M=Ca, Sr, Ba and Ra; $n=1$ and 2).	71
4.2	BS plots for $Ca^+$ -Ar and $Ca^{2+}$ -Ar.	72
4.3	MOLDEN contour diagrams of the Hartree-Fock HOMO for each of the $M^+$ -RG complexes.	80
<b>Chapter 5</b>		
5.1	MOLDEN contour diagrams of the Hartree-Fock HOMO for each $M^+$ -RG complex.	99
5.2	BS plots for $Be^+$ -RG.	102
5.3	BS plots for $Mg^+$ -RG.	103
5.4	Calculated potential curve for $Mg^{2+}$ -Rn.	105
5.5	Reduced potentials for $Be^+$ -RG.	106
5.6	Reduced potentials for $Mg^+$ -RG.	106
5.7	Plot of $\kappa$ for the complexes studied herein and selected $Alk^+$ -RG series.	108
5.8	Plot of $\kappa$ for $M^+$ -RG and $M^{2+}$ -RG (M=Ca-Ra).	111
<b>Chapter 6</b>		
6.1	Examples of different IVR behaviour.	118
6.2	The structure of a <i>para</i> -fluorotoluene molecule.	120
6.3	Fundamental vibrational modes of substituted toluene derivatives.	121
6.4	Tier model for IVR.	124
6.5	Raw image recorded by VMI.	129
6.6	Image produced by inversion using pBasex.	130
6.7	Two-colour REMPI spectrum for <i>p</i> FT.	133
6.8	High-resolution nanosecond REMPI spectrum of <i>p</i> FT in the region of the Fermi resonance.	134
6.9	ZEKE spectra <i>via</i> each of the two eigenstates of the Fermi resonance seen in the REMPI spectrum.	134
6.10	SEVI spectra at selected time delays recorded <i>via</i> the Fermi resonance at $\sim 800\text{ cm}^{-1}$ in the REMPI spectrum.	135

6.11	Area under features identified in Figure 6.10 plotted against pump-probe time delay.	136
6.12	ZEKE spectrum <i>via</i> the $18a^1$ peak seen at $845\text{ cm}^{-1}$ in the REMPI spectrum.	140
6.13	SEVI spectra at selected time delays recorded <i>via</i> the $18a^1$ peak at $845\text{ cm}^{-1}$ in the REMPI spectrum.	141
6.14	Area under the peak labelled <i>C</i> in Figure 6.13 plotted against time elapsed.	141
6.15	Area under the peak labelled <i>B</i> in Figure 6.13 plotted against time elapsed.	142
6.16	Area under the peak labelled <i>D</i> in Figure 6.13 plotted against time elapsed.	143
6.17	ZEKE spectrum recorded <i>via</i> the $13^1$ peak seen at $1,195\text{ cm}^{-1}$ in the REMPI spectrum.	145
6.18	SEVI spectra at selected time delays recorded <i>via</i> the $13^1$ peak at $1,195\text{ cm}^{-1}$ in the REMPI spectrum.	146
6.19	Area under the peak labelled <i>A</i> in Figure 6.18.	147
6.20	Area under the peak labelled <i>C</i> in Figure 6.18.	147
6.21	Area under regions labelled <i>D</i> and <i>E</i> in Figure 6.18.	148
6.22	ZEKE spectrum <i>via</i> the $7a^1$ peak seen at $\sim 1230\text{ cm}^{-1}$ in the REMPI spectrum.	150
6.23	SEVI spectra at selected time delays recorded <i>via</i> the $7a^1$ peak at $1,230\text{ cm}^{-1}$ in the REMPI spectrum.	151
6.24	Area under peak <i>A</i> ( $\Delta v=0$ ) in Figure 6.23 plotted against time delay.	151
6.25	Areas under peaks <i>B</i> and <i>C</i> in Figure 6.23 plotted against time delay.	152
6.26	Areas under regions <i>D</i> and <i>E</i> in Figure 6.23 plotted against time delay.	152

## Chapter 7

7.1	Plot of $R_e$ for $X^-$ -RG ( $X=\text{F-Br}$ ; $\text{RG}=\text{He-Rn}$ ).	163
7.2	Plot of $D_e$ for $X^-$ -RG ( $X=\text{F-Br}$ ; $\text{RG}=\text{He-Rn}$ ).	164
7.3	Plot of $k$ for $X^-$ -RG ( $X=\text{F-Br}$ ; $\text{RG}=\text{He-Rn}$ ).	164
7.4	Comparison of experimental and computed standard mobility values for $\text{Cl}^-$ in Ar at 297 K.	166
7.5	Comparison of experimental and computed reduced mobility values for $\text{Cl}^-$ in Ar at 297 K.	167

## Tables

### Chapter 3

3.1	Calculated spectroscopic parameters for $^{197}\text{Au}-^{132}\text{Xe}$ $X^2\Sigma^+$ .	27
3.2	Spectroscopic constants derived for the $D^2\Pi_{1/2}$ and unassigned $\Omega=1/2$ states for $^{197}\text{Au}-^{132}\text{Xe}$ .	29
3.3	Calculated spectroscopic constants for the $X^2\Sigma^+$ state of Au-RG.	40
3.4	Derived spectroscopic parameters for the $^{197}\text{Au}-^{20}\text{Ne}$ $D^2\Pi_{3/2}$ state.	43

### Chapter 4

4.1	Spectroscopic constants for $\text{Ca}^+$ -RG.	62
4.2	Spectroscopic constants for $\text{Sr}^+$ -RG.	63
4.3	Spectroscopic constants for $\text{Ba}^+$ -RG.	63
4.4	Spectroscopic constants for $\text{Ra}^+$ -RG.	64
4.5	Spectroscopic constants for $\text{Ca}^{2+}$ -RG.	64
4.6	Spectroscopic constants for $\text{Sr}^{2+}$ -RG.	65
4.7	Spectroscopic constants for $\text{Ba}^{2+}$ -RG.	65
4.8	Spectroscopic constants for $\text{Ra}^{2+}$ -RG.	65
4.9	Spectroscopic constants for $\text{Ca}^+$ -RG and $\text{Ca}^{2+}$ -RG calculated at the RHF level and RCCSD(T) level.	75
4.10	Spectroscopic constants for $\text{Sr}^+$ -RG and $\text{Sr}^{2+}$ -RG calculated at the RHF level and RCCSD(T) level.	75
4.11	Spectroscopic constants for $\text{Ba}^+$ -RG and $\text{Ba}^{2+}$ -RG calculated at the RHF level and RCCSD(T) level.	76
4.12	Spectroscopic constants for $\text{Ra}^+$ -RG and $\text{Ra}^{2+}$ -RG calculated at the RHF level and RCCSD(T) level.	76
4.13	Calculated $Z$ values with removal of terms in the model potential given in Equation 4.1.	78
4.14	Energies of the lowest $^2D$ states of $\text{Ca}^+$ , $\text{Sr}^+$ , $\text{Ba}^+$ and $\text{Ra}^+$ .	79
4.15	Comparison of $R_e$ values ( $\text{\AA}$ ) for $\text{Alk}^+$ -RG, $\text{M}^+$ -RG and $\text{M}^{2+}$ -RG.	82

<b>Chapter 5</b>		
5.1	Spectroscopic constants for Be <sup>+</sup> -RG.	92
5.2	Spectroscopic constants for Mg <sup>+</sup> -RG.	93
5.3	Spectroscopic constants for Be <sup>2+</sup> -RG.	94
5.4	Spectroscopic constants for Mg <sup>2+</sup> -RG.	94
5.5	Ratio of polarisabilities of successive rare gases compared with ratios of successive values of $D_e R_e^4$ for each of the M <sup>+</sup> -RG series.	101
<b>Chapter 6</b>		
6.1	Experimental and calculated fundamental vibrational frequencies for normal modes of <i>p</i> FT.	138
6.2	IVR lifetimes of the three vibrational states showing irreversible decay in the population of the bright state.	155
<b>Chapter 7</b>		
7.1	Spectroscopic constants for Cl <sup>-</sup> -RG.	160

# Publications

## Chapter 3

*Electronic spectroscopy of the Au–Xe complex*, R. J. Plowright, M. J. Watkins, A. M. Gardner, C. D. Withers, T. G. Wright and W. H. Breckenridge, *Phys. Chem. Chem. Phys.*, **11**, 1539 (2009).

**The author carried out some of the ground state calculations for Au–Xe and the Franck–Condon simulation shown in Figure 4.**

*Electronic Spectroscopy of the  $6p \leftarrow 6s$  Transition in Au–Ne: Trends in the Au–RG Series*, R. J. Plowright, A. M. Gardner, C. D. Withers, T.G. Wright, M. D. Morse and W. H. Breckenridge, *J. Phys. Chem. A*, **114**, 3103 (2010).

**The author worked with R. J. Plowright to collect the experimental data and carried out the Franck-Condon simulations shown in Figures 9 and 11 and the rotational profile simulation shown in Figure 10. The author also performed the RCCSD(T) calculations and analysis for the Au–He and Au–Ne ground states and calculated the spectroscopic constants for the Au–Ar  $D^2\Pi_{3/2}$  state.**

## Chapter 4

*Theoretical study of  $Ba^{n+}$ –RG (RG=rare gas) complexes and transport of  $Ba^{n+}$  through RG ( $n=1,2$ ; RG=He–Rn)*, M. F. McGuirk, L. A. Viehland, E. P. F. Lee, W. H. Breckenridge, C. D. Withers, A. M. Gardner, R. J. Plowright, and T. G. Wright, *J. Chem. Phys.*, **130**, 194305 (2009).

**The author calculated the spectroscopic constants for Ba–RG, investigated the trends in collaboration with other members of the group and carried out the literature study.**

*Theoretical study of the bonding in  $M^{n+}$ –RG complexes and the transport of  $M^{n+}$  through rare gas ( $M=Ca, Sr, \text{ and } Ra$ ;  $n=1$  and  $2$ ; and RG=He–Rn)*, A. M. Gardner, C. D. Withers, T. G. Wright, K. I. Kaplan, C. Y. N. Chapman, L. A. Viehland, E. P. F. Lee, and W. H. Breckenridge, *J. Chem. Phys.*, **132**, 054302 (2010).

**The author performed the RCCSD(T) calculations and analysis in collaboration with A.M. Gardner, investigated the trends in collaboration with other members of the group, carried out the literature study and wrote the first draft of the paper.**

## Chapter 5

*Theoretical Study of  $M^+$ –RG and  $M^{2+}$ –RG Complexes and Transport of  $M^+$  through RG ( $M=Be$  and  $Mg$ , RG = He–Rn)*, A. M. Gardner, C. D. Withers, J. B. Graneek, T. G. Wright, L. A. Viehland and W. H. Breckenridge, *J. Phys. Chem. A*, **114**, 7631 (2010).

**The author performed the RCCSD(T) calculations and analysis in collaboration with A. M. Gardner, investigated the trends in collaboration with other members of the group and carried out the literature study.**

## Chapter 7

*Theoretical Study of Cl<sup>-</sup>-RG Complexes and Transport of Cl<sup>-</sup> through RG (RG=He-Rn), C. D. Withers, T. G. Wright, L. A. Viehland, L. Grossman, C. C. Kirkpatrick and E. P. F. Lee, J. Chem. Phys, **135**, 024312 (2011).*

**The author calculated the spectroscopic constants for Cl<sup>-</sup>-RG, investigated the trends in the series, carried out the literature study and wrote the first draft of the paper.**

# 1. Introduction

## 1.1 *Interactions between Metals and Rare Gases*

There is considerable interest in the interactions between metals (neutrals and ions) and ligands. Such interactions are commonplace in the upper atmosphere<sup>1,2</sup> but also occur in biological processes<sup>3</sup> and are important in industrial applications.<sup>4,5</sup> Understanding the details of the chemistry is therefore very important in several different fields.

The interactions here concern diatomic systems, one metal atom or ion with a single rare gas atom. One might expect the behaviour of these complexes to be quite straightforward, with bonding attributable to purely physical interactions, i.e. inductive and van der Waals forces; however some unexpected trends have been uncovered and the bonding has proven to be far from simple.

CM–RG complexes (CM = coinage metal [Cu, Ag and Au]; RG = rare gas) have previously been studied experimentally by Duncan and co-workers (Cu–Kr, Ag–RG [RG = Ar, Kr, Xe] and Au–Ar)<sup>6,7,8</sup> and Jouvét (Ag–Ar).<sup>9</sup> The SOCAR group have added to this research with a re-investigation of Au–Ar<sup>10</sup> and a study on Au–Kr.<sup>11</sup> This work is continued here with Au–Xe and Au–Ne. The neutral complexes have been studied experimentally using resonance enhanced multiphoton ionisation (REMPI) spectroscopy; this work has been supplemented by theoretical calculations, which assist in assigning the spectra and provide further insight into the reasons certain electronic states can be observed experimentally in the spectroscopy of some Au–RG complexes but not others. Trends across the whole series (including theoretical results for Au–He and Au–Rn) are also discussed.

Group 2  $M^+$ -RG complexes are of interest in this context because, like Au, Group 2 metal monocations have a single electron in the outermost  $s$  orbital (the  $d$  orbitals of transition metals are filled before the  $ns$  orbital). They might therefore be expected to show some similar behaviour.

The interactions of Group 2 metal ions and dications with rare gases have been studied in this work employing *ab initio* calculations. Previous research involving similar systems has been extensive and the results were summarised in a review article by Bellert and Breckenridge published in 2002.<sup>12</sup> This article also introduced a model potential that could be used to describe such systems if their interactions were assumed to be purely physical in origin. The theoretical results in this thesis are discussed with reference to the model potential. Previous relevant experimental and theoretical results are also discussed in detail in the relevant chapters.

## 1.2 *Vibrational Dynamics in para-Fluorotoluene*

Intramolecular vibrational redistribution (IVR) is the randomisation of energy across a molecule following the initial excitation of a specific mode of vibration or wavepacket. The suggestion that in some cases this process could be slow compared with collisions between molecules has led to the idea of bond-selective chemistry, where reactions could be controlled by making a specific bond more susceptible to rupture.<sup>13</sup>

IVR rates and the factors influencing them have been the subject of many investigations.<sup>14, 15, 16, 17, 18</sup> However, it has so far proven impossible to produce a unifying theory that will enable the prediction of an IVR rate for a specific system or excitation. The focus is therefore on the collection and analysis of empirical data.

The work in this thesis continues from that of previous studies carried out by the SOCAR and Reid groups into *para*-fluorotoluene. This molecule has previously been studied by Okuyama *et al.*<sup>19</sup> using nanosecond fluorescence. The Reid group added to this research, employing picosecond photoelectron spectroscopy to estimate IVR lifetimes following excitation *via* several different vibrational modes. This work was supplemented by zero electron kinetic energy (ZEKE) spectroscopy data, which was carried out by the SOCAR group.<sup>20,21,22,23,24</sup> More recent ZEKE data is compared and contrasted here to time-resolved picosecond photoelectron spectra; the time-resolved data gives more detailed information than that previously available of the vibrational dynamics following excitation *via* four selected vibrational states in the  $S_1$  electronic excited state.

## References

- 
- <sup>1</sup> R. J. Plowright, T. J. McDonnell, T. G. Wright and J. M. C. Plane, *J. Phys. Chem. A*, **113**, 33, 9354 (2009).
- <sup>2</sup> R. J. Plowright, T. G. Wright and J. M. C. Plane, *J. Phys. Chem. A*, **112**, 29, 6550 (2008).
- <sup>3</sup> R. A. Kumpf and D. A. Dougherty, *Science*, **261**, 1708 (1993).
- <sup>4</sup> R. P. Andres, R. S. Averback, W. L. Brown, L. E. Brus, W. A. Goddard, A. Kaldor, S. G. Louie, M. Moscovits, P. S. Peercy, S. J. Riley, R. W. Siegel, F. Spaepen and Y. Wang, *J. Mater. Res.* **4**, 704 (1989).
- <sup>5</sup> M. A. Duncan, *Annu. Rev. Phys. Chem.*, **48**, 69 (1997).
- <sup>6</sup> L. R. Brock and M. L. R. Brock and M. A. Duncan, *J. Chem. Phys.*, **103**, 9200 (1995).
- <sup>7</sup> L. R. Brock and M. A. Duncan, *Chem. Phys. Lett.*, **247**, 18 (1995).
- <sup>8</sup> A. M. Knight, A. Stangassinger and M. A. Duncan, *Chem. Phys. Lett.*, **273**, 265 (1997).
- <sup>9</sup> C. Jouvét, C. Lardeux-Dedonder, S. Martrenchard and D. Solgadi, *J. Chem. Phys.*, **94**, 1759 (1991).

- 
- <sup>10</sup> R. J. Plowright, V. L. Ayles, M. J. Watkins, A. M. Gardner, T. G. Wright and W. H. Breckenridge, *J. Chem. Phys.*, **127**, 204308 (2007).
- <sup>11</sup> R. J. Plowright, M. J. Watkins, A. M. Gardner, T. G. Wright and W. H. Breckenridge, *J. Chem. Phys.*, **129**, 154315 (2008).
- <sup>12</sup> D. Bellert and W. H. Breckenridge, *Chem. Rev.*, **102**, 1595 (2002).
- <sup>13</sup> D. Boyall and K. L. Reid, *Chem. Soc. Rev.*, **26**, 223 (1997).
- <sup>14</sup> C. S. Parmenter and B. M Stone, *J. Chem. Phys.*, **84**, 4710 (1986).
- <sup>15</sup> G. A. Bethardy, X. L. Wang and D. S. Perry, *Can. J. Chem.*, **72**, 652 (1994).
- <sup>16</sup> J. B. Hopkins, D. E. Powers and R. E. Smalley, *J. Chem. Phys.*, **73**, 683 (1980).
- <sup>17</sup> P. M. Felker and A. H. Zewail, *J. Chem. Phys.*, **82**, 2961 (1985).
- <sup>18</sup> E. R. T. Kerstel, K. K. Lehmann, T. F. Mentel, B. H. Pate and G. Scholes, *J. Phys. Chem.*, **95**, 8282 (1991).
- <sup>19</sup> K. Okuyama, N. Mikami and M. Ito, *J. Phys. Chem.*, **89**, 5617 (1985).
- <sup>20</sup> J. A. Davies, K. L. Reid, M. Towrie and P. Matousek, *J. Chem. Phys.*, **117**, 9099 (2002).
- <sup>21</sup> S. M. Bellm, P. T. Whiteside and K. L. Reid, *J. Phys. Chem. A*, **107**, 7373 (2003).
- <sup>22</sup> A. K. King, S. M. Bellm, C. J. Hammond, K. L. Reid, M. Towrie and P. Matousek, *Mol. Phys.*, **103**, 1821 (2005).
- <sup>23</sup> C. J. Hammond, V. L. Ayles, D. E. Bergeron, K. L. Reid and T. G. Wright, *J. Chem. Phys.*, **125**, 124308 (2006).
- <sup>24</sup> V. L. Ayles, C. J. Hammond, D. E. Bergeron, O. J. Richards and T. G. Wright, *J. Chem. Phys.*, **126**, 244304 (2007).

## 2. Background and Methods Employed in the Study of Metal-Rare Gas Complexes

### 2.1 Introduction

One might consider diatomic complexes to be among the simplest of systems to study. However, the interactions between metals and rare gases have proved to be most unusual, showing unexpected trends and prompting one to ask exactly when an interaction can be viewed as physical and when it must be viewed as chemical.

In the systems considered in this work, there are two main physical attractive forces to consider. The first is inductive, which usually only occurs if one interacting partner has a permanent charge or dipole moment. Of interest to the present work is that a metal ion can induce a dipole moment in a rare gas atom, which leads to an attraction between them. The second type of force, dispersive (or van der Waals) interactions, occur even where no permanent charge, dipole moment or multipole moment exists in either atom; a random fluctuation in one creates an instantaneous dipole moment, which similarly induces a dipole moment in the other. Both inductive and dispersive interactions lead to many higher order terms (ion/induced quadrupole, etc.) in the interaction potential. An ion/induced dipole interaction energy has an  $R^{-4}$  dependence, while for a random dipole/induced dipole interaction it is  $R^{-6}$  (where  $R$  is the internuclear separation). In some cases, however, dispersive forces can still dominate the interaction, as will be seen in Chapter 4.

At short  $R$ , repulsive forces rapidly become more dominant. These include the electrostatic repulsion between the electrons and between the nuclei

and also Pauli repulsion, since electrons are fermions and therefore obey the Pauli Exclusion Principle.

## 2.2 Vibrational Levels and the Morse Potential

The behaviour of a diatomic system can be modelled by treating it as a quantum mechanical harmonic oscillator. Similar to a classical ball-and-spring, the potential energy,  $V$ , of the system is given by

$$V = \frac{1}{2}kx^2 \quad (2.1)$$

Here  $k$  represents the force constant and  $x$  is the displacement. If Equation 2.1 is substituted into the Schrödinger equation,

$$\left( -\frac{\hbar^2}{2m} \frac{d^2}{dx^2} + V(x) \right) \psi = E\psi \quad (2.2)$$

the solutions for the allowed vibrational energies can be shown to be

$$E_v = h\omega_e \left( v + \frac{1}{2} \right) \quad (2.3)$$

The mass,  $m$ , must be replaced by the reduced mass,  $\mu$ , unless one of the atoms can be assumed to be infinitely heavy. For a diatomic with different masses  $m_a$  and  $m_b$ :

$$\mu = \frac{m_a m_b}{m_a + m_b} \quad (2.4)$$

The harmonic vibrational frequency,  $\omega_e$ , is dependent on the force constant and the reduced mass:

$$\omega_e = \frac{1}{2\pi} \sqrt{\frac{k}{\mu}} \quad (2.5)$$

In spectroscopy, Equation 2.3 is usually expressed as a term value

$$G(v) = \omega_e \left( v + \frac{1}{2} \right) \quad (2.6)$$

When this form is employed, both  $G$  and  $\omega_e$  are usually expressed in wavenumbers ( $\text{cm}^{-1}$ ).

For a strongly bound system, the harmonic approximation can be used at low  $v$ . In reality, the potential of a diatomic system is anharmonic and the bond will break if sufficient energy is supplied. The true form of the potential is shown in Figure 2.1.

At very close range, nuclear, electronic and Pauli repulsion are dominant, while the attractive forces (see Section 2.1) are more significant at larger  $R$ . There have been attempts to describe the potential accounting for the repulsive and attractive parts, one of the most successful being the Morse potential.

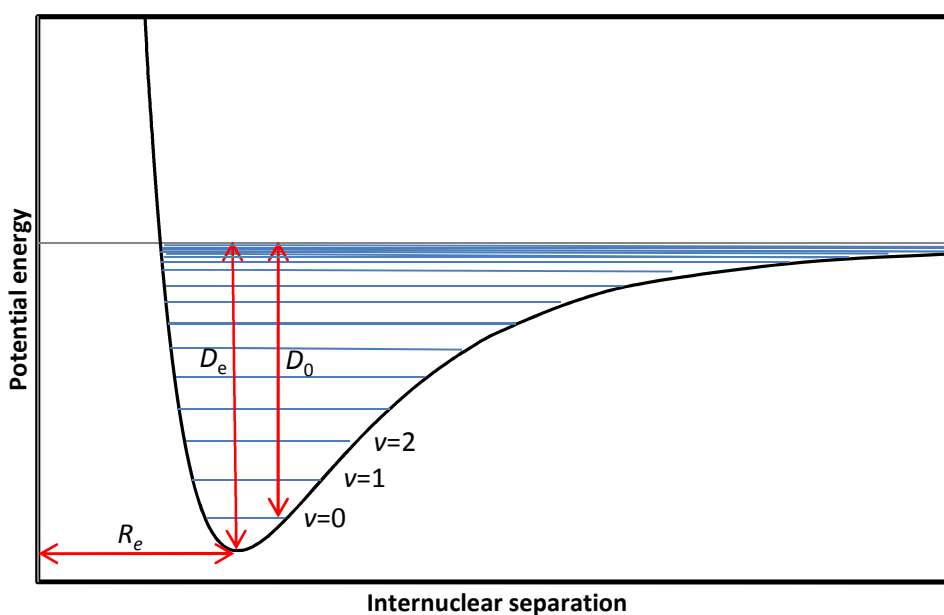


**Figure 2.1: General form of a diatomic potential energy curve. The parameters marked are  $D_e$ , the depth of the potential,  $D_0$ , the energy between the zero-point and the asymptote and  $R_e$ , the equilibrium bond separation.**

The Morse potential has the form

$$V = D_e[1 - e^{-a(r-r_e)}]^2 \quad (2.7)$$

$D_e$  is the depth of the potential well and  $a$  is a constant that depends on the molecule and electronic state.

Substituting this expression for the potential into the Schrödinger equation (2.2) gives

$$E_v = h\omega_e\left(v + \frac{1}{2}\right) - h\omega_e x_e\left(v + \frac{1}{2}\right)^2 \quad (2.8)$$

or, as a term value

$$G_v = \omega_e\left(v + \frac{1}{2}\right) - \omega_e x_e\left(v + \frac{1}{2}\right)^2 \quad (2.9)$$

The second term on the right-hand side of Equation 2.9 accounts for the anharmonicity and  $\omega_e x_e$  is known as the anharmonicity constant. The Morse potential works well near the bottom of the potential well, but fails at higher vibrational levels.

### 2.3 Rotational Energy Levels

Diatomic molecules or complexes have two axes of rotation, with the centre of mass as the origin. The moment of inertia is defined as

$$I = \mu R^2 \quad (2.10)$$

The total rotational angular momentum,  $M$ , is quantised and has the allowed values

$$M^2 = \hbar^2 N(N + 1) \quad (2.11)$$

$N$  is the rotational quantum number and can take the values 0, 1, 2, etc.

The classical rotational energy is given by

$$E_{rot} = \frac{M^2}{2I} \quad (2.12)$$

Substituting from Equations 2.10 and 2.11 gives the result

$$E_N = \frac{\hbar^2 N(N+1)}{2\mu R^2} = BN(N+1) \quad (2.13)$$

This gives the definition for the rotational constant,  $B$ , which is inversely proportional to the square of the internuclear separation.

## 2.4 Franck-Condon Factors

Electronic transitions occur when there is an interaction between the complex and a photon. The probability of a transition is given by  $|M_{21}|^2$ , where  $M_{21}$  is the transition dipole moment for a transition from level 1 to level 2. The transition dipole moment can be calculated from the rovibronic wavefunctions of the respective levels and the electric dipole moment operator,  $\mu$ .

$$M_{21} = \int \psi_2 \mu \psi_1 d\tau \quad (2.14)$$

The integral includes both spatial and spin coordinates. Using the Born-Oppenheimer approximation, the wavefunction can be factorised into its electronic, vibrational and rotational parts.

Ignoring the rotational part, which depends on the orientation of the molecule relative to an arbitrary axis, the transition dipole moment can be expressed in terms of the electronic and nuclear coordinates,  $r$  and  $R$ :<sup>1</sup>

$$M_{21} = \int \psi_{1e}(r, R_e) \mu_e \psi_{2e}(r, R_e) dr \int \psi_{1v}(R) \psi_{2v}(R) dR \quad (2.15)$$

It is assumed that the electronic wavefunction can be approximated at all times during a vibration by using the equilibrium nuclear separation,  $R_e$ . Equation 2.15 forms the basis of electronic and vibrational selection rules, determined by the first and second integrals on the right hand side respectively.

The square of the second integral is known as the Franck-Condon factor (FCF). The Franck-Condon principle states that an electronic transition is rapid when compared to the period of molecular vibration. The consequence of this is that when a diatomic molecule or complex is excited into a higher electronic state, the instantaneous value of  $R$  remains constant, i.e. only vertical transitions are allowed (see Figure 2.2).

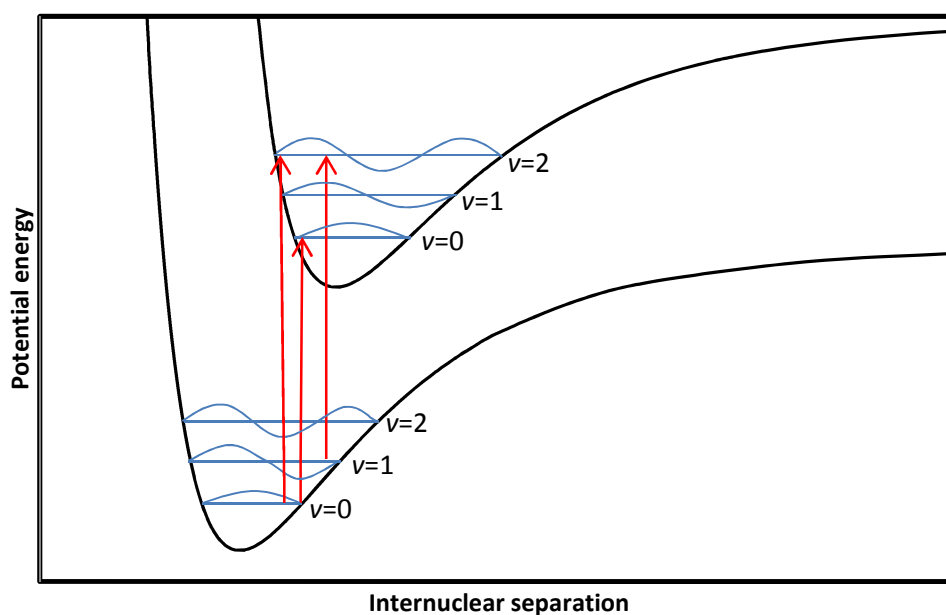


**Figure 2.2: Schematic diagram showing some allowed transitions to a higher excited electronic state.**

The FCF describes the extent to which the vibrational wavefunctions of the two levels involved in a transition overlap. In Figure 2.2 it can be seen that for the  $v'=0 \leftarrow v''=0$  transition the FCF will be small and excitation to a higher vibrational level is more likely. This would be reflected in the intensities of the relevant peaks in the spectrum. Franck-Condon simulations use calculated potential curves to estimate the appearance of a spectrum based on the Franck-Condon factors.

## 2.5 *Experimental Methods*

### 2.5.1 *REMPI Technique*

In this thesis, results will be presented that arise from the probing of the vibrational levels in selected electronic excited states of the neutral Au–Ne and Au–Xe complexes using resonance enhanced multiphoton ionisation (REMPI) spectroscopy. In a one-colour, two-photon REMPI process (1+1), the complex absorbs two photons from the same laser pulse. The probability of absorption is greater when the photon energy is resonant with a vibrational level in the excited electronic state. The laser is therefore scanned through a range of photon energies; when the energy is resonant with a vibrational level in the excited state, more ions will be detected. For a two-colour, two-photon REMPI process (1+1'), a separate laser is used for ionisation. The energy of this second laser can then be fixed; this has the advantage that levels at energies of less than half the ionisation potential of the complex can be scanned in a two-photon process.

### 2.5.2 *Equipment Employed in REMPI Experiments*

The equipment employed for REMPI experiments by the SOCAR group has already been described in detail in refs. 2, 3 and 4; a brief description is included here to provide context for the results presented in Chapter 3.

A gold rod (Goodfellow, 99.95%, 25 mm length, 5 mm diameter) was held in a custom-built laser vaporisation (LaVa) source. Au atoms were ablated using the second harmonic of a Nd:YAG laser (Continuum Minilite II, 532 nm, ~6 mJ/pulse). The rod was slowly translated and rotated by a four-phase stepper motor (Philips, unipolar 7.5° step angle, 12V 5.3W); this ensured continual ablation from a new area of the rod. The Au atoms were

picked up in a pulse of gas, which then passed through a narrow exit channel allowing collisional cooling of the Au atoms to occur before the gas pulse entered a high-vacuum chamber (working pressure  $\sim 8 \times 10^{-5}$  bar), resulting in a supersonic jet expansion.

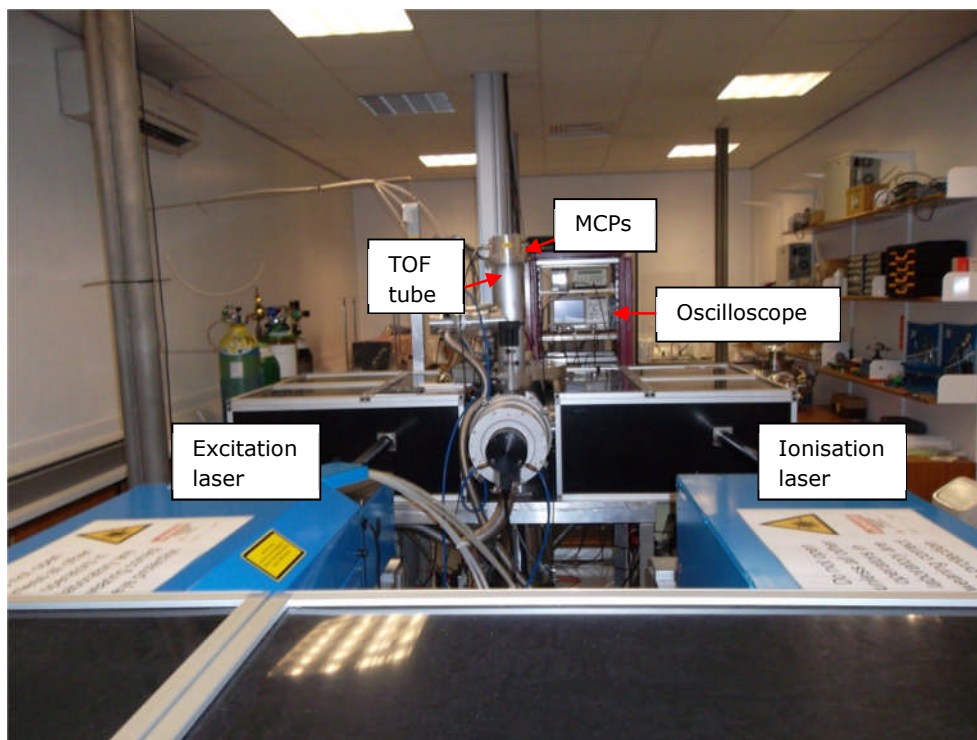


**Figure 2.3: Overview of REMPI apparatus. Lasers are labelled as for two-colour experiments; for one-colour experiments the same laser is used for both steps.**

The Au-RG complexes were formed in this expansion. On entering the ionisation chamber the pulse was intersected by the excitation/ionisation lasers (tunable dye lasers, Sirah Cobra Stretch). More details of the laser frequencies and dyes used are included in Chapter 3.

The ions were repelled into a time-of-flight (TOF) tube by plates held at a positive voltage before being detected by the microchannel plates (MCPs). The time taken to reach the MCPs was dependent on the mass and charge of the ion. The oscilloscope (LeCroy LT342 Waverunner) signal could

therefore be used as a mass spectrometer, showing the times at which ions were detected by the MCPs. The Au signal was easily identifiable and could therefore be used as a reference to identify other peaks by mass. By scanning the laser and monitoring the oscilloscope, it was therefore possible to find a resonant frequency for a complex since an ion peak was visible only when the appropriate frequency was reached.

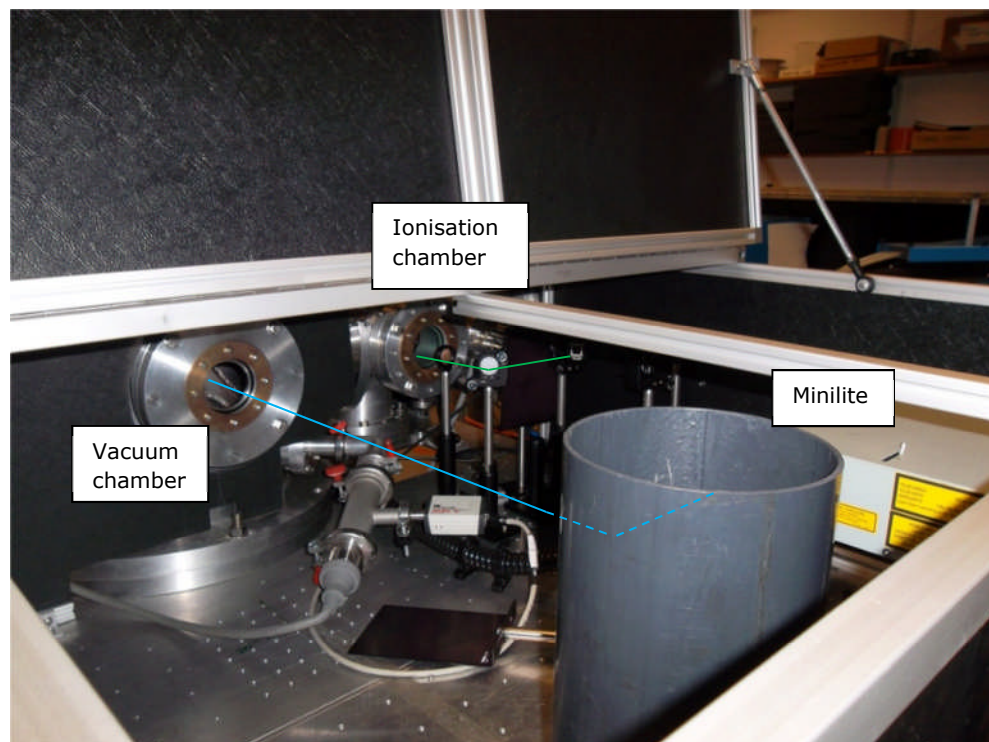


**Figure 2.4: Side view of vacuum chamber showing position of Minilite used for ablation of gold rod (path shown in blue).**

The apparatus is set up to detect signals at the TOF of the singly ionised complex. The excitation laser is then scanned in the region near the resonance. The signal was amplified (SRS SR445A) before being passed to the oscilloscope and then averaged by the boxcar (SRS SR250). Finally the data was received by a computer and recorded using the Stanford Research Systems SR272 data acquisition program.

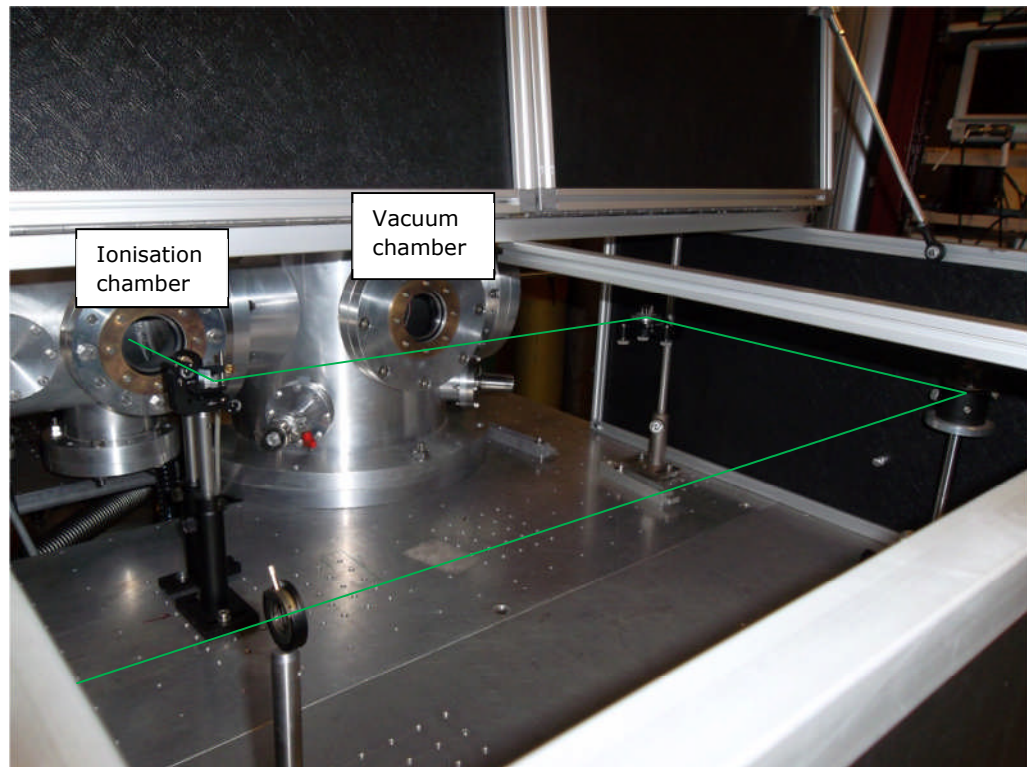


**Figure 2.5: Opposite side view of vacuum chamber to that shown in Figure 2.4. Path of ionisation laser is shown in green.**

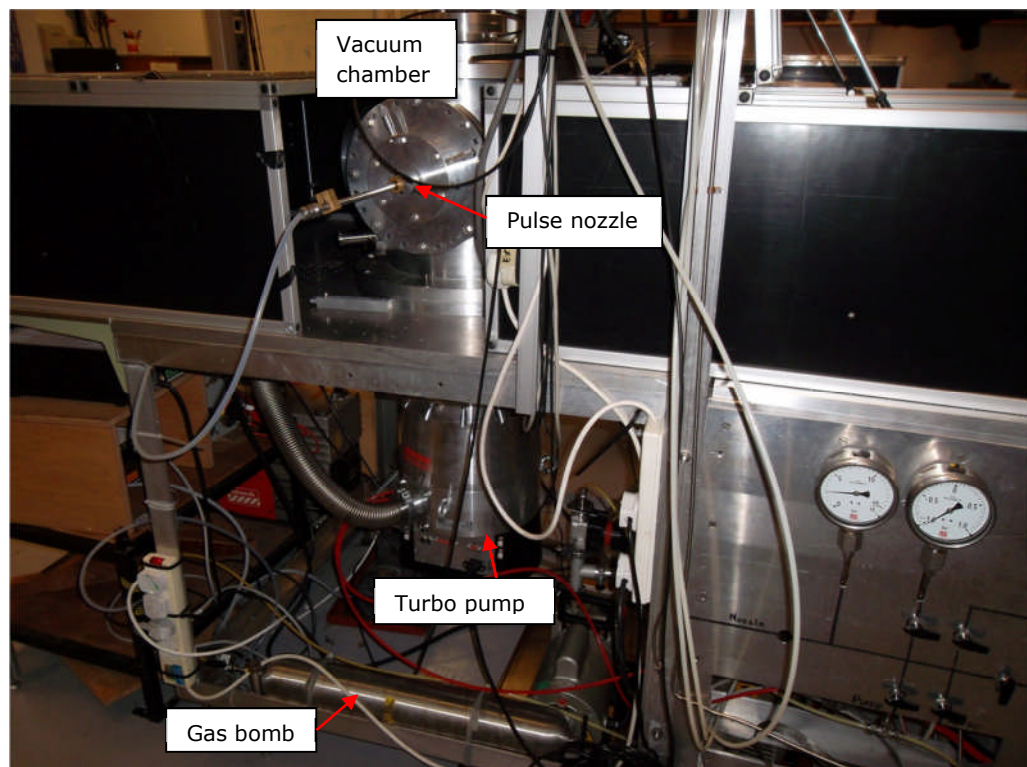


**Figure 2.6: Rear view of vacuum chamber.**

## 2.6 Analysing REMPI Data

### 2.6.1 Birge-Sponer Analysis

Once a REMPI spectrum has been obtained, from Equation 2.9 it can be shown that the spacing between the vibrational peaks,  $G_{v+1}-G_v$  is given by

$$\Delta G_{v+\frac{1}{2}} = \omega_e - 2\omega_e x_e (v + 1) \quad (2.16)$$

A plot of  $\Delta G_{v+\frac{1}{2}}$  against  $v+1$  can therefore be used to calculate the spectroscopic constants  $\omega_e$  and  $\omega_e x_e$  for the first excited state. This is described as a Birge-Sponer (BS) plot.

$D_0$  is simply given by the sum of the energy spacings, or the area under the plot. This can be shown to be given by

$$D'_0 = \frac{\omega_e'^2}{4\omega_e x_e'} - \frac{\omega_e'}{2} + \frac{\omega_e x_e'}{4} \quad (2.17)$$

The first term on the right-hand side of Equation 2.17 is equal to the depth of the potential:

$$D'_e = \frac{\omega_e'^2}{4\omega_e x_e'} \quad (2.18)$$

The ground state dissociation energy can then be estimated.

$$D''_0 = D'_0 + T_0 - \Delta E_M \quad (2.19)$$

The quantity  $T_0$  is the electronic transition energy for the  $v_0' \leftarrow v_0''$  transition and  $\Delta E_M$  is the energy of the equivalent transition in the free metal atom.

### 2.6.2 LeRoy-Bernstein Analysis

In practice, a BS plot will only be linear for vibrational levels near the base of the potential well. The gradient of the plot will tend to decrease as the dissociation limit is reached (see Figure 2.7). If the recorded spectrum shows vibrational levels near the dissociation limit the dissociation energy

may therefore be overestimated. In this case, the LeRoy-Bernstein (LB) analysis<sup>5,6</sup> may be more appropriate.

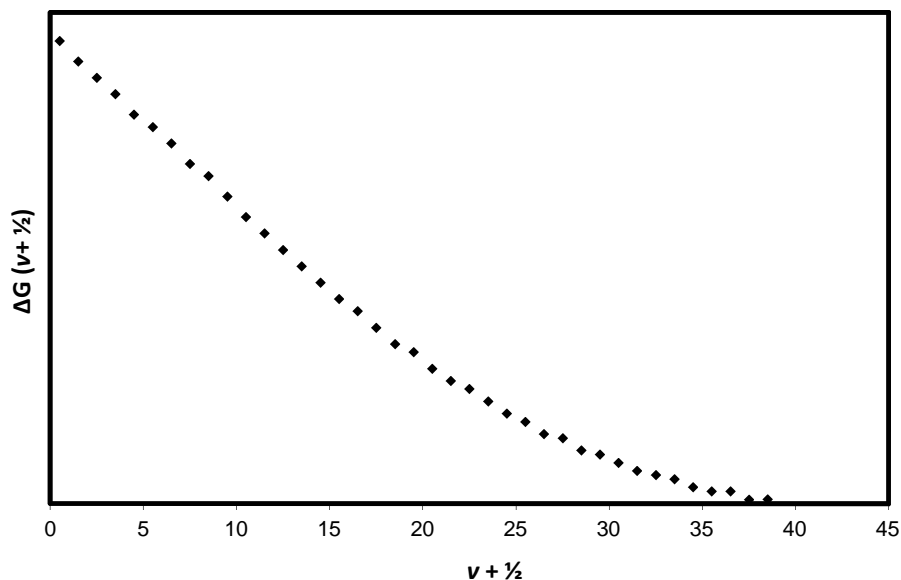


**Figure 2.7: An example of a Birge-Sponer plot from theoretical data and Equation 2.16. Note the curvature of the plot at high  $v$ .**

In their work, LeRoy and Bernstein suggested that if the attractive potential can be modelled as  $-\frac{C}{R^n}$  (where  $C$  and  $n$  are constants) and the vibrational first differences,  $\Delta G_v$ , are defined as

$$\Delta G_v = \frac{[E_{v-1} - E_{v+1}]}{2} \quad (2.20)$$

then

$$\Delta G_v \left[ \frac{2n}{(n+2)} \right] \propto D'_0 - E_v \quad (2.21)$$

where  $E_v$  is the vibrational energy of the state. In the case of the Au-RG complexes, the interaction is that of a random dipole/induced dipole and hence the potential varies as  $R^{-6}$  (i.e.  $n=6$ ). A plot of  $\Delta G_v^{3/2}$  against  $E_v$  should therefore be linear, with  $D_0$  as the intercept.

The LB method is expected to give more reliable values of  $D_0$  where spectra are recorded with vibrational levels near the dissociation limit. It is not appropriate for levels near the bottom of the potential unless the well is very shallow.

### 2.6.3 Isotopic Analysis

In order to determine the spectroscopic constants using either the BS or LB analyses, it is necessary first to assign an absolute vibrational numbering to the spectrum. If only one isotopologue of the complex can be seen experimentally, this is very difficult, although it may be achievable through a Franck-Condon simulation and high level *ab initio* calculations. The most reliable method is through isotopic analysis.

The vibrational levels of two different isotopologues of the same complex are slightly shifted relative to each other. The shift is given by the following formula

$$\Delta v = (1 - \rho)\omega_e' \left( v + \frac{1}{2} \right) - (1 - \rho)^2 \omega_e x_e' \left( v + \frac{1}{2} \right)^2 \quad (2.22)$$

where  $\rho$  is the square root of the ratio of the reduced masses of the two isotopologues.<sup>4</sup>

The first observed vibrational number is assigned the value  $\xi$ . A BS analysis can then be carried out for different values of  $\xi$ . From Equation 2.16,  $\omega_e x_e'$  can be determined from the gradient, which will be the same for each plot;  $\omega_e'$  will have a different value for each value of  $\xi$ . Using Equation 2.22, it is then possible to derive theoretical curves of  $\Delta v$  against  $v - \xi$  for different values of  $\xi$ . The experimental values can then be plotted and compared with the theoretical curves to determine the value of  $\xi$ .

## 2.7 Theoretical Methods

It is often useful to perform theoretical calculations in addition to carrying out experimental work. These can be compared to results obtained experimentally to check their accuracy, employed as a guideline when there are discrepancies in parameters derived from different experiments or using different methods and also used to investigate states and systems that cannot be studied experimentally, for example in the cases of Au–He or Au–Rn, where either the bond is too weak for the complex to be formed experimentally or because the chemicals are unsafe to use in a laboratory.

There are many computational methods available to calculate the potential energy curves of diatomic systems. Several of them have been employed by other researchers in previous investigations of some of the complexes described in Chapters 4 and 5. The methods are described in standard computational chemistry textbooks such as Ref. 7. As stated therein, in general the accuracy depends on the ability of the method to describe the electron correlation and, with a medium-sized basis set, is expected to follow the order below.

$$\text{HF} \ll \text{MP2} < \text{CISD} < \text{MP4}(\text{SDQ}) \sim \text{CCSD} < \text{MP4} < \text{CCSD}(\text{T}) \quad (2.23)$$

The method chosen depends on a balance between the accuracy required and the cost in computing time. In this work, the majority of calculations are at the RCCSD(T) level. This is the so-called ‘gold standard’ of quantum chemistry and is usually expected to give accurate results in these systems. For larger atoms only the outermost electrons are included in the correlation; the inner orbitals are approximated using an effective core potential (ECP). This is a reasonable approximation as the inner electrons are not usually involved in bonding. The details of basis sets used are given in the relevant chapters.

The calculations have included corrections for basis set superposition error (BSSE) effects. This arises because for calculations involving both atoms the basis sets of both atoms are used, whereas for calculations involving only one atom this will not be the case. This means that the energy in the former case will be artificially lower.

The full counterpoise correction accounts for this by using a 'dummy' atom; calculations employ the basis functions of the absent atom but not the nucleus or electrons. The correction can be calculated in terms of two atoms,  $A$  and  $B$  with energies calculated using the basis sets  $a$  and  $b$  respectively:

$$\Delta E_{CP} = E(A)_{ab} + E(B)_{ab} - E(A)_a - E(B)_b \quad (2.24)$$

For greater accuracy, the *ab initio* calculations can be performed using two basis sets (e.g. QZ and 5Z) and then extrapolated to the basis set limit (the energy that would be obtained were it possible to perform the calculation with an infinite number of basis functions). This is done using the two-point formula of Halkier *et al.*<sup>8,9</sup>

$$E_{\infty}(E_x, E_y) = \frac{x^3 E_x - y^3 E_y}{x^3 - y^3} \quad (2.25)$$

Chapter 3 also includes some CASSCF multi-reference calculations including spin orbit coupling (CASSCF+MRCI+SO), which are used for the excited states of Au-RG complexes. Multi-reference calculations are necessary when considering states that interact with each other.

## 2.8 Analysing Theoretical Results

The calculations in this work were performed using MOLPRO.<sup>10</sup> Potential energy curves have been calculated pointwise. This curve is then used as input to the LEVEL<sup>11</sup> program, which calculates an interpolated curve in addition to the values of  $E_v$  and  $B_v$  for each bound level in the complex.

A precise value for  $R_e$  can be obtained directly from the minimum of the curve. A fit to a plot of  $E_v$  against  $v+1/2$  for the lowest few levels can be used to obtain  $\omega_e$  and  $\omega_e x_e$  (see Equations 2.8 and 2.9). The values of  $\alpha$  and the equilibrium rotational constant,  $B_e$ , can be found by plotting  $B_v$  against  $v+1/2$  and using the equation

$$B_v = -\alpha \left( v + \frac{1}{2} \right) + B_e \quad (2.26)$$

## References

- 
- <sup>1</sup> A. Ellis, M. Feher and T. Wright, *Electronic and Photoelectron Spectroscopy Fundamentals and Case Studies*, Cambridge University Press, Cambridge (2005).
- <sup>2</sup> Richard Plowright, *Thesis*, Spectroscopy and Interactions of Metal and Metal Cation Complexes, University of Nottingham (2010)
- <sup>3</sup> R. J. Plowright, V. L. Ayles, M. J. Watkins, A. M. Gardner, R. R. Wright, T. G. Wright and W. H. Breckenridge, *J. Chem. Phys.*, **127**, 204308 (2007).
- <sup>4</sup> R. J. Plowright, A. M. Gardner, M. J. Watkins, T. G. Wright, W. H. Breckenridge, F. Wallimann and S. Leutwyler, *J. Chem. Phys.*, **129**, 154315 (2008).
- <sup>5</sup> R. J. LeRoy and R. B. Bernstein, *J. Chem. Phys.* **52**, 3869 (1970).
- <sup>6</sup> R. J. LeRoy and R. B. Bernstein, *J. Mol. Spec.*, **37**, 109 (1971).
- <sup>7</sup> F. Jensen, *Introduction to Computational Chemistry, Second Edition*, John Wiley & Sons Ltd., Chichester (2007).
- <sup>8</sup> A. Halkier, T. Helgaker, P. Jorgensen, W. Klopper, and J. Olsen, *Chem. Phys. Lett.*, **302**, 437 (1999).
- <sup>9</sup> A. Halkier, T. Helgaker, P. Jorgensen, W. Klopper, H. Kock, J. Olsen and A. K. Wilson, *Chem. Phys. Lett.*, **286**, 243 (1998).
- <sup>10</sup> R. D. Amos, A. Bernhardsson, A. Berning, P. Celani, D. L. Cooper, M. J. O. Deegan, A. J. Dobbyn, F. Eckert, C. Hampel, G. Hetzer, P. J. Knowles, T. Korona, R. Lindh, A. W. Lloyd, S. J. McNicholas, F. R. Manby, W. Meyer, M. E. Mura, A. Nicklass, P. Palmieri, R. Pitzer, G. Rauhut, M. Schütz, U. Schumann, H. Stoll, A. J. Stone, R. Tarroni, T. Thorsteinsson and H.-J. Werner, MOLPRO, a package of ab initio programs designed by H.-J. Werner and P. J. Knowles, Version 2002.1 (2002).

---

<sup>11</sup> R. J. LeRoy, Level 7.2—A computer program for solving the radial Schrödinger equation for bound and quasibound levels, and calculating various values and matrix elements, University of Waterloo Chemical Physics Research Program Report CP-555R (2000).

### 3. Electronic Spectroscopy of Au–RG Complexes (RG=Ne, Xe)

#### 3.1 Introduction

The experimental work on Au–Xe was completed before the author joined the Spectroscopy of Complexes and Radicals (SOCAR) group at the University of Nottingham. The experimental data for Au–Ne was collected in collaboration between Richard Plowright and the author. Several of the figures in this chapter were previously published in Ref. 1; these are acknowledged in the figure captions. In addition, a Franck-Condon simulation has been carried out by the author using experimental Au–Ar data previously published in ref. 2.

##### 3.1.1 Au–Xe

Following previous investigations into Au–Ar and Au–Kr complexes by the SOCAR group<sup>2,3</sup> Au–Xe has been studied using high resolution spectroscopy. This work has been supplemented with high-level *ab initio* calculations and Franck-Condon simulations, which provide further insight and assist with the assignment of the reported spectra.

The Au–Xe complex is of particular interest because, unlike others in the Au–RG series, some evidence of chemical bonding has been proposed in the cation.<sup>4,5,6,7,8</sup> However, these results contradict some conclusions made by others.<sup>9</sup>

An important step towards experimental study of the cation is the characterisation of electronic states in the neutral species. The region studied in this case is in the vicinity of the  $6^2P_J \leftarrow 6^2S_{1/2}$  Au atomic transition; the corresponding molecular orbitals are shown in Figure 3.1. It

was found for Au–Ar and Au–Kr that the  $D^2\Pi_{1/2}$  and  $D^2\Pi_{3/2}$  excited states are bound considerably more strongly than the  $X^2\Sigma_{1/2}^+$  ground state. This has been attributed to the shift in the electron density off the internuclear axis, thus allowing greater interaction between the rare gas atom and the cationic gold core. Related effects have been observed in the Group 2–RG cationic complexes (this will be discussed further in Chapters 4 and 5). The interactions in these excited states of Au–Xe may therefore be expected to mimic those in the cation.

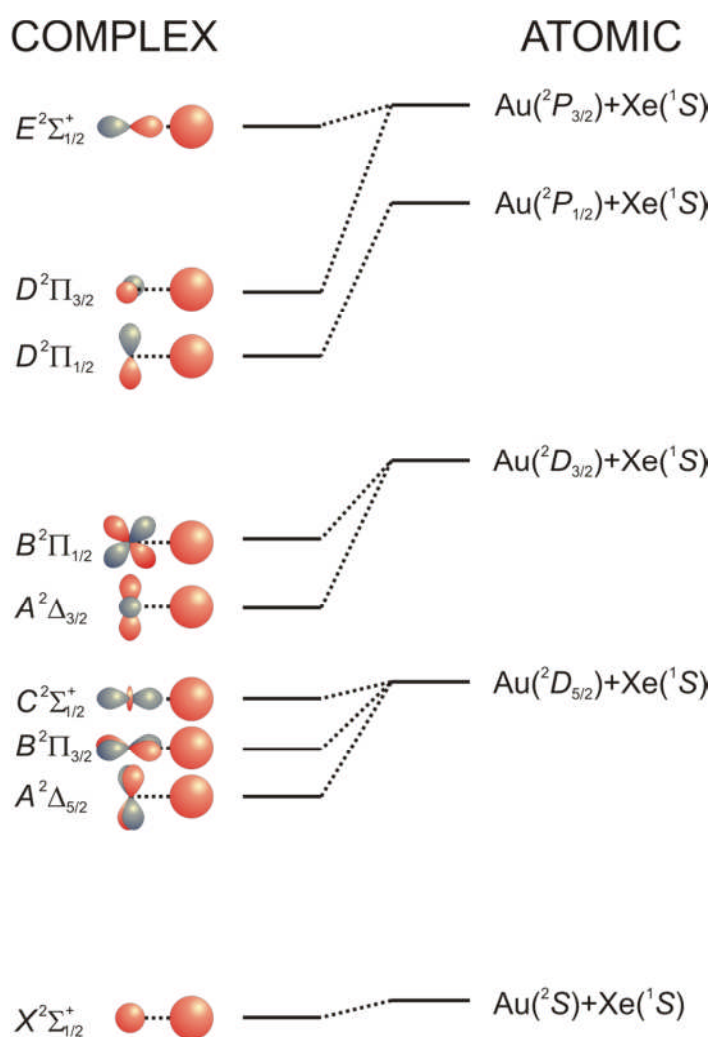


**Figure 3.1: Schematic diagram showing the relationship between the atomic state combinations (on the right-hand side of the figure), and the complex electronic states (left-hand side). The large, doubly occupied 6s orbital surrounding the much smaller, singly occupied 5d orbitals shown has been omitted from the  $5^2D$  states for clarity. Figure reproduced from Ref. 1.**

In contrast, electron density in the  $E^2\Sigma_{1/2}^+$  state is located along the internuclear axis, making the bond weaker. It is therefore unsurprising that this state has not been observed in Au–Ar or Au–Kr, although effects from its interaction with the  $D^2\Pi_{1/2}$  state were seen in Au–Ar; this caused a “shelf” in the outer wall of the  $D^2\Pi_{1/2}$  state, which was manifested in the spectrum as a sudden drop in the line spacing and symmetric rotational profiles at high energy.

There are a number of naturally occurring isotopes of xenon [the most abundant include  $^{128}\text{Xe}$ (1.9%),  $^{129}\text{Xe}$ (26.4%),  $^{130}\text{Xe}$ (4.1%),  $^{131}\text{Xe}$ (21.2%),  $^{132}\text{Xe}$ (26.9%),  $^{134}\text{Xe}$ (10.4%) and  $^{136}\text{Xe}$ (8.9%)],<sup>10</sup> which has allowed absolute vibrational numbering of the progressions in the spectra to be determined from the shifts observed for the different isotopologues (see Chapter 2).

### 3.1.2 Au–Ne

Au–Ne was similarly investigated to complete the work on the Au–RG series. No previous work on this complex was found in the literature; however the results obtained earlier for other complexes in this series indicated a clear relationship between the polarisability of the rare gas and the strength of the bond in the ground state of the complex. As noted above, the  $D^2\Pi_{\Omega}$  states are more strongly bound since the electron density is located off the internuclear axis. This effect would also be expected to increase with polarisability, which can be clearly seen in the recorded spectra as a red shift from the associated atomic transition. Given the low polarisability of Ne, one would expect the Au–Ne complex to be less strongly bound than any of the previous complexes studied, with the increase in bond strength between the  $X^2\Sigma_{1/2}^+$  state and the  $D^2\Pi_{1/2}$  and  $D^2\Pi_{3/2}$  excited states being less pronounced. A review by Bellert and

Breckenridge<sup>11</sup> notes that significantly weaker bonding in Ne complexes with isovalent alkaline earth metal cations has previously been attributed to its low polarisability.

As with Au–Xe, the current study has combined REMPI spectroscopic experiments in the vicinity of the  $^2P_J \leftarrow ^2S_{1/2}$  atomic Au transitions with high-level *ab initio* calculations, which have been used to characterise the potential energy curves of the ground state and the excited states of interest.

Neon has fewer stable isotopes than xenon; only two are found naturally in significant abundance [ $^{20}\text{Ne}$  (90.5%) and  $^{22}\text{Ne}$  (9.3%)]<sup>12</sup>. It was possible to obtain spectra for both these isotopes and hence derive the absolute vibrational numbering.

### 3.2 Experimental Methods

A thorough description of the experimental procedure for the Au–RG experiments can be found in Refs. 1, 2, and 3 and so only a brief description of the details specific to these experiments is presented here for completeness.

The rare gas [either Ne or a small quantity of Xe in a carrier gas (Ne or Ar)] was pulsed over a gold rod (Goodfellow, 99.95% pure) held in the LaVa source. The gas mixture originated from a holding cylinder, which was held at approximately 11 bar. Au atoms were ablated from the rod using the second harmonic of a Nd:YAG laser (Continuum Minilite II, 532 nm, ~6 mJ/pulse). Au–RG clusters were formed in the expansion following passage through a narrow exit channel into the vacuum chamber.

In the case of Au–Ne, one-colour REMPI was used for all experiments; specifically from the frequency-doubled output of a Sirah dye laser pumped

by the third harmonic of a Surelite III Nd:YAG laser (355 nm,  $\sim 120$  mJ/pulse). The investigations into the  $D^2\Pi_{1/2}$  state required Coumarin 540A as the laser dye, while Coumarin 480 was used for investigations of the  $D^2\Pi_{3/2}$  state.

For Au–Xe, both one-colour and two-colour ionisation schemes were employed. The  $^2P_{1/2} \leftarrow ^2S_{1/2}$  energetic region was investigated with one-colour REMPI; this employed the frequency-doubled output of a Sirah dye laser pumped by the second harmonic of a Surelite III Nd:YAG laser (532 nm,  $\sim 100$  mJ/pulse) with Coumarin 540A as the laser dye. Two-colour REMPI was employed for the  $^2P_{3/2} \leftarrow ^2S_{1/2}$  energetic region; this required the counter-propagating frequency-doubled outputs of two Sirah dye lasers, utilising the laser dyes Coumarin 480 for the excitation step and Rhodamine B for the ionisation step. The excitation step again employed the second harmonic of the Surelite III Nd:YAG laser as the pump for the dye laser; the third harmonic of the same laser (355 nm,  $\sim 130$  mJ/pulse) was used as a pump for the ionisation step.

### 3.3 Au–Xe Results

#### 3.3.1 Theoretical Results

The spectroscopic constants for the ground state of Au–Xe were calculated using standard high-level *ab initio* methods. The calculations were performed on Magellan<sup>13</sup> using MOLPRO.<sup>14</sup> A potential energy curve for the  $X^2\Sigma_{1/2}^+$  state was calculated using a series of single point RCCSD(T) calculations. In this case the relativistic effective core potentials ECP60MDF<sup>15</sup> and ECP28MDF<sup>16</sup> were used for Au and Xe respectively. The calculations were performed using QZ and 5Z quality basis sets, correlating only the 5s and 5p electrons of Xe and the 5d and 6s electrons of Au. The full counterpoise correction was used to correct for basis set superposition

error. The results were then extrapolated to the basis set limit. The LEVEL<sup>17</sup> program was then used to obtain the spectroscopic constants, which are shown in Table 3.1. The <sup>197</sup>Au-<sup>132</sup>Xe isotopologue was used in the calculations.

Further calculations have been performed by other members of the group; these will be referred to in Section 3.3.4 to maintain the flow of the discussion.

**Table 3.1: Calculated spectroscopic parameters for <sup>197</sup>Au-<sup>132</sup>Xe X<sup>2</sup>Σ<sup>+</sup>. R<sub>e</sub> is the equilibrium bond length, D<sub>0</sub> is the energy between the zero point vibrational energy and the asymptote, D<sub>e</sub> is the depth of the potential, ω<sub>e</sub> is the harmonic vibrational frequency and ω<sub>e</sub>x<sub>e</sub> is the anharmonicity constant.**

Basis set	R <sub>e</sub> /Å	D <sub>0</sub> ''/cm <sup>-1</sup>	D <sub>e</sub> ''/cm <sup>-1</sup>	ω <sub>e</sub> /cm <sup>-1</sup>	ω <sub>e</sub> x <sub>e</sub> /cm <sup>-1</sup>
<b>d-aVQZ</b>	3.54	408.9	419.9	22.2	0.258
<b>d-aV5Z</b>	3.48	452.8	464.4	23.4	0.248
<b>d-aV∞Z</b>	3.42	503.1	515.5	24.7	0.256

### 3.3.2 Experimental Results

Two experimental spectra for Au-Xe were obtained. The first, shown in Figure 3.2, is in the region of the <sup>2</sup>P<sub>1/2</sub> atomic transition (the transition lies to the blue of the spectrum). Several isotopologues were gated, which contributes to the width of the peaks. Figure 3.2 additionally shows a Franck-Condon simulation, which will be discussed in more detail in the next section.

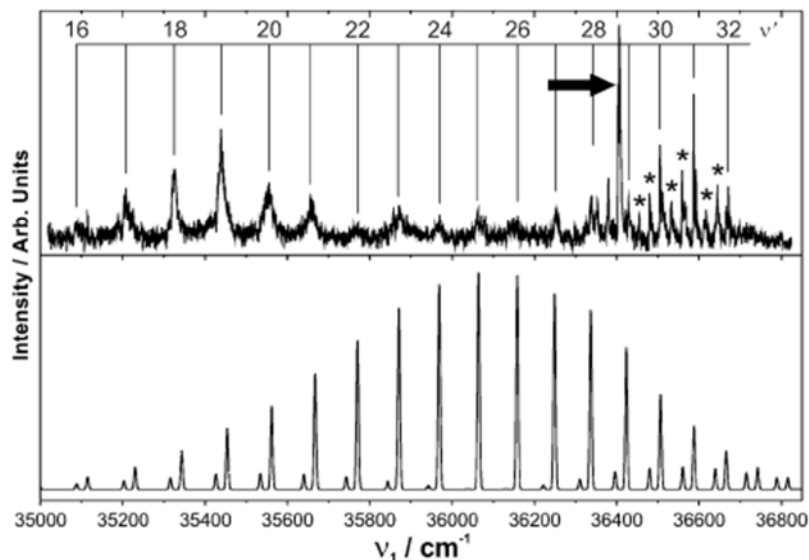


**Figure 3.2:** The top trace shows the REMPI spectrum obtained from the  $D^2\Pi_{1/2} \leftarrow X^2\Sigma_{1/2}^+$  transition in Au–Xe. The vibrational numbering was obtained from isotopic analysis of the higher energy features (above  $v'=28$ ) Hot bands are identified by asterisks. The strong feature marked with an arrow does not fit the vibrational series. Its intensity relative to the other features was affected by experimental conditions; its origin is unclear. The bottom trace shows a Franck-Condon simulation of the spectrum, which is discussed in Section 3.3.3. The figure was previously published in Ref. 1.

Figure 3.3 shows the spectrum recorded in the vicinity of the Au ( $6^2P_{3/2}$ ) atomic transition, the position of which is shown. Initially, a search was carried out to the red of the atomic transition, in accordance with the expected position of the  $D^2\Pi_{3/2}$  state, which was observed in both Au–Ar<sup>2</sup> and Au–Kr.<sup>3</sup> No spectrum was found in this region however, and this spectrum was recorded following a search to higher energy.

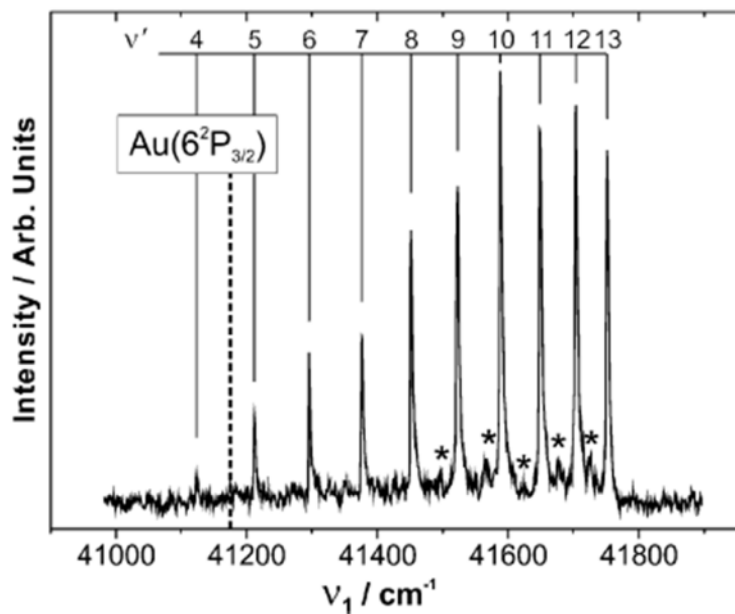


**Figure 3.3:** Two-colour REMPI spectrum of Au-Xe in the region of the Au ( $6^2P_{3/2}$ ) energy. Hot bands are identified by asterisks. Figure reproduced from Ref. 1.

The spectroscopic constants have been derived from a least-squares fit of the vibrational energy term values to the standard Morse expression (see Chapter 2) and the values for the  $^{197}\text{Au}-^{132}\text{Xe}$  isotopologue are given in Table 3.2.

**Table 3.2:** Spectroscopic constants derived for the  $D^2\Pi_{1/2}$  and unassigned  $\Omega=1/2$  states for  $^{197}\text{Au}-^{132}\text{Xe}$ . Symbols are defined in the header for Table 3.1.

	$D^2\Pi_{1/2}$	Unassigned $\Omega=1/2$
$\omega_e$	157.2	120.1
$\omega_e x_e$	1.230	2.724
$D_e'$	5,025	1,324
$D_0'$	4,947	1,265

### 3.3.3 Franck-Condon Simulation

A potential energy curve was calculated for the  $X^2\Sigma_{1/2}^+$  state using the MORSE program and the  $D_e$ ,  $\omega_e$  and  $R_e$  values obtained from the *ab initio* calculations using the extrapolation to the basis set limit. The experimental values of  $D_e$  and  $\omega_e$  obtained for the spectrum in the region of the  $^2P_{1/2}$  atomic transition were used to generate similar curves for the excited state. The curves could then be used to simulate the expected REMPI spectrum based on the Franck-Condon factor (FCF) using the SpecSim<sup>18</sup> program. The change in the equilibrium bond length between the two electronic states,  $\Delta R$ , was varied to find the best fit to the experimental data. The higher energy features were narrower, suggesting that their intensities were least likely to have been affected by any predissociation processes; the focus was therefore on matching the intensities in the simulated spectrum to these features. Figure 3.2 shows the simulation at  $\Delta R=0.65 \text{ \AA}$ . In addition to matching the intensities at the higher vibrational quantum numbers, the intensities at low  $v$  are also quite well reproduced. However, there is a dramatic loss of intensity in the centre of the spectrum, where one would expect to find the maximum. This indicates that there must be a mechanism by which these transitions are losing intensity.

It was not possible to reproduce the higher energy state satisfactorily with a Franck-Condon simulation. Figure 3.4 shows a simulation with  $\Delta R=1.2 \text{ \AA}$ . It is clear that the peak intensities at high  $v'$  have been reduced dramatically; it is therefore necessary to consider possible predissociation mechanisms for both states.

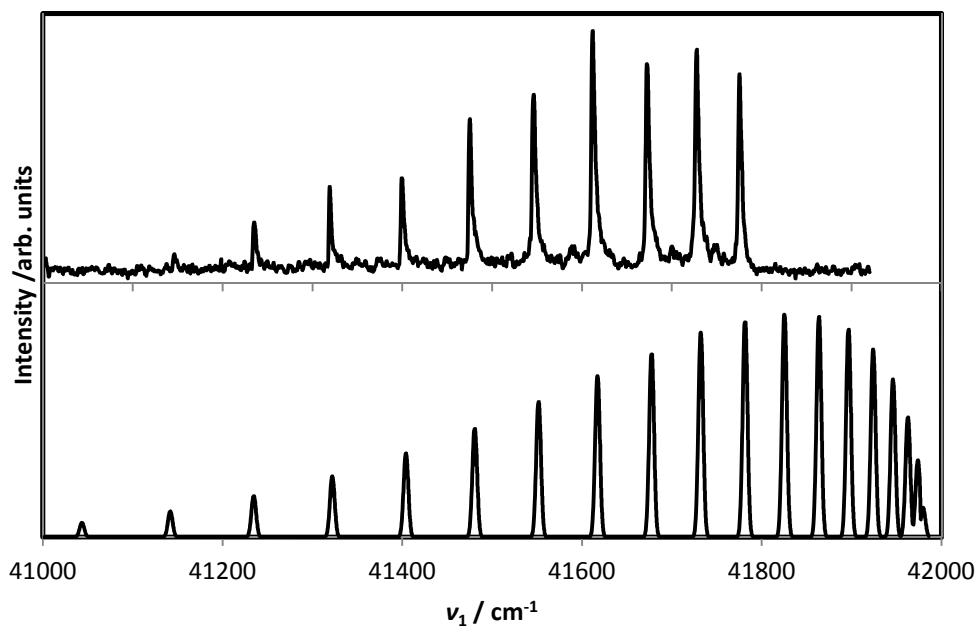


**Figure 3.4: Top trace shows the REMPI spectrum from Figure 3.3; bottom trace shows a Franck-Condon simulation.**

### 3.3.4 Discussion

The lower energy spectrum shown in Figure 3.2 has been assigned to the  $D^2\Pi_{1/2} \leftarrow X^2\Sigma_{1/2}^+$  transition. It is slightly red-shifted compared to the Au ( $6^2P_{1/2}$ )  $\leftarrow$  Au ( $6^2S_{1/2}$ ) atomic transition, which lies at  $37,358.9 \text{ cm}^{-1}$ .<sup>19</sup> A value for  $D_0'$  can be estimated using the Morse fit and the *ab initio* value of  $D_0''$ ; this gives a value of  $5,083 \text{ cm}^{-1}$ , which is close to the derived value in Table 3.2. However the other spectrum, shown in Figure 3.3, is to the blue of the atomic Au ( $6^2P_{3/2}$ )  $\leftarrow$  Au ( $6^2S_{1/2}$ ) transition. The vibrational numbering is much lower than that for the  $D^2\Pi_{1/2} \leftarrow X^2\Sigma_{1/2}^+$  transition and the derived dissociation energy is much lower, indicating a more weakly bound state; this is not consistent with findings for the  $D^2\Pi_{3/2} \leftarrow X^2\Sigma_{1/2}^+$  transition for Au-Ar<sup>2</sup> and Au-Kr<sup>3</sup>, where the values of  $\nu'$  are high. This indicates that the spectrum in Figure 3.3 is not the result of this transition.

From the Morse values, it is possible to derive  $T_0$  (the energy of the  $\nu'=0 \leftarrow \nu''=0$  transition) as  $40,621 \text{ cm}^{-1}$ ; hence the energy to the apparent

dissociation limit of this state is at  $41,886 \text{ cm}^{-1}$ . The atomic excitation energy ( $41,174 \text{ cm}^{-1}$ )<sup>19</sup> can be combined with the *ab initio*  $D_0''$  value to yield an asymptotic value of  $41,677 \text{ cm}^{-1}$ . This suggests that there is a barrier to dissociation with a height of  $\sim 200 \text{ cm}^{-1}$ ; however the accuracy of this calculation is limited by the accuracy of the *ab initio* calculation and the errors associated with the fitting procedure.

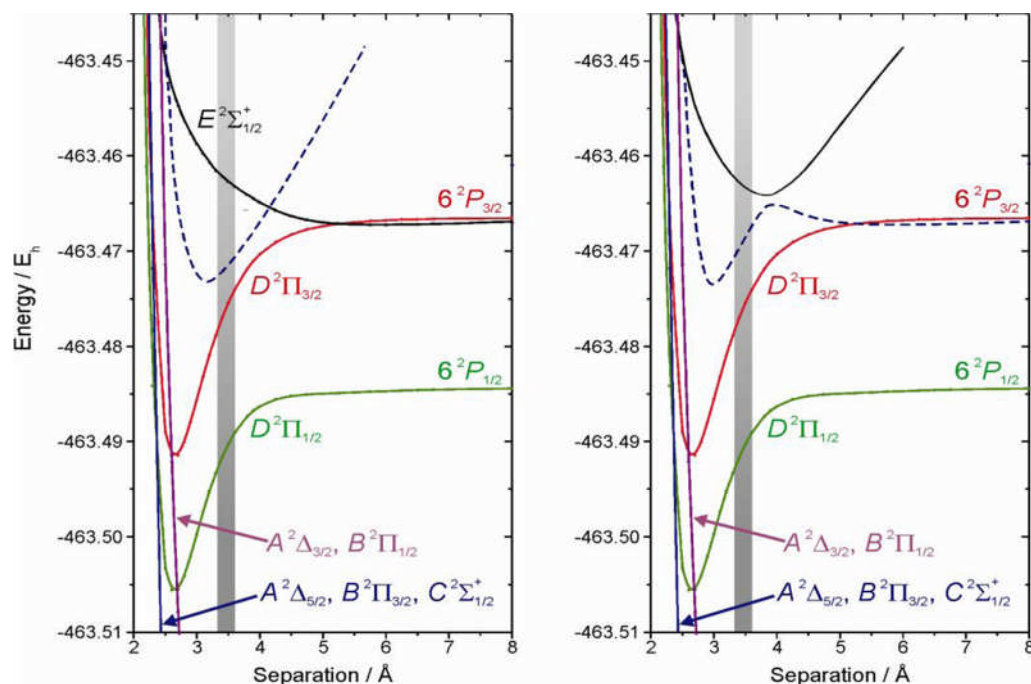


**Figure 3.5: Schematic energy level diagram showing the energy region close to the Au  $6^2P_j$  levels. The *A*, *B* and *C* states arise from  $\text{Au}(5d^96s^2) + \text{Xe}$  and are split into two groups correlating to the  $5^2D_j$  spin-orbit levels. The curves have been generated using RCCSD(T) methods and have been shifted according to the experimental atomic splitting (assuming the curves are not interacting with others). The *D* and *E* curves are CASSCF + MRCI + Q calculations, but shifted so that the atomic spin orbit asymptotes are at the correct energy. The dashed curve represents the state from which the spectrum in Figure 3.3 arises. The left-hand diagram is in the absence of interaction between the dashed curve and the *E* state; the right-hand diagram is in the presence of this interaction. Note the production of a “hump” consistent with observations. Figure reproduced from Ref. 1.**

There are several possibilities regarding the origin of this spectrum. Figure 3.5 shows a schematic diagram showing the approximate locations of the states in this region that are relevant to the following discussion. The dashed curve is a hypothetical illustration of the state that gives rise to the observed spectrum. Since it has been deduced that there is a barrier in the outer part of the curve, its minimum must lie below the  $E^2\Sigma_{1/2}^+$  state; there must therefore be interaction between these two states.

It is unlikely that the spectrum results from the  $E^2\Sigma_{1/2}^+ \leftarrow X^2\Sigma_{1/2}^+$  transition; as noted in Section 3.1, this state is expected to be very weakly bound and would not support the number of observed vibrational levels. However, there is the possibility that this state interacts with others resulting in the behaviour seen in these experiments.

Another possibility for the origin of the spectrum is a charge transfer (CT) state. Evidence for the mixing of CT states into metal dimer excited states has previously been reported.<sup>20,21,22</sup> Au has a very high electron affinity ( $\sim 19,000 \text{ cm}^{-1}$ )<sup>23</sup> and the lowest ionisation energies for Xe are 97,834 and 108,371  $\text{cm}^{-1}$  for the  $^2P_{3/2}$  and  $^2P_{1/2}$  states respectively. This, in combination with the Coulomb attraction between  $\text{Au}^-$  and  $\text{Xe}^+$  at separations close to the expected value of  $R_e$  for the higher energy state recorded, make it plausible that there could be CT states in this region. Ideally, one would incorporate repulsive terms and higher order ion-induced multipole terms into the calculation, but since these terms act in opposite directions the energy calculations here should be a reasonable approximation. The states arising from the  $\text{Au}^- + \text{Xe}^+(^2P_{3/2})$  asymptote are expected in this energy region, whereas those from the  $\text{Au}^- + \text{Xe}^+(^2P_{1/2})$  asymptote would be higher in energy. The "5p-hole" on  $\text{Xe}^+$  could either be aligned along or perpendicular to the internuclear axis, resulting in a  $CT\ ^2\Sigma_{1/2}^+$  or  $CT\ ^2\Pi_{3/2}$  state respectively. Both states are expected to be

strongly bound because of the Coulomb attraction; however the reduced repulsion in the former owing to the position of the hole on the axis would make it stronger than the latter.

Since the dissociation energy of the observed state is relatively low, it would therefore seem unlikely that it is a CT state. There could, however, be interaction between the  $CT\ ^2\Sigma_{1/2}^+$  state and the  $E^2\Sigma_{1/2}^+$  state *via* configuration interaction. The crossing between the states would need to occur above the  $Au(6^2P_{3/2}) + Xe$  asymptote (see Figure 3.5), as the convergence point is above this energy. The mixing between these states would therefore be expected to produce a curve as shown in Figure 3.5, with a local minimum near the  $R_e$  value of the  $CT\ ^2\Sigma_{1/2}^+$  state and the outer wall rising above the aforementioned atomic asymptote before the curve turns to converge to it.

A further possibility, if the binding energy of the complex is high enough, is that Au Rydberg states could be involved. A set of CASSCF + MRCI + Q + SO calculations were performed, keeping the Xe orbitals and the Au 5*d* and lower doubly occupied, to probe this region. States arising from the 7*s* and 7*p* Rydberg states were found and are shown in Figure 3.6. It can be seen that there is a configuration interaction between the  $E^2\Sigma_{1/2}^+$  state and the state arising from the 7*s* Rydberg asymptote. However, this interaction would be insufficient to produce the spectrum recorded and would be inconsistent with the convergence limit derived in the experiment.

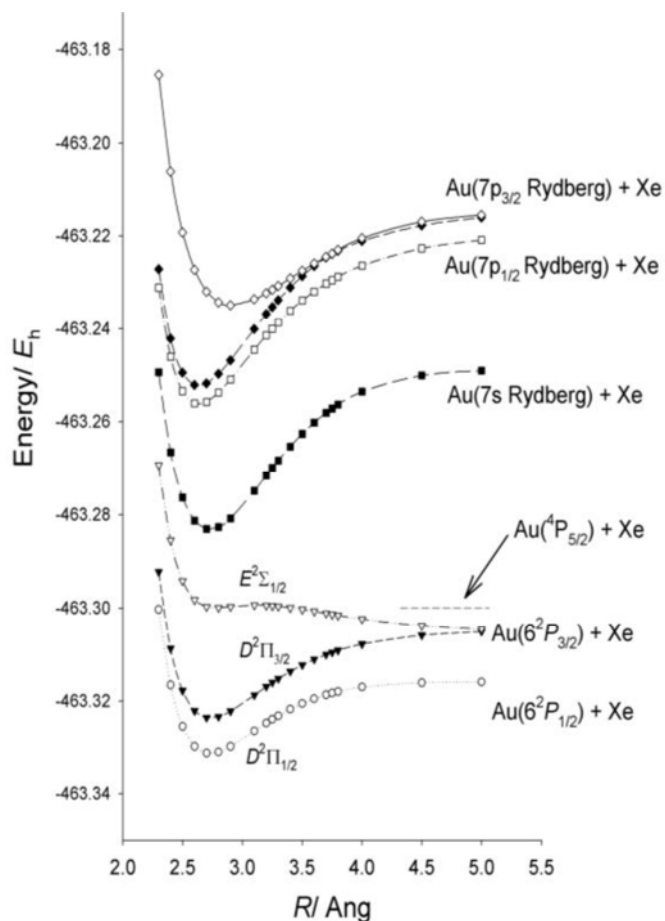


**Figure 3.6: CASSCF + MRCI + Q + SO calculations on the excited states of Au-Xe. The Xe orbitals and the 5d and lower-energy Au orbitals are kept doubly occupied in these calculations. The D and E states arise from the Au-localised  $6^2P_J \leftarrow 6^2S_{1/2}$  excitation, the other states correspond to excitation of the Au 6s electron to the 7s and 7p Rydberg orbitals. The position of the Au( $4P_{5/2}$ ) + Xe asymptote has been marked, using the experimental value for the Au( $4P_{5/2}$ )  $\leftarrow$  Au( $6^2S_{1/2}$ ) excitation energy. Figure reproduced from Ref. 1.**

The final possibility considered is the involvement of a molecular state correlating to a higher-lying Au ( $5d^96s6p$ ) + Xe state. These states are inverted owing to the  $d^9$  hole; the lowest level corresponds to the atomic Au ( $5d^96s6p$ ,  $4P_{5/2}$ ) state at  $42,164 \text{ cm}^{-1}$ .<sup>19</sup> This is only  $990 \text{ cm}^{-1}$  above the  $6^2P_{3/2}$  level<sup>19</sup> and could therefore interact with this state. An attractive  $\Omega = 1/2$  state [Au ( $5d^96s6pn$ )-Xe] could undergo a case (c) avoided crossing with the inner repulsive wall of the Au ( $5d^{10}6p\sigma$ )-Xe,  $\Omega = 1/2$  state; the

result would be a state bound by  $\sim 1,100 \text{ cm}^{-1}$  (see Figure 3.5). The Morse analysis indicated that the dissociation limit lies above the atomic asymptote (*vide supra*), and a small outer wall avoided crossing maximum in the potential curve would be consistent with this conclusion.

If spin-orbit coupling is neglected, a  $^4P$  atom interacting with a  $^1S$  atom can give rise to  $^4\Pi$  and  $^4\Sigma^+$  states; including spin-orbit coupling leads to the Au states  $^4P_{5/2}$ ,  $^4P_{3/2}$  and  $^4P_{1/2}$ , which each interact with Xe. The molecular states to be expected are  $^4\Pi_{5/2,3/2,1/2}$  and  $^4\Sigma_{3/2,1/2}^+$ . If Hund's case (c) coupling (or an intermediate case) is considered, one can expect molecular states of like- $\Omega$  to be mixed. It has already been noted that the  $d^9$  hole causes the states to be inverted and that the location of the electron density off the internuclear axis would cause the  $\Pi$  states to be bound more strongly than the  $\Sigma$  states. If the non-crossing rule is applied to states of like- $\Omega$  then it can be deduced that the lowest energy state will be a "pure  $\Pi$ "  $^4\Pi_{5/2}$  state; the other states can be expected to have mixed  $\Pi/\Sigma$  character. The next highest states expected are  $^4\Pi_{3/2}$  and  $^4\Pi_{1/2}$ , each of which correlate to the Au ( $^4P_{5/2}$ ) + Xe asymptote; other states correlating to higher atomic asymptotes will be found at higher energies.

RCCSD(T) potential energy curve (PEC) calculations have been performed on the  $^4\Pi$  state using aug-cc-pVQZ-PP and aug-cc-pV5Z-PP basis sets (neglecting spin-orbit coupling and the counterpoise correction). As for the ground state, the energies were extrapolated to the basis set limit. The spectroscopic constants derived were  $D_0=2,220 \text{ cm}^{-1}$ ,  $R_e=2.89 \text{ \AA}$ ,  $\omega_e=85.5 \text{ cm}^{-1}$  and  $\omega_e x_e=1.15 \text{ cm}^{-1}$ . However, since these values will be affected by interaction with  $CT$ , Rydberg and Au ( $5d^9 6s^2$ )-Xe states it is difficult to verify their accuracy without detailed multi-reference calculations including SO coupling.

The values can be compared to those of a similar system:  $D_0$  and  $R_e$  have been estimated for Hg ( $5d^{10}6s6p$ )–Xe  $^3\Pi$  states from spectroscopic experimental results.<sup>24</sup> For the  $^3\Pi_0$  state, which is “pure” Hg ( $6s6p$ )–Xe in nature, the values obtained were  $D_0=1,400\text{ cm}^{-1}$  and  $R_e=3.1\pm 0.2\text{ \AA}$ . The  $R_e$  value is similar to the *ab initio* result for Au–Xe ( $^4\Pi$ );  $D_0$  is significantly lower, but one would expect this owing to the extra  $5d$  electron, which would provide additional shielding of the core and reduce the bond strength.

The  $T_0$  value for the observed state is  $\sim 40,681\text{ cm}^{-1}$ . The Au ( $^4P_{5/2}$ ) + Xe lies at  $42,164\text{ cm}^{-1} + D_0'' (=42,667)$ ; therefore the dissociation energy of this state with respect to this asymptote can be calculated as  $1,986\text{ cm}^{-1}$ . This is quite close to the estimate from the *ab initio* calculation for the  $^4\Pi$  state.

This makes the  $^4\Pi_Q$  state seem a likely candidate for the spectrum in Figure 3.3; the possibilities are  $^4\Pi_{5/2}$ ,  $^4\Pi_{3/2}$  and  $^4\Pi_{1/2}$ .  $^4\Pi_{5/2}$  can be excluded on the grounds that it is not allowed in a single-photon transition from the  $X^2\Sigma_{1/2}^+$  state. It is unlikely that the  $^4\Pi_{3/2}$  state will be observed since it will be coupled to the  $D^2\Pi_{3/2}$  state, which appears to be fully predissociated in the Franck-Condon window. This leaves the  $^4\Pi_{1/2}$  state, mixed with the  $E^2\Sigma_{1/2}^+$ , as the most likely option; this is illustrated by the dashed line in Figure 3.5. However it is still possible that *CT* states are involved (*vide supra*).

The proposed avoided crossing results in a maximum in the lower  $\Omega=1/2$  curve at large  $R$  and a minimum at approximately  $3\text{ \AA}$ . The transition to this “mixed”  $\Omega=1/2$  state will retain some of the  $^2P_{3/2} \leftarrow ^2S_{1/2}$  atomic character; the electronic transition moment will vary strongly with  $R$ . This, in addition to the sudden drop-off in the Franck-Condon intensity as the

energy of the maximum is reached, could explain why it was not possible to simulate the unusual intensity profile seen in Figure 3.3.

It can be seen from Figure 3.5 that the repulsive regions of the  $A^2\Delta_{3/2}$  and  $B^2\Delta_{1/2}$  potential curves, which correlate to the higher  $Au(^2D_{3/2}) + Xe$  asymptote appear to cross both the  $D^2\Pi_{1/2}$  and  $D^2\Pi_{3/2}$  curves in the bound region. This would account for the absence of the  $D^2\Pi_{3/2}$  bands if there were complete dissociation on the REMPI timescale, owing to the efficient coupling between the repulsive wall of the  $A^2\Delta_{3/2}$  state and the inner limb of the strongly bound  $D^2\Pi_{3/2}$  state. If the  $D^2\Pi_{3/2}$  state has pure  $Au(6s6p\pi)$ -Xe character and the  $A^2\Delta_{3/2}$  state has pure  $Au(5d^96s^2)$ -Xe character then one would expect the coupling between them to be very weak, since it requires a two-electron orbital change, which is atomically forbidden. However it is known that, owing to the strong spin-orbit coupling of Au, the atomic  $Au(5d^{10}6p\ ^2P_{3/2,1/2})$  states have a small amount of  $Au(5d^96s6p)$  character, which can include spin-orbit mixing in of  $^4P$  character.<sup>25,26</sup> This would allow an efficient coupling *via* an allowed one-electron orbital change ( $5d^96s6p \leftarrow 5d^96s^2$ )

The  $D^2\Pi_{1/2}$  state, shown in Figure 3.2, seems to be predissociated in a  $v'$  dependent manner. This could possibly be explained by considering the relative atomic energy spacings of the two relevant asymptotic  $J=1/2$  states *versus* the two relevant asymptotic  $J=3/2$  states. The  $^4P_{3/2}$  state is  $5,833\text{ cm}^{-1}$  above the  $^2P_{3/2}$  state, while the  $^4P_{1/2}$  state is  $15,838\text{ cm}^{-1}$  above the  $^2P_{1/2}$  state<sup>19</sup> (owing to the inverted nature of the "d-hole"  $^4P$  states); consequently the mixing of the  $5d^96s6p\ ^4P_j$  character is expected to be much less for the  $^2P_{1/2}$  state than for the  $^2P_{3/2}$  state. On the REMPI timescale, the  $D^2\Pi_{1/2}$  state therefore appears to undergo relatively slow predissociation compared with that of the  $D^2\Pi_{3/2}$  state. It would then be deduced that the states from  $v' = 16-27$  overlap those of the repulsive

$d^9s^2B^2\Pi_{1/2}$  state with maximum probability at  $\sim v' = 24$ , while the  $^2\Pi_{1/2}$  vibrational states with  $v' = 28-32$  do not and are therefore largely unaffected.

### 3.4 Au–Ne Results

#### 3.4.1 Theoretical Results

The  $X^2\Sigma^+$  state was investigated employing *ab initio* methods as described in Chapter 2 and Section 3.3.1. In addition, calculations were performed for the ground states of Au–He and Au–Rn to complete the series. Calculations were performed over a range of interatomic spacings to generate a potential curve using MOLPRO.<sup>14</sup> As for Au–Xe, the calculations were performed employing standard Dunning style basis sets of QZ and 5Z quality for He and Ne; these were augmented by a set of diffuse functions, which were derived in an even-tempered fashion from the two most diffuse functions in the basis set. The basis sets cc-pwCVXZ-PP<sup>27</sup> and aug-cc-pVXZ-PP<sup>28</sup> were employed for Au and Rn respectively in addition to the relativistic effective core potential ECP60MDF<sup>29</sup>, which was employed for both. The basis sets were also augmented (doubly for Au and singly for Rn) with primitive diffuse functions, derived as above. The full counterpoise correction was employed to correct for BSSE and each point was extrapolated to the basis set limit. The LEVEL program<sup>17</sup> was again used followed by the least-squares fitting procedure to derive the spectroscopic constants, which are shown in Table 3.3, together with the results for Au–Ar and Au–Kr from refs 2 and 3. The lowest four energy levels were used for the fitting procedure, with the exception of Au–He, which was calculated to have only two bound levels. The <sup>197</sup>Au, <sup>4</sup>He, <sup>20</sup>Ne and <sup>222</sup>Rn isotopes were used in the calculations.

**Table 3.3: Calculated spectroscopic constants for the  $X^2\Sigma^+$  state of Au-RG.  $B_0$  is the equilibrium rotational constant in the lowest vibrational level; other constants are defined in the header to Table 3.1.**

<b>Complex</b>	<b>Basis set</b>	$R_e/\text{\AA}$	$D_e/\text{cm}^{-1}$	$D_0/\text{cm}^{-1}$	$B_0/\text{cm}^{-1}$
<b>Au-He</b>	<b>d-aVQZ</b>	4.11	14.6	5.7	0.203
	<b>d-aV5Z</b>	4.10	14.9	5.9	0.205
	<b>d-aV<math>\infty</math>Z</b>	4.08	15.3	6.1	0.207
<b>Au-Ne</b>	<b>d-aVQZ</b>	3.84	46.2	37.0	0.0599
	<b>d-aV5Z</b>	3.83	46.7	37.5	0.0601
	<b>d-aV<math>\infty</math>Z</b>	3.83	47.2	38.0	0.0603
<b>Au-Ar (ref. 2)</b>	<b>d-aV<math>\infty</math>Z</b>	3.73	176.5	163.9	0.0358
<b>Au-Kr (ref. 3)</b>	<b>d-aV<math>\infty</math>Z</b>	3.64	284.8	273.0	0.0214
<b>Au-Xe</b>	<b>d-aV<math>\infty</math>Z</b>	3.42	515.5	503.1	0.0181
<b>Au-Rn</b>	<b>d-aVQZ</b>	3.30	704.2	690.0	0.00147
	<b>d-aV5Z</b>	3.26	758.6	743.4	0.00151
	<b>d-aV<math>\infty</math>Z</b>	3.22	820.3	804.1	0.00155

RCCSD(T)/aVQZ calculations were also performed on the  $D^2\Pi$  state of Au-Ne (spin-orbit coupling was not included in the calculation; this would be expected merely to raise the  $D^2\Pi_{3/2}$  curve by a constant amount without affecting the other parameters). The calculated spectroscopic constants were:  $R_e=3.08 \text{ \AA}$ ,  $D_e=168 \text{ cm}^{-1}$ ,  $D_0=147 \text{ cm}^{-1}$ ,  $\omega_e=42 \text{ cm}^{-1}$  and  $\omega_e x_e=3.0 \text{ cm}^{-1}$ . In addition, CASSCF+MRCI+Q calculations have been performed by members of the group to generate potential energy curves for the  $^2\Pi_{1/2}$ ,  $^2\Pi_{3/2}$  and  $^2\Sigma_{1/2}^+$  states; these are shown in Figure 3.7.

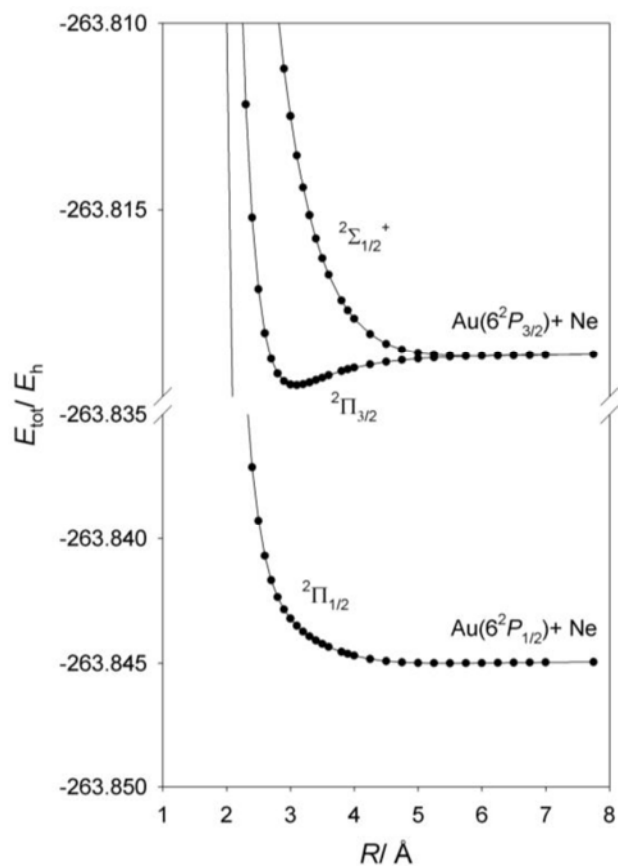


**Figure 3.7:** CASSCF+MRCI+Q/aVQZ calculations for the  $D^2\Pi_{1/2, 3/2}$  and  $E^2\Sigma_{1/2}^+$  states of Au–Ne. Figure reproduced from Ref. 1.

### 3.4.2 Experimental Results

The REMPI spectrum recorded for the  $D^2\Pi_{3/2} \leftarrow X^2\Sigma_{1/2}^+$  transition in  $^{197}\text{Au}-^{20}\text{Ne}$  is shown in Figure 3.8. It was also possible to obtain a spectrum for the  $^{197}\text{Au}-^{22}\text{Ne}$  isotopologue; this allowed the absolute vibrational numbering to be deduced (see Figure 3.9 and Chapter 2).

The non-resonant Au signal was extremely strong and the MCPs were not able to recover fully from this before the Au–Ne clusters were detected. This had a significant effect on the intensities of the peaks in the spectra, particularly at high  $\nu$ . The relatively low abundance of  $^{22}\text{Ne}$  meant that only the lower energy features could be observed; however this was sufficient to measure the isotopic shifts.

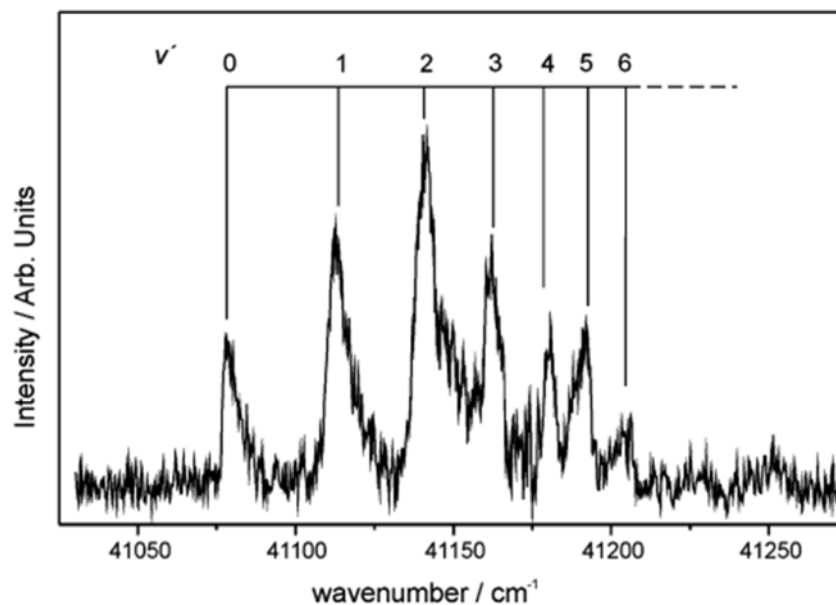


Figure 3.8: Single-colour REMPI of the  $D^2\Pi_{1/2} \leftarrow X^2\Sigma_{1/2}^+$  transition for  $^{197}\text{Au}-^{20}\text{Ne}$ . Figure previously published in Ref. 1.

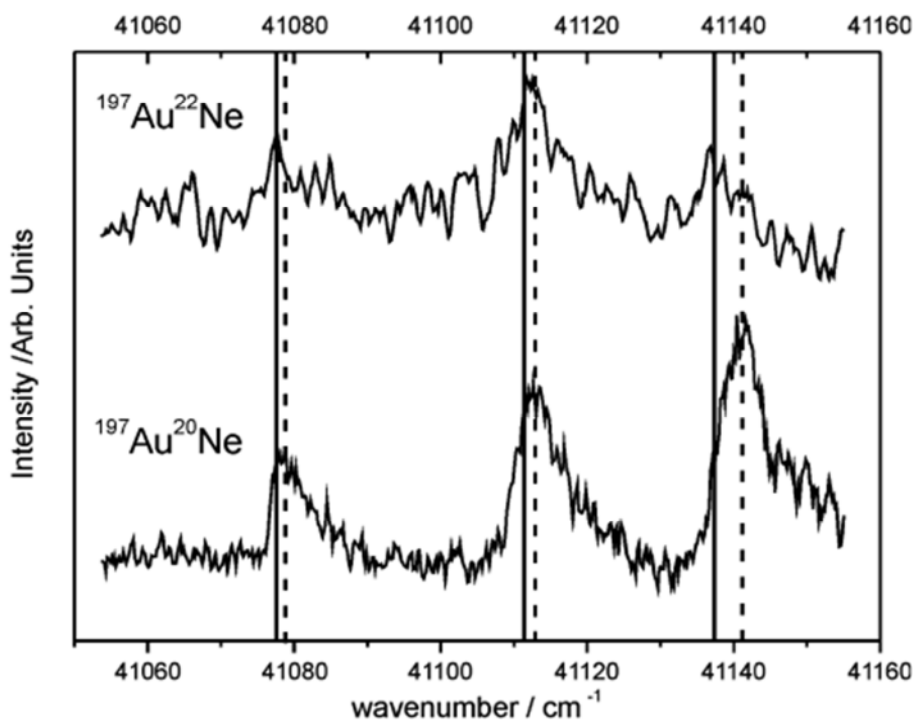


Figure 3.9: Low energy region of the  $D^2\Pi_{1/2} \leftarrow X^2\Sigma_{1/2}^+$  transition for  $^{197}\text{Au}-^{20}\text{Ne}$  and  $^{197}\text{Au}-^{22}\text{Ne}$ . Note the shift in the peak maxima, which enables the absolute vibrational numbering to be determined. Figure previously published in Ref. 1.

The spectroscopic constants were then derived using the standard Morse expression; the results are shown in Table 3.4.

**Table 3.4: Derived spectroscopic parameters for the  $^{197}\text{Au}-^{20}\text{Ne } D^2\Pi_{3/2}$  state. Symbols are defined in the header to Table 3.1. All values are in  $\text{cm}^{-1}$ .**

Parameter	Morse	LeRoy-Bernstein
$\omega_e$	36.9	
$\omega_e x_e$	2.35	
$D_e'$	145.1	153.9 <sup>a</sup>
$D_0'$	127.8	136.0
$D_0''$	31.4	40.0

<sup>a</sup>Estimated from the  $D_0'$  value using the Morse potential vibrational constants.

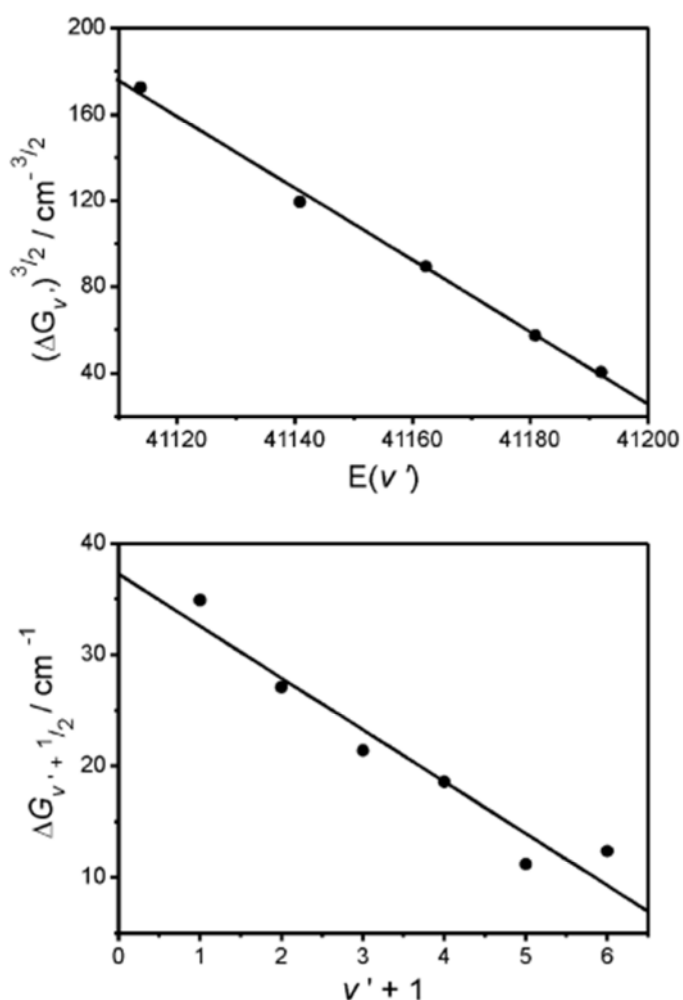


**Figure 3.10: LeRoy-Bernstein (top) and Birge-Sponer (bottom) plots for the observed  $^{197}\text{Au}-^{20}\text{Ne}$  spectrum. The solid circles indicate the experimental data points; the solid lines are the least squares fit. Figure previously published in Ref. 1.**

Figure 3.10 shows LeRoy-Bernstein<sup>30</sup> and Birge-Sponer plots (see Chapter 2). The LeRoy-Bernstein plot gives a better fit to the data and is in better agreement with the *ab initio*  $D_0$  values; this suggests that the values calculated from this method are the more reliable (they are also shown in Table 3.4). This may be expected, since the Birge-Sponer analysis is only reliable when applied to levels at low  $v'$ , near the bottom of the well. It could not therefore be expected to perform well for a species with few bound levels.

As previously stated in Section 3.2, it was necessary to switch the dye to investigate the  ${}^2P_{1/2} \leftarrow {}^2S_{1/2}$  atomic Au transition region, where one would expect the  $D^2\Pi_{1/2} \leftarrow X^2\Sigma_{1/2}^+$  transition to occur. When this was done, it was not possible to detect a Au-Ne signal. Switching the carrier gas to Ar confirmed that clustering was occurring, since the  $D^2\Pi_{1/2} \leftarrow X^2\Sigma_{1/2}^+$  transition of Au-Ar was detected immediately, as it had been before.<sup>2</sup> Returning to Ne as the carrier gas still yielded no spectrum for this region, although once the dye was switched back the upper state spectrum could again be recorded satisfactorily. It was therefore concluded that either the  $D^2\Pi_{1/2}$  state was very weakly bound or the Franck-Condon factors are too small in this region to allow the transition to be detected. This is also supported by the calculations shown in Figure 3.7.

### 3.4.3 Franck-Condon Simulations

A Franck-Condon simulation was performed for the Au-Ne spectrum; the method is the same as for the Au-Xe simulation (see Section 3.3.3). This is shown in Figure 3.11.

RCCSD(T) calculations for the non spin-orbit  $D^2\Pi$  state, which is expected to have the same shape as the  $D^2\Pi_{3/2}$  state, give an  $R_e$  value of 3.08 Å. Since, as explained in the previous section, the intensities of the peaks in

the spectrum are unreliable, it was decided to use this value in the simulation. The calculated values are in reasonably good agreement with the experimentally derived results. The experimental values of  $D_e$  and  $\omega_e$  are used, however, while the ground state potential energy curve is simulated using the calculated constants shown in Table 3.3.

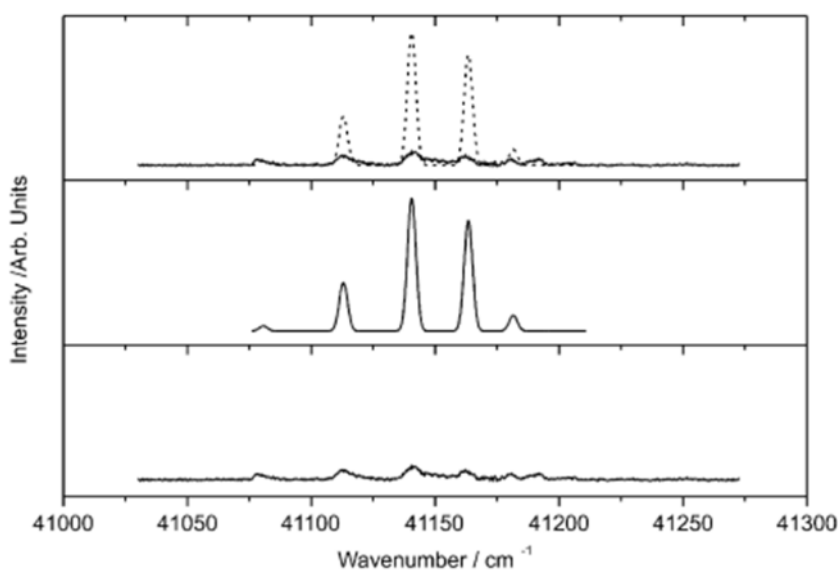


**Figure 3.11: Franck-Condon simulation of the observed  $^{197}\text{Au}-^{20}\text{Ne}$  spectrum, using parameters from *ab initio* calculations. Bottom trace is the experimental spectrum, middle trace is the simulation and top trace is both spectra overlaid. The intensities of the simulated spectrum have been scaled so that the  $\nu'=0$  intensity matches that of the experimental one (the first visible peak, seen at approximately  $41,075\text{ cm}^{-1}$ ). Figure previously published in Ref. 1.**

As expected, the intensities in the simulation are very different from those in the recorded REMPI spectrum. In addition to the problem with the non-resonant Au signal, the intense laser power required to observe the weaker features led to saturation of those that were most intense. The intensities have therefore been scaled using the first feature in the recorded spectrum; this is the feature least likely to have been saturated.

The rotational profiles of the bands have also been simulated using the  $B_v$  values from the RCCSD(T)/d-aVQZ calculation of the excited state and the  $B_0$  value from the ground state calculation. This simulation is shown in Figure 3.12. It is not possible to resolve the individual rotational lines in the recorded spectrum, so a Gaussian line profile has been used with the full width at half maximum set to  $0.8 \text{ cm}^{-1}$ . The simulated vibrational bands have been individually scaled to match the intensity of the recorded band, owing to the unreliability of the intensities. The rotational profile was most accurately reproduced with the rotational temperature set to 15 K.

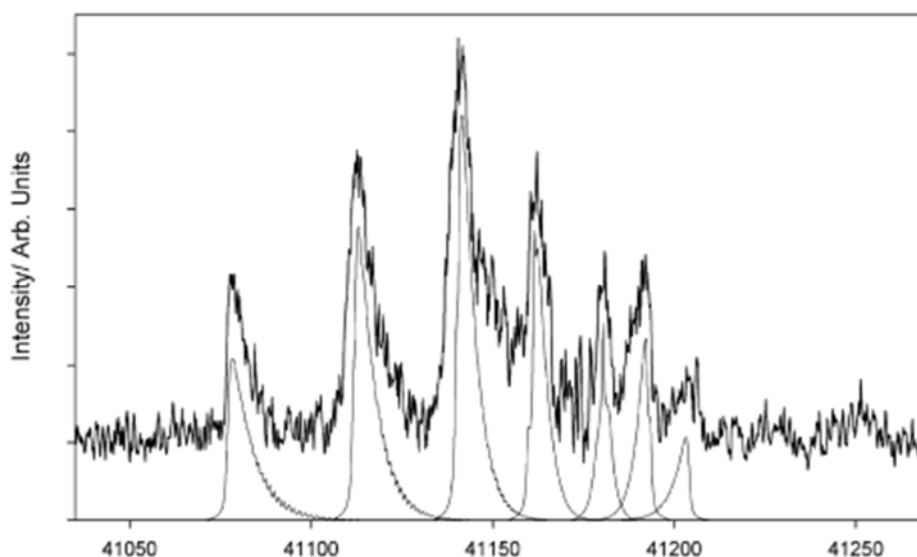


**Figure 3.12: Simulated rotational profiles for the vibrational features in the experimental Au-Ne spectrum, showing the gradual change from blue to red shaded bands. The simulations employ the calculated  $B_v$  values for the  $D^2\Pi_{3/2}$  state. The intensities of each band have been scaled to match the corresponding experimental value. Figure previously published in Ref. 1.**

A Franck-Condon simulation has also been calculated for the  $D^2\Pi_{3/2} \leftarrow X^2\Sigma_{1/2}^+$  Au-Ar spectrum originally reported in ref 2; this employed the *ab initio* (RCCSD(T)/d-aV $\infty$ Z) values for the ground state reported in that paper and some new RCCSD(T)/d-aVQZ calculations performed in this

work for the excited state. The derived constants for the excited states were:  $R_e=2.62 \text{ \AA}$ ,  $\omega_e=116 \text{ cm}^{-1}$  and  $D_e= 1,782 \text{ cm}^{-1}$ . The simulated spectrum can be seen in Figure 3.13. This has allowed an approximate absolute vibrational numbering of the spectrum, which was not possible before. The first band is assigned to  $v'=9$  and Morse fitting allows the derivation of the spectroscopic constants  $\omega_e=114 \text{ cm}^{-1}$  and  $\omega_e x_e=1.9 \text{ cm}^{-1}$ .

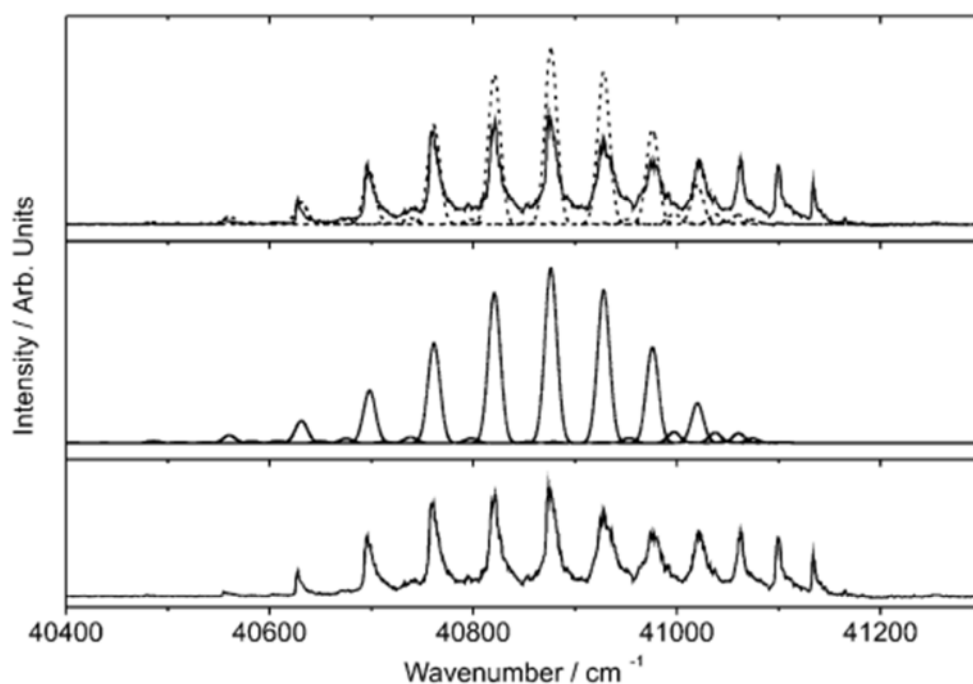


**Figure 3.13: Franck-Condon simulation of the  $D^2\Pi_{3/2} \leftarrow X^2\Sigma_{1/2}^+$  transition for Au-Ar, using parameters from the *ab initio* calculations reported in this work for the  $D^2\Pi_{3/2}$  state and from ref. 2 for the ground state. The bottom trace is the experimental spectrum, the middle trace is the simulation and the top trace is both spectra overlaid. The intensities of the simulated spectrum have been scaled so that the intensities of the first few bands match the experimental ones. Note that the hot band features (corresponding to excitation from  $v' = 1$  and 2) have also been simulated and scaled to give the best match to the experimental intensities; the relative intensities represent a vibrational temperature of about 15 K. Figure previously published in Ref. 1.**

### 3.4.4 Discussion

It was noted in Section 3.4.2 that the REMPI spectrum for the transition  $D^2\Pi_{1/2} \leftarrow X^2\Sigma_{1/2}^+$  in Au-Ne could not be observed. The CASSCF+MRCI+Q calculations can give some insight as to why this is the case. These calculations include the spin-orbit interaction and indicate a very clear difference between the potential energy curves for the  $D^2\Pi_{1/2}$  and  $D^2\Pi_{3/2}$  states. These states are expected to be more strongly bound than the  $E^2\Sigma_{1/2}^+$  state (see Section 3.1); however Figure 3.7 indicates that mixing occurs, leading to a  $D^2\Pi_{1/2}$  curve with a very shallow well and a shallow minimum at approximately 5.0 Å. Since for the ground state  $R_e=3.8$  Å (Table 3.3), the FCFs for this transition would be very small. They are much larger for the  $D^2\Pi_{3/2}$  state, which has a minimum at 3.08 Å.

The *ab initio* calculations have enabled simulations that have reproduced satisfactorily the spacings and rotational profiles in the recorded Au-Ne spectrum and have generated spectroscopic constants comparable with those derived experimentally. It can therefore be concluded that this level of calculation gives a reasonably good representation of the potential curves and one can be fairly confident of the vibrational assignments made for the Au-Ar spectrum.

It is interesting to note that both the Au-Ne and Au-Ar  $D^2\Pi_{3/2} \leftarrow X^2\Sigma_{1/2}^+$  spectra show intensities to high  $v'$  that are greater than those that the FC simulations predict. This could be explained by further configurational and spin-orbit mixing, perhaps from  $\Omega=3/2$  states arising from the lower Au ( $5^2D$ ) + RG ( $1S$ ) or higher Au ( $4P_{5/2}$ ) + RG ( $1S$ ) and Au ( $7p$ ) + RG ( $1S$ ) asymptotes.

Since this work was completed, photodissociation experiments of Au-Xe have been carried out by R. J. Plowright and collaborators at the University

of Oxford using velocity map imaging.<sup>31</sup> These studies showed that Au<sup>+</sup> ions were produced in the dissociation and possible mechanisms for charge transfer were therefore discussed in detail.

### 3.5 Trends in the Au–RG series

Table 3.3 shows the results of the RCCSD(T) calculations for the ground state of all the species in the Au–RG series. It is therefore possible to see how the spectroscopic constants change as the rare gases become heavier and more polarisable.

It is to be expected that the increased polarisability leads to stronger bonding, as has been seen in many previous studies of metal-rare gas complexes;<sup>11</sup> this is reflected in the value of  $D_e$ , which can be seen in Table 3.3 to increase with the size of the rare gas atom.

The change in  $R_e$ , by contrast, is not as one might expect. Although the van der Waals radii of the rare gas atoms increase considerably from He to Rn, the  $R_e$  values in the complex *decrease*. This behaviour has been seen for the lighter rare gases for other M–RG or M<sup>+</sup>–RG complexes; for example Na–RG (RG=Ne, Ar, Kr)<sup>32,33,34</sup>, Group 2 M<sup>+</sup>–RG ions (RG=He, Ne, Ar) (see Chapters 4 and 5) and Group 12 M<sup>+</sup>–RG (RG=He, Ne, Ar).<sup>35</sup> As with Au–RG, these complexes have a single, polarisable *s* electron on the metal/metal ion; it has been suggested that in some cases the *s*-electron cloud becomes distorted as the RG atom approaches. This may lead to deshielding of the core and enhanced attraction as *R* decreases and the RG polarisability increases. However, for the trend to continue to even the heaviest rare gases is believed to be unprecedented. In the same set of calculations, similar trends were also seen in *ab initio* calculations for Ag–RG and Cu–RG.<sup>36</sup> The calculated values of  $R_e$  and  $D_e$  for Au–He are very

similar to those obtained by Cargnoni *et al.*,<sup>37</sup> who also employed high-level *ab initio* methods and large basis sets.

It is difficult to compare the Au ( $6p$ ) states directly as the different complexes show very different spectroscopic behaviour. The  $D^2\Pi_{1/2}$  state is not observed in Au-Ne, whereas for Au-Ar<sup>2</sup> it was found to be significantly perturbed at high  $\nu'$  and a long progression was seen for Au-Kr.<sup>3</sup> In Au-Xe a long progression was also observed, but the centre of the spectrum shows a significant loss of intensity. The  $D^2\Pi_{3/2}$  spectrum was recorded for Au-Ne, Au-Ar and Au-Kr (although this progression was severely curtailed); however in Au-Xe this state could not be seen. Instead, a spectrum that has been attributed to a mixing of the  $E^2\Sigma_{1/2}^+$  state and a higher  $^4\Pi_{1/2}$  state was observed. These effects can be understood with reference to the *ab initio* calculations.

The mixing of the  $E^2\Sigma_{1/2}^+$  state with the  $D^2\Pi_{1/2}$  state is believed to occur throughout the series; however while in Au-Ne this leads to a very shallow well and small FCFs that make the state unobservable, in Au-Ar the state was seen but showed strong perturbation. In Au-Kr and Au-Xe, the most significant effects appear to be outside the FC window. It is very probable that similar mixing occurs in Au-He.

Another common effect is the interaction of the  $D^2\Pi_{3/2}$  state with others of like- $\Omega$ , as is seen here for Au-Xe; this results in the predissociation of the  $D^2\Pi_{3/2}$  state in this case (see Section 3.4.2). The interaction between the  $A^2\Delta_{3/2}$  and  $^2\Pi_{3/2}$  states was also deemed the most likely cause of the predissociation of the higher  $\nu'$  states in Au-Kr.<sup>3</sup>

### 3.6 Conclusions

REMPI spectra have been presented for the Au–Xe and Au–Ne complexes, obtained in the region of the strong  ${}^2P_J \leftarrow {}^2S$  atomic transition. It was possible to obtain spectra for more than one isotopologue in each case, enabling the assignment of absolute vibrational numbering.

The spectroscopy of these complexes has proven to be far from straightforward, and *ab initio* methods have therefore been employed to assist in assigning the spectra and explaining the unusual intensity profiles seen in many cases.

The lower energy state of Au–Xe has been assigned to the  $D^2\Pi_{1/2} \leftarrow X^2\Sigma_{1/2}^+$  transition. A Franck-Condon simulation was performed, which reproduced the intensities at both high and low energies reasonably well, however the centre of the spectrum showed an unexpected loss of intensity; this was explained by indirect coupling with the  $B^2\Pi_{1/2}$  state, leading to  $v$ -dependent predissociation.

The low vibrational numbering and dissociation energy of the Au–Xe spectrum recorded at higher energy led to the conclusion that it could not be from the  $D^2\Pi_{3/2} \leftarrow X^2\Sigma_{1/2}^+$  transition. Other possible assignments were discussed, employing *ab initio* calculations to support arguments; the most likely candidate was deemed to be a state arising from a case (c) interaction between the  $E^2\Sigma_{1/2}^+$  state and a  ${}^4\Pi_{1/2}$  state, with the latter arising from the Au( ${}^4P_{5/2}$ ) + Xe asymptote. However, it is possible that charge transfer states could also be involved. A non-FC profile is again observed; this may be explained by the  $R$ -dependence of the electronic transition moment and the presence of a barrier in the outer wall of the potential curve, leading to tunnelling/predissociation of states in the energy region of the barrier.

It was only possible to record spectra for one transition in Au-Ne, which has been assigned to  $D^2\Pi_{3/2} \leftarrow X^2\Sigma_{1/2}^+$ . The  $D^2\Pi_{1/2} \leftarrow X^2\Sigma_{1/2}^+$  transition could not be observed; this is believed to be due to mixing with the  $E^2\Sigma_{1/2}^+$  state, which results in a very weakly bound state and poor FCFs.

A Franck-Condon profile has been simulated for the spectrum recorded for Au-Ne employing the  $R_e$  values from *ab initio* calculations. The intensities cannot be reproduced; this is attributed to difficulties in subtracting the substantial non-resonant Au signal and the saturation of the most intense features. The rotational profile was well reproduced using  $B_v$  values from *ab initio* calculations; this simulation suggests a rotational temperature of approximately 15 K.

A Franck-Condon simulation has also been performed for a previously recorded spectrum of the  $D^2\Pi_{3/2} \leftarrow X^2\Sigma_{1/2}^+$  transition in Au-Ar using new *ab initio* calculations, which has allowed a suggested absolute vibrational numbering and the derivation of spectroscopic constants. From these simulations, it has been suggested that further configurational and spin-orbit mixings occur, which lead to a rise in intensity at high  $v'$ .

The trends across the Au-RG series have also been discussed. With reference to the *ab initio* calculations on the ground state, it has been noted that although the  $D_e$  values show the expected increase from He-Rn, the  $R_e$  values show an unexpected steady decrease. It was suggested that this could be a result of the distortion of the polarisable Au (6s) electron cloud as the RG atom approaches, which decreases the repulsion and increases the attraction. This effect will be discussed further in Chapters 4 and 5, where related phenomena are seen in the Group 2 metal ion-rare gas series.

For the spectroscopic results, it was noted that most of the differences in the spectra that could be observed for the different complexes could be explained by three main features: the mixing of the  $E^2\Sigma_{1/2}^+$  state with the  $D^2\Pi_{1/2}$  state, which leads to the non-observation of the  $D^2\Pi_{1/2} \leftarrow X^2\Sigma_{1/2}^+$  transition in Au–Ne and a strong perturbation in Au–Ar (this does not impact the spectra for heavier species as the main effect occurs outside the FC window); the interaction of the  $D^2\Pi_{3/2}$  state with others of like- $\Omega$ , which causes the  $D^2\Pi_{3/2} \leftarrow X^2\Sigma_{1/2}^+$  to be severely curtailed in Au–Kr and absent in Au–Xe; and the involvement of higher states arising from the Au ( $^4P_{5/2}$ ) + RG asymptote, which gives rise to the observation of a hypothesised mixed character  $\Omega=1/2$  state for Au–Xe close to the energy of the  $6^2P_{3/2}$  state.

## References

- 
- <sup>1</sup> R. J. Plowright, *Thesis, Spectroscopy and Interactions of Metal and Metal Cation Complexes*, University of Nottingham (2010).
  - <sup>2</sup> R. J. Plowright, V. L. Ayles, M. J. Watkins, A. M. Gardner, R. R. Wright, T. G. Wright and W. H. Breckenridge, *J. Chem. Phys.*, **127**, 204308 (2007).
  - <sup>3</sup> R. J. Plowright, A. M. Gardner, M. J. Watkins, T. G. Wright, W. H. Breckenridge, F. Wallimann and S. Leutwyler, *J. Chem. Phys.*, **129**, 154315 (2008).
  - <sup>4</sup> P. Pyykkö, *J. Am. Chem. Soc.*, **117**, 2067 (1995).
  - <sup>5</sup> D. Schröder, H. Schwarz, J. Hrusák and P. Pyykkö, *Inorg. Chem.*, **37**, 624 (1998).
  - <sup>6</sup> L. Belpassi, I. Infante, F. Tarantelli and L. Visscher, *J. Am. Chem. Soc.*, **130**, 1048 (2008).
  - <sup>7</sup> T. Zeng and M. Klobukowski, *J. Phys. Chem. A*, **112**, 5236 (2008)
  - <sup>8</sup> W. H. Breckenridge, V. L. Ayles and T. G. Wright, *J. Phys. Chem. A*, **112**, 4209 (2008).
  - <sup>9</sup> J. P. Read, and A. D. Buckingham, *J. Am. Chem. Soc.*, **119**, 9010 (1997).

- 
- <sup>10</sup> <http://www.webelements.com/xenon/isotopes.html>. (accessed 31/1/11)
- <sup>11</sup> D. Bellert and W. H. Breckenridge, *Chem. Rev.* **102**, 1595 (2002).
- <sup>12</sup> <http://www.webelements.com/neon/isotopes.html>. (accessed 31/1/11)
- <sup>13</sup> Magellan is a high-performance computer cluster owned by the UK National Service for Computational Chemistry Software (NSCCS).
- <sup>14</sup> R. D. Amos, A. Bernhardsson, A. Berning, P. Celani, D. L. Cooper, M. J. O. Deegan, A. J. Dobbyn, F. Eckert, C. Hampel, G. Hetzer, P. J. Knowles, T. Korona, R. Lindh, A. W. Lloyd, S. J. McNicholas, F. R. Manby, W. Meyer, M. E. Mura, A. Nicklass, P. Palmieri, R. Pitzer, G. Rauhut, M. Schütz, U. Schumann, H. Stoll, A. J. Stone, R. Tarroni, T. Thorsteinsson and H.-J. Werner, MOLPRO, a package of ab initio programs designed by H.-J. Werner and P. J. Knowles, Version 2002.1 (2002).
- <sup>15</sup> D. Figgen, G. Rauhut, M. Dolg and H. Stoll, *Chem. Phys.*, **311**, 227 (2005).
- <sup>16</sup> K. A. Peterson, D. Figgen, E. Goll, H. Stoll and M. Dolg, *J. Chem. Phys.*, **119**, 11113 (2003).
- <sup>17</sup> R. J. LeRoy, Level 7.2—A computer program for solving the radial Schrödinger equation for bound and quasibound levels, and calculating various values and matrix elements, University of Waterloo Chemical Physics Research Program Report CP-555R (2000).
- <sup>18</sup> SpecSim is a program developed by Kenneth Lawley at the University of Edinburgh.
- <sup>19</sup> <http://physics.nist.gov/cgi-bin/ASD/energy1.pl> (accessed 31/1/11).
- <sup>20</sup> G. A. Bishea, N. Marak and M. D. Morse, *J. Chem. Phys.*, **95**, 5618 (1991).
- <sup>21</sup> G. A. Bishea, J. C. Pinegar and M. D. Morse, *J. Chem. Phys.*, **95**, 5630 (1991).
- <sup>22</sup> G. A. Bishea and M. D. Morse, *J. Chem. Phys.*, **95**, 5646 (1991).
- <sup>23</sup> H. Hotop and W. C. Lineberger, *J. Phys. Chem. Ref. Data*, **14**, 731 (1985).
- <sup>24</sup> K. Yamanouchi, J. Fukuyama, H. Horiguchi, S. Tsuchiya, K. Fuke, T. Saito and K. Kaya, *J. Chem. Phys.*, **85**, 1806 (1986).
- <sup>25</sup> D. M. Gruen, S. L. Gaudioso, R. L. McBeth and J. L. Lerner, *J. Chem. Phys.*, **60**, 89 (1974).
- <sup>26</sup> D. Roser, R. Pellow, M. Eyring, M. Vala, J. Lignieres and J. C. Rivoal, *Chem. Phys.*, **166**, 393 (1992).
- <sup>27</sup> K. A. Peterson and C. Puzzarini, *Theor. Chem. Acc.*, **114**, 283 (2005).

- 
- <sup>28</sup> K. A. Peterson, D. Figgen, E. Goll, H. Stoll and M. Dolg, *J. Chem. Phys.* **119**, 11113 (2003).
- <sup>29</sup> D. Figgen, G. Rauhut, M. Dolg and H. Stoll, *Chem. Phys.*, **311**, 227 (2005)
- <sup>30</sup> R. J. LeRoy and R. B. Bernstein, *J. Chem. Phys.*, **52**, 3869 (1970)
- <sup>31</sup> W. S. Hopkins, A. P. Woodham, R. J. Plowright, T. G. Wright and S. R. Mackenzie, *J. Chem. Phys.*, **134**, 94311 (2011).
- <sup>32</sup> R. A. Gottscho, B. Ahmed-Bitar, W. P. Lapatovich, W. P. Renhorn, D. E. Pritchard, *J. Chem. Phys.*, **75**, 2546 (1981) and references therein.
- <sup>33</sup> G. Apfelbach, A. Nunemann and D. Zimmerman, *Chem. Phys. Lett.*, **96**, 311 (1983).
- <sup>34</sup> R. Bruhl, J. Kapetanakis and D. Zimmerman, *J. Chem. Phys.*, **94**, 5865 (1991).
- <sup>35</sup> E. Qing, L. A. Viehland, E. P. F. Lee and T. G. Wright, *J. Chem. Phys.*, **60**, 89 (1974).
- <sup>36</sup> A. M. Gardner, R. J. Plowright, M. J. Watkins, T. G. Wright and W. H. Breckenridge, *J. Chem. Phys.*, **132**, 184301 (2010).
- <sup>37</sup> F. Cargnoni, T. Kuś, M. Mella and R. J. Bartlett, *J. Chem. Phys.*, **129**, 204307 (2008).

## 4. Theoretical Study of $M^+$ -RG and $M^{2+}$ -RG Complexes ( $M=Ca-Ra$ ; $RG=He-Rn$ )

### 4.1 Introduction

In addition to high-resolution electronic spectroscopic experiments, members of the SOCAR group have previously calculated ground state potential energy curves (PECs) for the Group 1 metal cation-rare gas complexes using high level *ab initio* methods.<sup>1,2,3,4,5</sup> This chapter describes how this work has been continued with the Group 2 metals, in collaboration with Adrian Gardner of the SOCAR group and external collaborators.

The calculated PECs have been employed to derive spectroscopic parameters of the complexes and to learn more about the interactions between metal cations and rare gas atoms. The PECs have also been used by L. A. Viehland and co-workers at Chatham University, USA in order to calculate transport coefficients for metal cations and dications moving through a bath of rare gas atoms. These can be useful in understanding ion-molecule reactions.<sup>6,7,8,9,10</sup>

Employing RCCSD(T) methods similar to those described for the Au-RG ground state calculations in Chapter 3, spectroscopic constants have been derived for  $M^+$ -RG and  $M^{2+}$ -RG complexes ( $M=Be-Ra$ ;  $RG=He-Rn$ ). These results are compared with previous theoretical and experimental results where available. Some unusual trends have been seen in the series and these are discussed. It is noted that the complexes involving the lighter metals (Be and Mg), while showing similar trends to the heavier complexes, have a somewhat different rationale behind them; these are therefore discussed separately in Chapter 5.

The results will also be discussed with reference to a model potential proposed by Bellert and Breckenridge.<sup>11</sup> This model is based on a multipolar expansion and as such accounts for physical interactions only. It includes inductive attraction terms and dispersion terms, with the repulsive term modelled by an exponential form; attractive interactions are included to terms of order  $R^{-8}$ .

Bellert and Breckenridge suggested that the metal cation-rare gas interaction could be described using the following equation if the cation has no permanent quadrupole moment.

$$V(R) = \frac{-\alpha_{RGD}Z^2}{2R^4} - \frac{C_6}{R^6} - \frac{\alpha_{RGQ}Z^2}{2R^6} + \frac{B_{RG}Z^3}{2R^7} - \frac{C_8}{R^8} - \frac{\alpha_{RGO}Z^2}{2R^8} - \frac{\gamma Z^4}{24R^8} + Ae^{-bR} \quad (4.1)$$

$Z$  represents the "effective" charge on the metal cation.  $\alpha_{RGD}$ ,  $\alpha_{RGQ}$  and  $\alpha_{RGO}$  are the dipole, quadrupole and octopole polarisabilities of the rare gas atom respectively.  $B_{RG}$  is the higher order dipole-quadrupole polarisability of the rare gas and  $\gamma$  is the higher order second dipole hyperpolarisability of the rare gas. The  $C_6$  terms represent the first dispersive term (random-dipole/induced-dipole) and the  $C_8$  term represents the second dispersive term (random dipole/induced quadrupole, random-quadrupole/induced dipole). The  $C_6$  coefficient is calculated using the Slater-Kirkwood approximation,<sup>12</sup> and the  $C_8$  coefficient is calculated using the Koutselos-Mason approximation.<sup>13</sup> The simple  $Ae^{-bR}$  repulsive term was chosen due to its simplicity and ability to model the repulsion accurately<sup>14</sup> ( $Z$ ,  $A$  and  $b$  are fitted parameters).

## 4.2 Computational Details

For He-Ar, the standard aug-cc-pV5Z basis sets<sup>15,16,17</sup> were employed; for Kr-Rn the basis sets employed were the standard ECP+valence basis sets, ECP10MDF\_aV5Z-PP, ECP28MDF\_aV5Z-PP and ECP60MDF\_aV5Z-PP respectively.<sup>18</sup> The core electrons in each of the metals were described by a relativistic effective core potential (ECP); ECP10MDF, ECP28MDF, ECP46MDF and ECP78MDF for Ca, Sr, Ba and Ra respectively. The ECPs include relativistic effects, but not spin-orbit coupling. These were used in combination with valence basis sets, which were designed by E. P. F. Lee using the following method.

For calcium, an open-shell restricted Hartree-Fock (ROHF) calculation was carried out on  $\text{Ca}^+$  employing an uncontracted (19s17p) even-tempered basis set; 19s (centre=1.4; ratio=1.8) and 17p (centre=1.7; ratio=2.4) functions were used. The computed coefficients of the basis functions of the occupied atomic orbitals obtained from this calculation were used as the coefficients for the contracted [2s1p] basis functions designed to describe the 3s and 3p electrons of  $\text{Ca}^+$  and  $\text{Ca}^{2+}$  (since these may be considered as valence for the dication) and the 4s electron of  $\text{Ca}^+$ . To these, additional uncontracted basis functions were added<sup>19</sup> such that the basis set could be described as ECP10MDF [11s8p5d4f3g2h], which is approximately the same standard as an aug-cc-pV5Z basis set. The first and second ionisation energies have been calculated employing the RCCSD(T) method and this basis set, yielding 6.109 and 11.866 eV; these are in good agreement with experimentally obtained values of 6.113 and 11.872 eV.<sup>20</sup>

For strontium, the small core ECP28MDF basis set describes the  $[\text{Ar}]3d^{10}$  electrons. A valence basis set was designed using an ROHF calculation on

Sr<sup>+</sup> using an uncontracted (19s15p) even-tempered basis set; 19s (centre=0.5; ratio=1.7) and 15p (centre=1.0; ratio=1.5) functions were used. The computed coefficients of the basis functions of the occupied atomic orbitals obtained from this calculation were used as the coefficients for contracted [2s1p] basis functions to describe the 4s and 4p electrons of Sr<sup>+</sup> and Sr<sup>2+</sup> and also the 5s electron of Sr<sup>+</sup>. To these, additional uncontracted basis functions were added,<sup>21</sup> such that the basis set could be described as ECP28MDF [11s10p5d4f3g2h]. This can also be regarded as approximately the same standard as an aug-cc-pV5Z basis set. The first and second ionisation energies were calculated as for calcium, yielding 5.683 and 11.009 eV; again, these compare well with the experimental results, 5.695 and 11.031 eV.<sup>22</sup>

For barium, the small core ECP46MDF was employed to describe the [Kr]4d<sup>10</sup> electrons. In order to derive the valence basis set an ROHF calculation was run on Ba<sup>+</sup> using a (19s16p) even-tempered basis set; 19s (centre=1.0; ratio=1.7) and 16p (centre=1.1; ratio=1.5) functions were used. The computed coefficients were used to generate contracted [2s1p] basis functions used to describe the 5s and 5p electrons of Ba<sup>+</sup> and Ba<sup>2+</sup> and also the 6s electron of Ba<sup>+</sup>. Uncontracted basis functions were added to these<sup>23</sup> such that the overall basis set could be described as ECP46MDF [7s6p5d4f3g2h]; again, this can be regarded as approximately aug-cc-pV5Z standard. The calculated ionisation energies for barium were 5.186 and 9.958 eV, which again compare well with the experimental values (5.211<sup>24</sup> and 10.004 eV<sup>25</sup> respectively).

For radium, a valence basis set had previously been derived;<sup>26</sup> two *h* polarisation functions ( $\zeta=0.35$  and 0.05) were incorporated so that the overall basis set could be described as EPF60MDF [10s10p5d4f3g2h].

For  $\text{Ca}^{2+}\text{-Xe}$  the  $4d$  orbitals of Xe are lower in energy than the  $3p$  orbitals of  $\text{Ca}^{2+}$ ; for this reason they were correlated. The following tight functions were added to the basis set for Xe:  $d[\zeta=3.84 \text{ and } 1.92]$ ;  $f[\zeta=3.9146 \text{ and } 1.702]$ ;  $g[\zeta=2.8]$ ;  $h[\zeta=2.6]$ .

For  $\text{Ca}^{2+}\text{-Rn}$  and  $\text{Sr}^{2+}\text{-Rn}$  the  $5d$  orbitals of Rn have energies similar to those of the  $3p$   $\text{Ca}^{2+}$  orbitals and the  $4p$   $\text{Sr}^{2+}$  orbitals, so these were also correlated. The following tight functions were therefore added to the Rn basis set:  $d[\zeta=2.9 \text{ and } 1.3]$ ;  $f[\zeta=1.7]$ ;  $g[\zeta=1.7]$ ;  $h[\zeta=1.7]$ .

In all other cases for Kr-Rn the outermost occupied  $d$  orbitals were correlated as well as the valence  $s$  and  $p$  orbitals. For Ne, the  $1s$  orbital was frozen, as were the  $1s$ ,  $2s$  and  $2p$  orbitals of Ar. For the metal ions, all electrons were correlated except those described by the ECPs. The full counterpoise correction was applied and the internuclear separation,  $R$ , was varied over a wide range (1-50 Å). The step size was generally around 0.1 Å at short  $R$ , 0.025 Å around the minimum and gradually became larger at longer  $R$ .

As for the Au-RG ground states (see Chapter 3), the MOLPRO<sup>27</sup> suite of programs was employed for the calculations and the potential energy curves were used as input to the LEVEL<sup>28</sup> program. The spectroscopic constants were derived by using a least-squares fitting procedure to the standard Morse expressions for the lowest few energy levels. The most abundant naturally occurring isotope of each element was used (<sup>40</sup>Ca, <sup>88</sup>Sr, <sup>138</sup>Ba, <sup>226</sup>Ra, <sup>4</sup>He, <sup>20</sup>Ne, <sup>40</sup>Ar, <sup>84</sup>Kr, <sup>132</sup>Xe and <sup>222</sup>Rn).

### 4.3 Results

Tables 4.1–4.4 show the spectroscopic constants derived for  $M^+RG$  complexes. The force constants,  $k$ , have been calculated from the simple harmonic relationship

$$\nu = \frac{1}{2\pi} \sqrt{\frac{k}{\mu}} \quad (4.2)$$

$\nu$  is the frequency of the vibration, which can be calculated from  $\omega_e$ , and  $\mu$  is the reduced mass of the complex

$$\mu = \frac{m_A m_B}{m_A + m_B} \quad (4.3)$$

$D_e^{\text{MORSE}}$  has been determined from the standard Morse expression using the calculated values of  $\omega_e$  and  $\omega_e x_e$  (see Chapter 2). Previous theoretical and experimental results found in the literature are also included in the tables for comparison.

In general, good agreement is seen with previous experimental work. The results from theoretical studies have varied considerably; each species will be considered in turn.

**Table 4.1: Spectroscopic constants for Ca<sup>+</sup>-RG.  $R_e$  is the equilibrium bond length (Å),  $D_e$  is the depth of the potential,  $D_0$  is the energy between the zero-point and the asymptote,  $\omega_e$  is the harmonic vibrational frequency,  $\omega_e x_e$  is the anharmonicity constant,  $B_e$  is the equilibrium rotational constant at the minimum,  $\alpha$  is the spin-rotation constant (all in cm<sup>-1</sup>),  $k$  is the harmonic force constant (Nm<sup>-1</sup>). Results from this work are shown in bold.**

	$R_e$	$D_e$	$D_0$	$\omega_e$	$\omega_e x_e$	$B_e$	$\alpha$	$D_e^{\text{MORSE}}$	$D_e^{\text{MORSE}}/D_e$	$k$
<b>Ca<sup>+</sup>-He</b>	<b>4.259</b>	<b>35.9</b>	<b>23.3</b>	<b>25.6</b>	<b>4.884</b>	<b>0.264</b>	<b>7.30x10<sup>-3</sup></b>	<b>33.5</b>	<b>0.93</b>	<b>0.141</b>
Ref. 29 <sup>a</sup>	4.1	51.1								
Ref. 30 <sup>b</sup>	4.4	30								
Ref. 31 <sup>c</sup>	4.01	44.4								
<b>Ca<sup>+</sup>-Ne</b>	<b>3.760</b>	<b>109</b>	<b>97.4</b>	<b>24.8</b>	<b>1.503</b>	<b>0.0889</b>	<b>5.91x10<sup>-3</sup></b>	<b>102</b>	<b>0.94</b>	<b>0.484</b>
Refs. 11 and 32	3.70±0.05 <sup>d</sup>	115±5 <sup>d</sup>	103±5 <sup>d</sup>	26±2 <sup>d</sup>						
Ref. 3030 <sup>b</sup>	4.0	124								
Ref. 33 <sup>e</sup>	3.867	90.2		21.0						
Ref. 31 <sup>c</sup>	3.08	1.77								
<b>Ca<sup>+</sup>-Ar</b>	<b>3.256</b>	<b>742</b>	<b>712</b>	<b>60.6</b>	<b>1.590</b>	<b>0.0795</b>	<b>2.55x10<sup>-3</sup></b>	<b>577</b>	<b>0.78</b>	<b>4.33</b>
Refs.11,34,35,36,37	3.20±0.15 <sup>f</sup>	810±60 <sup>g</sup>		69±2 <sup>d</sup>						
Ref. 33 <sup>e</sup>	3.166	762.0		65.2						
Ref. 38 <sup>h</sup>	3.152	885	789	73	2.70					
Ref. 35 <sup>g</sup>			775±50							
Ref. 34 <sup>d</sup>			735±100							
Ref. 39 <sup>d</sup>			890±100							
<b>Ca<sup>+</sup>-Kr</b>	<b>3.305</b>	<b>1200</b>	<b>1160</b>	<b>69.7</b>	<b>1.307</b>	<b>0.0570</b>	<b>1.16x10<sup>-3</sup></b>	<b>929</b>	<b>0.78</b>	<b>7.76</b>
Refs.11,34,35,36,37,37	3.30±0.15 <sup>f</sup>	1280±80 <sup>g</sup>		77±2 <sup>d</sup>						
Ref. 38 <sup>h</sup>	3.202	1376	1252	68	1.49					
Ref. 35 <sup>g</sup>			1244±60							
Ref. 34 <sup>d</sup>			1400±150							
Ref. 39 <sup>d</sup>			840±100	74						
<b>Ca<sup>+</sup>-Xe</b>	<b>3.457</b>	<b>1780</b>	<b>1740</b>	<b>78.2</b>	<b>1.033</b>	<b>0.0460</b>	<b>6.35x10<sup>-4</sup></b>	<b>1480</b>	<b>0.83</b>	<b>11.1</b>
Refs.11,34,35,36,37	3.45±0.25 <sup>f</sup>	1850±100 <sup>g</sup>		84±2 <sup>d</sup>						
Ref. 3535 <sup>g</sup>			1811±80							
Ref. 34 <sup>d</sup>			2300±150							
<b>Ca<sup>+</sup>-Rn</b>	<b>3.487</b>	<b>2190</b>	<b>2150</b>	<b>81.9</b>	<b>0.878</b>	<b>0.0410</b>	<b>4.58x10<sup>-4</sup></b>	<b>1910</b>	<b>0.87</b>	<b>13.4</b>

<sup>a</sup>Model potential. <sup>b</sup>CI calculation. <sup>c</sup>B3LYP calculation. <sup>d</sup>Photodissociation spectroscopy. <sup>e</sup>MP2 calculation. <sup>f</sup>Estimate from  $R_e$  values of Ca-RG Rydberg states. <sup>g</sup>Two-colour photoionisation. <sup>h</sup>RCCSD(T) calculation.

**Table 4.2: Spectroscopic constants for Sr<sup>+</sup>-RG. Symbols and units used are as for Table 4.1. Results from this work are shown in bold.**

	$R_e$	$D_e$	$D_0$	$\omega_e$	$\omega_e x_e$	$B_e$	$\alpha$	$D_e^{\text{MORSE}}$	$D_e^{\text{MORSE}}/D_e$	$k$
<b>Sr<sup>+</sup>-He</b>	<b>4.547</b>	<b>28.9</b>	<b>18.5</b>	<b>21.1</b>	<b>4.12</b>	<b>0.220</b>	<b><math>6.52 \times 10^{-2}</math></b>	<b>27.1</b>	<b>0.94</b>	<b>0.10</b>
<b>Sr<sup>+</sup>-Ne</b>	<b>4.005</b>	<b>91.3</b>	<b>81.9</b>	<b>19.5</b>	<b>1.11</b>	<b>0.0650</b>	<b><math>3.98 \times 10^{-3}</math></b>	<b>85.6</b>	<b>0.94</b>	<b>0.37</b>
Ref. 40 <sup>a</sup>		77	67/85	19.5±1.5						
<b>Sr<sup>+</sup>-Ar</b>	<b>3.385</b>	<b>646</b>	<b>623</b>	<b>47.3</b>	<b>1.21</b>	<b>0.0535</b>	<b><math>1.62 \times 10^{-3}</math></b>	<b>464</b>	<b>0.72</b>	<b>3.63</b>
Ref. 41 <sup>a</sup>		827±244	803±244	49.5	0.75					
Ref. 42 <sup>b</sup>	3.662	694		38.7	0.72					
<b>Sr<sup>+</sup>-Kr</b>	<b>3.433</b>	<b>1050</b>	<b>1030</b>	<b>51.1</b>	<b>0.850</b>	<b>0.0333</b>	<b><math>5.78 \times 10^{-4}</math></b>	<b>765</b>	<b>0.73</b>	<b>6.62</b>
Ref. 43 <sup>a</sup>		1231	1205±580	52±1	0.6					
<b>Sr<sup>+</sup>-Xe</b>	<b>3.591</b>	<b>1560</b>	<b>1530</b>	<b>54.7</b>	<b>0.600</b>	<b>0.0248</b>	<b><math>2.78 \times 10^{-4}</math></b>	<b>1250</b>	<b>0.80</b>	<b>9.32</b>
Ref. 44 <sup>a</sup>		1974±435/1200		54.6	0.38					
<b>Sr<sup>+</sup>-Rn</b>	<b>3.617</b>	<b>1940</b>	<b>1910</b>	<b>55.4</b>	<b>0.470</b>	<b>0.0205</b>	<b><math>1.77 \times 10^{-4}</math></b>	<b>1630</b>	<b>0.84</b>	<b>11.4</b>

<sup>a</sup>Photodissociation spectroscopy. <sup>b</sup>icMRCI+Q calculation.

**Table 4.3 Spectroscopic constants for Ba<sup>+</sup>-RG. Symbols and units used are as for Table 4.1. Results from this work are shown in bold.**

	$R_e$	$D_e$	$D_0$	$\omega_e$	$\omega_e x_e$	$B_e$	$\alpha$	$D_e^{\text{MORSE}}$	$D_e^{\text{MORSE}}/D_e$	$k$
<b>Ba<sup>+</sup>-He</b>	<b>4.950</b>	<b>21.8</b>	<b>13.4</b>	<b>16.7</b>	<b>3.39</b>	<b>0.183</b>	<b><math>5.55 \times 10^{-2}</math></b>	<b>21</b>	<b>0.95</b>	<b>0.0636</b>
<b>Ba<sup>+</sup>-Ne</b>	<b>4.291</b>	<b>72.6</b>	<b>65.4</b>	<b>15.1</b>	<b>0.82</b>	<b>0.0529</b>	<b><math>2.91 \times 10^{-3}</math></b>	<b>70</b>	<b>0.95</b>	<b>0.235</b>
<b>Ba<sup>+</sup>-Ar</b>	<b>3.385</b>	<b>693.1</b>	<b>664.3</b>	<b>58.6</b>	<b>2.19</b>	<b>0.0476</b>	<b><math>1.47 \times 10^{-3}</math></b>	<b>392</b>	<b>0.57</b>	<b>6.27</b>
Ref. 45	3.364 <sup>a</sup>	680 <sup>b</sup>		61.7±1.5 <sup>c</sup>	2.3±0.2 <sup>c</sup>		[ $1.25 \times 10^{-3}$ ] <sup>d</sup>			
Ref. 46 <sup>e</sup>	3.47	~800		38.7	0.72					
<b>Ba<sup>+</sup>-Kr</b>	<b>3.479</b>	<b>1093.0</b>	<b>1066.3</b>	<b>53.9</b>	<b>1.02</b>	<b>0.0267</b>	<b><math>4.28 \times 10^{-4}</math></b>	<b>712</b>	<b>0.65</b>	<b>8.92</b>
<b>Ba<sup>+</sup>-Xe</b>	<b>3.653</b>	<b>1568.9</b>	<b>1542.9</b>	<b>52.3</b>	<b>0.61</b>	<b>0.0187</b>	<b><math>1.97 \times 10^{-4}</math></b>	<b>1121</b>	<b>0.71</b>	<b>10.87</b>
<b>Ba<sup>+</sup>-Rn</b>	<b>3.709</b>	<b>1916.2</b>	<b>1891.5</b>	<b>49.5</b>	<b>0.41</b>	<b>0.0144</b>	<b><math>1.11 \times 10^{-4}</math></b>	<b>1494</b>	<b>0.79</b>	<b>12.31</b>

<sup>a</sup> $R_0$  value from high-resolution laser induced fluorescence experiments. <sup>b</sup>Lower resolution dispersed fluorescence experiments.

<sup>c</sup>Fitted RKR potential from experiment. <sup>d</sup>Estimated. <sup>e</sup>Inversion of experimental transport data.

Table 4.4: Spectroscopic constants for  $\text{Ra}^+$ -RG. Symbols and units used are as for Table 4.1. Results from this work are shown in bold.

	$R_e$	$D_e$	$D_0$	$\omega_e$	$\omega_e x_e$	$B_e$	$\alpha$	$D_e^{\text{MORSE}}$	$D_e^{\text{MORSE}}/D_e$	$k$
$\text{Ra}^+$ -He	<b>4.885</b>	<b>23.3</b>	<b>14.5</b>	<b>17.6</b>	<b>3.55</b>	<b>0.186</b>	<b><math>5.53 \times 10^{-2}</math></b>	<b>21.8</b>	<b>0.94</b>	<b>0.0717</b>
$\text{Ra}^+$ -Ne	<b>4.276</b>	<b>76.5</b>	<b>68.6</b>	<b>16.3</b>	<b>0.917</b>	<b>0.0504</b>	<b><math>3.11 \times 10^{-3}</math></b>	<b>72.5</b>	<b>0.95</b>	<b>0.288</b>
$\text{Ra}^+$ -Ar	<b>3.759</b>	<b>486</b>	<b>469</b>	<b>34.3</b>	<b>0.776</b>	<b>0.0351</b>	<b><math>9.49 \times 10^{-4}</math></b>	<b>379</b>	<b>0.78</b>	<b>2.36</b>
$\text{Ra}^+$ -Kr	<b>3.775</b>	<b>793</b>	<b>775</b>	<b>34.9</b>	<b>0.520</b>	<b>0.0193</b>	<b><math>2.94 \times 10^{-4}</math></b>	<b>586</b>	<b>0.74</b>	<b>4.40</b>
$\text{Ra}^+$ -Xe	<b>3.917</b>	<b>1170</b>	<b>1160</b>	<b>35.9</b>	<b>0.351</b>	<b>0.0132</b>	<b><math>1.27 \times 10^{-4}</math></b>	<b>918</b>	<b>0.78</b>	<b>6.33</b>
$\text{Ra}^+$ -Rn	<b>3.944</b>	<b>1470</b>	<b>1450</b>	<b>34.6</b>	<b>0.248</b>	<b>0.00967</b>	<b><math>6.85 \times 10^{-5}</math></b>	<b>1210</b>	<b>0.82</b>	<b>7.89</b>

Table 4.5: Spectroscopic constants for  $\text{Ca}^{2+}$ -RG. Symbols and units used are as for Table 4.1. Results from this work are shown in bold.

	$R_e$	$D_e$	$D_0$	$\omega_e$	$\omega_e x_e$	$B_e$	$\alpha$	$D_e^{\text{MORSE}}$	$D_e^{\text{MORSE}}/D_e$	$k$
$\text{Ca}^{2+}$ -He	<b>2.351</b>	<b>1240</b>	<b>1110</b>	<b>279</b>	<b>17.8</b>	<b>0.841</b>	<b><math>6.05 \times 10^{-3}</math></b>	<b>1090</b>	<b>0.88</b>	<b>16.6</b>
Ref. 30 <sup>a</sup>	2.41	1160								
$\text{Ca}^{2+}$ -Ne	<b>2.461</b>	<b>2080</b>	<b>1990</b>	<b>183</b>	<b>4.67</b>	<b>0.209</b>	<b><math>5.59 \times 10^{-3}</math></b>	<b>1790</b>	<b>0.86</b>	<b>26.2</b>
Ref. 30 <sup>a</sup>	2.51	1680								
Ref. 3333 <sup>b</sup>	2.446	2062		185.6						
Ref. 47 <sup>c</sup>	2.472	1780								
$\text{Ca}^{2+}$ -Ar	<b>2.735</b>	<b>5670</b>	<b>5580</b>	<b>200</b>	<b>1.90</b>	<b>0.113</b>	<b><math>1.21 \times 10^{-3}</math></b>	<b>5260</b>	<b>0.93</b>	<b>47.1</b>
Ref. 3333 <sup>b</sup>	2.699	5873.1		203.4						
$\text{Ca}^{2+}$ -Kr	<b>2.865</b>	<b>7320</b>	<b>7230</b>	<b>179</b>	<b>1.14</b>	<b>0.0759</b>	<b><math>5.73 \times 10^{-4}</math></b>	<b>6990</b>	<b>0.95</b>	<b>51.1</b>
$\text{Ca}^{2+}$ -Xe	<b>3.04</b>	<b>9550</b>	<b>9460</b>	<b>173</b>	<b>0.804</b>	<b>0.0595</b>	<b><math>3.40 \times 10^{-4}</math></b>	<b>9340</b>	<b>0.98</b>	<b>54.4</b>
$\text{Ca}^{2+}$ -Rn	<b>3.115</b>	<b>10770</b>	<b>10690</b>	<b>165</b>	<b>0.601</b>	<b>0.0513</b>	<b><math>2.59 \times 10^{-4}</math></b>	<b>11380</b>	<b>1.06</b>	<b>54.7</b>

<sup>a</sup>CISD calculations. <sup>b</sup>MP2(full) calculations;  $D_e$  value corrected for BSSE. <sup>c</sup>CCSD(T) calculation. Corrected for BSSE.

Table 4.6: Spectroscopic constants for Sr<sup>2+</sup>-RG. Symbols and units used are as for Table 4.1. Results from this work are shown in bold.

	$R_e$	$D_e$	$D_0$	$\omega_e$	$\omega_e X_e$	$B_e$	$\alpha$	$D_e^{\text{MORSE}}$	$D_e^{\text{MORSE}}/D_e$	$k$
Sr <sup>2+</sup> -He	<b>2.565</b>	<b>914</b>	<b>805</b>	<b>224</b>	<b>12.8</b>	<b>0.672</b>	<b>5.25x10<sup>-2</sup></b>	<b>981</b>	<b>1.07</b>	<b>11.3</b>
Sr <sup>2+</sup> -Ne	<b>2.654</b>	<b>1600</b>	<b>1530</b>	<b>141</b>	<b>3.69</b>	<b>0.147</b>	<b>3.87x10<sup>-3</sup></b>	<b>1340</b>	<b>0.84</b>	<b>19.0</b>
Sr <sup>2+</sup> -Ar	<b>2.903</b>	<b>4580</b>	<b>4510</b>	<b>151</b>	<b>1.38</b>	<b>0.0728</b>	<b>7.18x10<sup>-4</sup></b>	<b>4160</b>	<b>0.91</b>	<b>37.1</b>
Sr <sup>2+</sup> -Kr	<b>3.026</b>	<b>6000</b>	<b>5940</b>	<b>128</b>	<b>0.727</b>	<b>0.0429</b>	<b>2.74x10<sup>-4</sup></b>	<b>5610</b>	<b>0.93</b>	<b>41.3</b>
Sr <sup>2+</sup> -Xe	<b>3.203</b>	<b>7970</b>	<b>7910</b>	<b>120</b>	<b>0.468</b>	<b>0.0312</b>	<b>1.44x10<sup>-4</sup></b>	<b>7710</b>	<b>0.97</b>	<b>44.9</b>
Sr <sup>2+</sup> -Rn	<b>3.265</b>	<b>8990</b>	<b>8930</b>	<b>111</b>	<b>0.351</b>	<b>0.0251</b>	<b>9.64x10<sup>-5</sup></b>	<b>8830</b>	<b>0.98</b>	<b>46.0</b>

Table 4.7: Spectroscopic constants for Ba<sup>2+</sup>-RG. Symbols and units used are as for Table 4.1. Results from this work are shown in bold.

	$R_e$	$D_e$	$D_0$	$\omega_e$	$\omega_e X_e$	$B_e$	$\alpha$	$D_e^{\text{MORSE}}$	$D_e^{\text{MORSE}}/D_e$	$k$
Ba <sup>2+</sup> -He	<b>2.842</b>	<b>637.6</b>	<b>552</b>	<b>175.7</b>	<b>14.0</b>	<b>0.542</b>	<b>4.88x10<sup>-2</sup></b>	<b>551</b>	<b>0.86</b>	<b>7.07</b>
Ba <sup>2+</sup> -Ne	<b>2.907</b>	<b>1162.5</b>	<b>1108</b>	<b>110.9</b>	<b>3.15</b>	<b>0.114</b>	<b>3.20x10<sup>-3</sup></b>	<b>976</b>	<b>0.84</b>	<b>12.6</b>
Ba <sup>2+</sup> -Ar	<b>3.130</b>	<b>3519.9</b>	<b>3459</b>	<b>122.1</b>	<b>1.19</b>	<b>0.0554</b>	<b>5.58x10<sup>-4</sup></b>	<b>3132</b>	<b>0.89</b>	<b>27.2</b>
Ba <sup>2+</sup> -Kr	<b>3.244</b>	<b>4682.6</b>	<b>4632</b>	<b>100.8</b>	<b>0.59</b>	<b>0.0307</b>	<b>1.92x10<sup>-4</sup></b>	<b>4305</b>	<b>0.92</b>	<b>31.3</b>
Ba <sup>2+</sup> -Xe	<b>3.413</b>	<b>6309.2</b>	<b>6262</b>	<b>94.0</b>	<b>0.37</b>	<b>0.0215</b>	<b>9.42x10<sup>-5</sup></b>	<b>5970</b>	<b>0.94</b>	<b>35.2</b>
Ba <sup>2+</sup> -Rn	<b>3.481</b>	<b>7218.8</b>	<b>7176</b>	<b>85.3</b>	<b>0.26</b>	<b>0.0164</b>	<b>5.77x10<sup>-5</sup></b>	<b>6996</b>	<b>0.96</b>	<b>36.5</b>

Table 4.8: Spectroscopic constants for Ra<sup>2+</sup>-RG. Symbols and units used are as for Table 4.1. Results from this work are shown in bold.

	$R_e$	$D_e$	$D_0$	$\omega_e$	$\omega_e X_e$	$B_e$	$\alpha$	$D_e^{\text{MORSE}}$	$D_e^{\text{MORSE}}/D_e$	$k$
Ra <sup>2+</sup> -He	<b>2.947</b>	<b>562</b>	<b>484</b>	<b>160</b>	<b>12.2</b>	<b>0.496</b>	<b>4.49x10<sup>-2</sup></b>	<b>528</b>	<b>0.94</b>	<b>5.96</b>
Ra <sup>2+</sup> -Ne	<b>3.001</b>	<b>1040</b>	<b>993</b>	<b>101</b>	<b>2.91</b>	<b>0.102</b>	<b>2.83x10<sup>-3</sup></b>	<b>869</b>	<b>0.83</b>	<b>11.0</b>
Ra <sup>2+</sup> -Ar	<b>3.214</b>	<b>3220</b>	<b>3170</b>	<b>111</b>	<b>1.08</b>	<b>0.0481</b>	<b>4.71x10<sup>-4</sup></b>	<b>2860</b>	<b>0.89</b>	<b>24.6</b>
Ra <sup>2+</sup> -Kr	<b>3.326</b>	<b>4320</b>	<b>4270</b>	<b>89.0</b>	<b>0.502</b>	<b>0.0249</b>	<b>1.47x10<sup>-4</sup></b>	<b>3940</b>	<b>0.91</b>	<b>28.6</b>
Ra <sup>2+</sup> -Xe	<b>3.495</b>	<b>5840</b>	<b>5800</b>	<b>81.3</b>	<b>0.300</b>	<b>0.0166</b>	<b>6.68x10<sup>-5</sup></b>	<b>5500</b>	<b>0.94</b>	<b>32.5</b>
Ra <sup>2+</sup> -Rn	<b>3.562</b>	<b>6690</b>	<b>6660</b>	<b>71.6</b>	<b>0.200</b>	<b>0.0119</b>	<b>3.73x10<sup>-5</sup></b>	<b>6420</b>	<b>0.96</b>	<b>33.9</b>

## $Ca^+-RG$

For  $Ca^+-He$ , the results here are in good agreement with the configuration interaction (CI) calculation of Czuchaj *et al.*,<sup>30</sup> but the B3LYP calculation<sup>31</sup> and the model potential by Monteiro *et al.*<sup>29</sup> both yield dissociation energies that are rather higher. Since coupled cluster calculations are expected to describe these weakly interacting systems more accurately than B3LYP calculations, this suggests that the value obtained from the model potential is an over-estimate.

$Ca^+-Ne$  has been the subject of photodissociation experiments by Reddic *et al.*<sup>32</sup> Their values for  $R_e$ ,  $D_e$  and  $\omega_e$  are all in excellent agreement with those reported here. The B3LYP calculation again yields a higher value for the dissociation energy,<sup>31</sup> the CI value is in reasonable agreement,<sup>30</sup> as is Kirschner's MP2(full)+ $\Delta$ BSSE calculation.<sup>33</sup>

A considerable amount of work has been done on  $Ca^+-Ar$ . There is fairly good agreement with the dissociation energies obtained from photodissociation<sup>34</sup> experiments of  $Ca^+-Ar$  and two-colour photoionisation threshold experiments<sup>35</sup> on the first metastable triplet state of  $Ca-Ar$ . This method uses accurate measurements of the ionisation potential of the excited state [ $IP(Ca^*-Ar)$ ], the known ionisation potential of  $Ca(4s^14p^1)$  [ $IP(Ca^*)$ ] and the value of  $D_0$  for the excited state [ $D_0(Ca^*-Ar)$ ], which is estimated from previous experiments and *ab initio* methods.  $D_0$  for the ionised complex can therefore be calculated from the equation

$$D_0(Ca^+Ar) = IP(Ca^*) - IP(Ca^*Ar) + D_0(Ca^*Ar) \quad (4.4)$$

The argument is that since the bond energy for a low energy metastable state of the neutral complex will be much smaller than the bond energy of the ionised complex, the relative error on the calculated bond energy of the ion will also be much smaller if it depends on the error on the bond

energy of the excited state. The value for the bond length, which has been estimated from spectroscopic studies on the Rydberg states of Ca–Ar,<sup>11,36,37</sup> is in excellent agreement with the value reported here. The MP2 calculation<sup>33</sup> is in better agreement than the CCSD(T) calculation of Heinemann *et al.*<sup>38</sup> Theoretical values of  $D_e=789\text{ cm}^{-1}$  and  $\omega_e=67.7\text{ cm}^{-1}$  reported in ref. 34 are in good agreement with the present study; however, no details of how the calculations were performed were given.

For  $\text{Ca}^+\text{–Kr}$ , two photodissociation experiments have been reported; Duncan’s group report a dissociation energy slightly higher than that presented herein,<sup>34</sup> while a much lower value was found by Buthelezi *et al.*<sup>39</sup> Buthelezi and co-workers studied a cationic state tentatively assigned to the  $C^2\Sigma^+$  state, which yielded a short progression. It has been suggested<sup>34</sup> that the three vibrational bands measured for  $\text{Ca}^+\text{–Kr}$  by Buthelezi and co-workers are insufficient for a reliable Morse extrapolation. Since they have only obtained results for one isotopologue of  $\text{Ca}^+\text{–Ar}$ , it is also possible that their vibrational numbering for  $\text{Ca}^+\text{–Ar}$  is incorrect; this may explain the unlikely similarity in the binding energies for the two complexes. Duncan’s group investigated the  $D^2\Pi$  cationic states, which yielded longer vibrational progressions; their extrapolation is therefore likely to give the more reliable results. The value obtained from photoionisation is only slightly above that obtained here.<sup>35</sup> As for  $\text{Ca}^+\text{–Ar}$ , theoretical values are given in ref. 34 that are in excellent agreement with the current study ( $D_e=1186\text{ cm}^{-1}$ ,  $\omega_e=72.8\text{ cm}^{-1}$ ), but no details about the calculation were given.

The  $D_e$  value found in the present study for  $\text{Ca}^+\text{–Xe}$  is considerably lower than that yielded by the photodissociation experiments of Duncan *et al.*<sup>34</sup> These experiments do show a reasonably long progression; however it is noted that the vibrational numbering has an uncertainty of  $v\pm 2$ . The

present value is well above the lower bound of Kaup and Breckenridge's value obtained from photoionisation.<sup>35</sup>

$R_e$  has been estimated for the cationic complexes from the Rydberg states of Ca-Ar, Ca-Kr and Ca-Xe;<sup>11,36,37</sup> these values are in excellent agreement with those reported here. In ref. 11,  $\omega_e$  has also been estimated from  $\Delta G_{1/2}$  values reported in refs. 34 and 32. Although these values are in reasonable agreement with those reported here, they are consistently slightly higher.

### $Sr^+-RG$

A considerable amount of work on  $Sr^+-RG$  complexes has been carried out by Velegrakis and co-workers. This has included spectroscopic work on  $RG=Ne-Xe$  and theoretical calculations on the  $Sr^+-Ar$  complex.<sup>40,41,42,43,44</sup>

For  $Sr^+-Ne$ , the values of  $\omega_e$  and  $\omega_e X_e$  obtained by Velegrakis *et al.*<sup>40</sup> are in excellent agreement with those reported herein. They have employed two methods to calculate the dissociation energy for the ground state. The first uses the spectroscopic constants that were calculated from vibrational analysis of the hot band separation; the second uses the  $D_e$  value for the excited states. The two values obtained are 85 and 67  $cm^{-1}$  respectively; the value calculated here is much closer to the former.

The Birge-Sponer (BS) and LeRoy-Bernstein (LB) methods have been employed to estimate  $D_0$  for  $Sr^+-Ar$ ,  $Sr^+-Kr$  and  $Sr^+-Xe$ .<sup>41,42,43</sup> The average of these values is given, with the results from the LB and BS analyses used as the upper and lower bounds respectively, for  $Sr^+-Ar$  and  $Sr^+-Kr$ . For  $RG=Ne-Xe$ ,  $D_e$  was also calculated from an electrostatic potential function including a simple  $\frac{A}{R^m}$  repulsive term and the ion-induced dipole attractive term. Upper and lower bounds have been found using the limits of 1e and 2e for the effective charge on the ion,  $q$ . They determined that the "best

value" for  $q$  was approximately 1.4 and for  $m$  approximately 8, using fits to their data from previous experiments and referring to previous work on model potentials by Bellert and Breckenridge.<sup>11</sup> The results given here are consistently within their limits, although towards the lower bound. The experimental results for  $\omega_e$  are in very good agreement with those obtained here. The  $\omega_e X_e$  values for RG=Ar-Xe are rather low; however this is unsurprising since those values were estimated from the only two observed energy levels using the Morse expression. Their theoretical spectroscopic parameters for Sr<sup>+</sup>-Ar have been obtained using the MRCI approach;<sup>42</sup> these are in fairly good agreement with those reported herein.

#### *Ba<sup>+</sup>-RG*

For the Ba<sup>+</sup>-RG series, high quality spectroscopic data is only available for the Ar complex; this work by Panov *et al.*<sup>45</sup> yields results in very good agreement with those presented here. It is interesting to note that the BS plot in ref. 45 was nonlinear, indicating a severe deviation from Morse-like behaviour. The dissociation energy was therefore estimated using a model potential, partly based on a Rydberg-Klein-Rees (RKR) fit to the data. The agreement with the spectroscopic values derived from ion mobility experiments<sup>46</sup> is not as good.

#### *Ra<sup>+</sup>-RG*

There do not appear to be any previous results for Ra<sup>+</sup>-RG for comparison.

#### *M<sup>2+</sup>-RG*

The spectroscopic constants for M<sup>2+</sup>-RG are shown in tables 4.5-4.8. No experimental values have been found for any of the species; however, since this work was carried out, Koyanagi and Bohme have reported the first observation of Ba<sup>2+</sup>-RG complexes.<sup>48</sup> The Ba dications were produced

by electrospray ionisation and the complexes formed in a selected ion flow tube; complexes with Ar, Kr, Xe and (tentatively) He were observed.

There have been some theoretical studies of  $\text{Ca}^{2+}$ -RG. The CISD study of Czuchaj *et al.*<sup>30</sup> generally shows good agreement with the present study, although the  $D_e$  value for  $\text{Ca}^{2+}$ -Ne is somewhat lower. Kirschner's MP2 results are in excellent agreement; B3LYP values in the same study were very similar.<sup>33</sup> The CCSD(T) calculations reported for  $\text{Ca}^{2+}$ -Ne yield a  $D_e$  value somewhat lower than that found in this study; however the  $R_e$  value is in much better agreement. No theoretical studies have been found for any of the other dicationic series investigated here.

#### 4.4 Trends

Figure 4.1 shows the variation in  $R_e$  with the rare gas for each of the different metal ions. It can be seen that there is a minimum at  $\text{M}^+$ -Ar for all four metals; however the decrease in bond length between  $\text{M}^+$ -Ne and  $\text{M}^+$ -Ar is not as substantial for Ca, Sr and Ra as it is for Ba. The  $D_e$  values follow a monotonically increasing trend with a significant increase between  $\text{M}^+$ -Ne and  $\text{M}^+$ -Ar. The values of  $\omega_e$  are quite similar for the lighter He and Ne complexes, there is a significant increase for  $\text{M}^+$ -Ar and the values remain constant for the heavier species. One might expect this since this parameter is dependent on the balance between the increasing interaction energy and reduced mass; the force constants are mass independent and show monotonically increasing trends from He to Rn, again with sharp increases (factors of  $9 \pm 1$ ) between  $\text{M}^+$ -Ne and  $\text{M}^+$ -Ar. The ratios  $D_e^{\text{MORSE}}/D_e$  indicate severe deviations from Morse-like behaviour for the heavier rare gases; this is particularly true for Ar and Kr, but the effect is still significant for Xe and Rn.

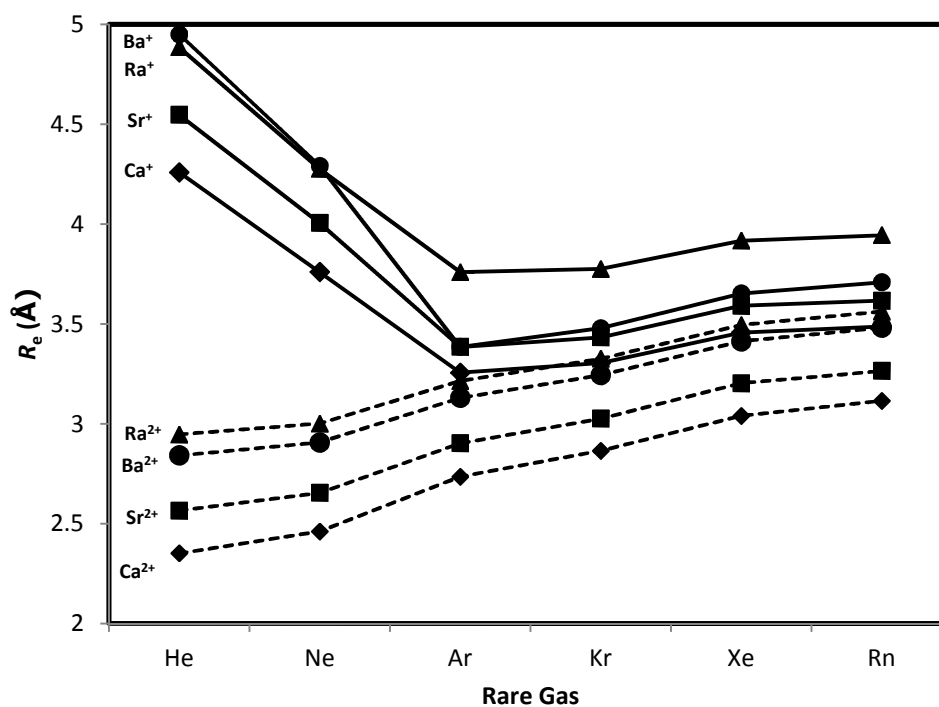


**Figure 4.1: Variation in  $R_e$  for  $M^{n+}$ -RG ( $M$ =Ca, Sr, Ba and Ra;  $n=1$  and 2). The solid lines are for the  $M^+$ -RG species, and the dashed lines are for the  $M^{2+}$ -RG species. Different symbols represent different metals: Ca, rhombi; Sr, squares; Ba, circles and Ra, triangles. Note the presence of a minimum in the  $R_e$  values observed at RG=Ar for each of the  $M^+$ -RG species; the  $M^{2+}$ -RG species do not have such a minimum.**

By contrast, the dicationic complexes show trends that are more similar to those seen in the isoelectronic alkali metal cation-RG complexes.<sup>5,6,7,8</sup>  $R_e$  and  $D_e$  increase gradually with the mass of the complex and the force constants do not show the same dramatic increase between Ne and Ar; the increase is only by a factor of 1.8-2.2. The  $R_e$  values for the dication complexes presented here are significantly smaller than those for the alkali metal cation complexes (this may be expected, since the dominant ion/induced-dipole term in these isoelectronic cases is proportional to  $Z^2$ ). The  $M^{2+}$  ions are also slightly smaller; the combination of these factors causes a substantial decrease in  $R_e$  and a correspondingly large increase in

$D_e$ .

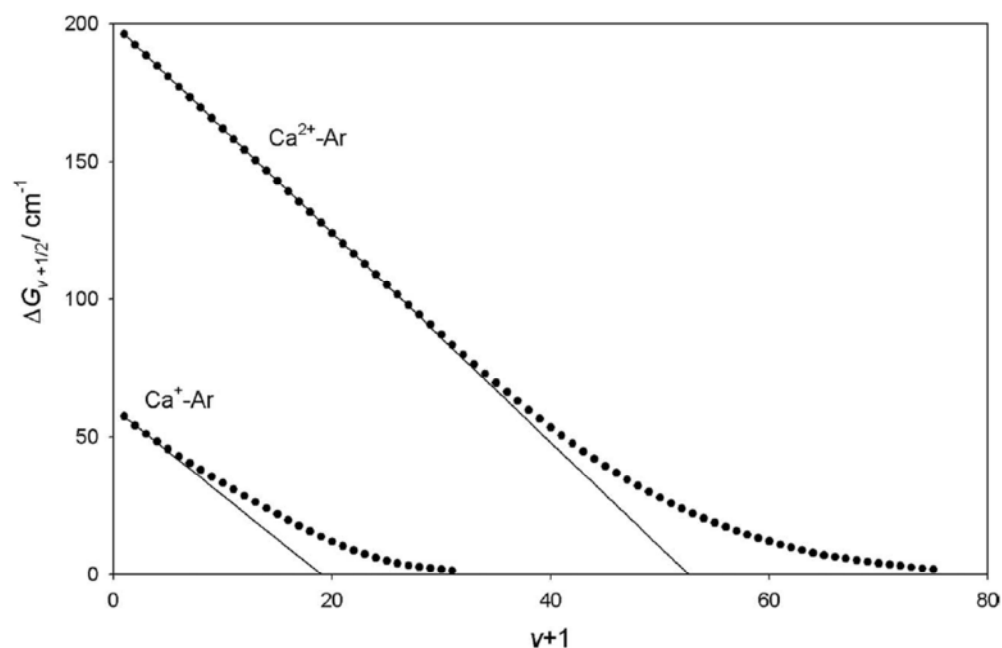


**Figure 4.2: BS plots for  $\text{Ca}^+\text{-Ar}$  and  $\text{Ca}^{2+}\text{-Ar}$  (dots) employing the calculated vibrational energy levels described herein. The lines are obtained by employing the Morse parameters that were obtained from the lowest few energy levels (see Tables 4.1 and 4.5).**

The  $D_e^{\text{MORSE}}/D_e$  ratios also indicate that the dication series show more Morse-like behaviour. This is illustrated in Figure 4.2, which shows BS plots for  $\text{Ca}^+\text{-Ar}$  and  $\text{Ca}^{2+}\text{-Ar}$ , based on the calculated potentials. It can be seen that  $\text{Ca}^+\text{-Ar}$  deviates from the Morse line very quickly, whereas  $\text{Ca}^{2+}\text{-Ar}$  shows Morse-like behaviour up to at least  $v=30$ . This may be expected because of the much deeper potential well of the dicationic species.

#### 4.5 Discussion

It was found in Chapter 3 that for the Au-RG complexes the  $R_e$  values decreased as the size of the rare gas atom increased. It was suggested that this could be due to the increasing polarisability, which led to the electron density shifting off-axis and consequent deshielding of the core, allowing the rare gas atom to move closer. It can be seen that, for the

lighter rare gases, a related effect seems to occur in the complexes studied here. It will be argued that, in both cases, the effect seen is hybridisation of the singly occupied, highly polarisable  $s$  orbital of the metal atom/ion with the lowest unoccupied orbital.

It has been noted that between the  $M^+-Ne$  and  $M^+-Ar$  complexes  $R_e$  decreases significantly, while  $D_e$  and  $k$  have a similarly large increase. This effect may be expected to some extent because of the relatively high polarisability of Ar when compared to He or Ne; this would lead to a rise in the attractive terms in the multipole expansion of the long range potential (see Equation 4.1), an effect seen previously in alkali metal cationic complexes.<sup>11, 49</sup> However, since it is expected that the leading charge-induced dipole term will be dominant, one might expect the increase to vary approximately linearly with the polarisability; thus a fourfold increase would be predicted. The substantial decrease observed in  $R_e$  induces an increase in both  $D_e$  and  $k$  that is much greater than this, indicating a stronger interaction than would be expected if only the physical forces described by Equation 4.1 were involved.

A substantial increase in  $D_e$  between  $M^+-Ne$  and  $M^+-Ar$  has previously been seen for  $M = Sc, Ti$  and  $Mn$  by Partridge and co-workers.<sup>50</sup> All of these metals have a  $3d^n4s^1$  electron configuration in the cation ground state. It was argued in ref. 50 that  $s-d\sigma$  hybridisation on the metal could be causing the electron density to move off-axis, resulting in reduced electron repulsion. This would allow the rare gas atom to move closer and increase the magnitude of the attractive induction and dispersion terms. The polarisability of He and Ne was deemed insufficient for the extra attractive interaction to overcome the energy required for hybridisation; this would explain the jump in  $D_e$  between Ne and Ar. Examining the Mulliken populations, Partridge *et al.* found that the  $3d$  population in  $Ti^+-Ar$

was 2.21e, compared with 2.00e and 2.09e for  $\text{Ti}^+\text{-He}$  and  $\text{Ti}^+\text{-Ne}$  respectively. The same effect occurs to a much lesser extent in the  $\text{Sc}^+\text{-RG}$  series, but it is noted that the same cannot occur for  $\text{Mn}^+$  as the relevant states are of different spin.

Examining the Mulliken populations for  $\text{Ba}^+\text{-Ar}$ , employing restricted Hartree-Fock (RHF) calculations and using the RCCSD(T) value for  $R_e$ , it was found that the 5d orbital showed an increase of 0.05e above the expected occupancy. For the other metals, the increase was much smaller, 0.003e, 0.012e and 0.012e for Ca, Sr and Ra respectively.

It is possible that the low  $R_e$  values are partly caused by dispersion effects; this would suggest that the calculated spectroscopic parameters would be greatly affected by the exclusion of electron correlation. Dispersion effects would then be neglected, reducing the attraction between the metal ion and the rare gas atom. In order to investigate this possibility, RHF calculations, which do not include dynamic electron correlation, were performed to determine  $R_e$  and  $D_e$ . The results are shown in Tables 4.9-4.12.

**Table 4.9: Spectroscopic constants for Ca<sup>+</sup>-RG and Ca<sup>2+</sup>-RG calculated at the RHF level and RCCSD(T) level (in square brackets). Symbols and units are as stated in header for Table 4.1.  $D_e$  ratio is the ratio RCCSD(T):RHF.**

	$R_e$	$D_e$	$D_e$ ratio		$R_e$	$D_e$	$D_e$ ratio
Ca <sup>+</sup> -He	4.93 [4.26]	14 [36]	2.6	Ca <sup>2+</sup> -He	2.42 [2.35]	975 [1240]	1.3
Ca <sup>+</sup> -Ne	4.70 [3.76]	29 [109]	3.8	Ca <sup>2+</sup> -Ne	2.53 [2.46]	1550 [2080]	1.3
Ca <sup>+</sup> -Ar	4.02 [3.26]	198 [742]	3.7	Ca <sup>2+</sup> -Ar	2.80 [2.74]	4710 [5670]	1.2
Ca <sup>+</sup> -Kr	3.67 [3.31]	417 [1200]	2.9	Ca <sup>2+</sup> -Kr	2.93 [2.87]	6120 [7320]	1.2
Ca <sup>+</sup> -Xe	3.70 [3.46]	803 [1780]	2.2	Ca <sup>2+</sup> -Xe	3.12 [3.04]	8130 [9550]	1.2
Ca <sup>+</sup> -Rn	3.71 [3.49]	1080 [2190]	2.0	Ca <sup>2+</sup> -Rn	3.19 [3.12]	9180 [10770]	1.2

**Table 4.10: Spectroscopic constants for Sr<sup>+</sup>-RG and Sr<sup>2+</sup>-RG calculated at the RHF level and RCCSD(T) level (in square brackets). Symbols and units are as stated in header for Table 4.1.  $D_e$  ratio is the ratio RCCSD(T):RHF.**

	$R_e$	$D_e$	$D_e$ ratio		$R_e$	$D_e$	$D_e$ ratio
Sr <sup>+</sup> -He	5.30 [4.55]	10 [29]	2.9	Sr <sup>2+</sup> -He	2.67 [2.57]	672 [914]	1.4
Sr <sup>+</sup> -Ne	5.05 [4.01]	22 [91]	4.1	Sr <sup>2+</sup> -Ne	2.75 [2.65]	1103 [1600]	1.4
Sr <sup>+</sup> -Ar	4.40 [3.39]	144 [646]	4.5	Sr <sup>2+</sup> -Ar	3.00 [2.90]	3591 [4580]	1.3
Sr <sup>+</sup> -Kr	3.92 [3.43]	304 [1050]	3.5	Sr <sup>2+</sup> -Kr	3.13 [3.03]	4760 [6000]	1.3
Sr <sup>+</sup> -Xe	3.91 [3.59]	611 [1560]	2.5	Sr <sup>2+</sup> -Xe	3.30 [3.20]	6426 [7970]	1.2
Sr <sup>+</sup> -Rn	3.91 [3.62]	843 [1940]	2.3	Sr <sup>2+</sup> -Rn	3.37 [3.27]	7307 [8990]	1.2

**Table 4.11: Spectroscopic constants for Ba<sup>+</sup>-RG and Ba<sup>2+</sup>-RG calculated at the RHF level and RCCSD(T) level (in square brackets). Symbols and units are as stated in header for Table 4.1. *D<sub>e</sub>* ratio is the ratio RCCSD(T):RHF.**

	<i>R<sub>e</sub></i>	<i>D<sub>e</sub></i>	<i>D<sub>e</sub></i> ratio		<i>R<sub>e</sub></i>	<i>D<sub>e</sub></i>	<i>D<sub>e</sub></i> ratio
Ba <sup>+</sup> -He	5.83 [4.95]	7 [22]	3.1	Ba <sup>2+</sup> -He	2.98 [2.84]	4.35 [638]	1.5
Ba <sup>+</sup> -Ne	5.54 [4.29]	15 [73]	4.9	Ba <sup>2+</sup> -Ne	3.05 [2.91]	739 [1162]	1.6
Ba <sup>+</sup> -Ar	4.84 [3.38]	99 [693]	7.0	Ba <sup>2+</sup> -Ar	3.26 [3.13]	2586 [3520]	1.4
Ba <sup>+</sup> -Kr	3.98 [3.48]	241 [1093]	4.5	Ba <sup>2+</sup> -Kr	3.38 [3.24]	3503 [4683]	1.3
Ba <sup>+</sup> -Xe	4.04 [3.65]	515 [1569]	3.1	Ba <sup>2+</sup> -Xe	3.54 [3.41]	4823 [6309]	1.3
Ba <sup>+</sup> -Rn	4.06 [3.71]	720 [1916]	2.7	Ba <sup>2+</sup> -Rn	3.61 [3.48]	5537 [7219]	1.3

**Table 4.12: Spectroscopic constants for Ra<sup>+</sup>-RG and Ra<sup>2+</sup>-RG calculated at the RHF level and RCCSD(T) level (in square brackets). Symbols and units are as stated in header for Table 4.1. *D<sub>e</sub>* ratio is the ratio RCCSD(T):RHF.**

	<i>R<sub>e</sub></i>	<i>D<sub>e</sub></i>	<i>D<sub>e</sub></i> ratio		<i>R<sub>e</sub></i>	<i>D<sub>e</sub></i>	<i>D<sub>e</sub></i> ratio
Ra <sup>+</sup> -He	5.78 [4.89]	7 [23]	3.3	Ra <sup>2+</sup> -He	3.10 [2.95]	372 [562]	1.5
Ra <sup>+</sup> -Ne	5.50 [4.28]	16 [77]	4.8	Ra <sup>2+</sup> -Ne	3.16 [3.00]	637 [1040]	1.6
Ra <sup>+</sup> -Ar	4.94 [3.76]	99 [486]	4.9	Ra <sup>2+</sup> -Ar	3.36 [3.21]	2303 [3220]	1.4
Ra <sup>+</sup> -Kr	4.60 [3.78]	184 [793]	4.3	Ra <sup>2+</sup> -Kr	3.47 [3.33]	3150 [4320]	1.4
Ra <sup>+</sup> -Xe	4.46 [3.92]	359 [1170]	3.3	Ra <sup>2+</sup> -Xe	3.64 [3.50]	4374 [5840]	1.3
Ra <sup>+</sup> -Rn	4.39 [3.94]	508 [1470]	2.9	Ra <sup>2+</sup> -Rn	3.70 [3.56]	5043 [6690]	1.3

As expected,  $R_e$  showed an increase for all complexes following the exclusion of electron correlation, while  $D_e$  decreased. The ratio of the RCCSD(T)  $D_e$  to the RHF  $D_e$  (denoted  $D_e$  ratio) gives an indication of the effect of the dispersive interactions. For  $\text{Ca}^+$ ,  $\text{Sr}^+$  and  $\text{Ra}^+$ , this ratio reaches a maximum for  $\text{M}^+\text{-Ne}$  and  $\text{M}^+\text{-Ar}$ , both of which have similar ratios.

However,  $\text{Ba}^+\text{-Ar}$  appears to be a special case where the ratio is much larger than for any of the other complexes in the series. The most likely cause of this is the very diffuse, polarisable 6s orbital of  $\text{Ba}^+$ , which causes a very large dispersive attraction between the ion and the rare gas atom. The attraction is counterbalanced by repulsive terms arising from the interaction with the rare gas electrons. The low polarisability of He and Ne makes the overall interaction very weak, despite the relatively low repulsion; the high polarisability of Kr, Xe and Rn results in a much stronger interaction, although this is partly balanced by increased repulsion. However, for  $\text{Ba}^+\text{-Ar}$  the balance appears to be in favour of the increased attraction, which outweighs the repulsion resulting in a much shorter  $R_e$  and a much higher dissociation energy.

For further evidence of the importance of dispersion effects Bellert and Breckenridge's<sup>11</sup> model potential equation (Equation 4.1) was employed to investigate the existence of factors affecting the potential beyond the normally expected physical interactions. The equation can be differentiated twice, with the first differential equation (set equal to zero) relating to the potential energy minimum at equilibrium bond length and the second describing the "curvature" of the potential (this is related to  $\omega_e$ ). Using the calculated values of  $R_e$ ,  $D_e$  and  $\omega_e$ , the three equations could be solved for  $Z$ ,  $b$  and  $A$ .

Table 4.13 shows the values of  $Z$ , the effective charge on the metal cation, for each of  $\text{Ba}^+ - \text{RG}$  ( $\text{RG} = \text{He} - \text{Xe}$ ). They have been calculated including all the terms and also by progressively omitting the higher order terms.

**Table 4.13: Calculated  $Z$  values with removal of terms in the model potential given in Equation 4.1 (terms removed include the term(s) stated and all those of higher order).**

Terms Removed	$\text{Ba}^+ - \text{He}$	$\text{Ba}^+ - \text{Ne}$	$\text{Ba}^+ - \text{Ar}$	$\text{Ba}^+ - \text{Kr}$	$\text{Ba}^+ - \text{Xe}$
None	1.190	1.169	0.422	0.803	0.860
<b>1<sup>st</sup> <math>R^8</math> (<math>C_8</math>)</b>	<b>1.238</b>	<b>1.258</b>	<b>0.862</b>	<b>0.987</b>	<b>1.064</b>
<b>2<sup>nd</sup> <math>R^8</math> (ion/induced octopole)</b>	1.190	1.170	0.423	0.808	0.867
<b>3<sup>rd</sup> <math>R^8</math> (<math>\gamma</math>)</b>	1.190	1.170	0.422	0.804	0.861
<b>all <math>R^8</math></b>	1.238	1.259	0.867	0.995	1.075
<b><math>R^7</math></b>	1.240	1.261	0.875	1.009	1.094
<b>1<sup>st</sup> <math>R^6</math> (<math>C_6</math>)</b>	<b>1.321</b>	<b>1.359</b>	<b>1.109</b>	<b>1.199</b>	<b>1.246</b>
<b>2<sup>nd</sup> <math>R^6</math> (ion/induced quadrupole)</b>	1.247	1.273	0.905	1.050	1.147
<b>all <math>R^6</math></b>	1.328	1.372	1.150	1.250	1.310

If the model is describing the system correctly, the value of  $Z$  should be approximately equal to 1. It is clearly much lower than this for the heavier rare gases, which implies that the model has failed for these systems. It was noted in ref 11 that while this model was shown to work well for many similar systems, it appeared to fail for  $\text{Au}^+ - \text{Xe}$  and  $\text{Ba}^+ - \text{Ar}$ . It was suggested that in the case of  $\text{Ba}^+ - \text{Ar}$  this could be because the values of  $R_e$ ,  $D_e$  and  $\omega_e$  (obtained from refs. 51 and 45) were inaccurate. It now seems more likely that the model fails because interactions of a more chemical nature are taking place that the model is not designed to describe. It can be seen that the removal of the dispersion terms, involving the  $C_6$  and  $C_8$  coefficients, has the largest effect on the value of  $Z$ , causing it to rise most dramatically. This indicates that these terms provide a large amount of the interaction energy, and hence that dispersion effects are very significant;

this supports the conclusions reached from the results of the RHF calculations.

The sharp increase in  $D_e$  between  $M^+-\text{Ne}$  and  $M^+-\text{Ar}$  in each of the series can be understood within this picture. The ratio of the increase in  $D_e$  between these two complexes calculated at the RCCSD(T) level is 6.8, 7.1, 9.5 and 6.4 for  $M=\text{Ca}$ ,  $\text{Sr}$ ,  $\text{Ba}$  and  $\text{Ra}$  respectively; this again indicates an enhanced effect in  $\text{Ba}^+-\text{Ar}$  compared with other  $M^+-\text{Ar}$  complexes. In contrast, for the  $M^{2+}$  complexes the ratios are much smaller ( $2.9\pm 0.2$ ).

This makes sense in the light of the higher occupancy of the  $(n-1)d$  orbital for  $\text{Ba}^+-\text{Ar}$  when compared with the other  $M^+-\text{Ar}$  complexes (*vide supra*).

It can be concluded that  $s-d\sigma$  hybridisation is the most likely cause of the increased attraction in  $\text{Ba}^+-\text{Ar}$  and that the effect is much smaller for the other metal cations.

**Table 4.14: Energies of the lowest  $^2D$  states of  $\text{Ca}^+$ ,  $\text{Sr}^+$ ,  $\text{Ba}^+$  and  $\text{Ra}^+$ . These states are formed from an excitation of the outermost  $ns$  electron into the  $(n-1)d$  orbital in each case. Values are taken from ref. 22.**

Ion	Excited state	Energy ( $\text{cm}^{-1}$ )
<b>Ca<sup>+</sup></b>	$^2D_{3/2}$	13,650
	$^2D_{5/2}$	13,710
<b>Sr<sup>+</sup></b>	$^2D_{3/2}$	14,560
	$^2D_{5/2}$	14,840
<b>Ba<sup>+</sup></b>	$^2D_{3/2}$	4,870
	$^2D_{5/2}$	5,670
<b>Ra<sup>+</sup></b>	$^2D_{3/2}$	12,080
	$^2D_{5/2}$	13,740

This can be understood with reference to Table 4.14, which shows the energy required to promote the outermost  $ns$  electron to the lowest  $^2D$  states of the  $M^+$  ions. The  $5d$  orbitals of  $\text{Ba}^+$  are very low-lying when compared to those of the other  $M^+$ . The high promotion energy of  $\text{Ra}^+$  relative to  $\text{Ba}^+$  is most likely due to the relatively greater stabilisation of

the 7s orbital versus the 6d orbital by the relativistic and lanthanide effects. In heavy atoms, electrons moving near the speed of light are affected by relativity, which causes the orbitals to be contracted. The occupation of the 3f lanthanide orbital and the substantial contraction of the Ra 7s orbital may in turn explain the slightly smaller  $R_e$  values for  $\text{Ra}^+\text{-He}$  and  $\text{Ra}^+\text{-Ne}$  when compared with the  $\text{Ba}^+$  species. However, the differences are very small and the errors on the values are difficult to quantify.

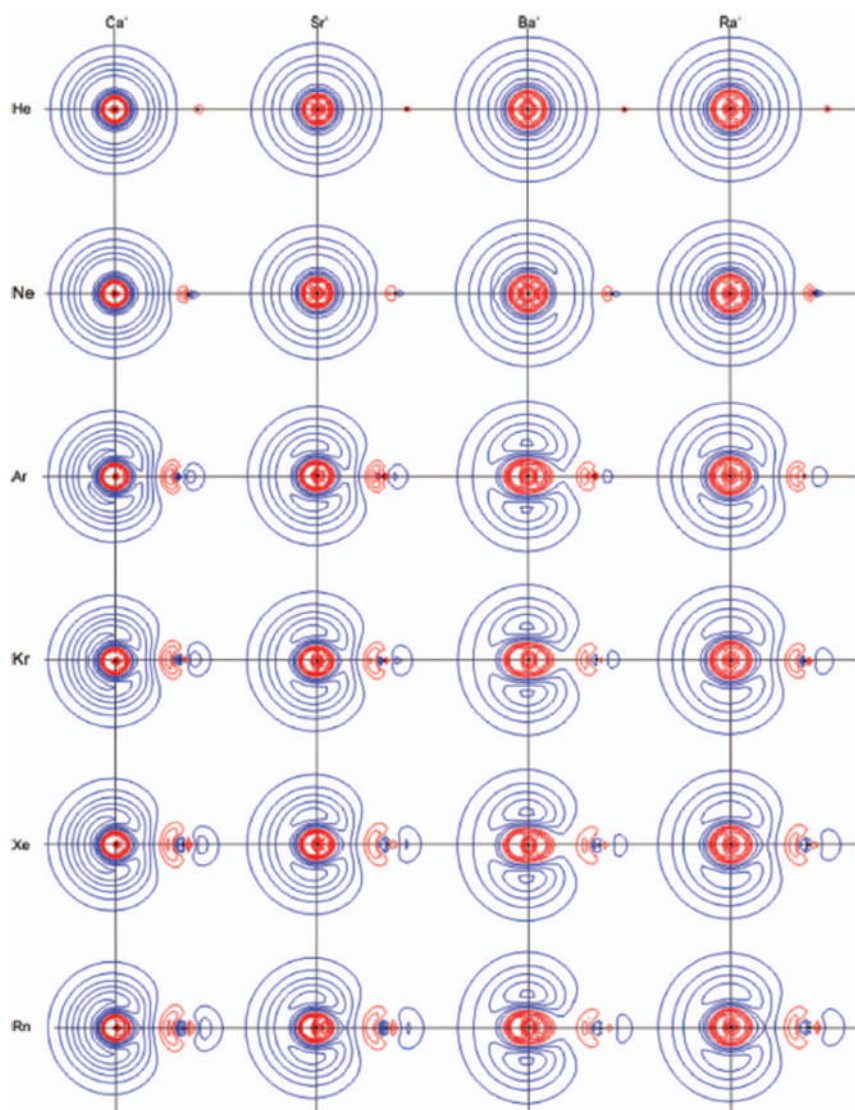


**Figure 4.3: MOLDEN<sup>52</sup> contour diagrams of the Hartree-Fock HOMO for each of the  $\text{M}^+\text{-RG}$  complexes calculated at the RCCSD(T)  $R_e$  value. The values of the contours were selected to show the details clearly and to allow comparison between the plots. The different colours indicate opposite signs of the wavefunction.**

MOLDEN<sup>52</sup> plots of contours of the RHF wavefunctions for the highest occupied molecular orbital (HOMO) were calculated by A. M. Gardner at the respective RCCSD(T)  $R_e$  value for each of the  $M^+$ -RG complexes; these are shown in Figure 4.3. No obvious deviations from the spherical  $ns$  orbital of the metal ion are apparent for any of the He complexes; slight perturbations are seen for the Ne species. For the  $M^+$ -Ar complexes, however, the electron density is shifted off-axis, consistent with the  $s$ - $d\sigma$  hybridisation indicated by the population analysis. It is unsurprising that similar effects are seen in  $M^+$ -Kr,  $M^+$ -Xe and  $M^+$ -Rn, which also show severe deviations from the spherical  $ns$  orbitals.

MOLDEN plots have also been calculated for Au-RG in ref. 53. These also show evidence for hybridisation, particularly for the heavier rare gases. In this case, the effect is  $sp$  hybridisation, resulting in a shift in electron density away from the Au atom but along the internuclear axis. Evidence was also seen in ref. 53 for charge transfer, which also increases with the atomic number of the rare gas. These effects not only serve to explain the unusual trend in  $R_e$  seen in Chapter 3, but also the failure of the model potential to describe the interaction of  $Au^+$ -Xe; if these effects are seen in the neutral species, they can be expected to be more substantial in the cation.

**Table 4.15: Comparison of  $R_e$  values (Å) for  $\text{Alk}^+\text{-RG}$  (refs. 5,6,7,8),  $\text{M}^+\text{-RG}$  and  $\text{M}^{2+}\text{-RG}$ .**

Alk	M	$\text{M}^{2+}$	$\text{Alk}^+$	$\text{M}^+$
		<b>He</b>		
<b>K</b>	<b>Ca</b>	2.35	2.83	4.26
<b>Rb</b>	<b>Sr</b>	2.57	3.07	4.55
<b>Cs</b>	<b>Ba</b>	2.84	3.36	4.95
<b>Fr</b>	<b>Ra</b>	2.95	3.47	4.89
		<b>Ne</b>		
<b>K</b>	<b>Ca</b>	2.46	2.92	3.76
<b>Rb</b>	<b>Sr</b>	2.65	3.14	4.01
<b>Cs</b>	<b>Ba</b>	2.91	3.40	4.29
<b>Fr</b>	<b>Ra</b>	3.00	3.49	4.28
		<b>Ar</b>		
<b>K</b>	<b>Ca</b>	2.74	3.22	3.26
<b>Rb</b>	<b>Sr</b>	2.90	3.43	3.39
<b>Cs</b>	<b>Ba</b>	3.13	3.64	3.39
<b>Fr</b>	<b>Ra</b>	3.21	3.71	3.79
		<b>Kr</b>		
<b>K</b>	<b>Ca</b>	2.87	3.36	3.31
<b>Rb</b>	<b>Sr</b>	3.03	3.56	3.43
<b>Cs</b>	<b>Ba</b>	3.24	3.76	3.48
<b>Fr</b>	<b>Ra</b>	3.33	3.83	3.78
		<b>Xe</b>		
<b>K</b>	<b>Ca</b>	3.04	3.56	3.46
<b>Rb</b>	<b>Sr</b>	3.20	3.75	3.59
<b>Cs</b>	<b>Ba</b>	3.41	3.95	3.65
<b>Fr</b>	<b>Ra</b>	3.50	4.01	3.92
		<b>Rn</b>		
<b>K</b>	<b>Ca</b>	3.12	3.64	3.49
<b>Rb</b>	<b>Sr</b>	3.27	3.84	3.62
<b>Cs</b>	<b>Ba</b>	3.48	4.03	3.71
<b>Fr</b>	<b>Ra</b>	3.56	4.09	3.94

Table 4.15 shows a comparison of the  $R_e$  values of the Group 2  $\text{M}^+(ns^1)$  ions with the Group 1  $\text{Alk}^+[(n-1)p^6]$  ions.<sup>5,6,7,8</sup> For He, the values for the Group 2 ions are all much larger than those of the Group 1 ions; this is expected since there is little distortion of the  $\text{M}^+(ns)$  orbital and these are known to be much larger than the  $\text{M}^+[(n-1)p]$  orbitals.<sup>54</sup> However, for Ar and the heavier rare gases the  $R_e$  values are comparable to, or even less than those for the equivalent  $\text{Alk}^+\text{-RG}$  complexes. This indicates that there must be a huge distortion of the large, polarisable  $\text{M}^+ ns$  electron clouds in these complexes, as is seen in Figure 4.3. It is remarkable that even a weak interaction with an inert gas such as Ar can generate such large shifts in the electron density in these ions. It is possible that if correlation

were included, further distortion of the  $ns$  orbitals would occur for the heavier complexes; however, since it can be clearly seen at the RHF level if the RCCSD(T)  $R_e$  value is used, it is apparent that the effect is mainly caused by the close proximity of the RG atom, which is permitted because of the dispersion effects included in the RCCSD(T) calculation.

Note that  $\text{Sr}^+-\text{Ar}$  and  $\text{Ba}^+-\text{Ar}$  have almost identical  $R_e$  values; for every other case for  $\text{Ar}-\text{Rn}$  in Table 4.15,  $R_e$  increases as the size of the ion increases. This is also likely to be a result of the increased  $s-d\sigma$  hybridisation that occurs for the  $\text{Ba}^+-\text{Ar}$  complex.

If the unusual behaviour seen in the Group 2  $\text{M}^+(ns^1)-\text{RG}$  complexes is partially due to  $s-d\sigma$  hybridisation, then one would not expect to see such behaviour in the Group 12  $\text{M}^+[(n-1)d^{10}ns^1]-\text{RG}$  complexes. In these species, the  $(n-1)d$  shells are filled and lower lying and the excited  $nd$  levels are much higher in energy; thus a much greater energy would be required to "promote" the electron and induce hybridisation.  $D_e^{\text{MORSE}}/D_e$  values for  $\text{M}^+-\text{RG}$  ( $\text{M}=\text{Zn}, \text{Cd}$  and  $\text{Hg}$ ) have been calculated from data previously published by the group<sup>55,56</sup> and found to be in the range of 0.86-1.20, indicating that these species show much more Morse-like behaviour.

With the evidence pointing to  $s-d\sigma$  hybridisation, it is unsurprising that the model potential described in ref. 11 fails to describe this system accurately, as it is designed to describe only physical interactions. The hybridisation will also affect the polarisability of the rare gas atoms, so the values used in the equation, which are for an unperturbed  $ns$  orbital, will not be correct in this instance.

## 4.6 Conclusions

Accurate *ab initio* interaction potentials have been calculated for  $M^{n+}$ -RG ( $M$ =Ca, Sr, Ba and Ra;  $n$ =1 and 2; RG=He-Rn) complexes. Spectroscopic constants derived from these curves have been compared to experimental results (where they exist) and good agreement has been demonstrated. As with the Au-RG series examined in Chapter 3, it appears that dispersive effects cause some unexpected results. For the Au-RG series it was suggested that the shift in electron density along the internuclear axis and away from the RG atom could be causing reduced repulsion and increased attraction due to the deshielding of the cationic core; this allowed the more polarisable rare gas atoms to move closer and led to an unexpected decrease in  $R_e$  as the van der Waals radius increased. In the complexes studied here, investigation of the occupancy of the  $(n-1)d$  orbitals at the RHF level and calculation of MOLDEEN molecular wavefunction plots has shown that  $s-d\sigma$  hybridisation is present in  $Ba^+$ -Ar and, to a lesser extent, in the other  $M^+$ -Ar complexes studied. Hybridisation is not noticeable in  $M^+$ -He and  $M^+$ -Ne; the polarisability of these rare gases is small and the increased attraction is not large enough to overcome the energy required for hybridisation. It has also been noted that the promotion energy from the  $ns$  to the  $(n-1)d$  orbitals in  $Ba^+$  is much lower than for  $Ca^+$ ,  $Sr^+$  and  $Ra^+$ ; this accounts for the smaller extent of hybridisation in the latter complexes, as again the increased attraction cannot overcome the cost. It was noted that similar MOLDEEN plots in ref 53 showed that  $sp$  hybridisation is present in the heavier Au-RG complexes, creating similar effects.

The results have also been discussed with reference to a model potential put forward by Bellert and Breckenridge;<sup>11</sup> since it cannot be used to

describe these systems correctly, this indicates that the interaction cannot be described purely by the physical processes, which is consistent with the idea of  $s$ - $d\sigma$  hybridisation.

## References

- 
- <sup>1</sup> P. Soldán, E. P. F. Lee, J. Lozeille, J. N. Murrell and T. G. Wright, *Chem. Phys. Lett.*, **343**, 429 (2001).
  - <sup>2</sup> J. Lozeille, E. Winata, P. Soldán, E. P. F. Lee, L. A. Viehland and T. G. Wright, *Phys. Chem. Chem. Phys.*, **4**, 3601 (2002).
  - <sup>3</sup> L. A. Viehland, J. Lozeille, P. Soldán, E. P. F. Lee and T. G. Wright, *J. Chem. Phys.*, **119**, 3729 (2003).
  - <sup>4</sup> L. A. Viehland, J. Lozeille, P. Soldán, E. P. F. Lee and T. G. Wright, *J. Chem. Phys.*, **121** (2004).
  - <sup>5</sup> H. L. Hickling, L. A. Viehland, D. T. Shepherd, P. Soldán, E. P. F. Lee and T. G. Wright, *Phys. Chem. Chem. Phys.*, **6**, 4233 (2004).
  - <sup>6</sup> J. Lozeille, E. Winata, L. A. Viehland, P. Soldán, E. P. F. Lee and T. G. Wright, *Phys. Chem. Chem. Phys.*, **4**, 3601 (2002).
  - <sup>7</sup> L. A. Viehland, J. Lozeille, P. Soldán, E. P. F. Lee and T. G. Wright, *J. Chem. Phys.*, **119**, 3729 (2003).
  - <sup>8</sup> L. A. Viehland, J. Lozeille, P. Soldán, E. P. F. Lee and T. G. Wright, *J. Chem. Phys.*, **121**, 341 (2004).
  - <sup>9</sup> H. L. Hickling, L. A. Viehland, D. T. Shepherd, P. Soldán, E. P. F. Lee and T. G. Wright, *Phys. Chem. Chem. Phys.*, **6**, 4233 (2004).
  - <sup>10</sup> M. J. H. Hogan, *J. Chem. Phys.*, **125**, 164325 (2006).
  - <sup>11</sup> D. Bellert and W. H. Breckenridge, *Chem. Rev. (Washington, D. C.)*, **102**, 1595 (2002).
  - <sup>12</sup> Stone, A. J., *The Theory of Intermolecular Forces*; Clarendon Press: Oxford (1996).
  - <sup>13</sup> A. D. Koutselos and, E. A. Mason, *J. Chem. Phys.*, **85**, 2154 (1986).
  - <sup>14</sup> J. O. Hirschfelder, C. F. Curtiss, R. B. Bird, *Molecular Theory of Gases and Liquids*, Wiley: New York (1954).
  - <sup>15</sup> D. E. Woon and T. H. Dunning, Jr., *J. Chem. Phys.*, **100**, 2975 (1994).
  - <sup>16</sup> T. H. Dunning, Jr., *J. Chem. Phys.*, **90**, 1007 (1989)

- 
- <sup>17</sup> D. E. Woon and T. H. Dunning, Jr., *J. Chem. Phys.*, **98**, 1358 (1993)
- <sup>18</sup> K. A. Peterson, D. Figgen, E. Goll, H. Stoll and M. Dolg, *J. Chem. Phys.*, **119**, 11113 (2003)
- <sup>19</sup>  $s$ [4.685120, 2.1296, 0.968, 0.44, 0.2, 0.090909, 0.041322, 0.018783, 0.008538];  $p$ [4.2592, 1.936, 0.88, 0.4, 0.181818, 0.082645, 0.037566];  $d$ [0.78125, 0.3125, 0.125, 0.05, 0.02];  $f$ [1.08, 0.36, 0.12, 0.04];  $g$ [0.8, 0.2, 0.05];  $h$ [0.8,0.04].
- <sup>20</sup> Y. Ralchenko, A. E. Kramida, K. Olsen and NIST ASD Team (2008). *NIST Atomic Spectra Database* (version 3.1.5), [online]. Available <http://www.nist.gov/pml/data/asd.cfm> (February 2011). National Institute of Standards and Technology, Gaithersburg, MD.
- <sup>21</sup>  $s$ [3.52, 1.76, 0.88, 0.44, 0.22, 0.11, 0.0275, 0.01375];  $p$ [6.4, 3.2, 1.4, 0.8, 0.4, 0.2, 0.1, 0.05, 0.025];  $d$ [3.24, 1.08, 0.36, 0.12, 0.04];  $f$ [1.31072, 0.4096, 0.128,0.04];  $g$ [0.6125, 0.175, 0.05];  $h$  [0.6, 0.06].
- <sup>22</sup> C. E. Moore, *Atomic Energy Levels*, Natl. Bur. Stand. (U.S.) Circ. No. **467** (1952), Vol. 2; Reprinted as Natl. Stand. Ref. Data Ser. (U.S. Natl. Bur. Stand.) **35** (1971).
- <sup>23</sup>  $s$ [0.375, 0.15, 0.06, 0.024, 0.0096];  $p$ [0.5, 0.2, 0.08, 0.032, 0.0128];  $d$ [1.2544, 0.448, 0.16, 0.0571428, 0.0204081];  $f$  [1.08, 0.36, 0.12, 0.04];  $g$  [0.735, 0.21, 0.06];  $h$  [0.5, 0.1].
- <sup>24</sup> C. E. Moore, *Ionization Potentials and Ionization Limits Derived from the Analyses of Optical Spectra*, Natl. Stand. Ref. Data Ser., (U.S. Natl. Bur. Stand., Gaithersburg, MD), Vol. **34** (1997)
- <sup>25</sup> Y. Ralchenko, A. E. Kramida, J. Reader, and NIST ASD Team (2008). *NIST Atomic Spectra Database* (version 3.1.5), [online]. Available <http://www.nist.gov/pml/data/asd.cfm> (February 2011) National Institute of Standards and Technology, Gaithersburg, MD.
- <sup>26</sup> E. P. F. Lee, P. Soldán and T. G. Wright, *Inorg. Chem.*, **40**, 5979 (2001).
- <sup>27</sup> R. D. Amos, A. Bernhardsson, A. Berning, P. Celani, D. L. Cooper, M. J. O. Deegan, A. J. Dobbyn, F. Eckert, C. Hampel, G. Hetzer, P. J. Knowles, T. Korona, R. Lindh, A. W. Lloyd, S. J. McNicholas, F. R. Manby, W. Meyer, M. E. Mura, A. Nicklass, P. Palmieri, R. Pitzer, G. Rauhut, M. Schütz, U. Schumann, H. Stoll, A. J. Stone, R. Tarroni, T. Thorsteinsson and H.-J. Werner, MOLPRO, a package of ab initio programs designed by H.-J. Werner and P. J. Knowles, Version 2002.1 (2002).
- <sup>28</sup> R. J. LeRoy, Level 7.2—A computer program for solving the radial Schrödinger equation for bound and quasibound levels, and calculating various values and matrix elements, University of Waterloo Chemical Physics Research Program Report CP-555R (2000).
- <sup>29</sup> T. S. Monteiro, I. L. Cooper, A. S. Dickinson and E. L. Lewis, *J. Phys. B.*, **19**, 4087 (1986).

- 
- <sup>30</sup> E. Czuchaj, F. Rebentrost, H. Stoll and H. Preuss, *Chem. Phys.*, **207**, 51 (1996).
- <sup>31</sup> A. F. Jalbout and M. Solimannejad, *J. Mol. Struct.: THEOCHEM*, **640**, 21 (2003).
- <sup>32</sup> J. E. Reddic, S. H. Pullins and M. A. Duncan, *J. Chem. Phys.*, **112**, 4974 (2000).
- <sup>33</sup> K. N. Kirschner, *J. Chem. Phys.*, **112**, 10228 (2000).
- <sup>34</sup> S. H. Pullins, C. T. Scurlock, J. E. Reddic and M. A. Duncan, *J. Chem. Phys.*, **104**, 7518 (1996).
- <sup>35</sup> J. G. Kaup and W. H. Breckenridge, *J. Chem. Phys.*, **107**, 4451 (1997).
- <sup>36</sup> J. G. Kaup and W. H. Breckenridge, *J. Chem. Phys.*, **107**, 5283 (1997).
- <sup>37</sup> J. G. Kaup and W. H. Breckenridge, *J. Chem. Phys.*, **107**, 5676 (1997).
- <sup>38</sup> C. Heinemann, W. Koch and H. Partridge, *Chem. Phys. Lett.*, **286**, 131 (1998).
- <sup>39</sup> T. Buthelezi, D. Bellert, V. Lewis and P. J. Brucat, *Chem. Phys. Lett.*, **246**, 145 (1995).
- <sup>40</sup> C. Lüder, D. Prekas, A. Vourliotaki and M. Velegrakis, *Chem. Phys. Lett.*, **267**, 149 (1997).
- <sup>41</sup> C. Lüder and M. Velegrakis, *J. Chem. Phys.*, **105**, 2167 (1996).
- <sup>42</sup> S. S. Xantheas, G. S. Fanourgakis, S. V. Farantos and M. Velegrakis, *J. Chem. Phys.*, **108**, 46 (1998).
- <sup>43</sup> D. Prekas, B.-H. Feng and M. Velegrakis, *J. Chem. Phys.*, **108**, 2712 (1998).
- <sup>44</sup> M. Massauoti, A. Sfounis and M. Velegrakis, *Chem. Phys. Lett.*, **348**, 47 (2001).
- <sup>45</sup> S. I. Panov, J. M. Williamson and T. A. Miller, *J. Chem. Phys.*, **102**, 7359 (1995).
- <sup>46</sup> L. A. Viehland and D. S. Hampt, *J. Chem. Phys.*, **97**, 4964 (1992).
- <sup>47</sup> T. J. Grey, J. D. Gale and D. Nicholson, *Mol. Phys.* **98**, 1565 (2000).
- <sup>48</sup> G. K. Koyanagi and D. K. Bohme, *J. Phys. Chem. Lett.* **1**, **41** (2010).
- <sup>49</sup> W. H. Breckenridge, V. L. Ayles and T. G. Wright, *Chem. Phys.*, **333**, 77 (2007).
- <sup>50</sup> H. Partridge, C. W. Bauschlicher, Jr. And S. R. Langhoff, *J. Phys. Chem.*, **96**, 5350 (1992).

- 
- <sup>51</sup> Schröder, D.; Schwarz, H.; Hrusak, J.; Pyykko, P. *Inorg. Chem.*, **37**, 624 (1998).
- <sup>52</sup> G. Schaftenaar and J. H. Noordik, *J. Comput.-Aided Mol. Des.* **14**, 123 (2000).
- <sup>53</sup> A. M. Gardner, R. J. Plowright, M. J. Watkins, T. G. Wright and W. H. Breckenridge, *J. Chem. Phys.*, **132**, 184301 (2010).
- <sup>54</sup> J. T. Waber and D. T. Cromer, *J. Chem. Phys.*, **42**, 4116 (1965).
- <sup>55</sup> E. P. F. Lee, B. R. Gray, N. A. Joyner, S. H. Johnson, L. A. Viehland, W. H. Breckenridge and T. G. Wright, *Chem. Phys. Lett.*, **450**, 19 (2007).
- <sup>56</sup> E. Qing, L. A. Viehland, E. P. F. Lee and T. G. Wright, *J. Chem. Phys.*, **124**, 044316 (2006).

## 5. Theoretical Study of $M^+-RG$ and $M^{2+}-RG$ Complexes ( $M=Be, Mg$ ; $RG=He-Rn$ )

### 5.1 Introduction

To complete the work on Group 2 metal ion–rare gas complexes described in the last chapter,  $M^+-Rg$  and  $M^{2+}-RG$  ( $M=Be, Mg$ ;  $RG=He-Rn$ ) have been investigated, in collaboration with Adrian Gardner from the SOCAR group.

The *ab initio* methods are the same as those described for Ca-Ra; however there are some striking differences in the results that indicate that these complexes do not show the same behaviour as those involving the heavier metals. These results are again compared with previous theoretical and experimental results where available. The trends seen in the series are discussed and possible explanations for the unusual behaviour are put forward.

As for the potential energy curves for  $M=Ca-Ra$  described in Chapter 4, the calculated curves described in this chapter have been used to generate ion mobility data by L. A. Viehland and co-workers at Chatham University, USA. This data has been made available to other users *via* the Chatham database.<sup>1</sup>

### 5.2 Computational Details

For He-Ar, the standard aug-cc-pVQZ and aug-cc-pV5Z basis sets<sup>2,3,4</sup> were employed; for Kr-Rn the basis sets employed were the standard ECP+valance basis sets, ECP10MDF\_pV5Z-PP, ECP28MDF\_pV5Z-PP and ECP60MDF\_pV5Z-PP respectively.<sup>5</sup> Tight functions were added to describe the correlation of the inner-valence *d* orbitals (see ref. 6 for functions and exponents). Standard aug-cc-pVQZ and aug-cc-pV5Z basis sets were

employed for beryllium and magnesium, each augmented with tight functions of each angular momentum type to allow description of core-valence correlation.<sup>3,7</sup> Each of the basis sets was augmented by an additional set of diffuse basis functions of each angular momentum type, obtained in an even-tempered way from the two lowest exponents in each case, so that each basis set was overall doubly augmented with diffuse functions.

For Kr-Rn, the outermost occupied *d* orbitals were correlated, along with the valence *s* and *p* orbitals. For He and Be, all electrons were correlated; for Mg and Ne only the 1*s* orbital was frozen, while for Ar the 1*s*, 2*s* and 2*p* orbitals were frozen.

The full counterpoise correction was applied and the internuclear separation, *R*, was varied over a range of approximately 1-10 Å. The step size was generally around 0.1 Å at short *R*, 0.025 Å around the minimum and gradually became larger at longer *R*.

As for the Au-RG ground states (see Chapter 3), MOLPRO<sup>8</sup> was employed for the calculations and the potential energy curves were used as input to the LEVEL<sup>9</sup> program. For RG=He-Ar, the interaction energy for each *R* was extrapolated to the basis set limit (see Chapter 2). The spectroscopic constants were derived by using a least-squares fitting procedure to the standard Morse expressions for the lowest few energy levels. The most abundant naturally occurring isotope of each element was used (<sup>9</sup>Be, <sup>24</sup>Mg, <sup>4</sup>He, <sup>20</sup>Ne, <sup>40</sup>Ar, <sup>84</sup>Kr, <sup>132</sup>Xe and <sup>222</sup>Rn).

### 5.3 Results

Tables 5.1 and 5.2 show the spectroscopic constants derived for  $M^+ - RG$ . The force constants,  $k$ , have been calculated from the simple harmonic relationship, which is described in Chapters 2 and 4.

$D_e^{MORSE}$  has been calculated from the standard Morse expression using the calculated values of  $\omega_e$  and  $\omega_e x_e$  (see Chapter 2). Previous theoretical and experimental results found in the literature are also included in the tables for comparison.

While previous experimental work is limited, there is good overall agreement with the current results, which will be discussed in detail below. As for the heavier metals in Group 2, the results from theoretical studies vary widely.

For  $Be^+ - He$ , the agreement is good; the current study yields both the shortest  $R_e$  value and the highest dissociation energy.

For  $Be^+ - Ne$ , the results presented here show reasonable agreement with the MP2 values of Bu *et al.*; however Frenking *et al.* report a shorter bond length for both MP2 and MP4 level of theory.<sup>13</sup> Their reported value of  $\omega_e$  is also four times that reported here, the latter being in much better agreement with the QCISD(T) value.<sup>11</sup> The larger value of  $\omega_e$  results in the substantial difference between  $D_e$  and  $D_0$  stated in ref. 13; however the reported BSSE of  $1,200 \text{ cm}^{-1}$  suggests that these results may be unreliable. The present values are obtained at a higher level of theory and are in good agreement with the QCISD(T) values of ref. 11.

**Table 5.1: Spectroscopic constants for Be<sup>+</sup>-RG.  $R_e$  is the equilibrium bond length (Å),  $D_e$  is the depth of the potential,  $D_0$  is the energy between the zero-point and the asymptote,  $\omega_e$  is the harmonic vibrational frequency,  $\omega_e x_e$  is the anharmonicity constant,  $B_e$  is the equilibrium rotational constant at the minimum,  $a$  is the spin-rotation constant (all in cm<sup>-1</sup>),  $k$  is the harmonic force constant (Nm<sup>-1</sup>). Results from this work are shown in bold.**

	$R_e$	$D_e$	$D_0$	$\omega_e$	$\omega_e x_e$	$B_e$	$a$	$D_e^{\text{MORSE}}$	$D_e^{\text{MORSE}}/D_e$	$k$
<b>Be<sup>+</sup>-He</b>	<b>2.924</b>	<b>133.1</b>	<b>97.8</b>	<b>76.3</b>	<b>11.7</b>	<b>0.723</b>	<b>0.142</b>	<b>125</b>	<b>0.94</b>	<b>0.950</b>
Ref. 10	3.132 <sup>a</sup>		70 <sup>b</sup>	68 <sup>a</sup>						
Ref. 11 <sup>c</sup>	2.96	124		73						
Ref. 12 <sup>a</sup>	3.104		60	65						
<b>Be<sup>+</sup>-Ne</b>	<b>2.454</b>	<b>407.2</b>	<b>375.3</b>	<b>65.2</b>	<b>1.47</b>	<b>0.456</b>	<b>6.07x10<sup>-3</sup></b>	<b>723</b>	<b>1.78</b>	<b>1.555</b>
(1s correlated)	<b>2.462</b>	<b>403.7</b>	<b>371.7</b>	<b>65.6</b>	<b>1.63</b>	<b>0.453</b>	<b>5.92x10<sup>-3</sup></b>			
Ref. 13 <sup>a</sup>	1.856			259						
Ref. 13 <sup>b</sup>	2.054	314	175							
Ref. 11 <sup>c</sup>	2.59	359		68						
<b>Be<sup>+</sup>-Ar</b>	<b>2.084</b>	<b>4427.7</b>	<b>4247.7</b>	<b>364.1</b>	<b>8.94</b>	<b>0.528</b>	<b>1.47x10<sup>-2</sup></b>	<b>3710</b>	<b>0.84</b>	<b>57.4</b>
Ref. 13 <sup>a</sup>	2.045			382						
Ref. 13 <sup>b</sup>	2.104	3812	3637							
Ref. 14 <sup>d</sup>		4500±700								
Ref. 15 <sup>e</sup>	2.0855±0.0006	4112±200	3933±200	362.7±0.1	8.92±0.05	0.5271±0.0003	(1.45±0.03)x10 <sup>-2</sup>			
<b>Be<sup>+</sup>-Kr</b>	<b>2.221</b>	<b>6053.2</b>	<b>5871.8</b>	<b>365.5</b>	<b>5.82</b>	<b>0.420</b>	<b>8.16x10<sup>-3</sup></b>	<b>5740</b>	<b>0.95</b>	<b>64.0</b>
Ref. 14 <sup>d</sup>		6500±1000								
Ref. 16 <sup>e</sup>	2.2201			367.14	6.21	0.42030	8.21x10 <sup>-3</sup>			
<b>Be<sup>+</sup>-Xe</b>	<b>2.407</b>	<b>8239.8</b>	<b>8054.3</b>	<b>372.8</b>	<b>4.04</b>	<b>0.345</b>	<b>4.86x10<sup>-3</sup></b>	<b>8600</b>	<b>1.04</b>	<b>69.0</b>
Ref. 14 <sup>d</sup>		10000±2000								
Ref. 17 <sup>f</sup>		~9000		~367	~3.7					
<b>Be<sup>+</sup>-Rn</b>	<b>2.486</b>	<b>9490.5</b>	<b>9305.7</b>	<b>371.0</b>	<b>3.32</b>	<b>0.315</b>	<b>3.81x10<sup>-3</sup></b>	<b>10400</b>	<b>1.10</b>	<b>70.1</b>

<sup>a</sup>MP2 calculation. <sup>b</sup>MP4/MP2 calculation. <sup>c</sup>QCISD(T) calculation. <sup>d</sup>Recommended value from review of data up to 2001. <sup>e</sup>High resolution emission experiments. <sup>f</sup>Emission experiments.

**Table 5.2: Spectroscopic constants for Mg<sup>+</sup>-RG. Symbols and units used are as for Table 5.1. Results from this work are shown in bold.**

	$R_e$	$D_e$	$D_0$	$\omega_e$	$\omega_e X_e$	$B_e$	$\alpha$	$D_e^{\text{MORSE}}$	$D_e^{\text{MORSE}}/D_e$	$k$
<b>Mg<sup>+</sup>-He</b>	<b>3.482</b>	<b>73.2</b>	<b>51.7</b>	<b>45.8</b>	<b>7.68</b>	<b>0.412</b>	<b>9.00x10<sup>-2</sup></b>	<b>68.3</b>	<b>0.95</b>	<b>0.424</b>
Ref. 18 <sup>a</sup>	3.565	70		21						
Ref. 19 <sup>b</sup>	3.56	65		44						
Ref. 20 <sup>c</sup>	3.611	30		44						
Ref. 21 <sup>c</sup>	3.685	76.6		42						
<b>Mg<sup>+</sup>-Ne</b>	<b>3.145</b>	<b>203.1</b>	<b>182.3</b>	<b>43.1</b>	<b>2.44</b>	<b>0.157</b>	<b>9.87x10<sup>-3</sup></b>	<b>191</b>	<b>0.94</b>	<b>1.19</b>
Ref. 14 <sup>d</sup>	3.15	216±100		46						
Ref. 18 <sup>a</sup>	3.298	170		33						
Ref. 22 <sup>b</sup>	3.25	179		39						
Ref. 23 <sup>e</sup>	3.17±0.05 <sup>f</sup>	117±50	96±50	41 <sup>g</sup>						
<b>Mg<sup>+</sup>-Ar</b>	<b>2.822</b>	<b>1298.6</b>	<b>1246.7</b>	<b>104.8</b>	<b>2.53</b>	<b>0.141</b>	<b>4.07x10<sup>-3</sup></b>	<b>1090</b>	<b>0.84</b>	<b>9.71</b>
Refs. 24,25 <sup>h</sup>			1237±40							
Ref. 14 <sup>d</sup>	2.81±0.03	1290±60		100±3						
Ref. 18 <sup>a</sup>	2.894	1140		92						
Ref. 26 <sup>i</sup>	2.854		1041	90 <sup>g</sup>						
Refs. 27,28 <sup>e</sup>	2.825±0.007 <sup>f</sup>		1281	96 <sup>g</sup>						
Refs. 28,29 <sup>j</sup>			1210±165							
<b>Mg<sup>+</sup>-Kr</b>	<b>2.884</b>	<b>1978.1</b>	<b>1919.4</b>	<b>118.4</b>	<b>2.08</b>	<b>0.109</b>	<b>2.13x10<sup>-3</sup></b>	<b>1690</b>	<b>0.85</b>	<b>15.4</b>
Refs. 30,31 <sup>h</sup>			1891±80							
Ref. 14 <sup>d</sup>	~2.80	1949±100		116						
Refs.27,28 <sup>e</sup>			1923	112 <sup>g</sup>						
Ref. 26 <sup>i</sup>	2.886		1863	115 <sup>g</sup>						
Refs.28,29 <sup>j</sup>			1812±591							
<b>Mg<sup>+</sup>-Xe</b>	<b>3.018</b>	<b>2972.7</b>	<b>2905.8</b>	<b>134.8</b>	<b>1.66</b>	<b>0.0912</b>	<b>1.23x10<sup>-3</sup></b>	<b>2740</b>	<b>0.92</b>	<b>21.7</b>
Refs. 30,31 <sup>h</sup>			2848±150							
Ref. 14 <sup>d</sup>	~2.90	2910±100		124						
Refs. 27,28 <sup>e</sup>			4182	120 <sup>g</sup>						
Refs. 28,29 <sup>j</sup>			3299±1654							
<b>Mg<sup>+</sup>-Rn</b>	<b>3.064</b>	<b>3639.0</b>	<b>3568.8</b>	<b>141.1</b>	<b>1.41</b>	<b>0.0830</b>	<b>9.19x10<sup>-4</sup></b>	<b>3530</b>	<b>0.97</b>	<b>25.4</b>

<sup>a</sup>MCPF calculation. <sup>b</sup>QCISD(T) calculation. <sup>c</sup>MP2 calculation. <sup>d</sup>Recommended value from review of data up to 2001. <sup>e</sup>Photodissociation experiments. <sup>f</sup> $R_0$  value.

<sup>g</sup> $\Delta G_{1/2}$  value <sup>h</sup>Photoionisation experiments. <sup>i</sup>CISD calculation. <sup>j</sup>Dissociation energies re-evaluated in consideration of near-dissociation behaviour.

**Table 5.3 Spectroscopic constants for Be<sup>2+</sup>-RG. Symbols and units used are as for Table 5.1. Results from this work are shown in bold.**

	$R_e$	$D_e$	$D_0$	$\omega_e$	$\omega_e x_e$	$B_e$	$a$	$D_e^{\text{MORSE}}$	$D_e^{\text{MORSE}}/D_e$	$k$
<b>Be<sup>2+</sup>-He</b>	<b>1.428</b>	<b>7574.5</b>	<b>7131.3</b>	<b>902.0</b>	<b>27.4</b>	<b>2.981</b>	<b>1.21x10<sup>-1</sup></b>	<b>7423</b>	<b>0.98</b>	<b>133</b>
Ref. 10	1.453 <sup>a</sup>		6610 <sup>b</sup>	829 <sup>a</sup>						
Ref. 11 <sup>c</sup>	1.43	7389		877						
<b>Be<sup>2+</sup>-Ne</b>	<b>1.577</b>	<b>10983</b>	<b>10648</b>	<b>675.0</b>	<b>10.5</b>	<b>1.091</b>	<b>2.35x10<sup>-2</sup></b>	<b>10850</b>	<b>0.99</b>	<b>167</b>
Ref. 11 <sup>c</sup>	1.58	10601		664						
<b>Be<sup>2+</sup>-Ar</b>	<b>1.867</b>	<b>24874</b>	<b>24530</b>	<b>691.9</b>	<b>5.15</b>	<b>0.658</b>	<b>7.38x10<sup>-3</sup></b>	<b>23240</b>	<b>0.93</b>	<b>207</b>
<b>Be<sup>2+</sup>-Kr</b>	<b>2.009</b>	<b>29875</b>	<b>29559</b>	<b>634.9</b>	<b>3.91</b>	<b>0.513</b>	<b>4.80x10<sup>-3</sup></b>	<b>25750</b>	<b>0.86</b>	<b>193</b>
<b>Be<sup>2+</sup>-Xe</b>	<b>2.197</b>	<b>36974</b>	<b>36677</b>	<b>594.3</b>	<b>3.37</b>	<b>0.414</b>	<b>3.42x10<sup>-3</sup></b>	<b>26200</b>	<b>0.71</b>	<b>175</b>
<b>Be<sup>2+</sup>-Rn</b>	<b>2.288</b>	<b>40496</b>	<b>40216</b>	<b>563.5</b>	<b>3.11</b>	<b>0.373</b>	<b>2.92x10<sup>-3</sup></b>	<b>25530</b>	<b>0.63</b>	<b>162</b>

<sup>a</sup>MP2 calculation. <sup>b</sup>MP4/MP2 calculation. <sup>c</sup>QCISD(T) calculation.

**Table 5.4: Spectroscopic constants for Mg<sup>2+</sup>-RG. Symbols and units used are as for Table 5.1. Results from this work are shown in bold.**

	$R_e$	$D_e$	$D_0$	$\omega_e$	$\omega_e x_e$	$B_e$	$a$	$D_e^{\text{MORSE}}$	$D_e^{\text{MORSE}}/D_e$	$k$
<b>Mg<sup>2+</sup>-He</b>	<b>1.885</b>	<b>2752.7</b>	<b>2526.8</b>	<b>462.3</b>	<b>21.1</b>	<b>1.38</b>	<b>7.47x10<sup>-3</sup></b>	<b>2532</b>	<b>0.92</b>	<b>43.2</b>
Ref. 19 <sup>a</sup>	1.91	2550		441						
Ref. 20 <sup>b</sup>	1.910	2144		434						
Ref. 32	2.054 <sup>b</sup>		2170 <sup>c</sup>							
Ref. 32	1.909 <sup>d</sup>									
<b>Mg<sup>2+</sup>-Ne</b>	<b>2.035</b>	<b>4224.1</b>	<b>4072.2</b>	<b>306.6</b>	<b>6.05</b>	<b>0.373</b>	<b>8.59x10<sup>-3</sup></b>	<b>3884</b>	<b>0.92</b>	<b>60.4</b>
Ref. 22 <sup>a</sup>	2.08	3806		285						
Ref. 32	2.058 <sup>b</sup>		3600 <sup>c</sup>							
Ref. 32	2.066 <sup>d</sup>									
<b>Mg<sup>2+</sup>-Ar</b>	<b>2.318</b>	<b>10894</b>	<b>10730.5</b>	<b>328.2</b>	<b>2.55</b>	<b>0.209</b>	<b>2.09x10<sup>-3</sup></b>	<b>10560</b>	<b>0.97</b>	<b>95.2</b>
Ref. 32	2.396 <sup>b</sup>		9881 <sup>c</sup>							
Ref. 32	2.345 <sup>d</sup>									
<b>Mg<sup>2+</sup>-Kr</b>	<b>2.453</b>	<b>13668</b>	<b>13520</b>	<b>296.8</b>	<b>1.63</b>	<b>0.150</b>	<b>1.11x10<sup>-3</sup></b>	<b>13510</b>	<b>0.99</b>	<b>96.9</b>
<b>Mg<sup>2+</sup>-Xe</b>	<b>2.632</b>	<b>17849</b>	<b>17707</b>	<b>284.3</b>	<b>1.20</b>	<b>0.120</b>	<b>6.99x10<sup>-4</sup></b>	<b>16840</b>	<b>0.94</b>	<b>96.7</b>
<b>Mg<sup>2+</sup>-Rn</b>	<b>2.711</b>	<b>20113</b>	<b>19978</b>	<b>271.0</b>	<b>1.02</b>	<b>0.106</b>	<b>5.56x10<sup>-4</sup></b>	<b>18000</b>	<b>0.89</b>	<b>93.7</b>

<sup>a</sup>QCISD(T) calculation. <sup>b</sup>MP2 calculations. <sup>c</sup>Obtained using a non-standard dG2thaw(QCI)//B3LYP/dB4G method. <sup>d</sup>B3LYP calculation.

High-resolution spectroscopic results from emission spectra are available for  $\text{Be}^+-\text{Ar}$ ; <sup>15</sup> these provide very precise values for the bond length and the vibrational and rotational constants. These show excellent agreement with the calculated values reported here for  $R_e$ ,  $\omega_e$ ,  $\omega_e x_e$ ,  $B_e$  and  $\alpha$ . The dissociation energy reported in ref. 15 was estimated from approximate potentials, with the values in Table 5.1 considered the "best" average values. However, Goble *et al.* <sup>33</sup> looked at the same data considering other model potential forms and suggested that  $4,157 \text{ cm}^{-1}$  was a reasonable lower bound for  $D_e$ ; LeRoy and Lam <sup>34</sup> considered the form of near-dissociation expansions and concluded that  $D_e = 4,500 \pm 50 \text{ cm}^{-1}$ . In view of the different interpretations of the data, Bellert and Breckenridge <sup>14</sup> recommended a value of  $4,500 \pm 700 \text{ cm}^{-1}$ . The excellent agreement with the other quantities determined by the high-resolution experiments suggests that the present calculated value is reliable. This value is in very good agreement with the value of LeRoy and Lam <sup>34</sup> and comfortably within the error limits given by Bellert and Breckenridge. <sup>14</sup> It is also consistent with the lower bound suggested by Goble *et al.* <sup>33</sup>

Coxon *et al.* <sup>17</sup> have provided results from high-resolution emission experiments for  $\text{Be}^+-\text{Kr}$ ; again, this yields very precise results that compare well with the present calculated values for the bond length and the vibrational and rotational constants. No dissociation energy was reported in this study; however a value of  $D_0 = \sim 6,000 \text{ cm}^{-1}$  from an earlier low-resolution study <sup>35</sup> and an estimate of  $D_e = 6,500 \pm 1,000 \text{ cm}^{-1}$  from Bellert and Breckenridge <sup>14</sup> are in very good agreement with the present calculation.

A low-resolution emission study of  $\text{Be}^+-\text{Xe}$  yielded vibrational constants in very good agreement with those obtained here. <sup>17</sup> The estimated value of the dissociation energy is also in fair agreement with the present result.

The estimate given in the review<sup>14</sup> was  $11,000 \pm 2,000 \text{ cm}^{-1}$ ; like the value for  $\text{Be}^+ - \text{Kr}$ , this estimate was made assuming the ratios to  $\text{Be}^+ - \text{Ar}$  would be similar to that in the  $\text{Mg}^+ - \text{RG}$  series. A recalculation suggests that the estimate given for  $\text{Be}^+ - \text{Xe}$  was a typographical error, the true value being  $10,000 \text{ cm}^{-1}$ .

No previous data was found for  $\text{Be}^+ - \text{Rn}$ .

There are no experimental values for  $\text{Mg}^+ - \text{He}$ , but several theoretical studies have been conducted. The present values of  $R_e$  and  $D_e$  are in good agreement with those from the modified coupled pair functional (MCPF) calculations,<sup>18</sup> however the  $\omega_e$  from that study is less than half of the current result. In contrast, the QCISD(T) calculations<sup>19</sup> and the MP2 results from both refs. 20 and 21 indicate an  $\omega_e$  value much closer to the present one. This suggests that the MCPF calculation is not sufficient to describe this system. The MP2 study of Bu and Zhong<sup>20</sup> yields a very low result for the dissociation energy; again, the other studies yield results much closer to the current one.

Duncan's group have performed ultraviolet photodissociation experiments on  $\text{Mg}^+ - \text{RG}$  for  $\text{RG} = \text{Ne}, \text{Ar}, \text{Kr}$  and  $\text{Xe}$ .<sup>23,27,28</sup> The dissociation energy obtained for  $\text{Mg}^+ - \text{Ne}$  is much smaller than the present value; this was derived from a Birge-Sponer (BS) extrapolation of the upper state (see Chapter 2). However, the hot band structure indicated a  $\Delta G_{1/2}$  value of  $41 \text{ cm}^{-1}$ , which is in good agreement with the result calculated here (the calculated value of  $\Delta G_{1/2}$  is  $38.2 \text{ cm}^{-1}$ ). Their  $R_0$  value is also very similar to the present  $R_e$  value. The QCISD(T) calculations of Leung *et al.*<sup>22</sup> yield results in reasonable agreement with the current values, although they indicate slightly weaker bonding. The MCPF calculations indicate even weaker bonding.<sup>18</sup>

For  $\text{Mg}^+\text{-Ar}$ , the experimentally derived values by Duncan<sup>28</sup> are in reasonable agreement with the present value (the present value of  $\Delta G_{1/2}$  has been calculated as  $99.8 \text{ cm}^{-1}$ ). In a similar way to that described for  $\text{Be}^+\text{-Ar}$  (*vide supra*) the data has also been reanalysed by LeRoy<sup>29</sup> in consideration of near-dissociation behaviour. Both the original experimental result and the current calculated value of  $D_0$  are well within the error range given by LeRoy. In separate experiments by Breckenridge and Massick,<sup>24,25</sup> ionisation potentials were found using photoionisation spectroscopy and used to estimate the ground state dissociation energy from the equation given below.

$$IP(\text{MgAr}) + D_0(\text{Mg}^+\text{Ar}) = D_0(\text{MgAr}) + IP(\text{Mg}) \quad (5.1)$$

Since the ionisation thresholds can be determined within a few wavenumbers, the results from this method are expected to be more reliable; the uncertainty essentially arises from the determination of  $D_0(\text{MgAr})$ . The authors of ref. 24 believe that careful consideration of several experimental estimates of this figure lead to a reasonably accurate result (they quote an error of  $\pm 40 \text{ cm}^{-1}$ ); the value of  $D_0(\text{Mg}^+\text{Ar})$  obtained with this method is very close to that presented here and in reasonable agreement with the photodissociation value (given the stated error range). The MCPF<sup>18</sup> and CISD<sup>26</sup> calculations are also in reasonable agreement, although the dissociation energies are a little low.

Duncan's experimental values for  $\text{Mg}^+\text{-Kr}$ <sup>27,28</sup> can be seen to be in very good agreement with those presented here, as can the value of  $D_0$  from the photoionisation experiments.<sup>30,31</sup> LeRoy's analysis of the spectroscopic data<sup>29</sup> again yields a value consistent with both the experimental results and the value calculated here, although the error range is very large. The CISD calculation<sup>26</sup> again yields a slightly lower dissociation energy, but the  $R_e$  and  $\omega_e$  values are in good agreement with those presented here.

For  $\text{Mg}^+\text{-Xe}$ , the value of  $D_0$  derived by Duncan and co-workers<sup>27,28</sup> is much higher than that presented here. The reanalysis by LeRoy, however, yields a much lower value and both the present value and the original experimental one are within the substantial error range. The photoionisation experiments of Breckenridge<sup>30,31</sup> yield a value in better agreement with the current study and with significantly smaller error limits.

No previous studies of  $\text{Mg}^+\text{-Rn}$  have been found with which to compare.

#### 5.4 Trends

In the Chapter 4, it was noted that there were unusual trends in the spectroscopic constants for the  $\text{M}^+\text{-RG}$  series ( $\text{M}=\text{Ca-Ra}$ ), which were attributed to  $s\text{-}d\sigma$  hybridisation. This mixing causes the electron density to move off the internuclear axis, which reduces the repulsion and allows the RG atom closer to the centre of the metal ion at equilibrium separations. This creates a synergistic increase in the attractive terms, particularly in the dispersion terms, which have great significance for these heavier species because of the large metal cation polarisability. The effect was enhanced in the  $\text{Ba}^+$  complex, which was attributed to the low-lying  $5d$  orbitals.

In the cases of  $\text{Be}^+$  and  $\text{Mg}^+$ , the lowest lying  $d$  orbitals lie above the lowest lying  $p$  orbitals; thus the effects seen here can be expected to result from  $sp$  mixing. It should be noted that the  $^2P$  states lie  $\sim 30,000\text{ cm}^{-1}$  above the  $^2S$  state;<sup>36</sup> this is a significant energy separation and it is therefore somewhat surprising that mixing is seen. This has again been shown using MOLDEN<sup>37</sup> wavefunction plots by A. M. Gardner, which are shown in Figure 5.1.

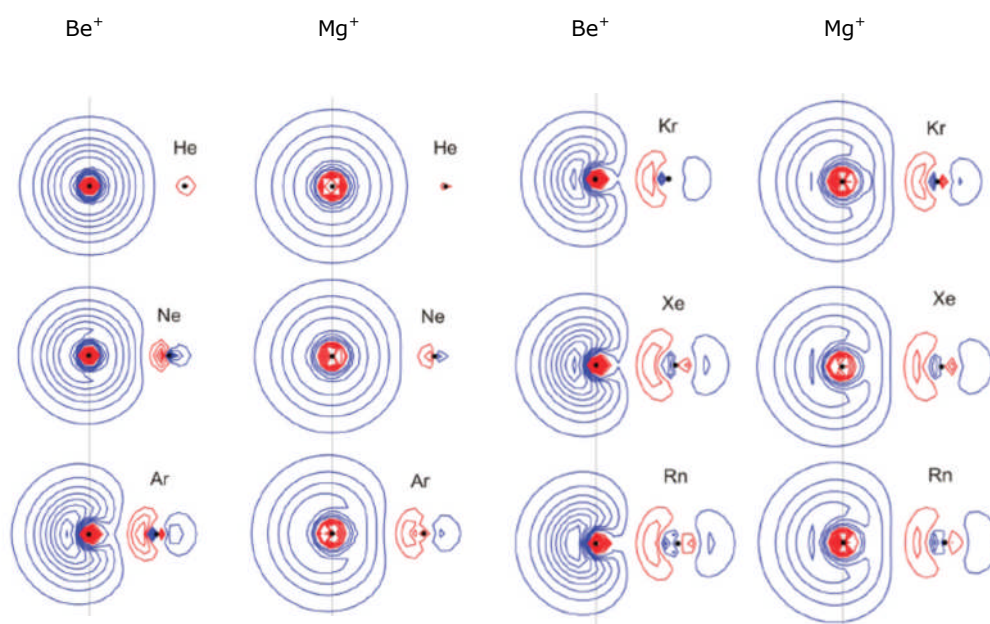


**Figure 5.1: MOLDEN contour diagrams of the Hartree-Fock HOMO for each  $M^+$ -RG complex, calculated at the RCCSD(T)  $R_e$  values. The values of the contours were selected to show the details clearly for all complexes and are identical to allow direct comparison between the plots. The different colours indicate opposite signs of the wavefunction.**

The plots show the wavefunction of the highest occupied molecular orbital (HOMO). In contrast to the heavier Group 2 metal ion complexes seen in Chapter 4, the shift in electron density is along the internuclear axis, though still away from the approaching RG atom. This represents an increasing amount of  $p$  character as the atomic number of the rare gas increases. The plots also indicate small amounts of charge transfer to the heavier rare gases. The distortion of the  $M^+$   $ns$  orbital is very small for both the weakly interacting He complexes; this was also the case for the  $M=\text{Ca-Ra}$  species. This is one observation that led to the proposition of a fundamental, consistent definition of the atomic ionic radii,  $R^{\text{He}}$ , which is the  $R_e$  value for a  $M^+$ -He complex minus the van der Waals radius of He (1.49 Å).<sup>38</sup>

It can be seen from Tables 5.1 and 5.2 that for both  $M^+$  there is a fall in the  $R_e$  values from  $M^+-\text{He}$  to  $M^+-\text{Ar}$  and thereafter the values gradually rise with the atomic number of the RG atom. This is similar to the trends seen for Ca-Ra and may be explained in a similar way: the movement of the electron density from between the two atoms increases the attractive terms and allows a closer approach, while the increasing repulsive terms for the heavier rare gases eventually outweighs this effect resulting in a gradual increase in  $R_e$ . Since the  $R_e$  value is the distance between the centres of mass, it is possible that for the larger rare gases this value increases while the outermost orbital of the RG atom is actually closer to the metal ion than in the smaller species. Again, for the dicationic species (Tables 5.3 and 5.4)  $R_e$  increases monotonically, consistent with normal  $\text{Alk}^+-\text{RG}$  trends<sup>14,39</sup> (see Chapter 4).

The trend in the dissociation energies is *prima facie* as one would expect, with an increase as the size and polarisability of the rare gas atom increases; however, as with the heavier Group 2 metals, the rise between Ne and Ar is greater than might be predicted. Using the rare gas polarisabilities reported in ref. 40, the successive polarisability ratios can be calculated as 1.9, 4.1, 1.5, 1.6 and 1.3. It was noted in Chapter 4 that if the charge/induced-dipole interaction were dominant then the successive  $D_e$  ratios might be expected to be similar; it was also noted that for  $M^+=\text{Ca}^+-\text{Ra}^+$  the rise in  $D_e$  between Ne and Ar was much greater than the predicted fourfold increase. This is also true for  $\text{Be}^+$  and  $\text{Mg}^+$ ; the ratios are 10.9 and 6.4 respectively. The ratios for  $M^+-\text{He}$  to  $M^+-\text{Ne}$  ( $M=\text{Be}-\text{Ra}$ ) are also consistently higher than the polarisability ratio of 1.9, ranging from 2.8-3.3. For the heavier rare gases, the  $D_e$  ratios are much closer to the polarisability ratios.

However, the leading term is also dependent on  $R_e$  (see Equation 4.1); Table 5.5 shows the ratios of successive  $D_e R_e^4$  values for each of the Group 2  $M^+$ -RG series. This indicates ratios that are generally comparable to the polarisability ratios. The major exception is for Be; the ratio between  $Be^+$ -He and  $Be^+$ -Ne is slightly low, while for  $Be^+$ -Ne to  $Be^+$ -Ar, the ratio is unexpectedly high. This indicates that in general it is the short  $R_e$  values that account for the large increase in  $D_e$ ; however the behaviour of  $Be^+$ -Ne suggests that this interaction is particularly unusual.

**Table 5.5: Ratio of polarisabilities of successive rare gases compared with ratios of successive values of  $D_e R_e^4$  for each of the  $M^+$ -RG series.**

	Polarisability	Be	Mg	Ca	Sr	Ba	Ra
Ne/He	1.9	1.52	1.85	1.85	1.90	1.88	2.00
Ar/Ne	4.1	5.66	4.14	3.82	3.61	3.70	4.07
Kr/Ar	1.5	1.76	1.66	1.71	1.72	1.76	1.53
Xe/Kr	1.6	1.88	1.80	1.78	1.77	1.74	1.65
Rn/Xe	1.3	1.31	1.30	1.28	1.28	1.30	1.24

The trends in  $\omega_e$  are similar to those seen for the heavier metal ions, with a large jump seen between Ne and Ar and the heavier species having very similar values; this is expected because of the competing effects of increasing interaction and reduced mass, which eventually balance out.

The value of  $k$  gives a better indication of the effects of increasing interaction since it is mass-independent. A monotonically increasing trend with a sharp increase between Ne and Ar can be seen for the monocations, which is similar to the results for Ca-Ra reported in Chapter 4. There is a decrease in  $k$  for the heavier dication complexes.

The  $\omega_e \times_e$  values show a general decrease from  $Be^+$ -He to  $Be^+$ -Rn, except for the value for  $Be^+$ -Ne, which is surprisingly low. The value for  $Mg^+$ -Ne is only very slightly lower than that for  $Mg^+$ -Ar. The values of  $\omega_e \times_e$  for the

Mg<sup>+</sup> series are also much lower than the corresponding values for the Be<sup>+</sup> complexes; the Be<sup>+</sup>-Ne value is the only exception to this, being slightly lower than that for Mg<sup>+</sup>-Ne. This again indicates some very unusual behaviour in the Be<sup>+</sup>-Ne complex.

To investigate this, the calculations were repeated with the Ne 1s orbital explicitly correlated, employing the d-aug-cc-pwCVQZ and d-aug-cc-pwCV5Z basis sets for neon<sup>41</sup> together with the basis sets previously described for beryllium. The energies were then extrapolated pointwise to the basis set limit. The spectroscopic constants were derived from the resulting PEC and are also shown in Table 5.1; it can be clearly seen that the effect of freezing the Ne 1s orbital is minimal.

### 5.5 Discussion

Figures 5.2 and 5.3 show BS plots for Be<sup>+</sup>-RG and Mg<sup>+</sup>-RG respectively, based on the calculated potentials and derived vibrational energy levels.

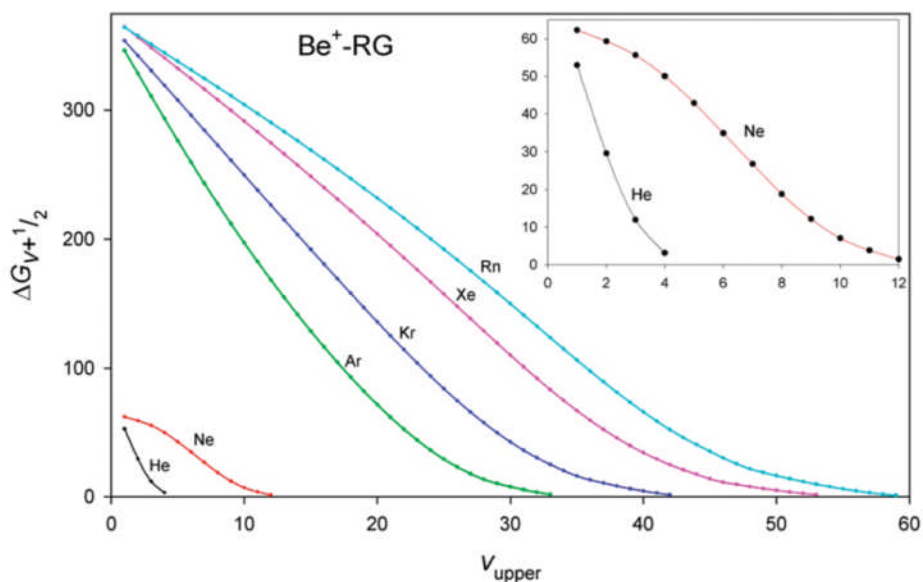


**Figure 5.2: BS plots of the vibrational term value separations vs the vibrational number of the upper level of each successive pair for Be<sup>+</sup>-RG. The inset is an expanded version of the bottom left-hand portion of the plot.**

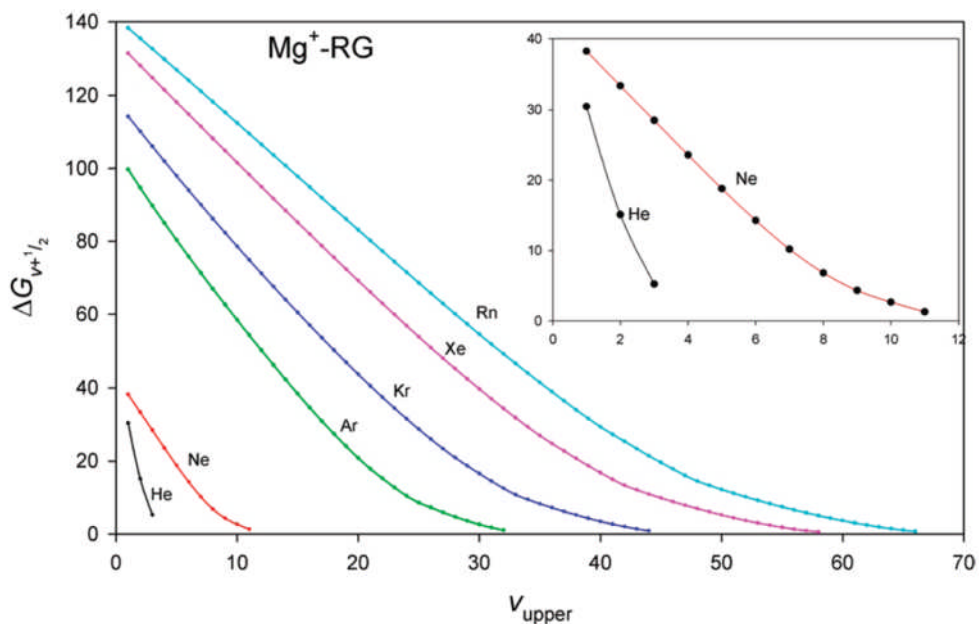


**Figure 5.3: BS plots of the vibrational term value separations vs the vibrational number of the upper level of each successive pair for Mg<sup>+</sup>-RG. The inset is an expanded version of the bottom left-hand portion of the plot.**

The Mg<sup>+</sup>-RG curves are as one might expect: they show a linear portion at low  $v$ , with a gradual lowering of the slope at high  $v$  (He is the exception, as it has very few vibrational levels and the BS plot is therefore not expected to be meaningful).

It can be seen from Table 5.1 that each of the  $D_e^{MORSE}/D_e$  ratios are less than 1. The value of  $D_e^{MORSE}$  is determined using the formula

$$D_e^{MORSE} = \frac{\omega_e^2}{4\omega_e x_e} \quad (5.2)$$

where  $\omega_e$  and  $\omega_e x_e$  are calculated using the linear portion of the BS plot. This leads to a value lower than the true  $D_e$  because it does not account for the lowering of the gradient at high  $v$ ; it is well known that the Morse potential fails near the dissociation limit.<sup>42</sup>

The BS plots for Be<sup>+</sup>-RG show more unusual behaviour. The Be<sup>+</sup>-Ar and Be<sup>+</sup>-Kr plots are similar to those seen for the Mg<sup>+</sup>-RG series and it can be

seen from Table 5.1 that the  $D_e^{\text{MORSE}}/D_e$  ratio for these complexes is also less than 1, as expected. However, for  $\text{Be}^+-\text{Ne}$ ,  $\text{Be}^+-\text{Xe}$  and  $\text{Be}^+-\text{Rn}$  the ratio is *greater* than 1, with the value for  $\text{Be}^+-\text{Ne}$  being exceptionally high. The plots for these three species have an atypical form, with the curve becoming *steeper* after the initial linear portion, before once again becoming shallower at high  $\nu$ . This results in an elongated "S" shape, which is most pronounced in the  $\text{Be}^+-\text{Ne}$  curve (the He plot again has too few levels for meaningful interpretation). Equation 5.2 therefore overestimates the values of  $D_e$  if the  $\omega_e$  and  $\omega_e x_e$  values determined from the lowest few vibrational levels are used, as this assumes a linear BS plot.

Most of the  $\text{M}^{2+}-\text{RG}$  complexes show  $D_e^{\text{MORSE}}/D_e$  ratios that are slightly below 1, which are expected due to the normal flattening of the BS plot near the dissociation limit. However, there are some notable exceptions, particularly the heavier  $\text{Be}^{2+}$  species. These ratios are far lower than would normally be expected. When the potential curves for  $\text{Be}^{2+}-\text{Kr}$ ,  $\text{Be}^{2+}-\text{Xe}$ ,  $\text{Be}^{2+}-\text{Rn}$  and  $\text{Mg}^{2+}-\text{Rn}$  were calculated, a second "minimum" was seen at large separations ( $>4 \text{ \AA}$ ). The curve for  $\text{Mg}^{2+}-\text{Rn}$  is shown in Figure 5.4 as an example. On inspection of the Mulliken populations, it was found that around this second minimum the charge on both the metal and the rare gas was close to 1. It was therefore concluded that the ground state of these  $\text{M}^{2+}-\text{RG}$  species undergoes an avoided crossing with a charge transfer state at long  $R$ . This is most likely also the cause of the unusual  $k$  values; multi-reference calculations would be necessary for reliable results.

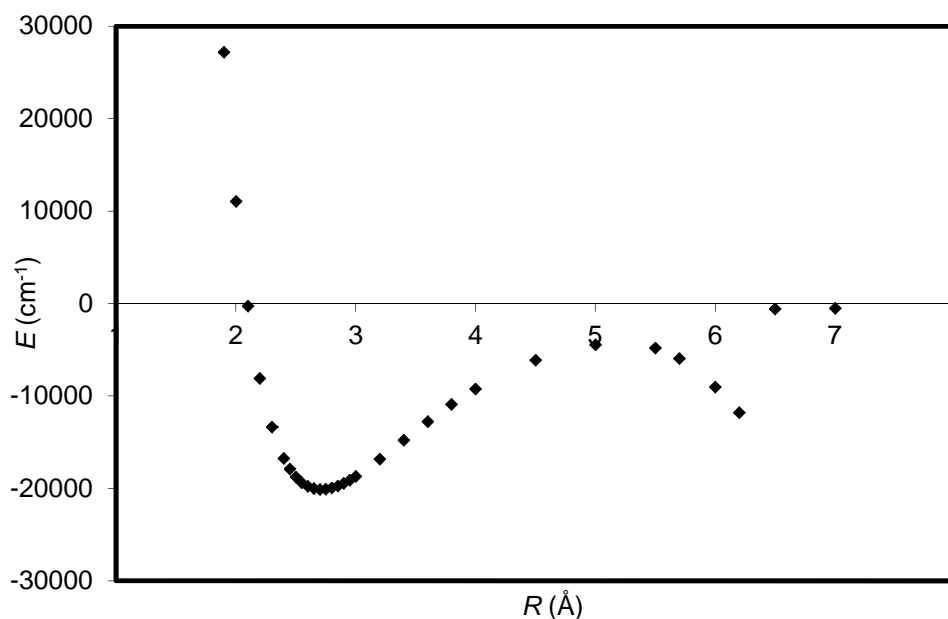


**Figure 5.4: Calculated potential curve for  $\text{Mg}^{2+}\text{-Rn}$ . Note the second dip in the potential at longer  $R$ .**

Returning to the monocationic species, an interesting way to compare the relative differences between species with very different potential well depths is to use reduced potential plots.<sup>33,43</sup> These have been examined by many workers<sup>44,45</sup> with a view to determining whether a universal diatomic function exists.<sup>46,47</sup> Reduced potentials are obtained by plotting  $E/D_e$  vs  $R/R_e$  for each species; this is shown for  $\text{Be}^+\text{-RG}$  in Figure 5.5 and for  $\text{Mg}^+\text{-RG}$  in Figure 5.6.

For the  $\text{Mg}^+\text{-RG}$  series, the reduced plots are very close together, which indicates that their interactions are similar in nature. For  $\text{Be}^+\text{-RG}$ , this holds true for Ar-Rn; however the  $\text{Be}^+\text{-Ne}$  curve is clearly very different. The  $\text{Be}^+\text{-He}$  curve is slightly steeper than the others, but is generally much closer.

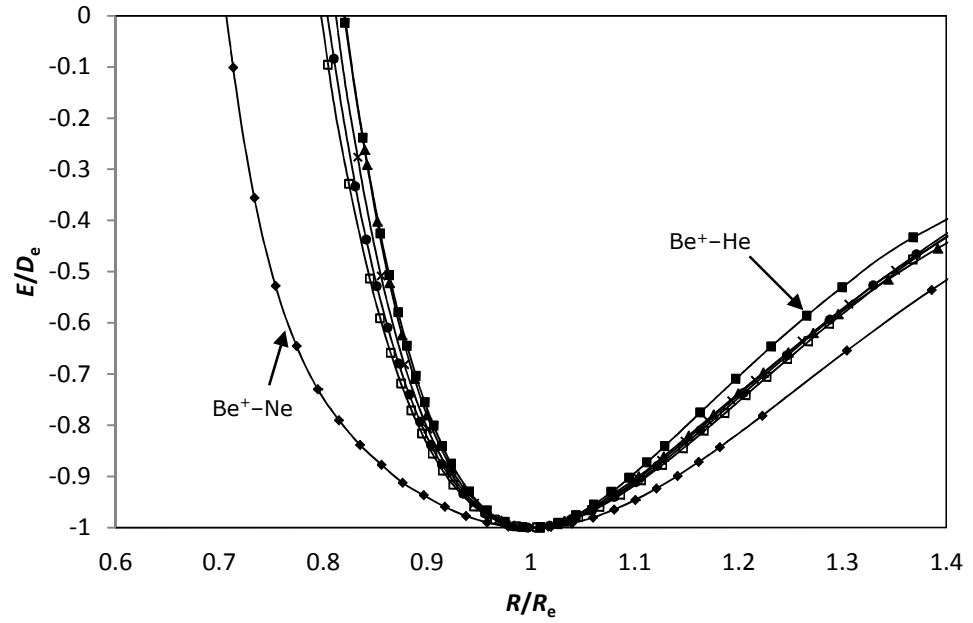


**Figure 5.5: Reduced potentials for  $\text{Be}^+\text{-RG}$ . The  $\text{Be}^+\text{-He}$  and  $\text{Be}^+\text{-Ne}$  curves are indicated; the others are very close together.**

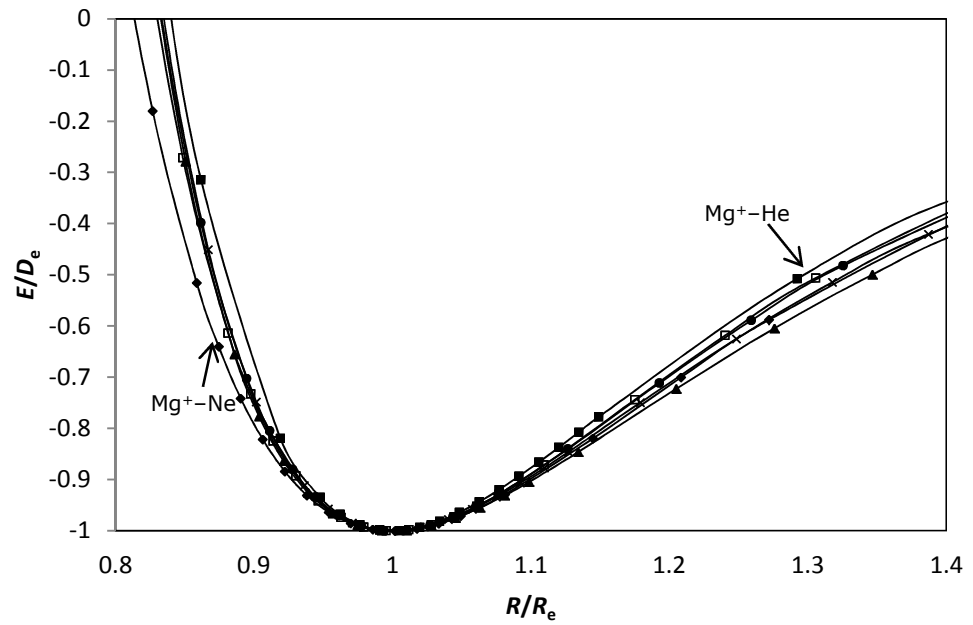


**Figure 5.6: Reduced potentials for  $\text{Mg}^+\text{-RG}$ . The  $\text{Mg}^+\text{-He}$  and  $\text{Mg}^+\text{-Ne}$  curves are indicated; the others are very close together.**

Calculating the  $\kappa$  parameter, which has been described as the “reduced curvature of the potential at  $R_e$ ”<sup>43</sup> is another way to investigate the difference between interactions. The  $\kappa$  parameter is essentially the Sutherland parameter put forward in 1938<sup>48</sup> and has been denoted  $\Delta$  in recent work by Xie and Hsu.<sup>47</sup>

$$\kappa = \frac{R_e^2}{D_e} \left( \frac{d^2V}{dR^2} \right)_{R_e} \quad (5.3)$$

This can also be expressed as

$$\kappa = \frac{\omega_e^2}{2B_e D_e} \quad (5.4)$$

$\omega_e$ ,  $B_e$  and  $D_e$  are defined in the caption to Table 1. As discussed in Ref. 33, smaller values of  $\kappa$  indicate a less steep potential near the minimum. Winn<sup>43</sup> found that for strongly bound chemical species  $\kappa$  values range from 0-20, whereas the values for  $\text{Be}^+\text{-Ar}$  and  $\text{Be}^+\text{-Kr}$  were found to be 27.5 and 29.1 respectively. It was suggested in ref. 48 that the values should be constant for particular groups of complexes; however this assumption was based on a rather simple form of interaction potential. One might, perhaps, expect to find similar values of  $\kappa$  and clear trends in these values for similar species.

The  $\kappa$  values for the complexes studied herein have been plotted in Figure 5.7, in addition to the alkali metal cation ( $\text{Alk}^+$ ) series  $\text{Li}^+\text{-RG}$  and  $\text{Na}^+\text{-RG}$  (values have been calculated from spectroscopic quantities presented in refs. 49, 50 and 51).

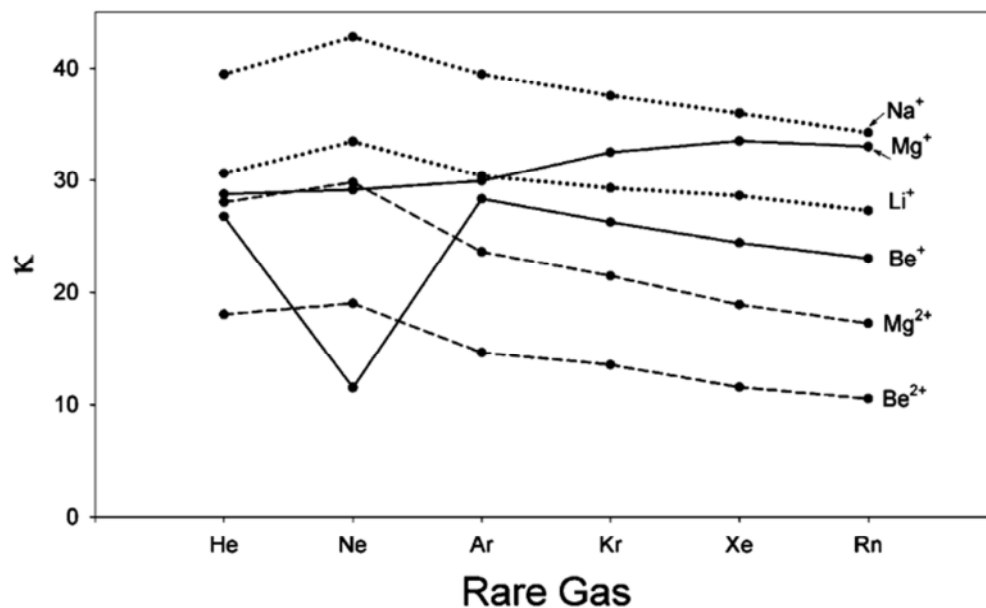


**Figure 5.7: Plot of  $\kappa$  for the complexes studied herein and selected  $\text{Alk}^+$ -RG series.**

For the  $\text{M}^{2+}$ -RG series and the isoelectronic  $\text{Alk}^+$ -RG series, the trends are very similar and the values of  $\kappa$  within a series are quite close. A small increase is seen between He and Ne, followed by a gradual decrease from Ne-Rn. For  $\text{Mg}^+$ -RG, the values are again quite similar within the series, but this time they increase gradually with the size of the rare gas atom. The  $\text{Be}^+$ -RG series, however, shows a trend more similar to the  $\text{M}^{2+}$ -RG and  $\text{Alk}^+$ -RG series, with the exception of the  $\text{Be}^+$ -Ne complex, which has a strikingly low value.

The increasing  $\kappa$  values seen in the  $\text{Mg}^+$ -RG series indicate the repulsive wall becoming steeper as the atomic number of the rare gas increases. The opposite is true for the  $\text{Be}^+$ -RG series (RG=Ar-Rn). On examination of the HOMO plots for these species in Figure 5.1, it can be seen that there is significantly reduced electron density along the internuclear axis, allowing a stronger interaction with the *dicationic* core. This may explain why this series is more similar to those of the dicationic complexes. The shift in electron density is very minimal for the He and Ne complexes; this is

consistent with the large rise in  $\kappa$  between the Ne and Ar complexes and is attributable to the low polarisabilities of helium and neon. The lowest unoccupied electronic orbitals on  $\text{Be}^+$  and  $\text{Mg}^+$  are  $p$  orbitals; as the rare gas atom approaches, the unpaired electron density moves into an  $s-p\sigma$  mixed orbital (see Section 5.4). The high charge density of  $\text{Be}^+$  results in a stronger interaction and a larger perturbation of the  $2s$  orbital; this strengthens the interaction and causes the observed increase in  $\kappa$  (*vide supra*). The  $\kappa$  values are seen to decrease with the increasing atomic number of the rare gas atom for the dicationic series; this is most likely attributable to the increasingly diffuse nature of the rare gas outer-shell orbitals. For  $\text{Mg}^+$ -RG, there is still significant electron density between the dicationic core and the RG atom. This leads to an increase in the repulsive terms as the atomic number of the rare gas increases; they appear to rise faster relative to the attractive terms in this case, resulting in a steeper repulsive potential.

The  $\kappa$  value of  $\text{Be}^+$ -He is comparable to others in the series; however, as has been noted,  $\text{Be}^+$ -Ne has a remarkably low value. A possible explanation for this relates to the observed  $s-p\sigma$  hybridisation. The  $2s$  electron density on  $\text{Be}^+$  is repelled by the  $p\sigma$  orbital of the RG atom, resulting in a mixing in of  $2p\sigma$  character. The repulsive wall of the potential therefore rises more gently and the value of  $\kappa$  is decreased. It appears that this effect is significantly more efficient in the case of  $\text{Be}^+$ -Ne than for the other  $\text{M}^+$ -RG species considered herein. There are two main factors contributing to this: firstly, the  $2p\sigma$  orbital of neon has a higher electron density than the corresponding orbitals of the heavier RG atoms, allowing for a stronger relative directional interaction with the  $\text{Be}^+$  electron density; secondly, in the case of  $\text{Be}^+$ -Ne, subtle changes in the repulsive terms as a function of  $R$  are more obvious because of the small total interaction

energy. For the heavier species, the much larger polarisabilities mean the attractive terms are much larger, as is the resultant  $sp$  mixing on  $\text{Be}^+$ , which reduces the repulsion (*vide supra*); hence such subtle changes in the repulsive potential are not so obvious. Considering the higher electron density of the neon orbital, combined with the small size of Ne and in the light of the HOMO plots in Figure 5.1, it seems possible that the  $2p\sigma$  orbital of Ne may be able to partially penetrate into the nodal region of the  $2s$  orbital of  $\text{Be}^+$ . Indeed, the unusual form of the  $\text{Be}^+$ -Ne potential likely arises from the fact that the  $\text{Ne}(2p\sigma)$  orbitals begin to sample the nodal region of the  $\text{Be}^+$   $2s$  orbital at small  $R$ , resulting in less relative repulsion near  $R_e$ .

This may lead to the expectation that  $\text{Be}^+$ -He would have a lower  $\kappa$  value still. However, the  $1s$  electron density in helium is spherical, whereas the  $2p\sigma$  orbital is much more directional, so the directed charge density is much higher.

In general, the  $\kappa$  values of the  $\text{Mg}^+$  complexes are higher than those for  $\text{Be}^+$ . This can be attributed to the fact that  $\text{Mg}^+$  has  $p$  electrons, so there is additional  $p\pi$ - $p\pi$  repulsion for  $\text{RG}=\text{Ne-Rn}$  compared with  $\text{Be}^+$  and also with the dications. This effect is likely to be contributing to the fact that the HOMOs in  $\text{Mg}^+$ -RG at  $R_e$  are less distorted than those for  $\text{Be}^+$ -RG, which in turn accounts for the lack of anomalous behaviour seen in the  $\text{Mg}^+$  series as opposed to the  $\text{Be}^+$  series. The  $p\pi$ - $p\pi$  repulsion most likely prevents the Ne atom from penetrating far enough into the  $3s$  orbital to experience the first nodal region.

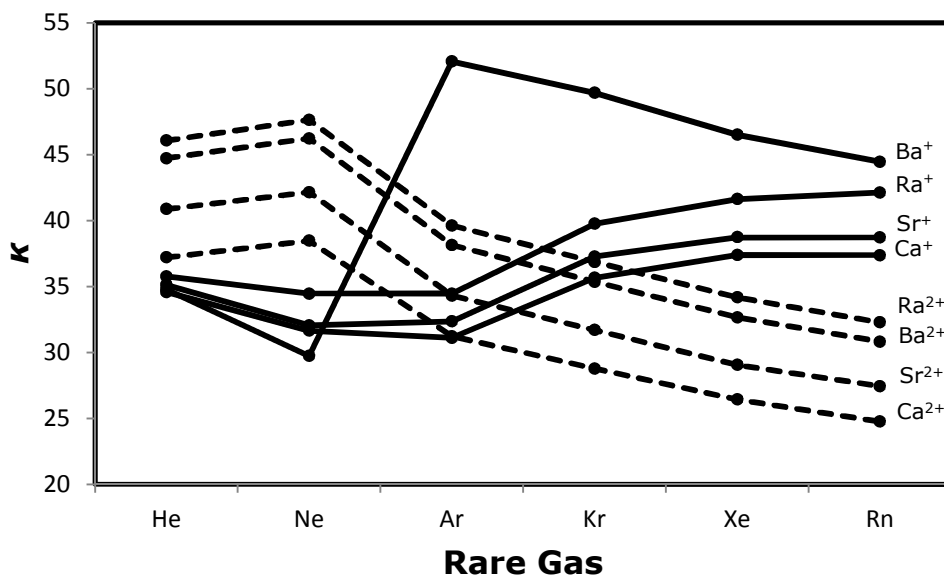


**Figure 5.8: Plot of  $\kappa$  for  $M^+-RG$  and  $M^{2+}-RG$  ( $M=Ca-Ra$ ).**

The trends in  $\kappa$  can also be compared with those from the rest of Group 2, which are shown in Figure 5.8. It is evident that most of the  $M^+$  series follow a similar trend to Mg, with the exception of Ba, which shows a trend more similar to Be and the dications. As with Be, the  $Ba^+$  complexes showed considerable reduction in electron density along the internuclear axis (see Chapter 4); this presumably causes a relatively much stronger interaction with the dicationic core, similar to that seen here in Be.

## 5.6 Conclusions

Accurate *ab initio* PECs have been calculated for  $Be^{n+}-RG$  and  $Mg^{n+}-RG$  complexes for  $n=1$  and 2. As for similar complexes involving Ca-Ra described in Chapter 4, excellent agreement is seen for the Be complexes with very precise spectroscopic constants obtained from high-resolution emission spectra where this is available ( $Be^+-Ar$  and  $Be^+-Kr$ ). Good agreement is also seen with lower resolution emission spectra for  $Be^+-Xe$  and previous theoretical results for  $RG=He, Ne$  and  $Rn$ .

The trends in  $R_e$  and  $D_e$  are quite similar to those seen in the  $M^+$ -RG (M=Ca-Ra) series. These results, while being unusual for  $M^+$ -RG complexes, were rationalised by providing evidence for  $s$ - $d\sigma$  hybridisation; the movement of electron density off the internuclear axis allowed for a stronger interaction. A similar effect seems to occur in the  $Be^+$  and  $Mg^+$  species, except that in this case the lowest unoccupied orbital is a  $p\sigma$  orbital, so the shift in electron density is away from the RG atom but along the internuclear axis. Some other results for  $Be^+$ -RG were very interesting, with  $Be^+$ -Ne showing an unusually low  $\omega_e X_e$  value. Further investigation showed that the reduced potential plot for this complex was very different from those of the rest of the series and also that the  $\kappa$  parameter was far lower than would be expected, indicating a more gentle rise of the repulsive potential. This was attributed to high electron density of the  $Ne(2p\sigma)$  orbital, which enables strong interaction with the  $Be^+$  2s electron density and enhanced relative  $sp$  mixing as electron density moves away from the approaching neon atom. In general, the trends in the  $\kappa$  parameter are similar to those in the dications; this is consistent with the deshielding of the dicationic core, evidenced by the HOMO plots. The Birge-Sponer plots for  $Be^+$ -RG (RG=Ne, Xe and Rn) were also very unusual, having an "S" shape, rather than the expected linear relationship at low  $v$  with the slope becoming gentler as the dissociation limit is approached. For  $Be^+$ -Ne, this could be caused by the approaching  $Ne(2p\sigma)$  orbital penetrating to the nodal region of the  $Be^+$  2s orbital. For the heavier RG atoms, the large polarisabilities lead to the subtle changes in the repulsive terms being overcome by the attractive ones.

The results for  $Mg^+$ -RG are much more straightforward; again, good agreement is seen with reliable experimental results where available. The dissociation energies from photoionisation experiments are in better

agreement with the present values than those from photodissociation experiments. The reduced potential and  $\kappa$  plots indicate that, unlike the  $\text{Be}^+$  potential curves, those for  $\text{Mg}^+$ -RG are very similar to each other. The presence of  $p\pi$ - $p\pi$  repulsion results in a much steeper repulsive wall.

The  $\text{Mg}^+$  and  $\text{Mg}^{2+}$   $\kappa$  trends are similar to those for Ca, Sr and Ra.  $\text{Ba}^+$  has a trend more similar to  $\text{Be}^+$  and the dications, although the Ne value is far more similar to the He value and the other  $\text{M}^+$ -Ne values, and the heavier  $\text{Ba}^+$  complexes have much higher  $\kappa$  values. This is presumably also caused by the deshielding of the dicationic core from the  $sd$  mixing, resulting in a stronger interaction.

In the calculations for some of the heavier dicationic complexes, it was seen that at longer  $R$  the ground state undergoes an avoided crossing with a charge transfer state. This was observed both in an unexpected drop in the potential curve and in the Mulliken population, which showed that the charge was shared equally by the metal and the rare gas at long  $R$ . While this should not affect the calculations for  $R_e$  and  $D_e$  multi-reference calculations are required to adequately describe the potential at longer  $R$  and obtain reliable values for  $\omega_e$  and  $k$ .

## References

---

<sup>1</sup> Instructions and a password for the database can be obtained by email to viehland@chatham.edu.

<sup>2</sup> D. E. Woon and T. H. Dunning, Jr., *J. Chem. Phys.*, **100**, 2975 (1994).

<sup>3</sup> T. H. Dunning, Jr., *J. Chem. Phys.*, **90**, 1007 (1989)

<sup>4</sup> D. E. Woon and T. H. Dunning, Jr., *J. Chem. Phys.*, **98**, 1358 (1993)

<sup>5</sup> K. A. Peterson, D. Figgen, E. Goll, H. Stoll and M. Dolg, *J. Chem. Phys.*, **119**, 11113 (2003)

- 
- <sup>6</sup> E. P. F. Lee, B. R. Gray, N. A. Joyner, S. H. Johnson, L. A. Viehland, W. H. Breckenridge and T. G. Wright, *Chem. Phys. Lett.*, **450**, 19 (2007).
- <sup>7</sup> K. A. Peterson, D. E. Woon, T. H. Dunning, Jr., (personal communication).
- <sup>8</sup> R. D. Amos, A. Bernhardsson, A. Berning, P. Celani, D. L. Cooper, M. J. O. Deegan, A. J. Dobbyn, F. Eckert, C. Hampel, G. Hetzer, P. J. Knowles, T. Korona, R. Lindh, A. W. Lloyd, S. J. McNicholas, F. R. Manby, W. Meyer, M. E. Mura, A. Nicklass, P. Palmieri, R. Pitzer, G. Rauhut, M. Schütz, U. Schumann, H. Stoll, A. J. Stone, R. Tarroni, T. Thorsteinsson and H.-J. Werner, MOLPRO, a package of ab initio programs designed by H.-J. Werner and P. J. Knowles, Version 2002.1 (2002).
- <sup>9</sup> R. J. LeRoy, Level 7.2—A computer program for solving the radial Schrödinger equation for bound and quasibound levels, and calculating various values and matrix elements, *University of Waterloo Chemical Physics Research Program Report CP-555R* (2000).
- <sup>10</sup> G. Frenking, W. Koch, D. Cremer, J. Gauss and J. F. Liebman, *J. Phys. Chem.*, **93**, 3397 (1989).
- <sup>11</sup> A. W. K. Leung, W. H. Breckenridge, *J. Chem. Phys.*, **111**, 9197 (1999).
- <sup>12</sup> X. Bu and C. Zhong, *Chem. Phys. Lett.*, **392**, 181 (2004).
- <sup>13</sup> G. Frenking, W. Koch, D. Cremer, J. Gauss and J. F. Liebman, *J. Phys. Chem.*, **93**, 3410 (1989).
- <sup>14</sup> D. Bellert and W. H. Breckenridge, *Chem. Rev.*, **102**, 1595 (2002).
- <sup>15</sup> K. V. Subbaram, J. A. Coxon and W. E. Jones, *Can. J. Phys.* **54**, 1535 (1976).
- <sup>16</sup> J. A. Coxon, W. E. Jones and K. V. Subbaram, *Can. J. Phys.*, **55**, 254 (1977).
- <sup>17</sup> J. A. Coxon, W. E. Jones and K. V. Subbaram, *Can. J. Phys.*, **53**, 2321 (1975).
- <sup>18</sup> H. Partridge, C. W. Bauschlicher, Jr. and S. R. Langhoff, *J. Phys. Chem.*, **96**, 5350 (1992).
- <sup>19</sup> A. W. K. Leung, R. R. Julian and W. H. Breckenridge, *J. Chem. Phys.*, **111**, 4999 (1999).
- <sup>20</sup> X. Bu and C. Zhong, *J. Mol. Struct.: THEOCHEM*, **726**, 99 (2005).
- <sup>21</sup> A.-M. Sapse, A. Dumitra and D. C. Jain, *J. Cluster Sci.*, **14**, 21 (2003).
- <sup>22</sup> A. W. K. Leung, R. R. Julian and W. H. Breckenridge, *J. Chem. Phys.*, **110**, 8443 (1999).
- <sup>23</sup> J. E. Reddic and M. A. Duncan, *J. Chem. Phys.*, **110**, 9948 (1999).
- <sup>24</sup> S. Massick and W. H. Breckenridge, *Chem. Phys. Lett.*, **257**, 465 (1996).

- 
- <sup>25</sup> S. Massick and W. H. Breckenridge, *J. Chem. Phys.*, **104**, 7784 (1996).
- <sup>26</sup> C. W. Bauschlicher, Jr. and H. Partridge, *Chem. Phys. Lett.*, **239**, 241 (1995).
- <sup>27</sup> C. T. Scurlock, J. S. Pilgrim and M. A. Duncan, *J. Chem. Phys.*, **103**, 3293 (1995). Erratum *J. Chem. Phys.*, 105, 7876 (1996).
- <sup>28</sup> J. S. Pilgrim, C. S. Yeh, K. R. Berry and M. A. Duncan, *J. Chem. Phys.*, **100**, 7945 (1994).
- <sup>29</sup> R. J. LeRoy, *J. Chem. Phys.*, **101**, 10217 (1994).
- <sup>30</sup> J. G. Kaup and W. H. Breckenridge, *J. Chem. Phys.*, **107**, 2180 (1997).
- <sup>31</sup> J. G. Kaup, A. W. K. Leung and W. H. Breckenridge, *J. Chem. Phys.*, **107**, 10492 (1997).
- <sup>32</sup> S. Petrie, *J. Phys. Chem. A*, **106**, 7034 (2002).
- <sup>33</sup> J. H. Goble, D. C. Hartman and J. S. Winn, *J. Chem. Phys.*, **67**, 4206 (1977).
- <sup>34</sup> R. J. LeRoy and W.-H. Lam, *Chem. Phys. Lett.*, **71**, 544 (1980).
- <sup>35</sup> K. V. Subbaram, J. A. Coxon and W. E. Jones, *Can. J. Phys.*, **53**, 2016 (1975).
- <sup>36</sup> NIST Atomic Spectra Database <http://physics.nist.gov/cgi-bin/ASD/energy1.pl> (accessed July 2011)
- <sup>37</sup> G. Schaftenaar and J. H. Noordik, *J. Comput.-Aided Mol. Des.* **14**, 123 (2000).
- <sup>38</sup> T. G. Wright and W. H. Breckenridge, *J. Phys. Chem. A*, **114**, 3182 (2010).
- <sup>39</sup> W. H. Breckenridge, V. L. Ayles and T. G. Wright, *Chem. Phys.*, **333**, 77 (2007).
- <sup>40</sup> P. Soldán, E. P. F. Lee and T. G. Wright, *Phys. Chem. Chem. Phys.*, **3**, 4661 (2001).
- <sup>41</sup> K. A. Peterson and T. H. Dunning, Jr., *J. Chem. Phys.* **117**, 10548 (2002).
- <sup>42</sup> R. J. LeRoy, *J. Chem. Phys.*, **101**, 10217 (1994).
- <sup>43</sup> J. S. Winn, *Acc. Chem. Res.*, **14**, 341 (1981).
- <sup>44</sup> J. Tellinghuisen, S. D. Henderson, D. Autin, K. P. Lawley and R. J. Donovan, *Phys. Rev. A*, **39**, 925 (1989).
- <sup>45</sup> G. Van Hooydonk, *Eur. J. Inorg. Chem.*, **1617** (1999).

- 
- <sup>46</sup> R.-H. Xie and J. Gong, *Phys. Rev. Lett.*, **95**, 263202 (2005).
- <sup>47</sup> R.-H. Xie and P. S. Hsu, *Phys. Rev. Lett.*, **96**, 243201 (2006).
- <sup>48</sup> G. B. B. M. Sutherland, *Proc. Ind. Acad. Sci.*, **8**, 341 (1938).
- <sup>49</sup> P. Soldán, E. P. F. Lee, J. Lozeille, J. N. Murrell and T. G. Wright, *Chem. Phys. Lett.*, **343**, 429 (2001).
- <sup>50</sup> J. Lozeille, E. Winata, P. Soldán, E. P. F. Lee, L. A. Viehland and T. G. Wright, *Phys. Chem. Chem. Phys.*, **4**, 3601 (2002).
- <sup>51</sup> L. A. Viehland, J. Lozeille, P. Soldán, E. P. F. Lee and T. G. Wright, *J. Chem. Phys.*, **119**, 3729 (2003).

## 6. Study of the Vibrational Dynamics of *para*-Fluorotoluene

### 6.1 Introduction

Intramolecular vibrational redistribution (IVR) is of great interest in chemistry, particularly because of its influence on reaction rates. It is assumed in standard Rice–Ramsperger–Kassel–Marcus (RRKM) theory that, following an initial localised excitation, the energy is redistributed across the whole molecule so quickly that a rupturing bond would display no memory of the original localisation.<sup>1</sup> Experimental studies have shown that IVR can be observed and measured in some systems, leading to a search for molecules with rates that are slow compared with collisions between molecules; this would give the possibility of bond-selective chemistry, where the bond broken would correspond to where the energy was initially localised.<sup>2</sup>

IVR occurs where two or more molecular vibrational levels of similar energies are coupled together. There has been considerable interest in studying IVR in electronically excited states.<sup>2</sup> If the energy of a vibrational state in  $S_1$  is known, it can easily be prepared using a tuneable laser. If the laser pulse used for excitation has a relatively wide bandwidth and a short duration then a superposition of eigenstates is excited. The initially excited superposition is known (in the harmonic approximation) as the zero-order bright state (ZOBS) because it resembles an optically accessible zero-order state; the inaccessible states to which the ZOBS is coupled are known as zero-order “dark” states. Following the initial excitation, energy then flows to the dark states as a result of IVR. In the simplest case, where only two states are coupled (a Fermi resonance), oscillations in the vibrational state

population can be observed where the energy is repeatedly transferred between the bright and dark states with a measurable time period that depends on the separation between the  $S_1$  eigenstates. The separation, in  $\text{cm}^{-1}$ , is given by:

$$\bar{\nu} = \frac{1}{100cT} \quad (6.1)$$

where  $c$  is the speed of light ( $\approx 3 \times 10^8 \text{ ms}^{-1}$ ) and  $T$  is the period of oscillation (in seconds). The oscillations are called *quantum beats*. If few dark states ( $< \sim 10$ ) are coupled to the bright state, it may be possible to observe a superposition of quantum beats with different periods that result in a complex pattern.<sup>3</sup> This is known as *restricted*, or *coherent* IVR. If, however, the coupling involves many dark states, the energy may quickly flow irreversibly from the bright state. Typically lifetimes are between 1 ps and a few nanoseconds.<sup>2,13</sup> This behaviour is described as *statistical*, or *dissipative* IVR. Examples of restricted and statistical IVR are shown in Figure 6.1.

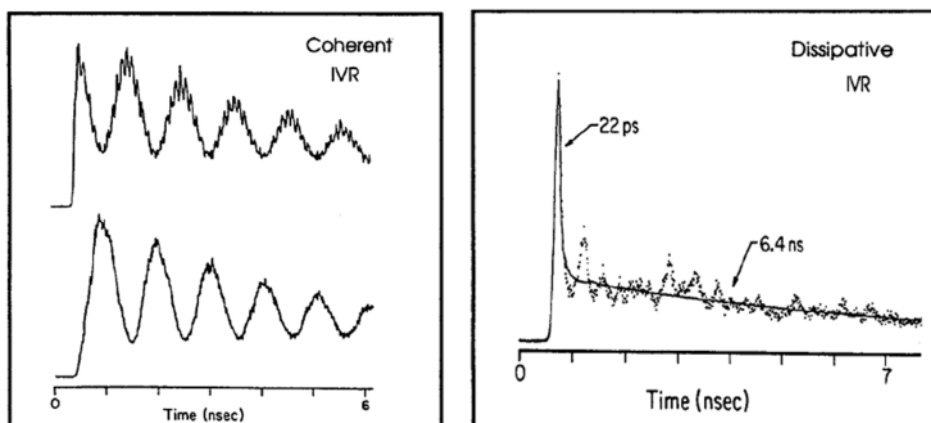


**Figure 6.1: Examples of different IVR behaviour; figure taken from Zewail.<sup>4</sup>**

If it is assumed that the density of states,  $\rho$ , is high, and the levels are equally coupled, then the IVR lifetime,  $\tau$ , can be found from the Fermi Golden Rule:<sup>5</sup>

$$\frac{1}{\tau} = 2\pi\langle V^2 \rangle \rho \quad (6.2)$$

The root mean square off-diagonal matrix element,  $\langle V^2 \rangle^{1/2}$ , is a measure of the coupling. In this case, the decay in the intensity,  $I$ , will be of the exponential form:

$$I(t) = Ae^{-\frac{t}{\tau}} + B \quad (6.3)$$

$A$  and  $B$  are parameters that will depend on the experimental set up and conditions. In the present work, these time-dependent effects are studied using picosecond photoelectron spectroscopy techniques, which will be described in Section 6.5. Briefly, a vibrational bright state is prepared in  $S_1$ . After a time delay, during which IVR occurs, the molecule is ionised using a second laser pulse. Measuring the kinetic energy of the photoelectron allows the internal energy of the cation to be deduced; thus a photoelectron spectrum showing the vibrational states in the cation can be obtained. If the time delay between excitation and ionisation is varied, the changes in the cation vibrational energy spectrum can be monitored, from which the IVR behaviour that occurred in  $S_1$  can be inferred.

If the bandwidth of the laser is much smaller, it is also possible to excite only one vibrational eigenstate. In this case, there will be no time dependence in the spectra observed because, by definition, a single eigenstate is stationary. If IVR is present, this is normally manifested as congestion in the spectrum, representing an eigenstate that involves vibration of many parts of the molecule, owing to many different zero order states being coupled together. Nanosecond laser zero electron kinetic energy (ZEKE) techniques are employed for this purpose to complement the picosecond experiments and will be described in Section 6.4; again, the coupling of states in  $S_1$  is deduced by probing the states in the cation using a multiphoton process.

## 6.2 Assignment of Vibrational Modes and Eigenstates

The molecule studied in this work is *para*-fluorotoluene (*p*FT). There are different methods of classifying vibrational modes in toluene derivatives. Varsanyi notation<sup>6</sup> was employed in previous related work by Okuyama and co-workers<sup>7</sup> and also by the SOCAR group<sup>8</sup> and will be used again here. This notation is designed to assign the same vibrational mode in different benzene derivatives with the same label. The modes in *p*FT that are associated with the methyl group cannot be assigned with this notation as they do not occur in benzene. However, these modes are not relevant to this work, so Vasanyi notation is sufficient.

There have been many studies of IVR in hydrocarbons.<sup>2</sup> Much of this has focussed on finding the IVR lifetimes of different vibrational modes using techniques such as infrared or fluorescence spectroscopy. It has previously been found that a methyl rotor acts as an accelerator, drastically reducing the IVR lifetime.<sup>9</sup> This is thought to be due to the coupling between vibrational and torsional levels, leading to more avenues through which IVR can take place. This has led to interest in molecules such as *p*FT, the structure of which is shown in Figure 6.2.

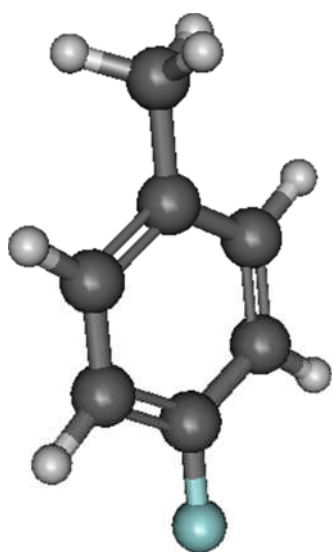


**Figure 6.2:** The structure of a *para*-fluorotoluene molecule. The fluorine atom is shown in blue, carbon dark grey, hydrogen light grey.

Employing a simple ball and spring model, vibrational states can be described in terms of bond stretching, rocking, ring breathing, bending, etc. In *p*FT there are known to be 39 pure fundamental vibrational modes. These modes can be classified into different symmetry groups. The treatment is greatly simplified by assuming that the methyl group can be treated as a point mass, thereby giving the molecule  $C_{2v}$  symmetry. The peaks in a REMPI, photoelectron or ZEKE spectrum are assigned in accordance with the fundamental vibrational modes, also including overtones and combination bands. The superscript after a mode indicates the quanta of that mode, e.g. a zero-order state described as  $6a^2$  indicates the overtone vibration that has two quanta of mode 6a. The combination band  $1^16a^1$  indicates a vibration has one quanta of mode 1 and one quanta of mode 6a. An overtone or combination band need not have the same symmetry as the fundamental(s). The most important modes for the discussion presented in this work are shown in Figure 6.3.

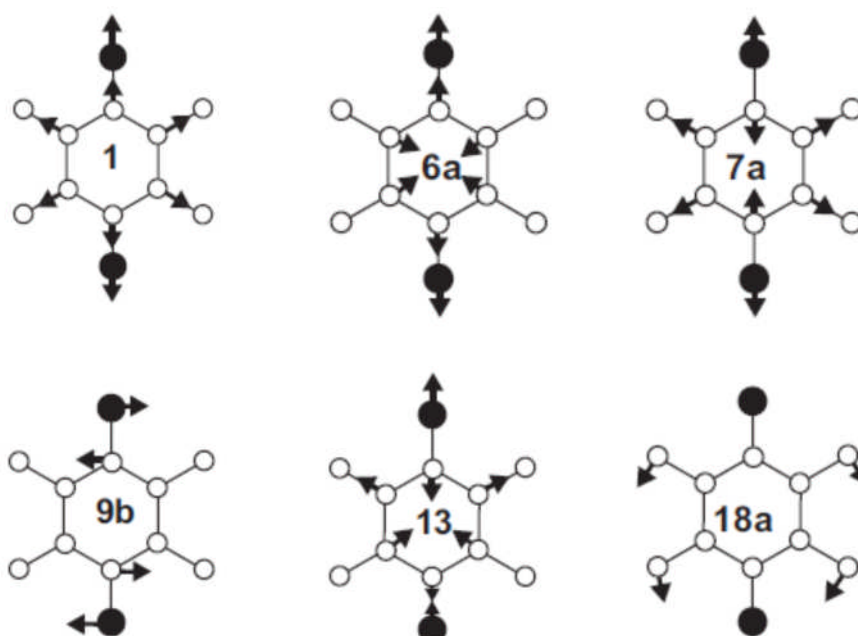


**Figure 6.3: Fundamental vibrational modes of substituted toluene derivatives that are relevant to this work. Adapted from ref. 10.**

In reality, zero-order states of similar frequencies and symmetries often couple together. The peaks seen in experimental spectra are therefore usually not strictly due to any single zero-order vibrational state; in fact they represent eigenstates that can contain the character of several different zero-order states. The assignment, therefore, is often used to refer to an eigenstate has only mostly the character of that zero-order state. In the simplest case of a two-component Fermi resonance, two eigenstates are seen in  $S_1$ , each of which has some character of each of the zero-order states. If one excites through each eigenstate separately, one may expect to see different spectra in each case; however if both eigenstates are excited simultaneously the photoelectron spectrum recorded for the cation will depend upon the form of the superposition in  $S_1$  at the time of ionisation. If a spectrum is obtained by excitation through a single eigenstate that contains the character of many different zero-order states, the spectrum is likely to show considerable congestion as many of these states will contribute to vibrational excitation in the cation upon ionisation of  $S_1$ . If a superposition of such a complicated eigenstate is prepared, one might expect to see statistical IVR; however there is a continuous evolution from restricted to statistical IVR and some oscillations may still be visible.

Selection rules formally prohibit transitions between vibrations in different symmetry groups and vibrational states with different symmetries do not couple; one would therefore expect the vibrational states seen in the cation to have the same symmetry as the vibrational state prepared in the electronically excited state. This is an important consideration when assigning spectra.

### 6.3 IVR Lifetimes

The IVR lifetime,  $\tau$ , is a quantity of great interest in terms of the idea of bond-selective chemistry. However, while there are certain factors that appear to influence the IVR lifetime, it has proven extremely difficult to predict the lifetime for any particular molecular vibration.

The choice of molecule is an important one. As mentioned in Section 6.2, one of the reasons that *p*FT is of interest is that methyl groups (and presumably other rotating ligands) are known to act as IVR accelerators. Bethardy *et al.*<sup>11</sup> believed that molecular flexibility could also be a strong influence. Their work is focussed on CH stretches and indicates some correlation between the IVR lifetime and the distance of the vibration from the centre of flexibility of the molecule for propargyl alcohol, pentyne and ethanol. However, strong coupling between the bright state and nearby dark states can cause the model to break down; the extent of such coupling cannot currently be predicted.

Since IVR relies on coupling to surrounding dark states, it seems logical that the density of states in the energy vicinity of a zero order vibration would have an effect on its IVR lifetime. This has been explored by Smalley and co-workers<sup>12</sup> in fluorescence studies of jet-cooled alkylbenzenes. The emission spectra became increasingly unstructured as the alkyl chains were extended; this is a strong indication of statistical IVR in later members of the series, where the density of states is larger. However, IVR lifetimes cannot be deduced from a non-time-resolved fluorescence spectrum; less structure does not necessarily imply faster IVR, only that there will be less structure in a time-resolved spectrum once the IVR has taken place. Time resolved studies also showed intermediate case IVR for early members of the series, while those with longer chains were

completely randomised within a nanosecond. Felker and Zewail<sup>3</sup> obtained more quantitative results in time-resolved studies of jet-cooled anthracene. They found very little IVR following excitation of vibrations with energies up to  $1,200\text{ cm}^{-1}$ . Intermediate case IVR occurred between  $1,380$  and  $1,520\text{ cm}^{-1}$ , while statistical IVR was observed above  $1,520\text{ cm}^{-1}$ . The link between the density of states and the IVR rate has led some to refer to an onset of IVR occurring at a particular energy.<sup>13</sup> However, since there is some debate as to how rapid the energy redistribution must be to be classed as true statistical IVR, such generalisations need to be used with caution.

Another factor thought to influence IVR lifetimes is the existence of so-called "doorway states". The model, which is illustrated in Figure 6.4, proposes that the bright state is coupled strongly to several dark states; these in turn are strongly coupled to many more dark states. The energy may flow through the "tiers" more quickly than if the bright state were less strongly coupled to many more dark states. Strong oscillations can be observed as well as an overall exponential decay.

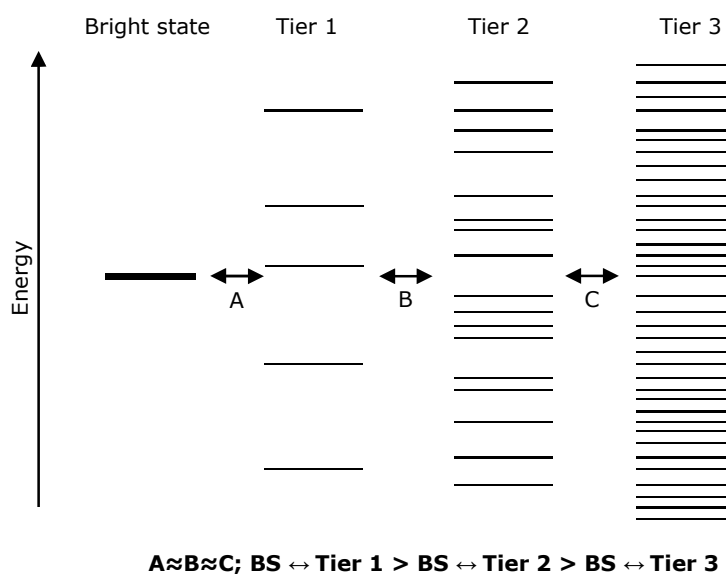


**Figure 6.4: Tier model for IVR. Adapted from ref. 5.**

The presence of doorway states and their influence on IVR lifetimes cannot currently be predicted; however, their existence can be inferred from experimental data, as will be seen later in this chapter.

## 6.4 *Nanosecond Zero Electron Kinetic Energy Spectroscopy*

### 6.4.1 *ZEKE Technique*

The zero electron kinetic energy (ZEKE) spectroscopy experiments described in this study have been carried out by Adrian Gardner and other members of the SOCAR group at the University of Nottingham. The general technique is described below.

The energies of the vibrational levels in the first excited electron state ( $S_1$ ) of the molecule to be studied are found from a REMPI scan (see Chapter 2). The "pump" laser can then be tuned to the energy of one of these levels. Following excitation, a second laser is used to ionise the molecules. In theory, if this second laser is resonant with a vibrational level in the cation the electrons should have no kinetic energy following ionisation. If a delayed pulsed voltage is applied, it is possible to detect these electrons. By scanning the ionising laser over a range of frequencies, it is therefore possible to probe the states in the cation that can be accessed by excitation through a chosen vibrational level in the  $S_1$  state. (It should be noted that in practice it is not very practical to detect free electrons with zero kinetic energy; in fact, usually the electrons detected are still bound in very high Rydberg states. Ionisation occurs as a result of the applied pulsed voltage, which reduces the ionisation potential.)

The advantage of ZEKE spectroscopy is that it gives high energy resolution (a working resolution of  $\sim 7\text{-}9\text{ cm}^{-1}$  is estimated; the unresolved rotational structure and the pulsed voltage ionisation process cause broadening

effects).<sup>14</sup> The bandwidth of the nanosecond lasers is  $\sim 0.3 \text{ cm}^{-1}$ , which allows excitation through a single vibrational eigenstate. The resulting spectra are therefore not time-dependent. However, if zero-order states are coupled then evidence of them will often be seen when an eigenstate containing some of their character is excited. The presence of dissipative IVR can be deduced through a rise in the baseline near the  $\Delta v=0$  peak and congestion in the spectrum; this is an indication of coupling to many dark states.

#### 6.4.2 *Equipment Employed in ZEKE Experiments*

ZEKE spectroscopy employs the same equipment described in Chapter 2 and refs. 15, 16 and 17 for the REMPI experiments, with some modifications to allow the study of  $p$ FT. Further details for ZEKE experiments can also be found in ref. 8.

The backing gas (argon) is passed over the  $p$ FT, which is placed in a bubbler. The  $p$ FT is picked up in the gas flow, which then passes through a narrow exit channel into the vacuum chamber. The resulting free jet expansion passes unskimmed into the ionisation chamber. As for the two-colour REMPI experiments described in Chapter 2, the beam is intersected by counterpropagating, coaxially, the output of the two dye lasers. The excitation laser is tuned to the energy determined by the REMPI scan for each level. Once it is determined that the REMPI signal is almost 100% two-colour, the voltages are adjusted to detect electrons instead of ions. The ionisation laser is then scanned over the region of interest to probe the vibrational levels in the cation. Following the second laser pulse, the voltage is applied after a delay of several microseconds to allow the electrons emitted with kinetic energy (prompt electrons) to move away. As

for REMPI spectroscopy, the signal detected by the MCPs is averaged by the boxcar and recorded by the computer.

## 6.5 Picosecond Photoelectron Spectroscopy

### 6.5.1 Photoelectron Spectroscopy Technique

Photoelectron spectroscopy (PES) experiments using velocity map imaging (VMI)<sup>18</sup> are carried out by the Reid group at the University of Nottingham. The picosecond lasers employed have a bandwidth of  $\sim 13 \text{ cm}^{-1}$ . It is therefore not often possible to excite a single eigenstate, and a group of eigenstates within the energy range will be prepared coherently. The resulting spectra are therefore time-dependent, and the temporal resolution of the lasers allows this time dependence to be monitored.

Unlike REMPI and ZEKE spectroscopy, VMI-PES does not require either laser to be scanned through a range of frequencies. For a simple photoelectron spectrum, the pump laser is tuned to a selected vibrational mode in the first excited electronic state,  $S_1$ . The second laser is tuned to a frequency that is above the ionisation limit. The resulting cations will have an internal energy distribution dependent on the cationic vibrational levels accessed; the excess energy will be carried away by the photoelectrons. By measuring the kinetic energy of the photoelectrons it is therefore possible to deduce the internal energy of the cation, using the formula below.

$$E_{int} = h\nu_{pump} + h\nu_{probe} - IE - eKE \quad (6.4)$$

The objective of the experiments is to investigate IVR processes following excitation to the selected vibrational level in  $S_1$ . This is achieved by varying the time delay between excitation and ionisation, allowing IVR to take place.

The energy resolution obtained from these experiments is quite poor compared with that achievable with ZEKE. However, it can be improved using a technique known as slow electron velocity imaging (SEVI).

The choice of wavelength for the ionising, or probe laser is a delicate balance. A lower energy pulse will give better resolution, but only the lower energy cationic states can be accessed. Typically, a 284 nm probe will give a resolution  $>100\text{ cm}^{-1}$  at the origin, which can improve to  $\sim 45\text{ cm}^{-1}$  for cation internal energies above  $2,000\text{ cm}^{-1}$ . In the present work, the SEVI, spectra are recorded using four or five different probe wavelengths between 283 and 295 nm. These spectra are then spliced together such that each region of the spectrum uses data from the lowest energy probe possible. This results in an overall spectrum with the best possible resolution, typically around  $40\text{-}55\text{ cm}^{-1}$  across the spectrum.

The experimental work analysed in this thesis was carried out by Julia Davies of the Reid group. Details of the equipment employed can be found in ref. 19.

### *6.5.2 Analysing VMI-PES Data*

An example of an image recorded following an ionisation event is shown in Figure 6.5. The intensity of the electron signal at any point on the detector is indicated by the brightness of the corresponding pixel in the image.

Each of the rings in the image shown in Figure 6.5 is made by electrons of equal kinetic energy and hence ejected from molecules resulting in the same cationic vibrational state. An inversion program called pBasex<sup>20</sup> has been designed to restore a slice through the original three-dimensional distribution from the two-dimensional image and produce a plot showing

the photoelectron intensity against the radius of the image. The inversion of the image is shown in Figure 6.6.

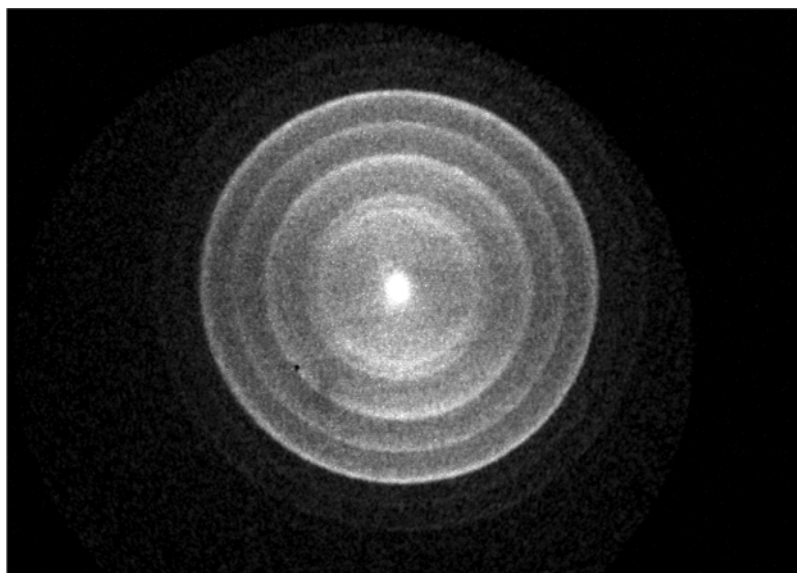


**Figure 6.5: Raw image recorded by VMI. Each ring corresponds to a vibrational level in the cation.**

The next step is to subtract the background signal. Single-colour ionisation events can occur if a molecule absorbs multiple photons from one laser source instead of being excited by the pump and ionised by the probe. To compensate for this, images are recorded with the probe beam arriving *before* the pump. The spectrum recorded in this way will contain no two-colour ionisation events and can therefore be subtracted from the spectra at positive time delays to eliminate the background caused by single-colour events.

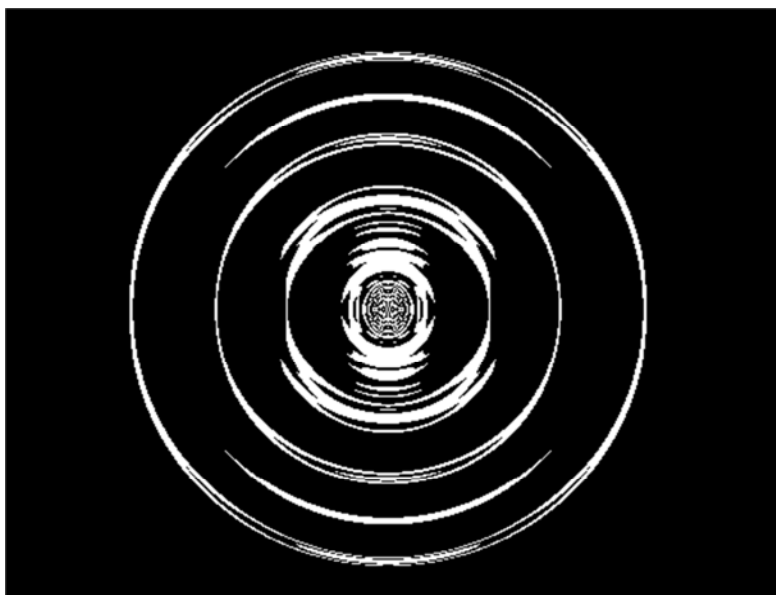


**Figure 6.6: Image produced by inversion using pBasex. This process restores a slice through the original 3D distribution.**

The pBasex program produces an output file that contains the photoelectron intensity, which is normalised to give unity as the maximum value, and the distance from the centre of the image, which is measured in pixels. This distance is directly proportional to the speed of the photoelectrons, so using the known values of the pump and probe energies and the ionisation potential of pFT ( $70,940.0 \text{ cm}^{-1}$ )<sup>21</sup> it is possible to calibrate the energy scale. The scale is set to  $0 \text{ cm}^{-1}$  at the origin peak, which can usually be identified and centred using a Gaussian function.

The energy of the probe laser must be chosen with care. A higher energy probe will give access to more vibrational levels in the cation; however, better resolution of the lower energy levels can be achieved by using a probe of lower energy. This is because the kinetic energy is proportional to the square of the radius; therefore the best resolution will be achieved when the photoelectrons strike near the centre of the detector. Where high energy probes are used, ionisation to the low cation levels will produce fast electrons that reach close to the edge of the detector.

The SEVI technique (described in Section 6.5.1) can be used to show the more obvious changes in the spectra with time; however it is very time consuming. For more detailed time-resolved work, where spectra must be recorded at many time delays, it is necessary to select a single probe wavelength for all spectra.

In all cases, to make any comparisons between spectra it is necessary to normalise them. For SEVI, the spectra are normalised by taking the integral of a common energy range and making it equal to 100 units, usually the energy range will include either the origin or  $\Delta\nu=0$  peak (it is best to use the  $\Delta\nu=0$  peak, as it is usually the most intense; however, if the lowest energy probe data does not include it the origin must be used instead). To compare the completed SEVI spectrum with others recorded *via* the same  $S_1$  vibrational level but at different time delays they must then be normalised over the whole range of interest ( $-200$  to  $2,200\text{ cm}^{-1}$ ). The PES recorded at many time delays using the same probe wavelength are each normalised over the same range as the SEVI.

The background subtraction, calibration and normalisation procedures, as well as the splicing of SEVI spectra, are carried out using Matlab. The original data analysis programs, which have been adapted for the purpose of this study, were written by Alistair Green of the Reid group.

The effects of IVR are most easily demonstrated by plotting the change in the area under (or between) the peaks with time. This gives a better indication than the change in the intensity because of the poor energy resolution and the fact that the peaks can sometimes shift slightly in energy with time. The area in the regions between the peaks sometimes increases as the dark states become populated. The areas are measured using the trapezium rule.

## 6.6 Introduction to Current Study

Intramolecular vibrational redistribution (IVR) has previously been studied in *para*-fluorotoluene (*p*FT) by the Reid and SOCAR groups at the University of Nottingham.<sup>22,23,24,14,8</sup> In addition to finding approximate IVR lifetimes for different vibrational modes, the time-resolved studies of the Reid group have been compared with frequency-resolved studies by the SOCAR group to gain better understanding of the complicated dynamics occurring within the molecule. The present study seeks to take this further: a thorough analysis of new time-resolved photoelectron spectroscopy data, which has been recorded by Reid group, is combined with new zero electron kinetic energy (ZEKE) spectroscopy data gathered by the SOCAR group. In particular, the work presented here focuses on four different vibrational levels in the  $S_1$  excited state. The combination of the two techniques gives a clearer picture than could be achieved with only one set of data.

## 6.7 REMPI

Figure 6.7 shows a picosecond resonance enhanced multiphoton ionisation (REMPI) spectrum (see Chapter 2) for *p*FT, from which the different vibrational states in  $S_1$  can be identified and assigned in accordance with the nanosecond fluorescence excitation spectrum measured by Okuyama *et al.*<sup>7</sup> Okuyama's assignments are also used in the nanosecond REMPI in Figure 6.8, which shows a smaller energy range at much higher energy resolution. Each of the four vibrational states indicated in the ps REMPI spectrum was prepared using a picosecond pump laser and investigated using time-resolved photoelectron spectroscopy (PES) and slow electron velocity-map imaging (SEVI). Nanosecond ZEKE spectra were also

recorded. Each of the states indicated showed very different behaviour and will therefore be discussed separately.

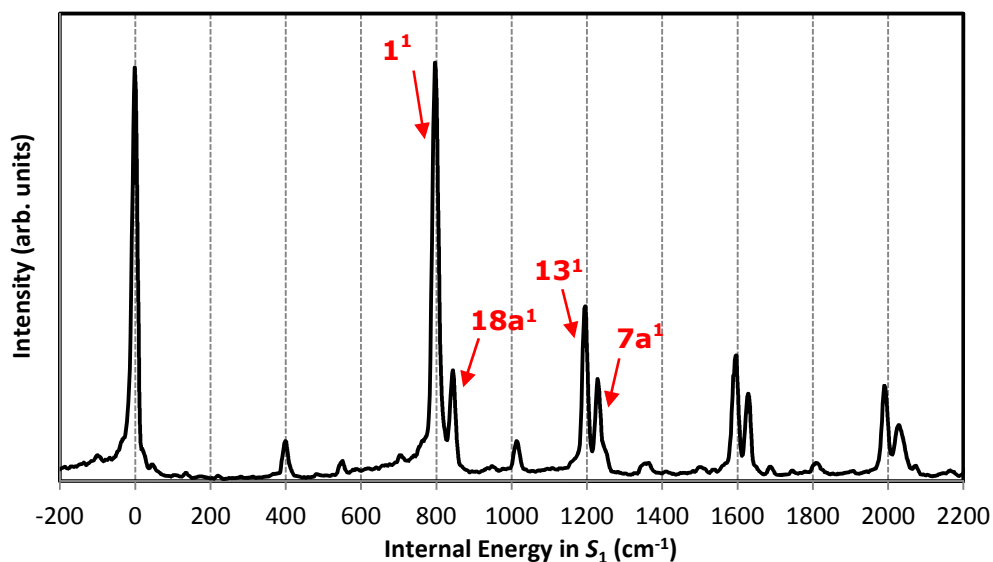
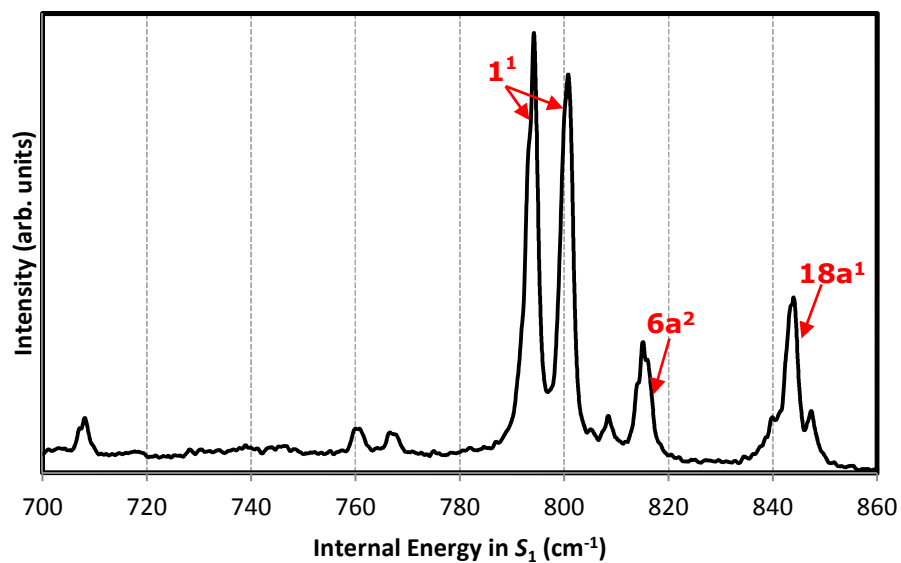


**Figure 6.7: Two-colour REMPI spectrum for *p*FT from data recorded by Julia Davies using a 10ps delay between the pump and probe pulses. The four states discussed in this work are indicated.**

## 6.8 $S_1$ $1^1$ Fermi Resonance

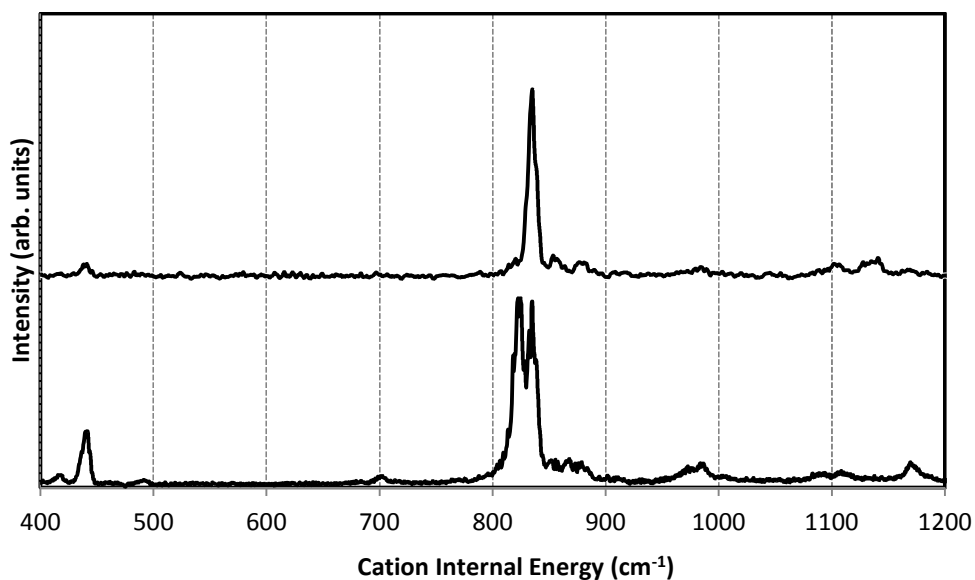
### 6.8.1 Results

Figure 6.8 shows a high-resolution nanosecond REMPI of the region from 700-860  $\text{cm}^{-1}$ . It can be seen that the peak identified as the  $1^1$  is in fact two separate peaks. With the nanosecond lasers used for the ZEKE experiments, which have a bandwidth of only  $0.3 \text{ cm}^{-1}$ , it is possible to excite *via* each  $S_1$  vibrational eigenstate separately; however the picosecond lasers have a much wider bandwidth ( $\sim 13 \text{ cm}^{-1}$ ) and must therefore excite a superposition of the two eigenstates.



**Figure 6.8: High-resolution nanosecond REMPI spectrum of *p*FT in the region of the Fermi resonance (from data recorded by Adrian Gardner).**

The close proximity and similar intensities of the peaks in the REMPI spectrum suggests that the zero-order states may be strongly coupled together if they have the same symmetry.



**Figure 6.9: ZEKE spectra *via* the lower energy eigenstate at 794  $\text{cm}^{-1}$  (bottom trace) and higher energy eigenstate at 801  $\text{cm}^{-1}$  (top trace) of the Fermi resonance seen in the REMPI spectrum.**

ZEKE spectra are shown in Figure 6.9. The two peaks seen in the spectra are further evidence of coupling. The spectrum recorded *via* the lower energy  $S_1$  eigenstate shows two peaks that are almost equal in intensity, while in the higher energy eigenstate spectrum the first peak is much weaker. Factors such as differences in the ionisation cross section of the two vibrational states could cause this kind of discrepancy. There is very little congestion in the ZEKE spectra and the baseline does not show a substantial rise near the  $\Delta v=0$  peak. The absence of these signatures, which are normally associated with statistical IVR, suggests that no exponential decay will be seen in the time-resolved experiments.

Figure 6.10 shows time-resolved SEVI spectra recorded following excitation of a superposition of the two  $S_1$  vibrational eigenstates.

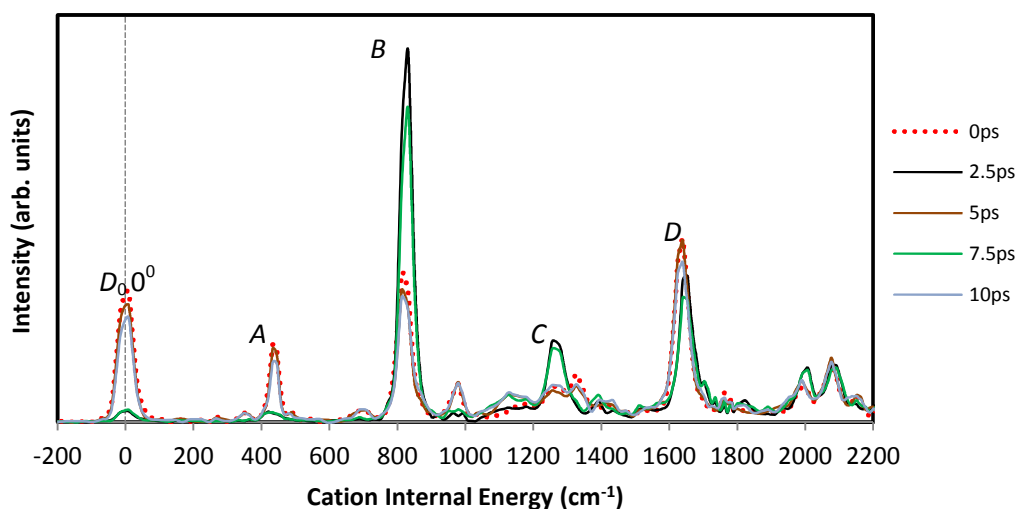


**Figure 6.10: SEVI spectra at selected time delays recorded *via* the Fermi resonance at  $\sim 800 \text{ cm}^{-1}$  in the REMPI spectrum. The four peaks labelled *A*, *B*, *C* and *D* are at approximately  $435$ ,  $815/830$ ,  $1,255$  and  $1,640 \text{ cm}^{-1}$  respectively.**

It can be seen that the intensities of the peaks in the SEVI spectra vary considerably with time; the origin peak can be seen to be much larger at 0, 5 and 10 ps than at 2.5 and 7.5 ps, while for the strong  $\Delta v=0$  peak

(labelled *B* in Figure 6.10) the situation is reversed. The time dependence can be examined more easily by plotting the area under the peaks (which has been calculated using the trapezium rule) against the time elapsed. Photoelectron spectra were recorded at many time delays (at least every picosecond from 0-50 ps). The time dependence of the areas under the peaks is shown in Figure 6.11. In these experiments, the time delay occurs while the molecule is in the  $S_1$  state; therefore the time-dependent changes observed in the ion peak intensities reflect the IVR that occurs in  $S_1$ .

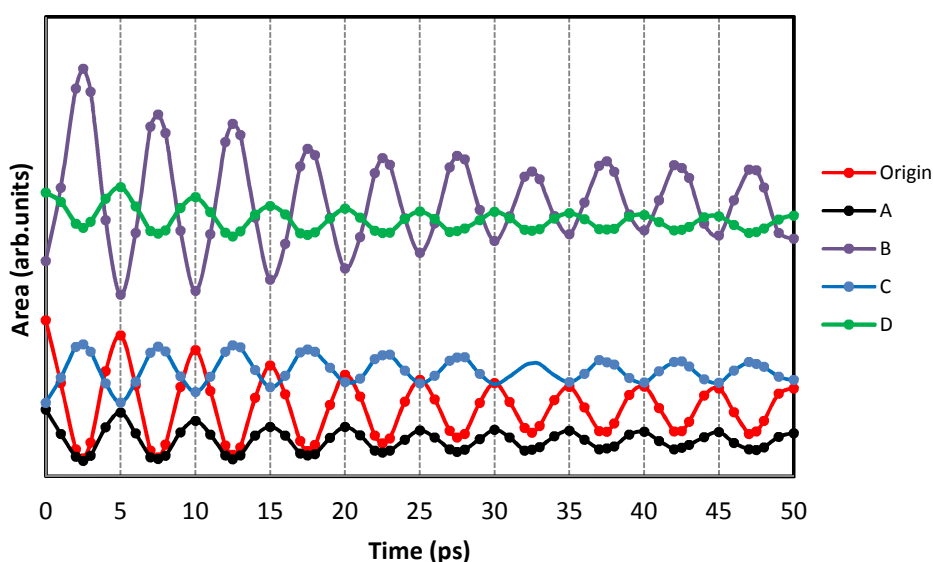


**Figure 6.11: Area under features identified in Figure 6.10 plotted against pump-probe time delay. The persistent quantum beats and the absence of exponential decay in the area under the peaks are clear indications of Fermi coupling. The areas are taken in the ranges: *Origin* (-114–166  $\text{cm}^{-1}$ ), *A* (348–538  $\text{cm}^{-1}$ ), *B* (749–943  $\text{cm}^{-1}$ ) *C* (1,199–1,313  $\text{cm}^{-1}$ ), *D* (1,537–1,739  $\text{cm}^{-1}$ ).**

Quantum beats are evident in all five of the peaks. The period is 5 ps, which corresponds to an  $S_1$  eigenstate energy separation of approximately 7  $\text{cm}^{-1}$ . This is in good agreement with the separation of the eigenstates in the nanosecond REMPI spectrum. It is worth noting that in ref. 8 the peaks were reported to be at 793 and 803  $\text{cm}^{-1}$ ; however on re-examination of

the data this appears to be an error, with the true position of the higher energy eigenstate being  $800\text{ cm}^{-1}$ .

### 6.8.2 Discussion

In ref. 8, the Fermi resonance peak to lower energy in the REMPI spectrum was assigned as the  $12^1$  and the peak to higher energy assigned to the  $1^1$  (using Varsanyi<sup>6</sup> notation), although a previous paper by Okuyama *et al.*<sup>7</sup> assigned both peaks simply as the " $1^1$  Fermi resonance". However, it is unusual to see two fundamental vibrations coupled together as they are expected to be relatively well separated in energy. One would normally expect to see a strong fundamental coupled with a combination band or an overtone. Table 6.1 shows some experimental and calculated values of fundamental vibrational frequencies. (The reader is reminded that pure vibrational zero-order states are rarely seen in real molecules except at very low energies; when an assignment is made it means only that the vibration has mostly the character of that state. See Section 6.2 for further discussion.)

The ground state calculations are in very good agreement with the experimental results. The excited state calculation for the  $12^1$  mode is  $695\text{ cm}^{-1}$ , which is in very poor agreement with the wavenumber of the lower energy eigenstate, at  $794\text{ cm}^{-1}$  in the nanosecond REMPI spectrum. The calculated value for the  $12^1$  in the cation at  $718\text{ cm}^{-1}$  is also in poor agreement with the ZEKE data, which indicates two  $\Delta v=0$  peaks at approximately  $822$  and  $834\text{ cm}^{-1}$  (see Figure 6.9). This discrepancy was also noted in ref. 8. In contrast, the calculated value of  $822\text{ cm}^{-1}$  for mode 1 in the cation is in good agreement with the ZEKE data.

**Table 6.1: Experimental and calculated fundamental vibrational frequencies for normal modes of pFT.**

Mode	Symmetry	Ground State <sup>a</sup>	Ground State <sup>b</sup>	Excited State <sup>c</sup>	Cation <sup>b</sup>
<b>1</b>	a <sub>1</sub>	842	840	801	822
<b>12</b>	a <sub>1</sub>	728	726	695	718
<b>6a</b>	a <sub>1</sub>	455	453	405	443
<b>17a</b>	a <sub>2</sub>	956	953	669	994
<b>10a</b>	a <sub>2</sub>	810	815	540	777
<b>16a</b>	a <sub>2</sub>	404	418	194	359
<b>5</b>	b <sub>1</sub>	929	929	725	993
<b>17b</b>	b <sub>1</sub>	817	822	676	835
<b>4</b>	b <sub>1</sub>	695	699	528	668
<b>16b</b>	b <sub>1</sub>	502	508	464	494
<b>10b</b>	b <sub>1</sub>	342	336	246	270
<b>11</b>	b <sub>1</sub>	158	144	111	111
<b>6b</b>	b <sub>2</sub>	638	644	550	574
<b>9b</b>	b <sub>2</sub>	424	422	396	417
<b>15</b>	b <sub>2</sub>	313	303	303	318

<sup>a</sup>Infrared spectroscopy experiments from ref. 25.

<sup>b</sup>Harmonic B3LYP/6-311G\*\* calculation (scaling factor 0.986) from ref. 26.

<sup>c</sup>Harmonic CIS/6-311G\*\* calculation (scaling factor 0.905) from ref. 26.

If it is assumed that the lower energy eigenstate in  $S_1$  is a combination band or overtone, the most likely candidate, given the calculated values and symmetry considerations, seems to be the  $9b^2$ . From the calculated values in Table 6.1, this would be expected to be at  $\sim 792 \text{ cm}^{-1}$  in the excited state, which is in much better agreement with the nanosecond REMPI value of  $794 \text{ cm}^{-1}$ . Furthermore, the calculated value of  $\sim 834 \text{ cm}^{-1}$  for  $9b^2$  in the cation is in excellent agreement with the ZEKE spectrum. It also has the same symmetry ( $a_1$ ) as  $1^1$ .

It has already been noted that the strong peak labelled  $B$  in the SEVI spectra in Figure 6.10 is the  $\Delta v=0$  peak. In fact, peak  $B$  contains two  $\Delta v=0$  peaks from ionisation of  $S_1 1^1$  and  $S_1 9b^2$  respectively. The quantum beats clearly indicate a Fermi resonance (further measurements have shown that strong oscillations are still present up to 500 ps) and the result of this is that two different SEVI spectra can be observed. At 0 ps (and at each 5 ps

interval thereafter) peak *B* corresponds to the  $D_0$   $1^1$  ion peak, since ionisation is from the bright state. Using previous assignments from ref. 7, peaks *A*, *C* and *D* seen in the spectra at these time intervals can be assigned to the ion  $6a^1$ ,  $1^16a^1$  and  $1^2$  cation states respectively. This is in agreement with the ion vibrational state series identified by Bellm *et al.* of  $X^m$ ,  $X^m6a^1$ ,  $X^m1^1$ ,  $X^m9a^1$  following ionisation of  $X^m$  in  $S_1$ .<sup>23</sup> However, at 2.5 ps (and further 5 ps intervals), the spectrum is obtained by ionising from the dark state,  $9b^2$ . *A*, *B*, *C* and *D* can therefore be assigned to the  $6a^1$ ,  $9b^2$ ,  $9b^26a^1$  and  $9b^21^1$  respectively. It is possible to discern that the  $\Delta v=0$  peak (labelled *B* in Figure 6.10) shifts slightly in energy, approximately between 813 and 832  $\text{cm}^{-1}$ , as it oscillates between the two states. These energies are in reasonable agreement with the ion peak energies of 822 and 834  $\text{cm}^{-1}$  measured in the nanosecond ZEKE spectra.

While the quantum beats are steady, the amplitude decreases with time. This is thought to be caused by the differences in the rotational constants for the bright and dark zero-order vibrational states in  $S_1$ . This would mean that the quantum beats are actually a superposition of many oscillations of very slightly different periods: thus at later time delays they become out of phase leading to destructive interference. This “rotational dephasing” has been shown to increase with rotational temperature, with the oscillations in two-level systems dying away more quickly when more of the rotational levels in the ground state are initially populated.<sup>27</sup>

## 6.9 $S_1$ $18a^1$

### 6.9.1 Results

The next case that will be considered in this study is excitation through the peak at approximately  $845\text{ cm}^{-1}$  in the REMPI spectrum in Figure 6.7. This peak was assigned to  $S_1$   $18a^1$  in both refs. 7 and 8. The ZEKE spectrum recorded is shown in Figure 6.12.

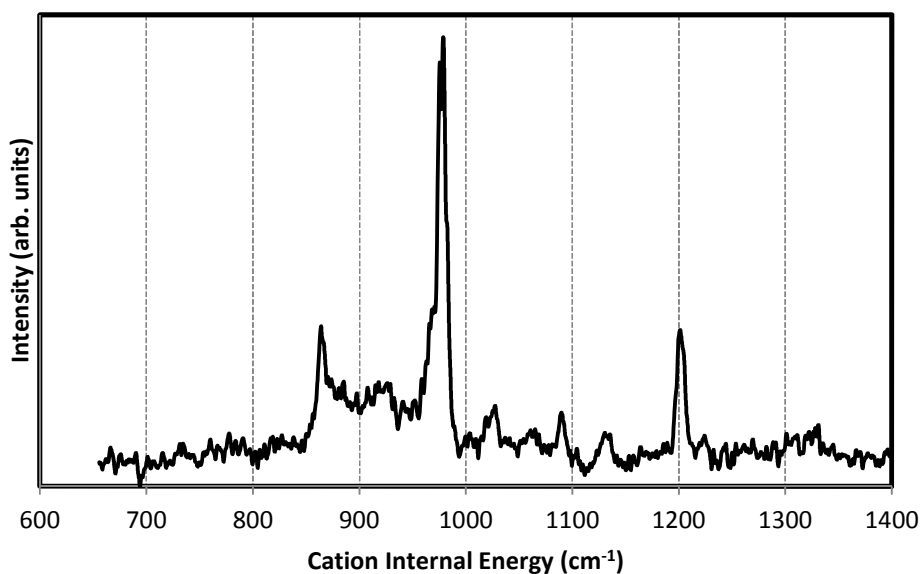


**Figure 6.12: ZEKE spectrum via the  $18a^1$  peak seen at  $845\text{ cm}^{-1}$  in the REMPI spectrum.**

The ZEKE spectrum shows several strong peaks. Some congestion is observed in the vicinity of the  $\Delta\nu=0$  peak at  $979\text{ cm}^{-1}$ , which is characteristic of statistical IVR. This suggests that energy is lost from the bright state over time to a large number of coupled dark states.

Figure 6.13 shows the SEVI spectra at different time delays. In this case, the change in ion peak area with time will be examined for three peaks that show different behaviour. The first, the  $\Delta\nu=0$  peak (labelled C in the SEVI spectrum) is shown in Figure 6.14.

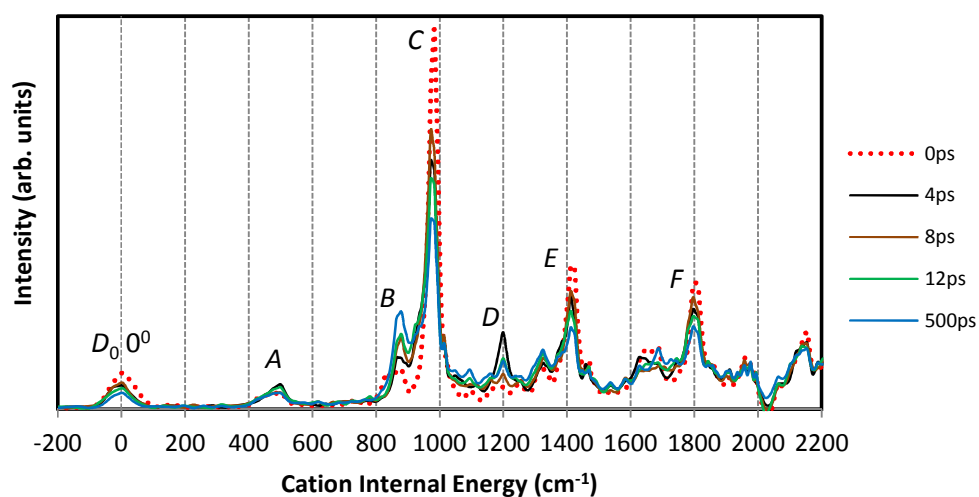


**Figure 6.13:** SEVI spectra at selected time delays recorded *via* the  $18a^1$  peak at  $845 \text{ cm}^{-1}$  in the REMPI spectrum. The four peaks labelled *A*, *B*, *C*, *D*, *E* and *F* are at approximately  $490$ ,  $880$ ,  $970$ ,  $1,200$ ,  $1,420$  and  $1,805 \text{ cm}^{-1}$  respectively.

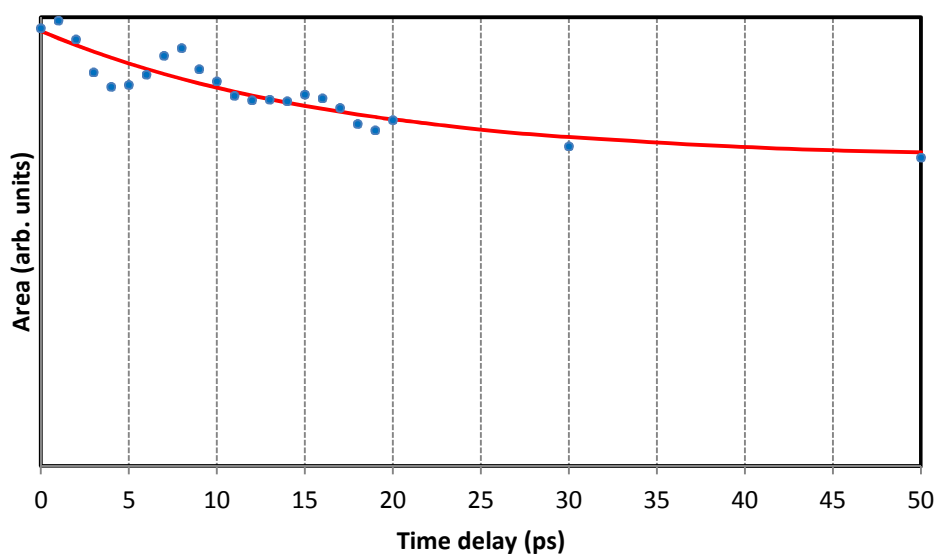


**Figure 6.14:** Area under the peak labelled *C* in Figure 6.13 plotted against time elapsed. Several oscillations are visible in addition to an exponential decrease overall. The area is taken in the range  $936\text{--}1,003 \text{ cm}^{-1}$ .

The oscillations seen in Figure 6.14 are not as distinct as those seen for the  $S_1$  Fermi resonance, discussed above. They have a period of

approximately 8 ps, indicating an energy separation of  $4 \text{ cm}^{-1}$ . The data have been fitted to an exponential equation of the form:

$$I(t) = Ae^{-\frac{t}{\tau}} + B \quad (6.5)$$

Here,  $\tau$  indicates the IVR lifetime (see Section 6.3). In this case, the fit gives an IVR lifetime of approximately 17 ps. The error on this figure is difficult to quantify. The time delay can be measured very accurately and the variation in the data when a scan is repeated has been found to be very small. The main sources of error are therefore likely to be in the measurement of the area under the peak and the fit to the data. The error in the area will vary depending on the resolution of the peak and its intensity relative to the background, the number of data points and the relative change in area with time. Since in this case the peak is very intense and the change in area is quite significant, the error is estimated to be  $\sim 5\%$  ( $\pm 1$  ps).

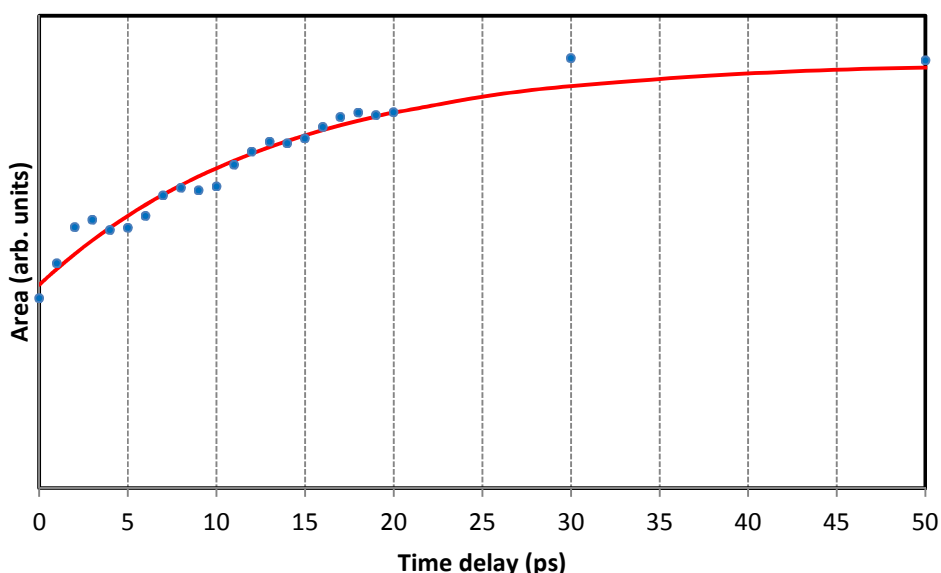


**Figure 6.15:** Area under the peak labelled *B* in Figure 6.13 plotted against time elapsed. Oscillations are regular, but very small in amplitude. The area is taken in the range  $842\text{--}902 \text{ cm}^{-1}$ .

The second peak considered is that to the left of the strongest peak, labelled *B* in Figure 6.13. This peak shows the opposite behaviour to peak *C*, actually growing larger with time (Figure 6.15).

The equation of the exponential rise is of the form:

$$I(t) = A\left(1 - e^{-\frac{t}{\tau}}\right) + B \quad (6.6)$$

Here,  $\tau = 13.5$  ps. This peak is considerably smaller than the  $\Delta\nu=0$  peak, so the error on this figure will be much larger. Again, oscillations are visible in Figure 6.15; in this case the period is 5 ps, indicating an  $S_1$  eigenstate energy separation of approximately  $7 \text{ cm}^{-1}$ .

The final peak to be considered here is that at  $1,200 \text{ cm}^{-1}$ , which is labelled *D* in Figure 6.13. This peak has negligible intensity at  $t=0$  ps, but appears later with a maximum at 4 ps. This is illustrated in Figure 6.16.

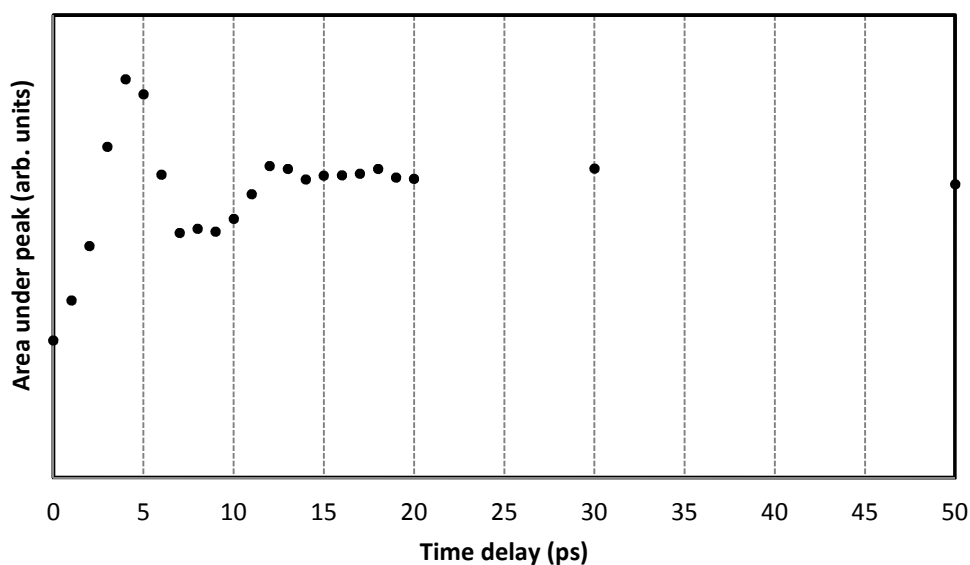


**Figure 6.16: Area under the peak labelled *D* in Figure 6.13 plotted against time elapsed. Oscillations are visible very early, but die away quickly, after which the area is almost constant. The area is taken in the range  $1,162\text{--}1,222 \text{ cm}^{-1}$ .**

The early oscillations quickly die away in Figure 6.16. The largest oscillation visible has a period of approximately 8 ps, indicating an energy

separation of approximately  $4 \text{ cm}^{-1}$ ; however the peak settles quickly to an almost constant area for time delays  $> \sim 12 \text{ ps}$ , which is a further indication that there is actually a superposition with one or more oscillations in addition to the one that is measurable. These oscillations interfere destructively, resulting in a constant peak intensity.

### 6.9.2 Discussion

The strong peak labelled *C* at  $\sim 970 \text{ cm}^{-1}$  in the SEVI spectra in Figure 6.13 has already been identified as the  $18a^1$  ( $\Delta v=0$ ) peak. Bellm *et al.*<sup>23</sup> saw ion peaks at 433, 944, 1,361 and  $1,733 \text{ cm}^{-1}$  in the ZEKE spectrum *via* the  $S_1$   $18a^1$ , which they assigned to the  $6a^1$ ,  $18a^1$ ,  $18a^16a^1$  and  $18a^11^1$  respectively. The work by Ayles *et al.*<sup>8</sup> placed the  $18a^1$  peak at  $984 \text{ cm}^{-1}$  and the current ZEKE data shows it at  $978 \text{ cm}^{-1}$ . This suggests that there may be a calibration issue associated with the Bellm data and that the peaks seen here at 490, 1,420 and  $1,805 \text{ cm}^{-1}$  (labelled *A*, *E* and *F* in Figure 6.13) are the same as those assigned by Bellm. However, while peaks *E* and *F* are approximately where one would expect to see the  $18a^16a^1$  and  $18a^11^1$ , peak *A* is a little high for the  $6a^1$ , which was seen at  $\sim 435 \text{ cm}^{-1}$  in the SEVI obtained *via* the Fermi resonance (Figure 6.10) and at  $440 \text{ cm}^{-1}$  by Ayles. Ayles *et al.* also saw a peak at  $\sim 500 \text{ cm}^{-1}$ , which they assigned to the  $11^116a^1$ ; Peak *D* was assigned to the  $18a^115^1$  in the same paper. Peak *B* is currently unassigned

Combining the time-resolved area data from the three peaks analysed above, it appears that the bright state in this case is coupled to two "doorway states", which are further coupled to a large number of other dark states (see Section 6.3). This would explain the two distinct oscillation periods of 5 and 8 ps and the exponential decay with a timescale of  $\sim 17 \text{ ps}$ . Peaks *C* and *D* each show oscillations with periods of 8 ps; however the

oscillations are out of phase with each other, with peak *C* showing a maximum at 0 ps and peak *D* at 4 ps. This indicates that peak *C* originates from ionisation from the bright state, while *D* comes from ionisation from a dark state. The loss of structure at long time delays is consistent with the congestion seen in the ZEKE spectrum.

## 6.10 $S_1$ $13^1$

### 6.10.1 Results

The peak at approximately  $1,195\text{ cm}^{-1}$  in the REMPI spectrum is identified as the  $13^1$  in refs. 7 and 8. The ZEKE spectrum recorded *via* this state is shown in Figure 6.17.

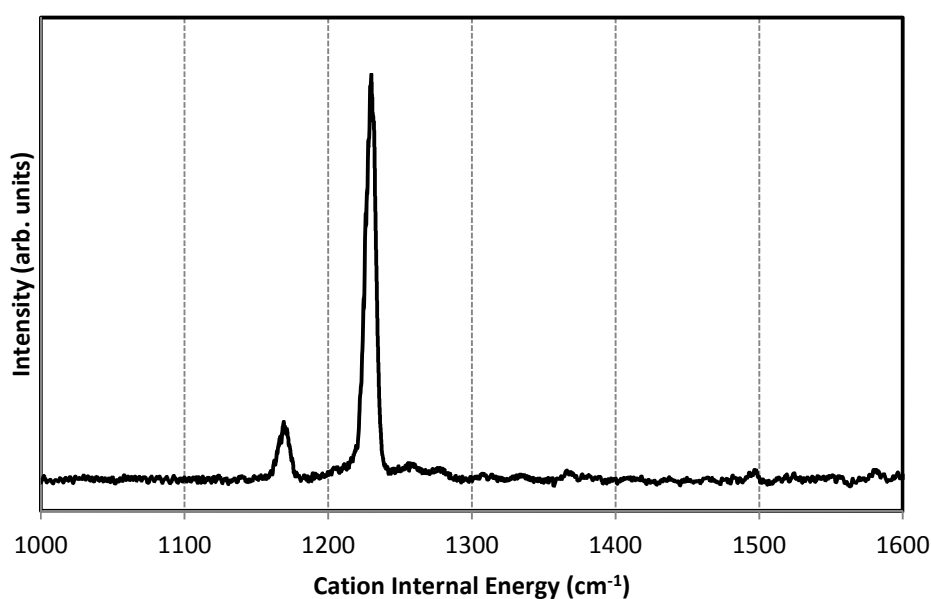


**Figure 6.17: ZEKE spectrum recorded *via* the  $13^1$  peak seen at  $1,195\text{ cm}^{-1}$  in the REMPI spectrum.**

The spectrum shows a very small rise in the baseline around the  $\Delta\nu=0$  peak; however there is very little congestion, suggesting that clear structure will still be seen in the time-resolved experiments even at long time delays.

The time-resolved SEVI spectra recorded *via* the  $13^1$  is shown in Figure 6.18.

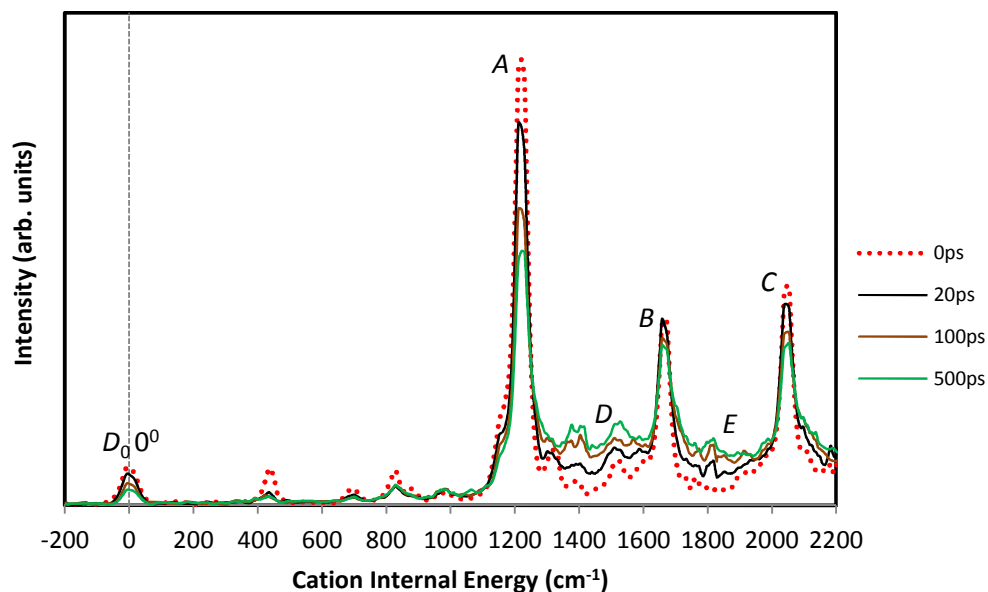


**Figure 6.18:** SEVI spectra at selected time delays recorded *via* the  $13^1$  peak at  $1,195 \text{ cm}^{-1}$  in the REMPI spectrum. The peaks labelled *A*, *B* and *C* are at approximately  $1,230$ ,  $1,670$  and  $2,050 \text{ cm}^{-1}$  respectively.

The spectra show clear time dependence; all of the peaks decrease in intensity, while the regions between the peaks show the characteristic rise associated with irreversible IVR. There is, however, still considerable structure to the spectrum even after 500 ps; peaks *A*, *B* and *C* are still clearly identifiable above the background. Figures 6.19 and 6.20 show the change in the area of peaks *A* and *C* as time progresses, together with exponential fits to the data. The relative change in the area of peak *B* is very small, so this has not been plotted as the data would be less reliable.

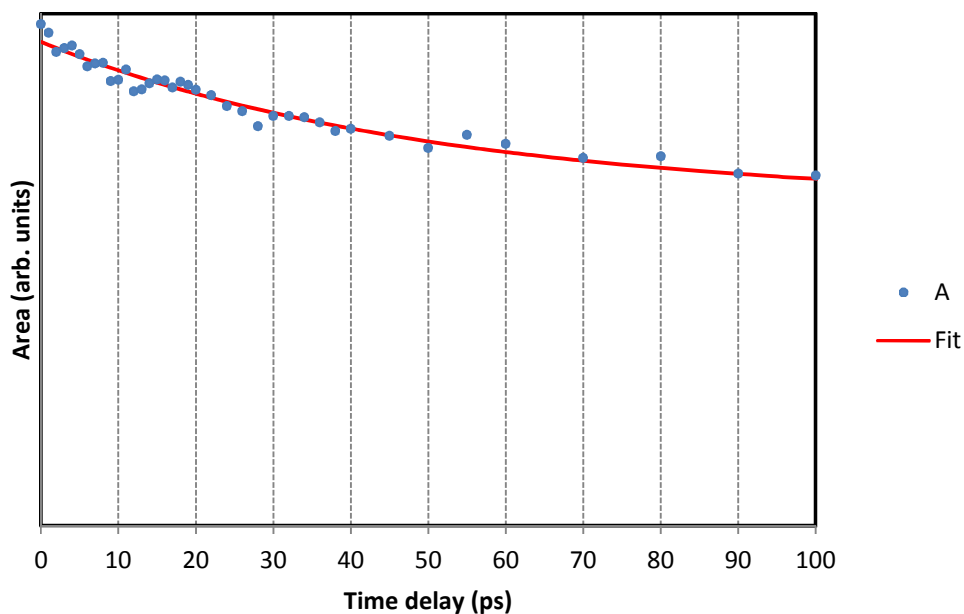


**Figure 6.19:** Area under the peak labelled A in Figure 6.18. The decay is exponential and no regular oscillations are visible. The area has been taken in the range 1,211–1,243  $\text{cm}^{-1}$ .

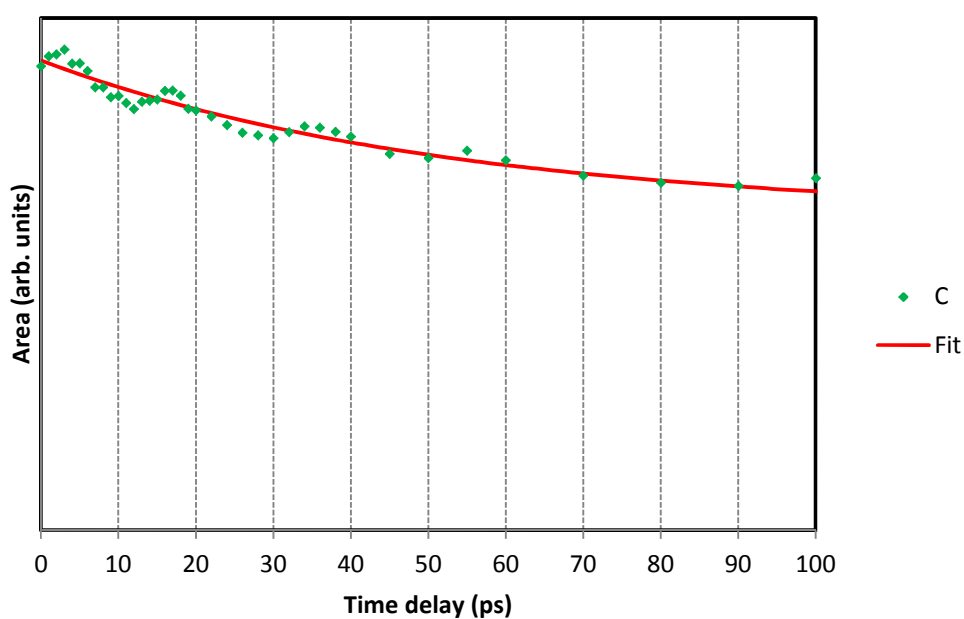


**Figure 6.20:** Area under the peak labelled C in Figure 6.18. The decay is exponential. Although oscillations are visible, this should be treated with caution as the relative change in the area of peak C is quite small so the errors in the data may be larger than the amplitude of the oscillations. The area has been taken in the range 2,037–2,052  $\text{cm}^{-1}$ .

Each of these figures show an exponential decay but no conclusive evidence for oscillations such as were seen for the 18a<sup>1</sup>. The equations for the decay fits, based on Equation 6.5, yield IVR lifetimes of 50.6 and 52.3 ps for *A* and *C* respectively. This shows very good agreement; the lifetime can therefore be estimated to be  $\sim 51 \pm 3$  ps.

Figure 6.21 shows the rise in the background between the peaks in the regions *D* and *E*. These can be seen to rise exponentially as the dark states are populated. The equations of the fits (which have the form of Equation 6.6) yield lifetimes of 44 and 37 ps for *D* and *E* respectively. These figures are not included in the average lifetime calculation; since it is impossible to tell how many states are in these regions and the intensities are very low the errors are expected to be much larger.

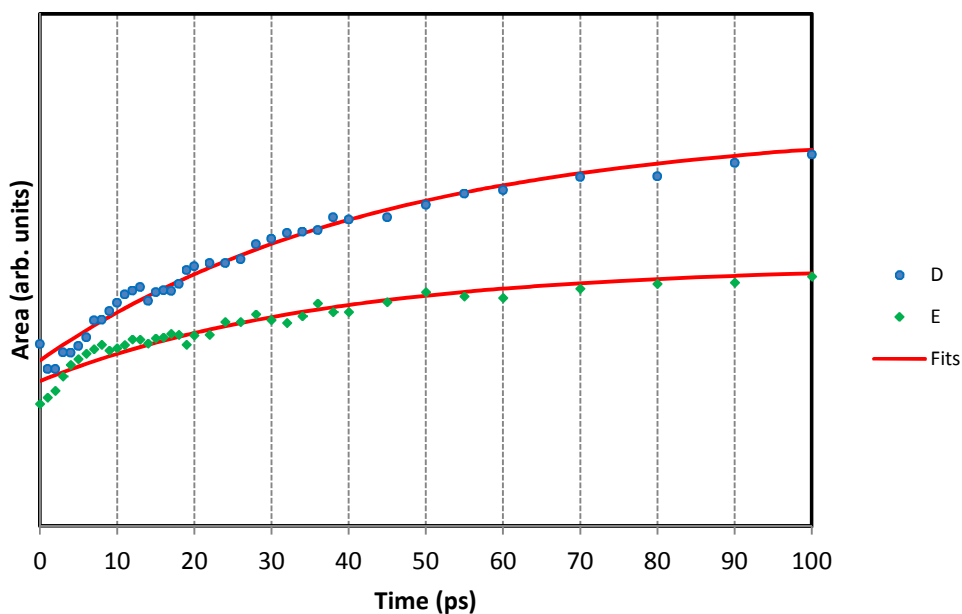


**Figure 6.21: Area under regions labelled D and E in Figure 6.18. Areas are taken in the ranges *D* (1,367-1,577 cm<sup>-1</sup>), *E* (1,737-1,916 cm<sup>-1</sup>).**

### 6.10.2 Discussion

The ion peak labelled *A* in Figure 6.18 is the  $13^1$  ( $\Delta v=0$ ). The most likely assignments for *B* and *C* are  $13^16a^1$  and  $13^11^1$ .

In contrast to the time-resolved data obtained *via* the  $18a^1$  peak (*vide supra*), there are no oscillations visible in the decay for the  $\Delta v=0$  peak, which leads to the conclusion that in this case no strongly coupled doorway states are involved. There appear to be oscillations in peak *C*, but since they are small enough in amplitude to be within experimental error and are not seen in any of the other data this is not conclusive. The energy loss is irreversible, indicating that the bright state could be directly coupled to a large number of dark states. The rise in the population of the dark states can also be seen in the exponential rise in the background.

The IVR rate is slower than for the  $18a$ ; this may be counterintuitive since the  $13^1$  is at higher energy and the region will therefore have a higher density of states. However, the absence of strong coupling to doorway states may slow down the process. The clear structure still evident at 500 ps is consistent with the evidence of the ZEKE spectrum, which shows less congestion than the  $18a^1$ .

## 6.11 $S_1$ $7a^1$

### 6.11.1 Results

The peak which can be seen in the REMPI spectrum at  $\sim 1,230$   $\text{cm}^{-1}$  was assigned in both refs. 7 and 8 as  $S_1$   $7a^1$ . The ZEKE spectrum recorded *via* this peak is shown in Figure 6.22.

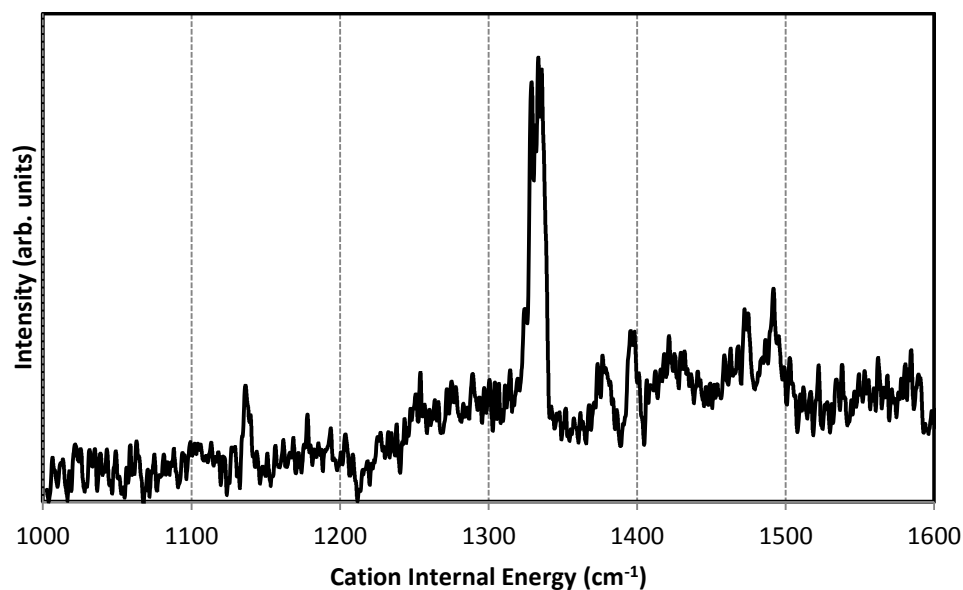


**Figure 6.22: ZEKE spectrum via the  $7a^1$  peak seen at  $\sim 1,230 \text{ cm}^{-1}$  in the REMPI spectrum.**

It can be seen that there is very little structure in the spectrum in Figure 6.22, with only the  $\Delta v=0$  peak clearly visible at  $\sim 1,333 \text{ cm}^{-1}$ ; other peaks are only just discernible above the rising baseline in the vicinity of the peak and at higher energy. This suggests a large number of populated dark states and, consequently, a statistical IVR process.

The SEVI spectra at selected time delays are shown in Figure 6.23. At 0 ps, three sharp peaks are observed; however, the structure is very quickly lost amid the rapidly rising baseline. This again shows that statistical IVR is the dominant process for this state.

The variation in area under peaks *A*, *B* and *C* in the SEVI spectrum is shown in Figures 6.24 and 6.25. The variation is also shown for the areas of dark states, labelled *D* and *E* in Figure 6.26.

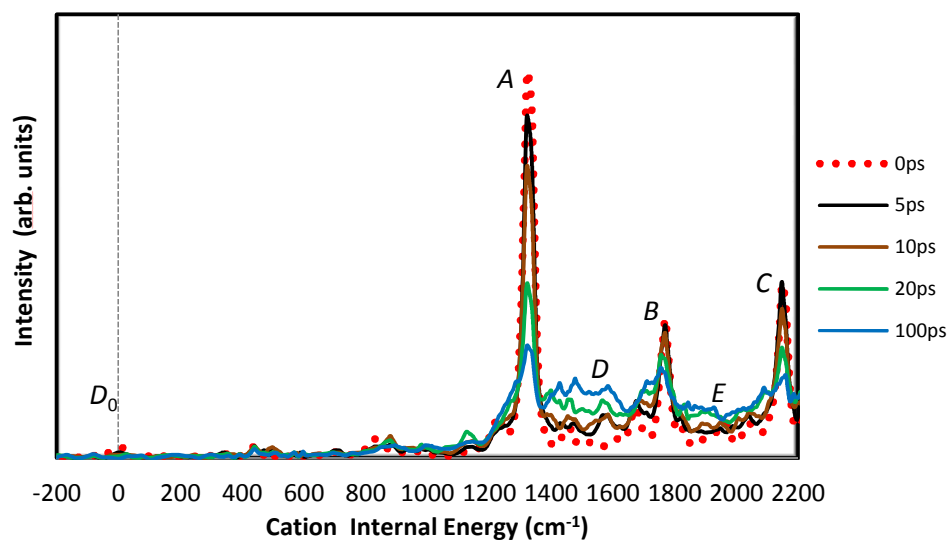


**Figure 6.23: SEVI spectra at selected time delays recorded via the  $7a^1$  peak at  $1,230 \text{ cm}^{-1}$  in the REMPI spectrum. The three peaks labelled *A*, *B*, and *C* are at approximately  $1,333$ ,  $1,772$  and  $2,146 \text{ cm}^{-1}$  respectively.**

As observed in the time-resolved data recorded via the  $13^1$ , the exponential fall in the areas under the peaks are mirrored by an exponential rise in the background between the peaks. A fitting procedure has been employed to each series.

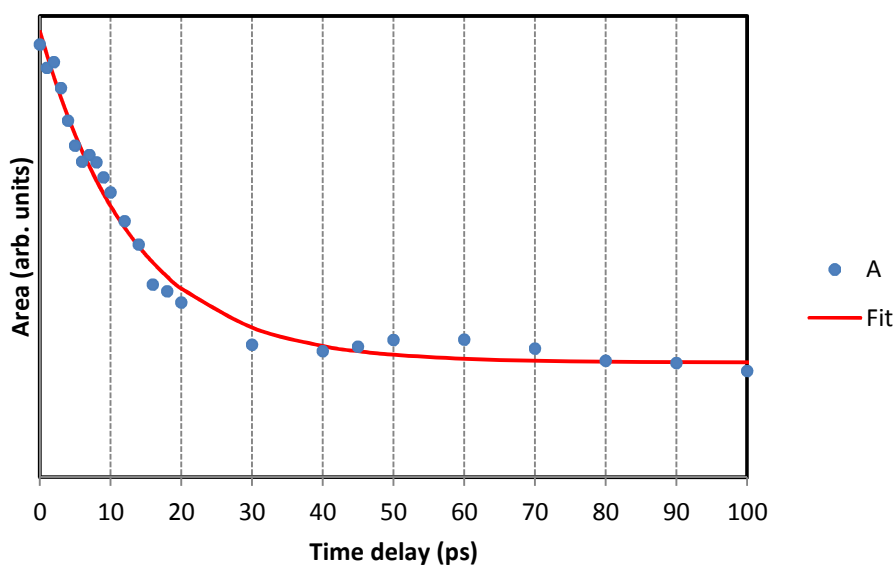


**Figure 6.24: Area under peak *A* ( $\Delta\nu=0$ ) in Figure 6.23 plotted against time delay. Area is taken in the range  $1,195$ - $1,259 \text{ cm}^{-1}$ .**

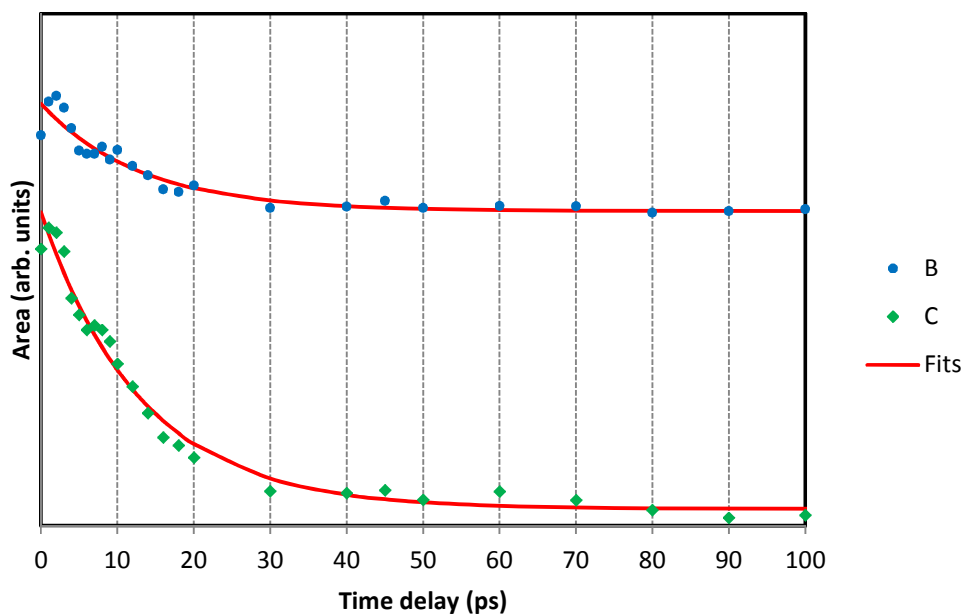


**Figure 6.25: Areas under peaks *B* and *C* in Figure 6.23 plotted against time delay. Areas are taken in the ranges 1,654-1,678 and 2,037-2,052  $\text{cm}^{-1}$  respectively.**

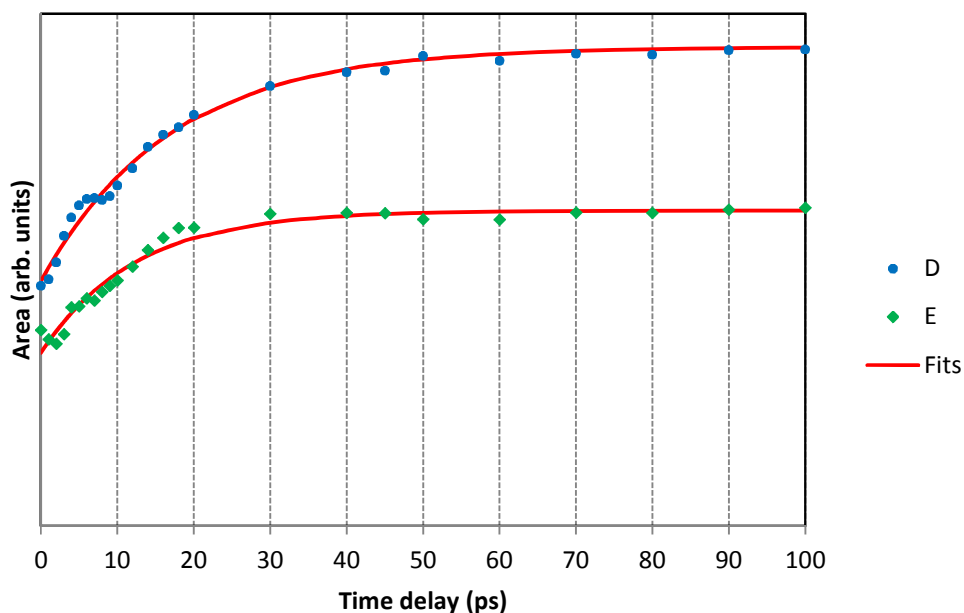


**Figure 6.26: Areas under regions *D* and *E* in Figure 6.23 plotted against time delay. Areas are taken in the ranges 1,366-1,482 and 1,748-1,867  $\text{cm}^{-1}$  respectively.**

From the fits to the data from peaks *A*, *B* and *C*, the IVR lifetimes are calculated as 13.3, 13.0 and 13.2 ps respectively. This shows excellent agreement and the value can therefore be given as  $13 \pm 1$  ps. The lifetimes obtained from regions *D* and *E* are 17.0 and 12.2 ps; again, the very low intensities in these regions will increase the errors.

### 6.11.2 Discussion

As has been noted, the  $\Delta v=0$  peak appears at  $1,330 \text{ cm}^{-1}$  in the SEVI spectrum (labelled *A* in Figure 6.23). This has been assigned to the  $7a^1$ . The peaks labelled *B* and *C* are assigned to the combination bands  $7a^16a^1$  and  $7a^11^1$  respectively.

It is clear that in this case the sharp structure observed at 0 ps is rapidly lost to a rising signal from the dark states. The irreversible flow of energy away from the bright state is characteristic of statistical IVR.

Although there may be some oscillations in Figure 6.25, it is not possible to conclusively determine any strong coupling to doorway states in this experiment. It is possible that the bright state is directly coupled to many dark states.

The IVR rate of approximately 13 ps, is shorter than both the  $18a^1$  and the  $13^1$  state. This may be expected since the  $7a^1$  is at the highest energy and will therefore be more likely to be in a region with a higher density of states. This leads to more states available to which the bright state can couple and is thought to be a strong contributing factor to IVR lifetimes<sup>27,28</sup> (see Section 6.3 for a more complete discussion). However, since the difference in energy between the  $S_1$  states is relatively small, there are likely to be other factors with a more significant influence in this case.

## 6.12 Conclusions

Nanosecond ZEKE and picosecond SEVI spectra have been recorded *via* four different vibrational levels of  $p$ FT. The first set of experiments revealed a Fermi resonance between the  $1^1$  fundamental mode and the  $9b^2$  overtone. The assignment of the lower energy eigenstate to  $9b^2$  is in contrast to ref. 8 and has been made using harmonic mode calculations and symmetry considerations. The ZEKE spectra revealed coupling between the two zero-order states following separate excitations of the eigenstates. The time resolved experiments, which excite both eigenstates coherently, revealed clearly defined quantum beats with a regular period of 5 ps. This indicated an  $S_1$  eigenstate energy separation of approximately  $7\text{ cm}^{-1}$ , which was found to be in good agreement with the separation of the eigenstates in the REMPI spectrum. The quantum beats have a decaying amplitude, a result of rotational dephasing.

The other three states studied showed an exponential decrease in the population of the bright state, indicating an irreversible redistribution of energy consistent with statistical IVR. The IVR lifetimes have been calculated from fits to the exponential decay of the areas under selected peaks; these are shown in Table 6.2. The time-resolved photoelectron spectra *via*  $S_1\ 18a^1$  states also showed quantum beats with measurable periods, indicating the presence of doorway states. Oscillations with two different periods are identifiable; the  $S_1$  eigenstate separations are measured as 4 and  $7\text{ cm}^{-1}$ .

**Table 6.2: IVR lifetimes of the three vibrational states showing irreversible decay in the population of the bright state.**

Vibrational level	Energy in $S_1$	IVR lifetime
<b>18a<sup>1</sup></b>	845 cm <sup>-1</sup>	17±1 ps
<b>13<sup>1</sup></b>	1,195 cm <sup>-1</sup>	51±3 ps
<b>7a<sup>1</sup></b>	1,230 cm <sup>-1</sup>	13±1 ps

If the density of states is noticeably greater at higher energies in this region and this influences the IVR lifetimes (*vide supra*), then the lifetime *via* the  $S_1$  18a<sup>1</sup> is relatively fast. This may be explicable with reference to the doorway state model (described in Section 6.3), in which the bright state couples strongly to one or more secondary states, which are further coupled to many other dark states. It is plausible that this could accelerate the process of IVR, since the doorway states act as an intermediate step to enhance the coupling to the other dark states. The  $S_1$  13<sup>1</sup> state shows an exponential decay with no strong oscillations, indicating that no strongly coupled doorway states are available; this may be why it shows a much slower rate of IVR than the 18a<sup>1</sup>.

## References

- 
- <sup>1</sup> P. J. Robinson and K. A. Holbrook, *Unimolecular Reactions*, Wiley, New York, 1971, pp. 64-92, and references therein.
  - <sup>2</sup> D. Boyall and K. L. Reid, *Chem. Soc. Rev.*, **26**, 223 (1997).
  - <sup>3</sup> P. M. Felker and A. H. Zewail, *J. Chem. Phys.*, **82**, 2961 (1985).
  - <sup>4</sup> A. H. Zewail, *J. Chem. Phys. A*, **104**, 5660 (2000).
  - <sup>5</sup> D. J. Nesbitt and R. W. Field, *J. Phys. Chem.*, **100**, 12735 (1996).
  - <sup>6</sup> G. Varsanyi and L. Lang, *Assignments for Vibrational Spectra of Seven Hundred Benzene Derivatives*, Wiley, New York (1974).
  - <sup>7</sup> K. Okuyama, N. Mikami and M. Ito, *J. Phys. Chem.*, **89**, 5617 (1985).
  - <sup>8</sup> V. L. Ayles, C. J. Hammond, D. E. Bergeron, O. J. Richards and T. G. Wright, *J. Chem. Phys.*, **126**, 244304 (2007).

- 
- <sup>9</sup> C. S. Parmenter and B. M Stone, *J. Chem. Phys.*, **84**, 4710 (1986).
- <sup>10</sup> C. J. Hammond, *Thesis*, Studies of Intramolecular Vibrational Redistribution in Excited State Toluene Derivatives, University of Nottingham (2008).
- <sup>11</sup> G. A. Bethardy, X. L. Wang and D. S. Perry, *Can. J. Chem.*, **72**, 652 (1994).
- <sup>12</sup> J. B. Hopkins, D. E. Powers and R. E. Smalley, *J. Chem. Phys.*, **73**, 683 (1980).
- <sup>13</sup> E. R. T. Kerstel, K. K. Lehmann, T. F. Mentel, B. H. Pate and G. Scholes, *J. Phys. Chem.*, **95**, 8282 (1991).
- <sup>14</sup> C. J. Hammond, V. L. Ayles, D. E. Bergeron, K. L. Reid and T. G. Wright, *J. Chem. Phys.*, **125**, 124308 (2006).
- <sup>15</sup> R. J. Plowright, *Thesis*, Spectroscopy and Interactions of Metal and Metal Cation Complexes, University of Nottingham (2010).
- <sup>16</sup> R. J. Plowright, V. L. Ayles, M. J. Watkins, A. M. Gardner, T. G. Wright and W. H. Breckenridge, *J. Chem. Phys.*, **127**, 204308 (2007).
- <sup>17</sup> R. J. Plowright, M. J. Watkins, A. M. Gardner, T. G. Wright and W. H. Breckenridge, *J. Chem. Phys.*, **129**, 154315 (2008).
- <sup>18</sup> A. T. J. B. Eppink and D. H. Parker, *Rev. Sci. Instrum.*, **68**, 3477 (1997).
- <sup>19</sup> J. A. Davies and K. L. Reid, *J. Chem. Phys.*, **135**, 124305 (2011).
- <sup>20</sup> G. A. Garcia, L. Nahon and I. Powis, *Rev. Sci. Instrum.*, **75**, 4989 (2004).
- <sup>21</sup> K. Takazawa, M. Fujii and M. Ito, *J. Chem. Phys.*, **99**, 3205 (1993).
- <sup>22</sup> J. A. Davies, K. L. Reid, M. Towrie and P. Matousek, *J. Chem. Phys.*, **117**, 9099 (2002).
- <sup>23</sup> S. M. Bellm, P. T. Whiteside and K. L. Reid, *J. Phys. Chem. A*, **107**, 7373 (2003).
- <sup>24</sup> A. K. King, S. M. Bellm, C. J. Hammond, K. L. Reid, M. Towrie and P. Matousek, *Mol. Phys.*, **103**, 1821 (2005).
- <sup>25</sup> J. H. S. Green, *Spectrochimica Acta* **26A**, 1503 (1970).
- <sup>26</sup> Julia Davies, unpublished.
- <sup>27</sup> P. M. Felker and A. H. Zewail, *J. Chem. Phys.*, **82**, 2994 (1985).
- <sup>28</sup> E. R. T. Kerstel, K. K. Lehmann, T. F. Mentel, B. H. Pate and G. Scholes, *J. Phys. Chem.*, **95**, 8282 (1991).

## 7. Theoretical Study of $\text{Cl}^-$ -RG Complexes (RG=He-Rn)

### 7.1 Introduction

High-level *ab initio* potential energy curves have previously been published for  $\text{F}^-$  and  $\text{Br}^-$  and  $\text{I}^-$  interacting with each of the rare gases.<sup>1,2,3,4</sup> This work is continued here with the corresponding  $\text{Cl}^-$  complexes, in collaboration with C. C. Kirkpatrick and E. P. F. Lee. Employing CCSD(T) methods similar to those described for the Au-RG ground state calculations in Chapter 3 and the Group 2 metal ion-rare gas calculations described in Chapters 4 and 5, spectroscopic constants have been derived for  $\text{Cl}^-$ -RG complexes (RG=He-Rn). The potential curves calculated here have also been used by L. A. Viehland and co-workers at Chatham University, USA in order to calculate transport coefficients for  $\text{Cl}^-$  ions moving through a bath of atoms of each rare gas. A considerable amount of transport data are available for these species;<sup>5,6,7,8,9,10,11,12,13</sup> with somewhat more limited scattering<sup>14,15</sup> and spectroscopic<sup>16,17,18,19,20</sup> data. The spectroscopic results presented herein are compared with previous theoretical and experimental results.

There have been several previous theoretical studies of  $\text{Cl}^-$  at the CCSD(T) level; Bera and Das<sup>21</sup> studied RG=He-Kr employing aug-cc-pVTZ basis sets and Naumkin and McCourt<sup>22</sup> employed aug-cc-pVQZ basis sets for RG=He-Ar. Buchachenko *et al.*<sup>23</sup> have investigated  $\text{Cl}^-$ -Ar and  $\text{Cl}^-$ -Kr using aug-cc-pVTZ and aug-cc-pVQZ basis sets augmented with bond functions. Irikura<sup>24</sup> and Sun *et al.*<sup>25</sup> have also studied  $\text{Cl}^-$ -Ar using aug-cc-pV(T+d)Z and aug-cc-pVQZ basis sets respectively. In addition, there are experimental values available via the ZEKE spectra for RG=Ar-Xe by Neumark's group<sup>16,17,20</sup> and for  $\text{Cl}^-$ -Ar by Distelrath and Boesl.<sup>18</sup> No

previous *ab initio* results have been found for Cl<sup>-</sup> complexes involving Xe or Rn and no experimental spectroscopy results have been found for He, Ne or Rn.

## 7.2 Computational Details

CCSD(T) calculations have been carried out on these closed-shell systems. For RG=He-Ne, standard aug-cc-pV5Z and aug-cc-pV6Z basis sets have been employed,<sup>26, 27, 28</sup> with aug-cc-pV(5+d)Z and aug-cc-pV(6+d)Z employed for Ar;<sup>29</sup> for all of these, one further diffuse function of each angular momentum type was added, obtained by an even tempered extrapolation of the two most diffuse functions in the standard basis set. For RG=Kr-Rn the relativistic small-core potentials ECP10MDF, ECP28MDF and ECP60MDF were employed together with the aug-cc-pVQZ-PP and aug-cc-pV5Z-PP valence basis sets;<sup>30</sup> these were again augmented by diffuse functions derived in a similar fashion. In all cases, the corresponding aug-cc-pV(X+d)Z basis sets<sup>29,30</sup> were used for chlorine.

Each potential energy curve was calculated using MOLPRO<sup>31</sup> on the Magellan<sup>32</sup> computer system for about 50 interatomic separations covering a wide range of  $R$  ( $\sim 1.5$  to  $50 \text{ \AA}$ ). Each point was corrected for BSSE using the full counterpoise correction. For RG=He-Ar, the interaction energies obtained using the quintuple- $\zeta$  and hextuple- $\zeta$  basis sets were pointwise-extrapolated to the basis set limit using the two-point cubic formula of Halkier *et al.*<sup>33,34</sup> For RG=Kr-Rn the extrapolation was carried out from curves obtained using the QZ and 5Z basis sets. The extrapolated curves were employed in the calculation of the spectroscopic constants. The constants have been derived using the LEVEL<sup>35</sup> program as described in Chapters 2, 4 and 5. The most abundant naturally occurring isotope of

each element was used in all cases ( $^{35}\text{Cl}$ ,  $^4\text{He}$ ,  $^{20}\text{Ne}$ ,  $^{40}\text{Ar}$ ,  $^{84}\text{Kr}$ ,  $^{132}\text{Xe}$  and  $^{222}\text{Rn}$ ).

### 7.3 Results

The calculated spectroscopic constants are shown in Table 7.1, together with the results from previous research by other groups.

There have been many theoretical studies of  $\text{Cl}^-$ -RG; only those at the CCSD(T) level are discussed here, as the lower level results have been discussed in earlier work<sup>21,22,24,25</sup> and the CCSD(T) results are concluded to be more reliable. These have all been carried out using smaller basis sets than those employed here and only the  $\text{Cl}^-$ -Ar  $D_e$  value of Irikura<sup>24</sup> was derived with an extrapolation to the basis set limit; it is therefore unsurprising that the previously calculated dissociation energies are consistently smaller than those presented here.

Both the studies of Bera and Das<sup>21</sup> and Naumkin and McCourt<sup>22</sup> yield  $R_e$  values close to the present results for  $\text{Cl}^-$ -He and  $\text{Cl}^-$ -Ne. The  $D_e$  values of Bera and Das are considerably lower than those presented here; those of Naumkin and McCourt are slightly higher than the former (since they used larger basis sets), with the value for  $\text{Cl}^-$ -He in quite good agreement with the present result.

**Table 7.1: Spectroscopic constants for Cl<sup>-</sup>-RG.  $R_e$  is the equilibrium bond length (Å),  $D_e$  is the depth of the potential,  $D_0$  is the energy between the zero-point and the asymptote,  $\omega_e$  is the harmonic vibrational frequency,  $\omega_e x_e$  is the anharmonicity constant,  $B_e$  is the equilibrium rotational constant at the minimum,  $\alpha$  is the spin-rotation constant (all in cm<sup>-1</sup>),  $k$  is the harmonic force constant (Nm<sup>-1</sup>). Results from the present work are shown in bold.**

	$R_e$	$D_e$	$D_0$	$\omega_e$	$\omega_e x_e$	$B_e$	$A$	$D_e^{\text{MORSE}}$	$D_e^{\text{MORSE}}/D_e$	$k$
<b>Cl<sup>-</sup>-He</b>	<b>3.96</b>	<b>44.2</b>	<b>29.3</b>	<b>26.3</b>	<b>4.18</b>	<b>0.298</b>	<b>7.51x10<sup>-2</sup></b>	<b>41.4</b>	<b>0.94</b>	<b>0.147</b>
Ref. 21 <sup>a</sup>	4.05	24.2		29.9	12.00	0.48				
Ref. 2222 <sup>b</sup>	4.02	39.4								
<b>Cl<sup>-</sup>-Ne</b>	<b>3.74</b>	<b>119.1</b>	<b>103.7</b>	<b>31.4</b>	<b>2.37</b>	<b>0.0953</b>	<b>8.30x10<sup>-3</sup></b>	<b>103.7</b>	<b>0.87</b>	<b>0.739</b>
Ref. 21 <sup>a</sup>	3.83	88.7		28.1	3.74	0.10				
Ref. 22 <sup>b</sup>	3.80	101.4								
<b>Cl<sup>-</sup>-Ar</b>	<b>3.67</b>	<b>515.4</b>	<b>488.8</b>	<b>54.0</b>	<b>1.68</b>	<b>0.0671</b>	<b>2.17x10<sup>-3</sup></b>	<b>433.9</b>	<b>0.84</b>	<b>3.21</b>
Ref. 16 <sup>c</sup>	3.71±0.08	523±5		53.1						
Ref. 18 <sup>c</sup>		354/507	330/480	53.4						
Ref. 23 <sup>b</sup>	3.69	500.6								
Ref. 22 <sup>b</sup>	3.71	476.9								
Ref. 25 <sup>b</sup>	3.67	493.4								
Ref. 24 <sup>d</sup>	3.72	434.5								
Ref. 24 <sup>e</sup>		514.9 <sup>e</sup>								
Ref. 21 <sup>a</sup>	3.72	443.6		52.2	2.73	0.07				
<b>Cl<sup>-</sup>-Kr</b>	<b>3.67</b>	<b>778.1</b>	<b>749.8</b>	<b>57.1</b>	<b>1.25</b>	<b>0.0508</b>	<b>1.14x10<sup>-3</sup></b>	<b>653.4</b>	<b>0.84</b>	<b>4.75</b>
Ref. 17 <sup>c</sup>	3.83±0.10	772±8		55.5						
Ref. 23 <sup>a</sup>	3.73	719.6								
Ref. 21 <sup>a</sup>	3.72	718			2.05	0.05				
<b>Cl<sup>-</sup>-Xe</b>	<b>3.70</b>	<b>1184.4</b>	<b>1152.5</b>	<b>64.3</b>	<b>1.031</b>	<b>0.0445</b>	<b>7.34x10<sup>-4</sup></b>	<b>1002.4</b>	<b>0.85</b>	<b>6.74</b>
Ref. 20 <sup>c</sup>	3.57±0.03	1176±10		41.43						
Ref. 36 <sup>a</sup>	3.80	980								
<b>Cl<sup>-</sup>-Rn</b>	<b>3.68</b>	<b>1473.7</b>	<b>1439.9</b>	<b>68.1</b>	<b>0.927</b>	<b>0.0412</b>	<b>5.80x10<sup>-4</sup></b>	<b>1250.9</b>	<b>0.85</b>	<b>8.27</b>

<sup>a</sup>CCSD(T)/aug-cc-pVTZ. <sup>b</sup>CCSD(T)/aug-cc-pVQZ. <sup>c</sup>ZEKE spectroscopy. <sup>d</sup>CCSD(T)/aug-cc-pV(T+d)Z. <sup>e</sup>Calculation extrapolated to basis set limit using up to 6Z basis set energies.

There has been considerably more interest in  $\text{Cl}^-$ -Ar. Neumark's group<sup>16</sup> have derived  $R_e$  and  $D_e$  values from potentials that have been obtained by fitting to ZEKE spectra. These values are in good agreement with the present results, as is their value of  $\omega_e$ . Distelrath and Boesl<sup>18</sup> have used two methods to calculate  $D_e$  from their ZEKE experiments; the lower value is obtained from a Birge-Sponer (BS) analysis and is very low compared to the theoretical value calculated here. The second method employed the measured electron affinities together with the BS extrapolated  $D_0$  value of the neutral  $\text{Cl}^-$ -Ar complex. This value is in much better agreement with the present figure. The value of  $\omega_e$  is again in excellent agreement with that calculated here.

It can be seen that there is generally very good agreement for  $R_e$  from all the research conducted. However, the variation in the values of  $D_e$  and the fact that the results most consistent with the experimentally derived values are those employing extrapolation to the basis set limit suggest that large basis sets and rigorous electron correlation methods are required to describe these weakly interacting systems accurately.

Neumark's group have also carried out ZEKE experiments on  $\text{Cl}^-$ -Kr<sup>17</sup> and  $\text{Cl}^-$ -Xe.<sup>20</sup> The values for  $D_e$  in both cases are very close to those presented here; however the value of  $R_e$  is slightly higher for Kr and slightly lower for Xe. Their value of  $\omega_e$  for  $\text{Cl}^-$ -Xe is much lower than the present value; this is surprising because the values for Ar and Kr are in very good agreement and one would expect an increase in the vibrational frequency to be more likely as the RG atoms become heavier and more polarisable.

The theoretical studies for Kr<sup>21,23</sup> and Xe<sup>36</sup> again show quite good agreement for the  $R_e$  values, but the values of  $D_e$  are lower than those found in the present study.

For completeness, it is noted that Bera and Das<sup>21</sup> also reported spectroscopic parameters obtained from fitted Lennard-Jones potentials for Cl<sup>-</sup>-He and Cl<sup>-</sup>-Ne. For He they obtain  $\omega_e=29.9\text{ cm}^{-1}$ , which is close to the value calculated here; however the value for  $\omega_e x_e$  is significantly larger than the present result. This is consistent with their use of a wide range of  $R_e$  in the fitting procedure, hence deviations from Morse like behaviour are likely to be large. A similar situation holds for Cl<sup>-</sup>-Ne, where the values of  $\omega_e$  are again in good agreement, whereas their  $\omega_e x_e$  value is larger than the result obtained here.

Rotational constants were also calculated by Bera and Das;<sup>21</sup> in general these are in good agreement with the present results, although the value for Cl<sup>-</sup>-He appears high. To investigate this,  $B_e$  was calculated using their value of  $R_e$ ; this yielded  $B_e=0.286\text{ cm}^{-1}$ , which is in much better agreement with the result obtained here.

#### 7.4 Trends

The trend in  $R_e$  for the first three halide anions interacting with rare gases can be seen in Figure 7.1. The trend for Cl<sup>-</sup>-RG is similar to that for F<sup>-</sup> and Br<sup>-</sup> in that there is a slight decrease from He to Ne, after which the value is almost constant. The variation in  $R_e$  is much smaller than was seen in the Group 2 M<sup>+</sup>-RG complexes (see Chapters 4 and 5).

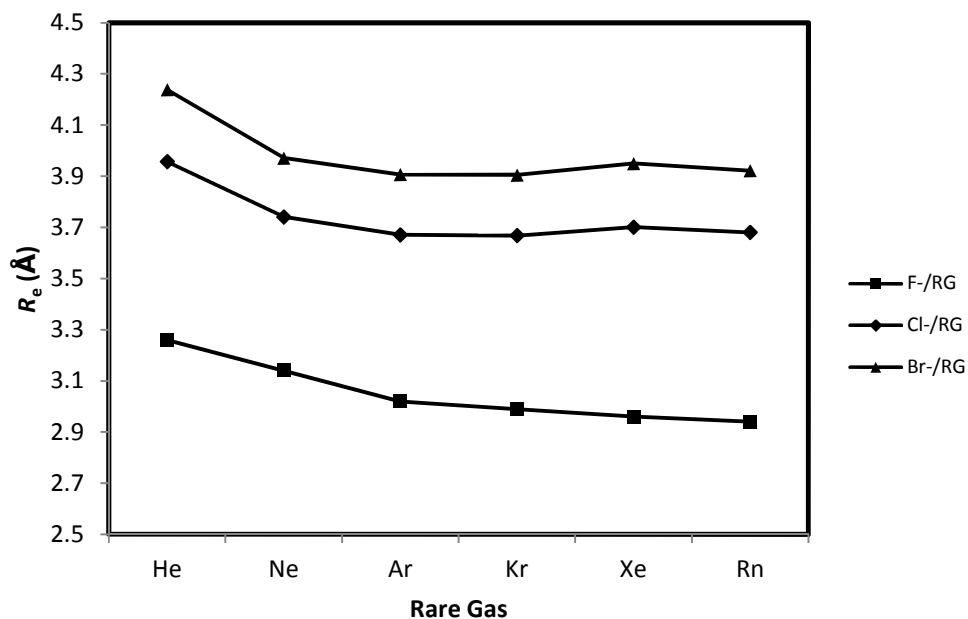


**Figure 7.1: Plot of  $R_e$  for  $X^-$ -RG ( $X=F$ -Br; RG=He-Rn). Values for  $Fl^-$  and  $Br^-$  are taken from refs. 1 and 3.**

The variation in  $D_e$  is shown in Figure 7.2. As expected, an increase is seen as the size and polarisability of the rare gas atom increases. The ratio of the increase between successive rare gases is comparable to the ratio of the polarisabilities, as predicted by the model potential of Bellert and Breckenridge<sup>37</sup> when the variation in  $R_e$  is small (see Chapter 4).

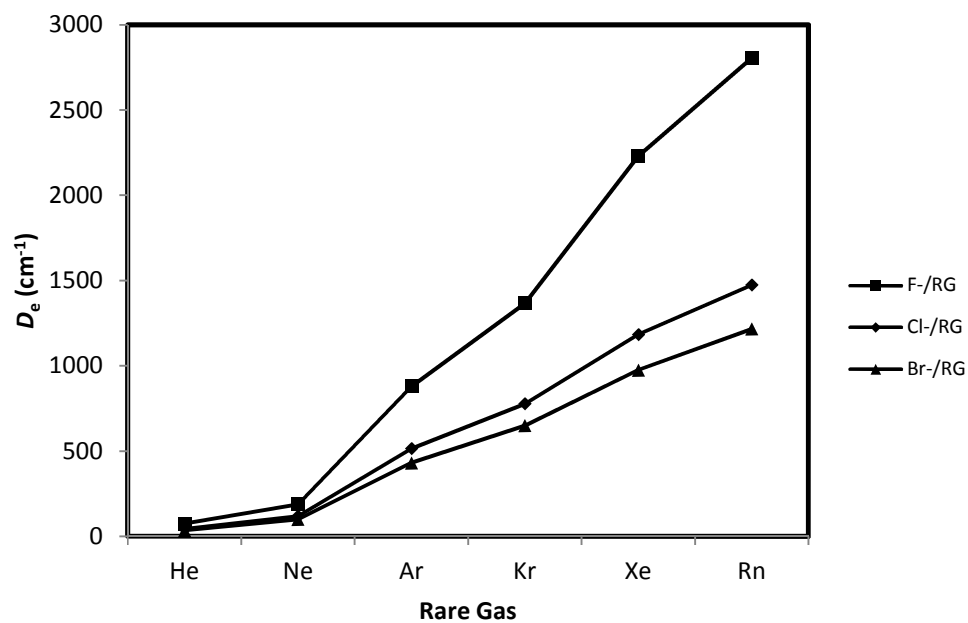


**Figure 7.2:** Plot of  $D_e$  for  $X^-$ -RG ( $X=F-Br$ ;  $RG=He-Rn$ ). Values for  $Fl^-$  and  $Br^-$  are taken from refs. 1 and 3.

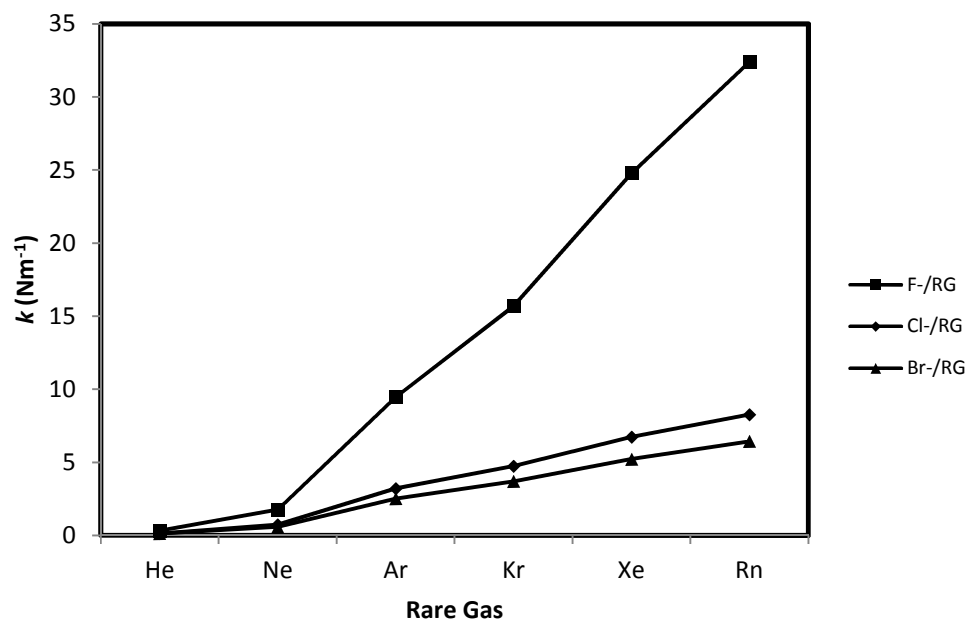


**Figure 7.3:** Plot of  $k$  for  $X^-$ -RG ( $X=F-Br$ ;  $RG=He-Rn$ ). Values for  $Fl^-$  and  $Br^-$  are calculated from data published in refs. 1 and 3.

The trends for  $k$  are similarly plotted in Figure 7.3. These also show the expected monotonic rise with the polarisability of the rare gas atom, similar to  $D_e$ . However, the relative rise between He and Ne is rather higher than the polarisability ratio, a consequence of the larger  $R_e$  value of  $\text{Cl}^-$ -He.

In general, the trends seen in the  $\text{Cl}^-$ -RG series are very similar to those seen for the other halide anions. Since these are closed-shell systems with significant repulsive terms, they do not show any of the unusual "chemical" behaviour seen for Au or the Group 2 metal cations. The ratios  $D_e^{\text{MORSE}}/D_e$  are very close to 1, indicating that these species generally show reasonably Morse-like behaviour.

## 7.5 Discussion

The choice of basis set and correlation method can be crucial to the accuracy of the interaction potential: since so much previous work has been devoted to  $\text{Cl}^-$ -RG, this is the ideal system to use to investigate the reliability of the curves calculated here.

Figure 7.4 shows the standard mobility of  $\text{Cl}^-$  in argon calculated by L. A. Viehland using the curves discussed here; a curve generated using the 6-311++G(3df, 3pd) basis set is also employed to calculate the reduced mobility and the results are compared with experimental data from ref. 42.

It can be seen that the data obtained using the 6-311++G(3df, 3pd) basis set does not yield transport data within the range of experimental error; however the aug-cc-pVXZ ( $X = \text{Q}, 5, 6, \infty$ ) converge to the actual data points upon reaching the basis set limit. This seems to suggest that the uncertainties in the experimental data<sup>38, 39, 40, 41</sup> are smaller than those originally reported. All of the tested basis sets predicted mobility values

within the limits of experimental error at high  $E/n_0$ , but they differ substantially at lower values. Since mobilities at low and high  $E/n_0$  values are associated with the long- and short-range potential values respectively, it can be concluded that all of these basis sets are adequate for predicting short-range repulsive interactions, but larger basis sets (at least quadruple- $\zeta$ ) are required at large internuclear separations.

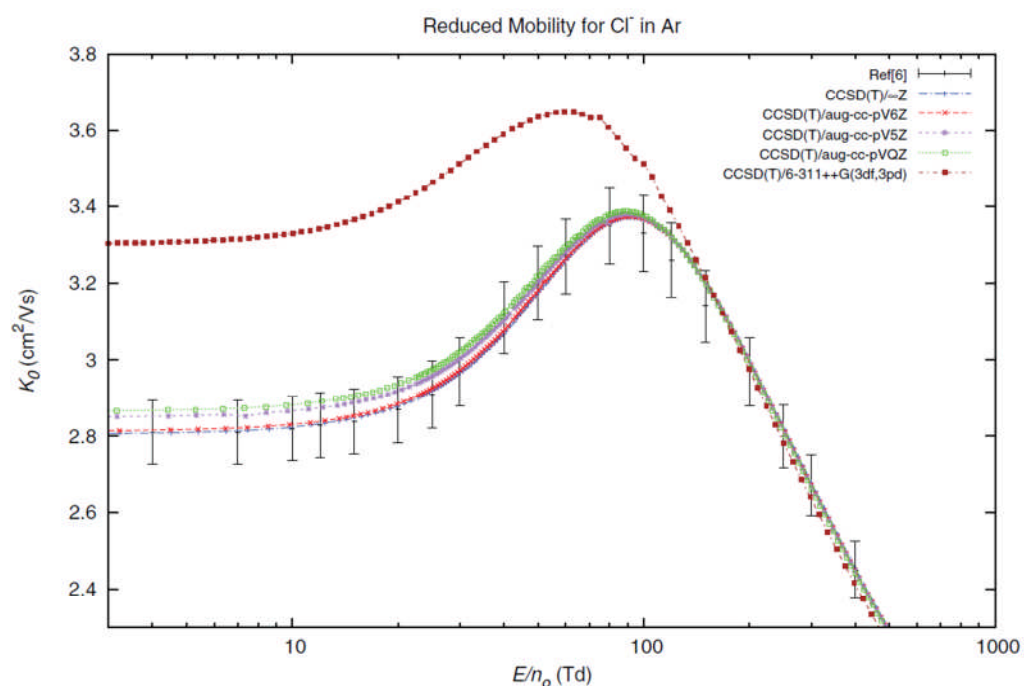


**Figure 7.4: Comparison of experimental<sup>42</sup> and computed standard mobility values for  $\text{Cl}^-$  in Ar at 297 K with selected basis sets and constant correlation method. All values are corrected for BSSE on a point-by-point basis.**

Figure 7.5 shows reduced mobility curves generated using the same basis set (quintuple- $\zeta$ ) but different correlation methods. It can be seen that the perturbation methods (MP2 and MP4) and the coupled-cluster method (CCSD(T)) generated potentials that yielded mobility values within the range of experimental error across the entire range of  $E/n_0$  values. The RHF method, however, is clearly insufficient to describe this system; dynamic electron correlation must be included.

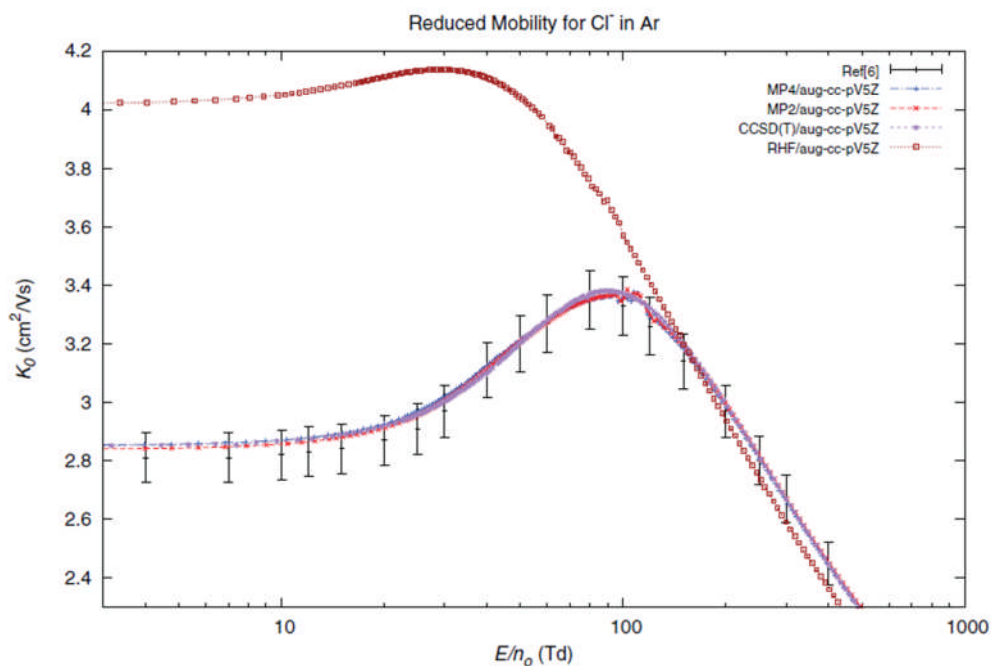


**Figure 7.5: Comparison of experimental<sup>42</sup> and computed reduced mobility values for Cl<sup>-</sup> in Ar at 297 K with selected correlation methods and quintuple- $\zeta$  basis set. All values are corrected for BSSE on a point-by-point basis.**

## 7.6 Conclusions

High-level *ab initio* potential curves have been calculated for Cl<sup>-</sup>-RG (RG=He-Rn). The curves have been employed to calculate the spectroscopic constants and the results have been compared to existing experimental and theoretical data where available. The agreement with experimental data is generally very good, which suggests that this level of theory provides reliable results. The trends seen in the series are consistent with expectations and with results seen in previous calculations for halide anion-rare gas complexes.

The curves have been used by L. A. Viehland and co-workers to calculate transport coefficients for Cl<sup>-</sup> ions moving through a bath of rare gas atoms. These also show excellent agreement with previous experimental results, which is further evidence of the reliability of the potential curves. The

reduced mobility curves demonstrate that a large basis set is required to describe the potential accurately, particularly at large internuclear separations. The mobility values appear to be calculated with good accuracy across the considered range by the MP2, MP4 and CCSD(T) methods using a quintuple- $\zeta$  basis set.

## References

- 
- <sup>1</sup> B. R. Gray, T. G. Wright, E. L. Wood and L. A. Viehland, *Phys. Chem. Chem. Phys.*, **8**, 4752 (2006).
  - <sup>2</sup> A. A. Buchachenko, J. Klos, M. M. Szczeniak, G. Chałasiński, B. R. Gray, T. G. Wright, E. L. Wood, L. A. Viehland and E. Qing, *J. Chem. Phys.*, **125**, 64305 (2006).
  - <sup>3</sup> A. A. Buchachenko, T. A. Grinev, T. G. Wright and L. A. Viehland, *J. Chem. Phys.*, **128**, 64317 (2008).
  - <sup>4</sup> A. A. Buchachenko, T. V. Tscherbul, J. Kłos, M. M. Szczeniak, G. Chałasiński, R. Webb and L. A. Viehland, *J. Chem. Phys.*, **122**, 194311 (2005).
  - <sup>5</sup> I. Dotan, W. Lindinger and D. L. Albritton, *J. Chem. Phys.*, **64**, 4544, (1976).
  - <sup>6</sup> H. W. Ellis, R. Y. Pai, E. W. McDaniel, E. A. Mason and L. A. Viehland, *At. Data Nucl. Data Tables*, **17**, 177 (1976).
  - <sup>7</sup> I. Dotan, D. L. Albritton, and F. C. Fehsenfeld, *J. Chem. Phys.*, **66**, 2232 (1977).
  - <sup>8</sup> I. Dotan and D. L. Albritton, *J. Chem. Phys.*, **66**, 5238 (1977).
  - <sup>9</sup> H.W. Ellis, E.W.McDaniel, D. L. Albritton, L. A. Viehland, S. L. Lin and E. A. Mason, *At. Data Nucl. Data Tables*, **22**, 179 (1978).
  - <sup>10</sup> M. G. Thackston, F. L. Eisele, W. M. Pope, H. W. Ellis, I. R. Gatland and E. W. McDaniel, *J. Chem. Phys.*, **70**, 3996 (1979).
  - <sup>11</sup> F. L. Eisele, M. G. Thackston, W. M. Pope, H. W. Ellis and E. W. McDaniel, *J. Chem. Phys.*, **70**, 5918 (1979).
  - <sup>12</sup> L. A. Viehland and E. A. Mason, *At. Data Nucl. Data Tables*, **60**, 37 (1995).
  - <sup>13</sup> M. G. Thackston, F. L. Eisele, W. M. Pope, H. W. Ellis, E. W. McDaniel and I. R. Gatland, *J. Chem. Phys.*, **73**, 3183 (1980).
  - <sup>14</sup> C. de Vreugd, R. W. Wignandts van Resandt and L. Los, *Chem. Phys. Lett.*, **65**, 93 (1979).

- 
- <sup>15</sup> S. Kita, K. Noda and H. Inouye, *J. Chem. Phys.*, **64**, 3446 (1976).
- <sup>16</sup> T. Lenzer, I. Yourshaw, M. R. Furlanetto, G. Reiser and D. M. Neumark, *J. Chem. Phys.*, **110**, 9578 (1999).
- <sup>17</sup> I. Yourshaw, T. Lenzer, G. Reiser and D. M. Neumark, *J. Chem. Phys.*, **109**, 5247 (1998).
- <sup>18</sup> V. Distelrath and U. Boesl, *Faraday Discuss.*, **115**, 161 (2000).
- <sup>19</sup> A. A. Buchachenko, M. M. Szczyński and G. Chałasiński, *J. Chem. Phys.*, **114**, 9929 (2001).
- <sup>20</sup> T. Lenzer, I. Yourshaw, M. R. Furlanetto, N. L. Pivonka and D. M. Neumark, *J. Chem. Phys.*, **116**, 4171 (2002).
- <sup>21</sup> N. C. Bera and A. K. Das, *Mol. Phys.*, **105**, 1433 (2007).
- <sup>22</sup> F. Y. Naumkin and F. R. W. McCourt, *Chem. Phys. Lett.*, **292**, 63 (1998).
- <sup>23</sup> A. A. Buchachenko, R. V. Krems, M. M. Szczyński, Y.-D. Xiao, L. A. Viehland and G. Chalasinski, *J. Chem. Phys.*, **114**, 9919 (2001).
- <sup>24</sup> K. K. Irikura, *Int. J. Mass Spectrom.*, **228**, 667 (2003).
- <sup>25</sup> Y. B. Sun, D. Wu, Z. R. Li and C. C. Sun, *Chem. J. Chin. Univ.*, **23**, 121 (2002).
- <sup>26</sup> T. H. Dunning, Jr., *J. Chem. Phys.*, **90**, 1007 (1989).
- <sup>27</sup> D. E. Woon and T. H. Dunning, Jr., *J. Chem. Phys.*, **100**, 2975 (1994).
- <sup>28</sup> A. K. Wilson, T. V. Mourik and T. H. Dunning, Jr., *J. Mol. Struct.: THEOCHEM*, **388**, 339 (1996).
- <sup>29</sup> T. H. Dunning, Jr., K. A. Peterson and A. K. Wilson, *J. Chem. Phys.*, **114**, 9244 (2001).
- <sup>30</sup> K. A. Peterson, D. Figgen, E. Goll, H. Stoll and M. Dolg, *J. Chem. Phys.*, **119**, 11113 (2003).
- <sup>31</sup> R. D. Amos, A. Bernhardsson, A. Berning, P. Celani, D. L. Cooper, M. J. O. Deegan, A. J. Dobbyn, F. Eckert, C. Hampel, G. Hetzer, P. J. Knowles, T. Korona, R. Lindh, A. W. Lloyd, S. J. McNicholas, F. R. Manby, W. Meyer, M. E. Mura, A. Nicklass, P. Palmieri, R. Pitzer, G. Rauhut, M. Schütz, U. Schumann, H. Stoll, A. J. Stone, R. Tarroni, T. Thorsteinsson and H.-J. Werner, MOLPRO, a package of ab initio programs designed by H.-J. Werner and P. J. Knowles, Version 2002.1 (2002).
- <sup>32</sup> Magellan is a high-performance computer cluster owned by the UK National Service for Computational Chemistry Software (NSCCS).
- <sup>33</sup> A. Halkier, T. Helgaker, P. Jorgensen, W. Klopper, H. Koch, J. Olsen and A. K. Wilson, *Chem. Phys. Lett.*, **286**, 243 (1998).

- 
- <sup>34</sup> A. Halkier, T. Helgaker, P. Jorgensen, W. Klopper and J. Olsen, *Chem. Phys. Lett.*, **302**, 437 (1999).
- <sup>35</sup> R. J. LeRoy, Level 7.2—A computer program for solving the radial Schrödinger equation for bound and quasibound levels, and calculating various values and matrix elements, University of Waterloo Chemical Physics Research Program Report CP-555R (2000).
- <sup>36</sup> D. Schröder, J. N. Harvey, M. Aschi and H. Schwarz, *J. Chem. Phys.*, **108**, 8446 (1998).
- <sup>37</sup> D. Bellert and W. H. Breckenridge, *Chem. Rev. (Washington, D. C.)*, **102**, 1595 (2002).
- <sup>38</sup> I. Dotan, D. L. Albritton and F. C. Fehsenfeld, *J. Chem. Phys.*, **66**, 2232 (1977).
- <sup>39</sup> I. Dotan and D. L. Albritton, *J. Chem. Phys.*, **66**, 5238 (1977).
- <sup>40</sup> H. W. Ellis, E. W. McDaniel, D. L. Albritton, L. A. Viehland, S. L. Lin and E. A. Mason, *At. Data Nucl. Data Tables*, **22**, 179 (1978).
- <sup>41</sup> M. G. Thackston, F. L. Eisele, W. M. Pope, H. W. Ellis, I. R. Gatland and E. W. McDaniel, *J. Chem. Phys.*, **70**, 3996 (1979).
- <sup>42</sup> H. W. Ellis, R. Y. Pai, E. W. McDaniel, E. A. Mason and L. A. Viehland, *At. Data Nucl. Data Tables*, **17**, 177 (1976).

## Appendix A

### Glossary of Acronyms/Abbreviations

BS	Birge-Sponer
BSSE	Basis Set Superposition Error
CASSCF	Complete Active Space Self-Consistent Field
CI	Configuration Interaction
CM	Coinage Metal
CT	Charge Transfer
ECP	Effective Core Potential
FCF	Franck-Condon Factor
HOMO	Highest Occupied Molecular Orbital
IVR	Intramolecular Vibrational Redistribution
LaVa	Laser Vaporisation
LB	LeRoy-Bernstein
MCP	Microchannel Plate
MCPF	Modified Coupled Pair Functional
MRCI	Multi-reference Configuration Interaction
PEC	Potential Energy Curve
PES	Photoelectron Spectroscopy
<i>p</i> FT	<i>para</i> -fluorotoluene
RCCSD(T)	Restricted Coupled Cluster Singles Doubles (Triples)
REMPI	Resonance Enhanced Multiphoton Ionisation
RG	Rare Gas
RHF	Restricted Hartree-Fock
RKR	Rydberg-Klein-Rees
ROHF	Restricted Open-shell Hartree-Fock
RRKM	Rice-Ramsperger-Kassel-Marcus
SEVI	Slow Electron Velocity-map Imaging
SO	Spin Orbit

SOCAR	Spectroscopy of Complexes and Radicals
TOF	Time-Of-Flight
VMI	Velocity Map Imaging
ZEKE	Zero Electron Kinetic Energy
ZOBS	Zero-Order Bright State